Numerical modeling of micro-scale wind-induced pollutant dispersion in the built environment

Please check the document version of this publication:

• A submitted manuscript is the version of the article upon submission and before peer-review. There can be important differences between the submitted version and the official published version of record. People interested in the research are advised to contact the author for the final version of the publication, or visit the DOI to the publisher's website.
• The final author version and the galley proof are versions of the publication after peer review.
• The final published version features the final layout of the paper including the volume, issue and page numbers.

[Link to publication](#)

Numerical Modeling of Micro-Scale Wind-Induced Pollutant Dispersion in the Built Environment

PROEFSCHRIFT

ter verkrijging van de graad van doctor aan de
Technische Universiteit Eindhoven, op gezag van de
rector magnificus, prof.dr.ir. C.J. van Duijn, voor een
commissie aangewezen door het College voor
Promoties in het openbaar te verdedigen
op maandag 26 november 2012 om 14.00 uur

door

Pierre Gousseau

geboren te Douai, Frankrijk

Dit proefschrift is goedgekeurd door de promotoren:

prof.dr.ir. B. Blocken
en
prof.dr.ir. G.J.F. van Heijst

« It was something formidable and swift, like the sudden smashing of a Vial of Wrath. It seemed to explode all around the ship with an overpowering concussion and a rush of great waters, as if an immense dam had been blown up to windward. It destroyed at once the organised life of the ship by its shattering effect. In an instant the men lost touch of each other. This is the disintegrating power of a great wind. It isolates one from one's kind. »

Joseph Conrad, *Typhoon*

Summary

Despite recent efforts directed towards the development of cleaner and more efficient energy sources, air pollution remains a major problem in many large cities worldwide, with negative consequences for human health and comfort. If the transport of pollutants by wind in urban areas can be predicted in an accurate way, remedial measures can be implemented and the exposure of people and goods to pollution can be decreased to limit these negative effects. This prediction can be achieved by experimental techniques, on-site or in wind tunnels, but also numerically, with the use of Computational Fluid Dynamics (CFD).

In this thesis CFD is used to simulate wind-induced pollutant dispersion in the built environment. The accuracy of this approach in terms of pollutant concentration prediction always needs to be assessed. The reason is twofold. First, the wind flow around buildings is turbulent and cannot be solved exactly with CFD. This type of flow must therefore be approximated with so-called turbulence models. Second, various types of errors are present in the numerical solution and can affect its accuracy.

The Reynolds-Averaged Navier-Stokes (RANS) and Large-Eddy Simulation (LES) turbulence modeling approaches are the most widely used in computational wind engineering. They are compared in this thesis, and evaluated by comparison with reference wind-tunnel experiments. In the first part, several generic cases of simplified isolated buildings are considered and, in the second part, an applied case of pollutant dispersion in an actual urban area (part of downtown Montreal) is studied. In the computations, care is taken to accurately simulate three key aspects of urban pollutant dispersion: (1) the atmospheric boundary layer flow, (2) the wind flow around buildings, and (3) the dispersion process.

On average, the transport of pollutants by wind can be seen as the combination of, on the one hand, the transport by the mean flow and, on the other hand, the transport by the turbulent fluctuations. This decomposition is used here to evaluate the RANS – with various turbulence models – and LES approaches. Overall, the better performance of LES in terms of flow and concentration field prediction is demonstrated. In addition, LES has the advantage to provide the time-resolved velocity and concentration fields.

Given the good accuracy of LES, this approach is used to investigate the physical mechanism of pollutant dispersion for the case of a simplified isolated building. The vortical structures present in the shear layers developing from the roof and sides of the building are shown to play a crucial role in the turbulent mass transport process. LES used as a research tool also allows evaluating models employed with RANS for turbulent mass transport, which is often assumed to act as a diffusion mechanism. The results of this study show that this hypothesis is not always valid and in some cases the turbulent mass flux in the streamwise direction is directed from the low to high levels of mean concentration (counter-gradient diffusion).

Acknowledgements

Table of contents

Nomenclature

Abbreviations

ABL	Atmospheric boundary layer
CFD	Computational fluid dynamics
CG	Counter-gradient
CWE	Computational wind engineering
DNS	Direct numerical simulation
FAC2	Fraction of predictions within a factor of 2 of observations
FB	Fractional bias
GD	Gradient-diffusion
LES	Large-eddy simulation
LES_IQ	LES index of quality
NMSE	Normalized mean square error
Q	Quadrant
RANS	Reynolds-averaged Navier-Stokes
RLZ	Realizable k-ɛ model
RNG	Renormalization group k-ɛ model
RSM	Reynolds-stress model
SGMV	Systematic grid and model variation
SGS	Subgrid-scale
SKE	Standard k-ɛ model
SL	Stack location
SW	South-west
V&V	Validation and verification
VM	Vortex method
W	West

Notations

For a given variable x:

$X=<x>$	Time-averaged value
x'	Fluctuation
$\bar{x}$	Filtered value

Subscripts

avg	Average value

CFD	Numerical value
Exp	Experimental value
H	Value at building height
i	i-th component of the vector
in	Inlet value
k	k-th sample value
m	Molecular/modeling
max	Maximum value
med	Median value
min	Minimum value
n	Numerical
P	Value at the centroid of the wall-adjacent cell
rms	Root mean square
sgs	Subgrid-scale
t	Turbulent

Roman symbols

Variables followed by the subscript i (resp. ij) are the components of a vector (resp. tensor). The unit of Q_e varies depending on the chapter; it is explicitly mentioned when introduced.

B	Building side	m
c	Concentration	kg m^{-3}
C_0	Reference concentration	kg m^{-3}
C_r	Roughness constant	-
C_s	Smagorinsky coefficient	-
d	Distance to the closest wall	m
D	Mass diffusivity	m^2 s^{-1}
D_h	Hydraulic diameter	m
D_q	Hit-rate relative threshold	-
e	Error	Depends on variable
f	Frequency	-
H	Building height	m
h_c	Cell size	m
h_s	Stack height	m
k	Turbulent kinetic energy	m^2 s^{-2}
k_s	Roughness height	m
K_a	Kurtosis of a	-
K	Non-dimensional concentration coefficient	-
K_{inst}	Instantaneous non-dimensional concentration	-
L_x	Domain length	m

L_{int}	Integral length scale	m
M	Velocity ratio	-
n	Power-law exponent	-
N_v	Number of vortices (vortex method)	-
N	Number of samples	-
p	Pressure	Pa
q	Hit rate	-
q_i	Mass flux	kg m^{-2} s^{-1}
Q_0	Reference mass flux	kg m^{-2} s^{-1}
Q_e	Pollutant exhaust rate	kg s^{-1}; m^3 s^{-1}
$R_{u_i u_j}$	Cross-correlation coefficient	-
Re	Reynolds number	-
S	Characteristic strain rate	s^{-1}
S_{ij}	Strain rate tensor	s^{-1}
S_a	Skewness of a	-
s_c	Source in the dispersion equation	kg m^{-3} s^{-1}
Sc	Schmidt number	-
t	Time	s
T_{avg}	Averaging period	s
T_{ft}	Flow-through time	s
T_{init}	Initialization period	s
t_u	Time unit	s
t^*	Non-dimensional time ($=t/t_u$)	-
$u_i=(u, v, w)$	Velocity vector	m s^{-1}
u^*	Friction velocity	m s^{-1}
U_{ref}	Reference velocity	m s^{-1}
V_c	Cell volume	m^3
W_q	Hit-rate absolute threshold	Depends on variable
x	Streamwise coordinate	m
X_r	Rooftop recirculation length	m
X_w	Wake recirculation length	m
y	Lateral coordinate	m
y_{stack}	Lateral coordinate of the stack	m
z	Vertical coordinate	m
z_0	Aerodynamic roughness length	m
z^+	Wall units	-
z^*	Dimensionless wall distance	-
z_{ref}	Reference height	m

Greek symbols

α	Grid coarsening factor	-
β	Model variation factor	-
Δ	Filter width	m
Δt	Time step	s
ε	Turbulent dissipation rate	$m^2\ s^{-3}$
θ	Wind direction	° from north
$\varkappa$	von Karman constant	-
μ	Dynamic viscosity	$kg\ m^{-1}\ s^{-1}$
ν	Kinematic viscosity	$m^2\ s^{-1}$
ϱ	Density	$kg\ m^{-3}$
σ	Velocity standard deviation	$m\ s^{-1}$
τ_{ij}	(Subgrid-scale) Reynolds stress tensor	$m^2\ s^{-2}$
χ	Mass fraction	-

Chapter I
Introduction

I.1   Urban air pollution: a major environmental issue

Air pollution can be defined as the presence of contaminant or pollutant substances in the air at a concentration that interferes with human health or welfare, or produces other harmful environmental effects [www.europa.eea.eu, 2012]. The sources of pollution can be divided into natural sources such as forest fires or volcanoes and emissions due to human activities, also called anthropogenic sources. In the latter category, traffic and transportation in general, energy production, industry, and domestic fuel combustion are among the activities which contribute most to the pollution of air. They are mainly concentrated in cities, and are likely to be even more concentrated in the future, following the increasing urbanization of populations worldwide.

The populations living in cities are not only exposed to polluted air in the outdoor environment but also inside buildings where pollution can be transferred via ventilation. Indoor air quality deteriorates in this way, with negative effects on health and comfort of the building occupants [Jones, 1999]. In addition to inhalation, the transmission of pollutants also operates by the contamination of vegetation and water which are directly ingested by humans or indirectly via for instance meat, milk or seafood. The consequences of air pollution on human health are nowadays relatively well known. The contact, inhalation and ingestion of substances such as nitrogen oxides (NOx), carbon monoxide and dioxide (CO, CO_2), sulfur dioxide (SO_2), ozone (O_3), particulate matter (PM) or heavy metals can cause disturbances and diseases that go from eye irritation to premature mortality, depending on the type of pollutant(s) and the level of exposure. The cardio-vascular and respiratory systems are primarily affected by polluted air [Kampa and Castanas, 2008]. According to the World Health Organization, 2.4 million people die each year from causes directly attributable to air pollution [Monks et al., 2009]. In addition to these dramatic effects on human health, the effects of air pollution on climate and biodiversity are also important, as well as the impact of pollution on preservation of buildings and cultural heritage [Rabl, 1999]. In a recent report [EEA, 2011], the European Environment Agency has quantified the damage costs to health and the environment from pollutants emitted by industrial facilities in Europe: it is estimated to be at least 102-169 billion Euros for the year 2009, that is approximately 200-330 Euros on average for each European citizen.

Figure I.1. Three examples of visible air pollution. Left: the effect of wind on chimney smoke in Goteborg, Sweden [*flickr.com/Brintam*]. Middle: a smoggy day in Salt Lake City, USA [*flickr.com/InfiniteWorld*]. Right: urban air pollution in Shanghai, China [*flickr.com/gmoorenator*].

Awareness of these disastrous effects of air pollution was mainly established during the second half of the twentieth century and was at the origin of clean-air policies in developed countries. Some regulatory policies and technological advances allowed decreasing significantly the total emissions in Europe and North America but air quality remains problematic in many cities. In other regions of the world, in countries with fast-growing economies, the inverse trend is observed and the ever-increasing energy needs in constantly-growing cities are associated with considerable amounts of emissions. In Asia for example, the total emissions of NOx, SO_2, CO have been multiplied by a factor 2.8 from 1980 to 2003 [Chan and Yao, 2008].

It seems that the emissions of hazardous materials will remain a major concern for at least this century. Besides the efforts directed toward the development of more efficient and less polluting energy sources, understanding the transport of pollutants in the urban environment is needed in order to decrease the exposure of urban populations to polluted air and minimize the negative effects of pollution on health, buildings and goods. Once emitted by the various sources enounced earlier, the pollutant gases or particles are transported by the wind flow within the urban area – or accumulate due to the absence of wind. Precise knowledge of the source characteristics and of the chemical reactions possibly taking place, combined with the accurate prediction of the wind-induced pollutant dispersion should – ideally – allow determining the composition of the ambient air which is inhaled by the city-dwellers. However, the prediction of wind flow and dispersion in urban areas is known to be a complicated task due to the complexity of the physical phenomena and geometries involved. Several techniques exist to investigate this problem; they are exposed and briefly described in the next section.

I.2   Method

I.2.1   Three approaches to predict pollutant dispersion

Overall, the existing techniques to predict wind-induced pollutant dispersion can be classified into three categories:

1. Semi-empirical dispersion models;

2. Experiments (on-site or in wind-tunnel laboratories);

3. Numerical methods, including computational fluid dynamics.

Several examples of semi-empirical dispersion models are the ASHRAE dilution model [ASHRAE, 2007], or the Gaussian plume model [Sutton, 1947]. These models provide concentration estimates for dispersion from various types of sources. They are generally simple to use but their applicability is limited to simple configurations, with poor accuracy in more complex cases [Stathopoulos et al., 2004; Blocken et al., 2008; Hajra et al., 2010].

The experimental approach is still widely used in wind engineering. The field experiments have the advantage to measure dispersion on site, with modeling reduced to its strict minimum and can therefore be considered as the best representation of reality. However, such experimental campaigns are generally costly, time-consuming and complex to set up. The wind conditions (e.g. the wind speed and direction) are constantly changing, which renders the identification of the parameters influencing pollutant dispersion very difficult. A better control of the boundary conditions is possible with wind-tunnel modeling [Robins, 2003] and this is the reason why wind-tunnel measurements are often used for the validation of numerical models. Furthermore, this technique allows for a-priori testing, for instance in the design phase of a building before it is eventually built. However, in most cases the similarity requirements ensuring the same flow behavior at two different scales cannot be met due to the down-scaling of the model and the flow reproduced in the wind tunnel is therefore not strictly the same as in reality.

The numerical approach is the one which has been chosen in the present thesis to study wind-induced pollutant dispersion in the built environment, using Computational Fluid Dynamics (CFD). Note that non-CFD numerical tools such as the Atmospheric Dispersion Modeling System (ADMS) [www.cerc.co.uk, 2012] or the Quick Urban & Industrial Complex (QUIC) dispersion modeling system [www.lanl.gov, 2012] can also be used to solve urban dispersion problems but they have not been considered here. Like wind-tunnel experiments, a-priori testing is possible with CFD but without the need for reducing the scale of the model, which means that the simulation can potentially reflect exactly the same conditions as in reality. CFD also provides data everywhere in the domain under study, whereas experiments only provide information at specific locations

chosen beforehand by the experimentalist. Furthermore, a CFD simulation is relatively cheap and fast to conduct, allowing for parametric studies. The aforementioned advantages, combined with the fact that CFD applied to wind engineering problems (also called Computational Wind Engineering, CWE) is a relatively new technique with ongoing developments, motivated the choice of this approach to study pollutant dispersion in this project. However, as explained in more detail in the next section, in most cases CFD cannot provide the exact solution of the flow equations: the numerical solution is affected by several sources of error and more or less elaborate models are used in an attempt to represent the physics of the problem. The proof that the numerical solution is sufficiently accurate must be provided, often by comparing the numerical results to measurements provided by wind-tunnel experiments – whose accuracy should also be evaluated. Hence, the experimental and numerical approaches are used in a complementary way rather than being alternative techniques.

I.2.2   CFD and turbulence modeling

The equations that describe the motion of fluids, namely the Navier-Stokes equations, do not possess an analytical solution for a large majority of flow problems. With CFD, an estimation of the solution can be obtained by transforming the set of partial differential equations into a system of algebraic equations that can be solved with a computer. Among the existing discretization methods, the finite volume method is the one used in this thesis and described in the present section. As a first step of a CFD simulation, the geometry of the fluid-flow problem under study is reproduced and the resulting computational domain is decomposed into a number of control volumes (or cells). This ensemble of cells constitutes the computational grid. The grid quality, determined by the arrangement, size and shape of its cells, should be adapted to a particular flow as it plays a major role in guaranteeing the accuracy of the numerical solution. At the boundaries of the computational domain, the boundary conditions are defined by imposing the values of the variables or of their gradient.

With the finite volume method, the conservation laws (for pressure, velocity, pollutant gas concentration, etc.) are applied in their integral form to each cell. For a given cell, a discrete equation can be obtained by estimating each term of the conservation laws (generally: convective, diffusive and source terms) based on the variable values at its center and at the center of the neighboring cells. Various techniques exist to perform this interpolation and discretization step [Ferziger and Peric, 2002]; the choice is generally guided by considerations on the stability, rapidity and accuracy of the method. In the present work, the schemes used to discretize the flow equations will be enounced in the description of the numerical model for each simulation. The resulting system of algebraic equations is solved iteratively with the algebraic multi-grid technique [Ansys Inc., 2009]. In the end, the values of the variables at every cell are computed, which constitutes a discrete representation of the solution of the problem. The accuracy

of this solution strongly depends on the discretization schemes used and level of convergence reached within the iterative procedure (i.e. how the equations are solved).

Another important aspect that determines the accuracy of the flow field simulated with CFD is the appropriateness of the models used to represent the physical flow phenomena (i.e. which equations are solved). In particular, for wind engineering problems, modeling of turbulence is crucial because of the turbulent nature of the wind flow around buildings. When the importance of the non-linear term of the momentum equation is growing compared to the viscous effects – i.e. above a certain value of the Reynolds number (Re) – the flow becomes turbulent. In this case, it is characterized by the presence of unsteady three-dimensional structures with a large variety of time- and length-scales and causing a high degree of mixing in the flow (one can infer that this mixing will play a crucial role if some particles or pollutant gas are injected in the flow). The numerical simulation of turbulent flows which resolves the complete range of spatial scales, from the smallest (the Kolmogorov scale) to the largest one, is possible with Direct Numerical Simulation (DNS) but, because the cost of such a simulation increases as $Re^{9/4}$, it is limited to relatively low Reynolds numbers, much lower than those encountered in typical wind engineering problems (of the order of 10^6-10^7). Note however that a few earlier studies have applied DNS to idealized urban configurations such as building arrays [Coceal et al., 2007a; Coceal et al., 2007b; Lee et al., 2011] or isolated cubical buildings [Yakhot et al., 2006a; Yakhot et al., 2006b; Rossi et al., 2010], with Reynolds numbers up to 5.8×10^4. In a large majority of cases, a somehow simplified description of the flow can only be made, and the information that is lost by doing so is mimicked in what is usually referred to as turbulence modeling. Two main turbulence modeling approaches are generally used in CWE:

- Reynolds-Averaged Navier-Stokes (RANS);

- Large-Eddy Simulation (LES).

With RANS, the variables are decomposed into their mean value and their turbulent fluctuation, following the Reynolds decomposition. The flow equations are averaged and then solved in terms of the mean variables. When being averaged, new unknowns appear in the momentum equations: the Reynolds stresses, representing the effect of the turbulent fluctuations on the mean flow. The way in which these stresses are evaluated defines each particular model of the RANS approach. For example, transport equations for the individual components of the Reynolds-stress tensor are derived and solved with the so-called Reynolds-stress model. Often, the computation of these unknown stresses is performed via additional variables introduced in the problem and transport equations for these turbulence variables are solved in addition to the average flow equations. For example, the k-ε models – widely used in CWE – solve equations for the turbulent kinetic energy k and the turbulence dissipation rate ε together with the mean continuity and momentum equations. Note that in studies of air pollution the equation describing the dispersion of pollutant is also averaged, which introduces a new unknown in the

problem: the turbulent mass flux. Accurately modeling this type of flux is crucial for the RANS simulation of pollutant dispersion, as will be explained in more detail later. The RANS approach has the advantage to be relatively economical in terms of computing resources, while providing sufficiently accurate results for a wide range of engineering flows. However, a steady RANS approach only resolves the mean variables and, if needed, the fluctuations can only be estimated based on this information. The performance of RANS models is also known to deteriorate in flows where the influence of the unsteady flow patterns is high such as the flow around bluff bodies.

LES is the other turbulence modeling approach used in this thesis. As explained earlier, in order to simulate the behavior of the smallest scales of motion, an extremely fine computational grid would be needed which would make the simulation unaffordable from a computational point of view. Fortunately, contrary to the energy-carrying large eddies which are to a large extent determined by the geometry of the flow, the small eddies are known to have a more universal behavior, which means that they are not differing significantly from one flow configuration to the other, and have a relatively low influence on the transport of the conserved properties [Ferziger and Peric, 2002]. To take into account the largest scales of motions only, a filtering operator, corresponding to a local spatial averaging, is applied to the flow equations. The LES turbulence modeling approach consists in solving the resulting filtered equations and in modeling the effect of the scales that are smaller than the filter width – equal to the grid size with the finite volume method and implicit filtering – with a so-called subgrid-scale (SGS) model. LES solves the filtered flow equations in a time-dependent way, which allows describing the turbulent structures in the flow and their evolution in time. This is one of the reasons why LES generally performs better in simulating flows where unsteady turbulent patterns are important. For dispersion studies, this feature also gives access to the concentration statistics, for instance to the pollution peak at a given location in the city. Despite its numerous advantages, the use of LES was still marginal in CWE until recently because this turbulence modeling approach is rather demanding in terms of computing resources. Nowadays, computers able to afford LES computations on large computational grids are more widespread and the shift from steady turbulence models to the LES technique is progressively taking place.

The working principles of the RANS and LES modeling approaches are schematized for the case of air flow around a building in Figure I.2. The experimental approach is also represented, on the left-hand side of the drawing. One has to keep in mind that experiments also constitute a non-exact representation of the real flow field – which is essentially unknown – since they also involve modeling (e.g. of the ABL flow in the wind tunnel), as well as sampling and measurement error. Nevertheless, they constitute what Oberkampf and Trucano [2002] call "our best indication of reality" and this is the reason why they are often used as a reference for CFD validation. This comparison between numerical and experimental results will be performed for every simulation presented in this thesis as a way to evaluate the accuracy of the numerical
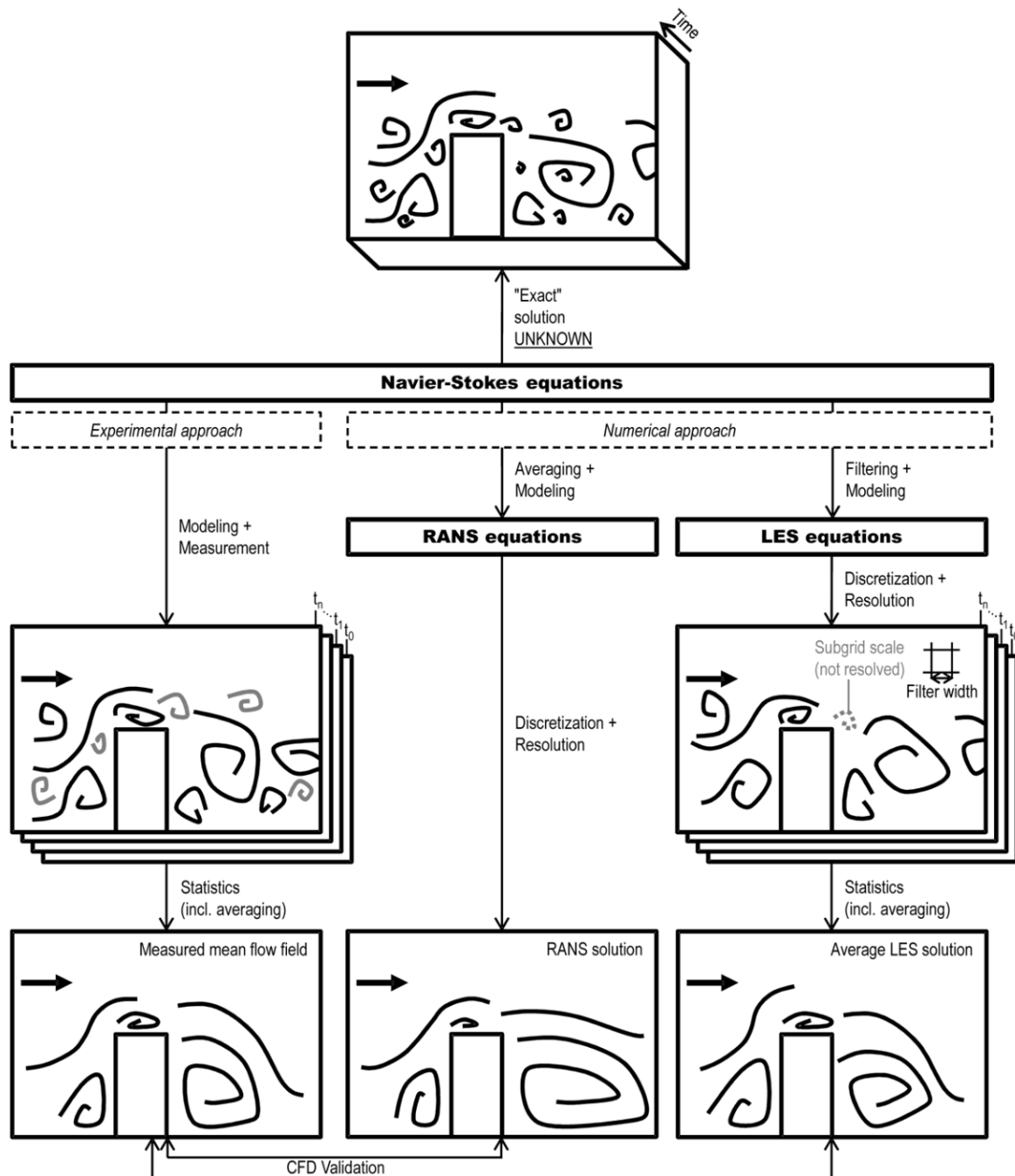
Figure I.2. Schematic illustration of the RANS and LES turbulence modeling approaches.

results and the relevance of the physical models. A numerical model which is proven to be accurate on a validation case can subsequently be applied with reasonable confidence to a case with similar properties whose solution is unknown. As indicated by the bottom horizontal arrows in Figure I.2, the CFD validation is performed via the statistics of the flow field, for example by comparing the measured and computed mean velocity or turbulent kinetic energy values at several locations of the flow domain. With RANS (middle column of Fig. I.2), this average flow field is a direct output of the model

whereas with LES (right column of Fig. I.2) the statistics are computed based on the instantaneous flow field at a certain number of successive time steps ($t_0,\ldots,t_n$).

I.3   Formulation of the problem

From a practical point of view, the relevant information that should be provided by wind-induced pollutant dispersion simulations is a quantification of the exposure of people and goods to polluted air. In other words, the simulation should provide the concentration field with sufficient spatial resolution (depending on the application) and, if possible, information about the time-behavior of the concentration field. Note that knowledge about the source and the meteorological conditions is needed to answer this question. The results can subsequently be used in the design phase of a building, for instance to determine which locations on a building facade are suitable to place the ventilation intakes or how high an exhaust stack should exceed roof height of a factory to avoid contamination of the pedestrians in the neighboring street. Remedial measures to improve the air quality in a problematic area can also be tested using CFD, for example to determine the required height of anti-pollution screens to be placed along a busy highway, or whether planting trees in a given street is likely to enhance pollutant removal by wind. Another application of CFD to dispersion problems is the simulation of emergency situations such as industrial accidents that would force the evacuation of the city inhabitants far from the most hazardous zones.

The possibility to use CFD to solve this kind of problems is already established and testified by the large number of scientific publications written on the topic. With the development of high-performance personal computers and the release of user-friendly and robust codes, performing CFD simulations is nowadays more accessible than ever. However, as explained in the previous section, the error in the numerical solution due to modeling and discretization can be significant and reporting CFD results should therefore include a proof of their accuracy or at least an estimation of how reliable they are. This is one of the focuses of the present thesis: to evaluate the accuracy of CFD applied to urban dispersion problems, and to determine which models (including the computational grid and the boundary conditions), computational settings and parameters can lead to accurate results.

Once the accuracy of a given CFD simulation is proven, for instance, by showing the good agreement of the numerical results with measurements of the same flow, the numerical model can be used to investigate a physical phenomenon which is not yet fully understood. This constitutes another aspect of the present thesis: to explore and analyze the complex processes of gas dispersion around bluff bodies like buildings in order to provide support for the development of new models and the selection of existing ones.

In summary, the present thesis constitutes an attempt to answer the following questions:

How are pollutants transported by the wind flow in the built environment?

Can CFD provide an accurate prediction of the wind flow and dispersion around isolated/multiple building(s)?

Which physical models are the most suitable to ensure accuracy of the simulation of pollutant dispersion around buildings?

I.4   CFD modeling of wind-induced pollutant dispersion in urban areas: the key aspects

Wind-induced pollutant dispersion is a complex problem involving physical phenomena at various scales. When simulating it with CFD, one can distinguish several key aspects listed hereafter and schematized in Figure I.3. They must all be considered with equal care in the numerical simulation to ensure the accurate prediction of pollutant dispersion.

1. Simulation of the atmospheric boundary layer;
2. Simulation of the wind flow in the built environment;
3. Simulation of the dispersion process;
4. Modeling of the source.

   Note that while these four aspects are considered separately in the present section in order to clarify the presentation of the problem, they strongly interact in reality and can hardly be tackled separately. As an example, it is known that the features of the flow around an isolated building strongly depend on the incident flow characteristics such as the boundary layer height or the level of turbulence [Castro and Robins, 1977; Tamura, 2008].

   The modeling of the source will not be treated in the present thesis: in all the cases studied here, the characteristics of the pollutant source (geometry, exhaust rate, composition, etc.) are considered to be known from the experiment that is reproduced.
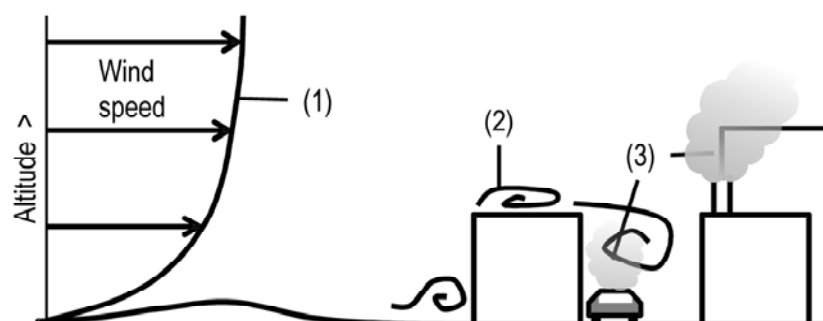
Figure I.3. The three components of the pollutant dispersion simulation: (1) simulation of the ABL; (2) simulation of the wind flow around buildings; and (3) simulation of the dispersion process.

For practical applications however, this is often a crucial point. For example, in the study of dispersion of vehicle exhaust gases, one has to create a computational model for the shape, composition and intensity of the source depending on the traffic conditions, the location of the considered street and various other parameters. Another example is the complex problem of modeling accidental releases.

The three other elements constituting the problem under study are briefly described in this section. Considering the dense literature existing on each of these three topics, it is clear that this section is not intended to provide an exhaustive description or review. Rather, the aim is to introduce important concepts used in the core of this thesis, to precise its scope and to state the assumptions made. A concise literature review is also given, focusing on the CFD studies. A more precise review discussing the material relevant to each chapter is given in the introduction of each individual chapter.

I.4.1   *Simulation of the wind flow in the atmospheric boundary layer*

In micro-scale urban dispersion studies, horizontal scales of motions below 5 km are considered. This, combined with the fact that the pollutant source is usually located close to the ground, allows limiting the modeling of the atmosphere to its lower part, namely the atmospheric boundary layer (ABL). In the ABL, the flow is driven by the geostrophic wind flowing above and is at the same time largely influenced by the ground surface. Thus, the ABL characteristics (e.g. its height, the velocity and turbulence intensity distribution, etc.) will significantly differ depending on the type of terrain, for example if we consider wind flow over sea, forest or a city with many buildings. Each of these terrain types is characterized by a specific roughness quantifying the resistance that the terrain opposes to the wind flow. It is usually expressed in terms of the aerodynamic roughness length (z_0) or the equivalent sand-grain roughness height (k_s). Temperature stratification is another important feature determining the structure of the ABL. When the potential temperature is decreasing with height, buoyancy effects tend to increase the level of turbulence due to velocity gradients: this is the so-called unstable (or convective) ABL. Inversely, the turbulence generated by shear is damped by buoyancy when the potential temperature is increasing with height: this corresponds to the stable case. When the potential temperature is constant with height or, more generally, when buoyancy effects are negligible compared to shear – which generally occurs at high wind speeds – the ABL is said to be neutral. Despite the high influence of temperature stratification on pollutant dispersion, the neutral ABL remains the most studied case, experimentally and numerically. This case is also the one considered in the present thesis.

The characteristics of the ABL are generally an input of the CFD model applied to micro-scale dispersion studies, via the boundary condition imposed at the upstream extremity of the computational domain, namely the inlet. Proper numerical simulation of the ABL flow can be summarized into two crucial requirements: first, prescribing

appropriate ABL characteristics representative of the full-scale configuration (or of the wind-tunnel experiment in case of validation study) and, second, preserving these characteristics along the upstream part of the computational domain to ensure that the flow that is prescribed at the inlet of the domain is eventually the one flowing at the location of the obstacles and/or pollutant source. These two aspects are treated differently, depending on which turbulence modeling approach is used.

With RANS, the mean velocity profile has to be prescribed at the inlet of the computational domain, as well as the mean temperature profile in the case of stratified flow, and the variables used to model turbulence. When the CFD results are intended to be compared to wind-tunnel measurements, these profiles are usually identical to those provided by the experimental report. In studies where measurements of the wind flow are not available, the terrain, the meteorological conditions, and some known characteristics of the site under study (e.g. the predominant wind direction given by the wind rose) will be taken into account to provide a realistic model for the ABL. The Monin-Obukhov similarity theory [Monin and Obukhov, 1959] is often applied for this purpose; it provides the vertical evolution of the mean velocity and turbulence quantities. For the neutral ABL, the mean velocity profile is generally described by a logarithmic law (see also [Tennekes, 1973]). Note that in a large majority of CFD studies the logarithmic velocity profile is assumed to be valid on the whole height of the computational domain whereas in real urban areas, because of the presence of buildings, it is valid only above a certain height known as the displacement height. A power-law can also be used to describe the ABL mean velocity profile in the neutral case; it has the advantage to be easier to fit to experimental data.

In general, the ABL profiles prescribed as an inflow boundary condition do not correspond to the exact solution of the equations solved by a particular RANS turbulence model and this is one of the reasons why a degradation of the prescribed profiles along the computational domain is observed. One way to counteract this effect is to impose ABL profiles which are known to be an exact solution of the RANS equations (e.g. [Richards and Hoxey, 1993] for the standard k-ε model) possibly modified via the adjustment of the model constants [Richards and Hoxey, 1993; Alinot and Masson, 2005; Gorlé et al., 2009] or the addition of source terms [Pontiggia et al., 2009]. The boundary conditions imposed at the external faces of the domain must also be adapted to the ABL flow, for example by imposing the velocity value at the top of the domain or by correctly taking into account the roughness in the wall functions that compute the variables in the cells adjacent to the ground surface [Blocken et al., 2007a; Blocken et al., 2007b; Hargreaves and Wright, 2007].

With LES the flow equations are resolved in a time-dependent manner, so an instantaneous velocity profile must be prescribed at the inlet of the domain at each time step of the simulation, while ensuring that the statistics of the target ABL are verified. Adding random noise on top of the average velocity profile is known to perform poorly
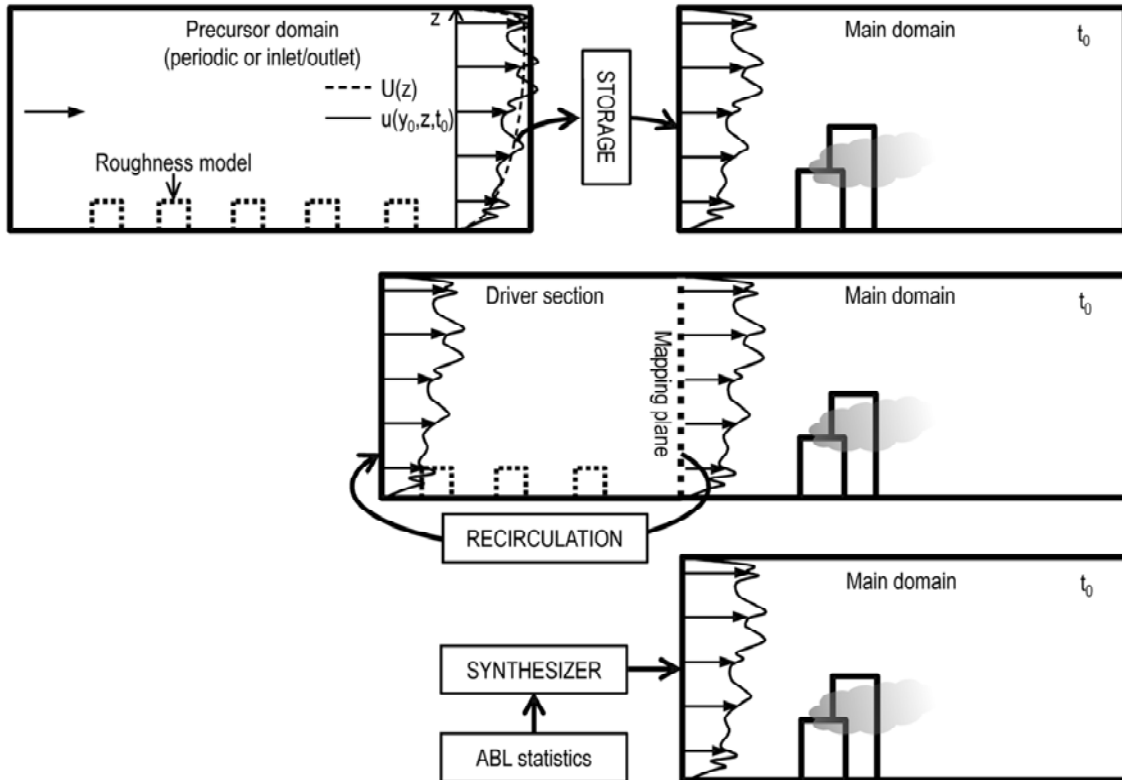
Figure I.4. The three methods used in CWE to generate a turbulent inflow with LES.

because the absence of coherent motion results in a rapid decrease of turbulence. A review of three techniques which are commonly used in CWE can be found in [Jiang et al., 2012] and are depicted in Figure I.4. The first one consists in simulating – prior to the "main" simulation – the ABL flow in a precursor domain. Periodic boundary conditions are often used in the streamwise and spanwise directions. The roughness of the ground surface can be implemented via a suitable wall model that generally relates the shear stress at the wall to the velocity at the wall-adjacent cells (e.g. [Schumann, 1975; Moeng, 1984; Thomas and Williams, 1999; Xie et al., 2004a; Xie et al., 2004b]) or, in the case of a wind-tunnel flow, by modeling explicitly the roughness elements used in the test section. Then, the three velocity components are sampled in a cross-plane of the precursor domain, stored and finally prescribed as an inflow of the main simulation. Examples of the application of this technique can be found in [Tominaga et al., 2008a; Yoshie et al., 2011]. The accuracy of the precursor method in terms of turbulence statistics is high but it demands a significant additional amount of computational time for the precursor simulation. Another turbulent inflow generation technique consists in adding extra length to the computational domain upstream of the model to be tested and imposing recirculation of the flow on this length. This cyclic treatment of the flow in the so-called driver section mimics a long domain which allows obtaining a fully-developed ABL flow and a realistic time-dependent velocity field at the inlet of the main simulation. This technique was first introduced by Lund et al. [1998] for general boundary layer flows and revisited in [Kataoka and Mizuno, 2002; Nozawa and Tamura, 2002] for atmospheric

applications. Finally, the so-called synthetic methods can be used to generate ABL inflow turbulence. In this case, neither additional simulation nor extra domain length is required and the velocity fluctuations super-imposed to the mean velocity profile are directly computed, based on information about the turbulence spectrum [Maruyama et al., 1999; Xie and Castro, 2008] or about the intensity of the velocity fluctuations [Mathey et al., 2006].

Once the ABL profiles are generated and prescribed at the inlet of the domain, the same problem as the one encountered with the RANS approach about preserving the ABL characteristics along the domain arises. Explicit modeling of simplified buildings around the area of interest is one option [Xie and Castro, 2009]. Implicit treatment of the roughness is also possible and is often implemented by imposing the wall shear stress at the ground. This technique is however generally used in empty domains with periodic streamwise boundary conditions and to the author's knowledge it is seldom applied when a building model is present in the domain and inlet/outlet type boundary conditions are used. Reducing as much as possible the empty length of the domain upstream of the building model is then necessary to limit the longitudinal degradation of the inlet profiles.

I.4.2   Simulation of the wind flow in the built environment

Overall, the configurations encountered in the wind engineering literature correspond either to real urban areas or to simplifications of the urban environment. The simulation of pollutant dispersion in real cities (see Chapter V for several examples from literature) usually corresponds to applied studies whose objective is to predict the polluted zones for a release in a particular urban configuration. In this case, the path of pollutants among the multiple buildings is complex and not evident to predict beforehand. These simulations are usually expensive in terms of computational resources due to the high dimensions of the domain, the large number of buildings to model and the large range of scales involved. The validation of CFD simulations for this type of configurations is not always possible because wind-tunnel measurements of dispersion in real urban areas are rare. Such a validation study will be presented in this thesis, in Chapter V, for the case of downtown Montreal, Canada. The corresponding wind-tunnel experiment [Stathopoulos et al., 2004] has been selected because it focuses on the near-field dispersion, with measurements of pollutant concentration on the roof of the emitting building, which corresponds to a region where the concentrations are high and particularly challenging to predict.

The CFD studies which are aiming at validating numerical models and/or exploring the physical mechanism involved in pollutant dispersion are often performed on simplified urban geometries. Figure I.5 shows three examples of generic configurations that are the object of many experimental and numerical studies in the literature: the isolated building, the street canyon, and the array of buildings. In terms of generic configurations, this report – as well as the present section – has been chosen to focus on
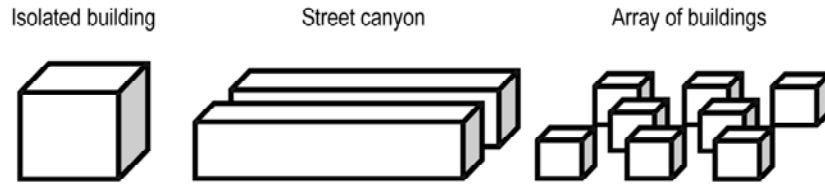
Figure I.5. Three examples of common generic configurations in wind engineering: (a) the isolated building; (b) the street canyon; and (c) the array of buildings.

the isolated building configuration with the incoming wind flow perpendicular to the windward facade (Chapter II, Chapter III and Chapter IV). Despite the limitations implied by the choice of this geometry and flow incidence, this configuration has been selected because it is very well documented and it is expected to reveal the fundamental flow mechanisms involved in dispersion around bluff bodies. Note that an attempt to link the results of the two types of configurations (idealized and real urban areas) is made in Chapter VI.

Figure I.6 depicts in a schematic way the flow patterns around a wall-mounted cubical obstacle (comparable to a building model in our case) immerged in a wind flow. This figure is extracted from [Peterka et al., 1985] and adapted from [Hunt et al., 1978]. Knowledge about this type of flow was first provided by wind-tunnel experiments; many of them are reviewed in detail in [Hosker Jr., 1984]. When approaching the obstacle, the flow decelerates in the streamwise direction and accelerates laterally and vertically. Because of the vertical velocity gradient characterizing the ABL flow, the stagnation pressure on the upper part of the windward facade is higher than the one on its lower part, which creates a downward flow and explains the presence of a horizontal-axis standing vortex around the basis of the windward facade. The intensity and size of this vortex depends on the geometry of the building (e.g. width-to-height ratio) and on the intensity of shear in the incoming flow. The incident flow trails the standing vortex on the sides of the building, which gives it its characteristic horseshoe shape. Flow detachment occurs at the front edges of the building, leading to the presence of backflow regions on the roof and sides of the building. Reattachment can possibly take place, depending on the geometry of the building. A large recirculation zone is observed in the wake of the building; its size can vary up to several building heights, depending on the building shape and the characteristics of the approaching flow [Castro and Robins, 1977]. It should be noted that the aforementioned patterns correspond to an average picture of the flow. In reality, they are not fixed in time because of the turbulent fluctuations present in the flow.

An appropriate CFD simulation of the wind flow around a building must be able to reproduce these characteristics. In this respect, LES generally performs better than the RANS turbulence modeling approach [Murakami, 1993; Rodi, 1997; Tominaga et al., 2008a]. The main reason is that the flow patterns described above correspond to the mean flow, i.e. the average on a large number of instantaneous states with very complex
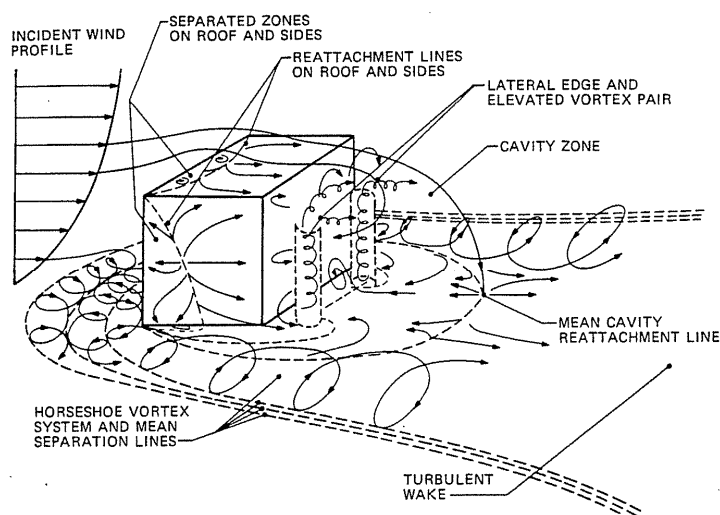
Figure I.6. Mean flow patterns around a wall-mounted cube immerged in an ABL flow [Peterka et al., 1985].

structure resulting from both the ABL and building-generated turbulence. While LES is able to reproduce these instantaneous flow patterns (under certain conditions and proper use, see Chapter II), steady RANS models cannot retrieve the information which is lost by averaging the flow equations, resulting in a loss of accuracy on the prediction of the mean flow.

Even if dispersion in the built environment is primarily affected by the presence of buildings, it can also be altered by some other elements constitutive of urban areas. Vegetation is one of them. Several studies in the literature have focused on the way in which trees can affect flow and dispersion, both with experimental and numerical approaches (e.g. [Gromke et al., 2008; Endalew et al., 2009; Salim et al., 2011b]). However, it will not be considered in the present study. Besides being a source of pollutant gases, circulating vehicles generate turbulence by their motion and have in this way a significant effect on dispersion [Bäumer et al., 2005; Solazzo et al., 2008]. Traffic-induced turbulence is also considered out-of-scope for the present study.

I.4.3   Simulation of the dispersion process

Modeling of dispersion is either performed with the Lagrangian or the Eulerian approach. The former consists in following (tracking) the fluid particles in their motion. This method is powerful and has been used to derive statistical theories of turbulent diffusion but the Lagrangian governing equations are complex, which explains why this approach is less used in applied studies of urban pollutant dispersion [Kao, 1984]. In this framework, a good estimate for the Lagrangian time scale is needed to ensure accurate simulation of dispersion [Gorlé, 2010].

The Eulerian approach is the one which has been selected for the present study. The pollutant concentration is treated as a scalar transported by an advection-diffusion

equation. It should be noted that, in order to guarantee fidelity between the CFD simulations presented in this thesis and the corresponding wind-tunnel experiments, the properties of the tracer gases – different from those of air – have been taken into account in the numerical model. Despite the low concentrations of tracer gases considered in the various cases (except for Chapter III) and the fact that the flows will be modeled under isothermal conditions and without chemical reactions, the pollutant concentration is not strictly a "passive scalar" in the sense that it influences the flow.

In the CFD model, the dispersion equation is either averaged with RANS or filtered with LES before being solved, in the same way as the Navier-Stokes equations. This operation results in the emergence of new unknowns (the turbulent and SGS mass flux for RANS and LES, respectively) which have to be modeled in order to close the problem. With LES a model is needed for the effect of the scales that are smaller than the filter width on dispersion. By analogy, since with RANS only the mean flow is resolved, the way in which the velocity fluctuations affect the transport of pollutant must be modeled. Modeling of the turbulent mass flux with this turbulence modeling approach will be shown to be crucial in guaranteeing the accuracy of the numerical solution. The gradient-diffusion hypothesis, assuming the turbulent mass flux to be proportional and opposite to the mean concentration gradient, is often used in CWE. Its formulation is simple and, when implemented in the CFD code, it shows good numerical stability without requiring significant additional computational cost. With this model, the dimensionless parameter known as the turbulent Schmidt number has a high influence on the results [Tominaga and Stathopoulos, 2007; Blocken et al., 2008]. This issue will be addressed at several occasions in this thesis, in Chapter III and Chapter V for instance. More elaborate models for the turbulent mass flux are reviewed and implemented for passive scalar transport in [Izarra, 2009], including the algebraic models by [Daly and Harlow, 1970] (generalized gradient-diffusion model), [Launder, 1988], [Abe and Suga, 2001], [Younis et al., 2005] and [Abe, 2006]. In comparison with the simple gradient-diffusion hypothesis, these models constitute a better representation of the physics of turbulent transport by relating the flux to the mean gradient via a tensor diffusivity which is a function of the Reynolds stresses and, for the models by [Launder, 1988] and [Younis et al., 2005], of the mean velocity gradients. In this way, the anisotropy of turbulent transport can be taken into account. Note that these models have rarely been applied to pollutant dispersion studies; see [Rossi and Iaccarino, 2009; Rossi et al., 2010] for recent examples.

It should be mentioned that chemical reactions which can take place in the atmosphere are not considered in the present study. They can be implemented by the addition of source and sink terms in the dispersion equation. The process of deposition is not taken into account either. Furthermore, the dispersion of dense gases – for which the buoyancy forces are dominant (see e.g. [Robins et al., 2001a; Robins et al., 2001b; Mokhtarzadeh-Dehghan et al., 2012]) – is not studied in this thesis. Finally, the fact that the transport of scalars in turbulent flows is generally described by a similar equation as

the one considered here for concentration is noteworthy: it extends the applicability of our study to other scalars (for example temperature for heat transfer studies, provided that the buoyancy effects are taken into account).

I.5   Structure of the thesis

The core of the thesis is divided into two parts. Part 1 (p. 19) is composed of Chapters II to IV and their appendices and deals with the simulation of flow and dispersion around idealized buildings. Pollutant dispersion in an actual urban area is considered in Part 2 (p. 101), containing Chapters V and VI. A general conclusion (Chapter VII) is intended to summarize the results of all chapters and to provide some recommendations for future work.

The next five chapters of this thesis correspond to articles which have been published (Chapter III, Chapter IV and Chapter V) or submitted (Chapter II and Chapter VI) to peer-reviewed international journals, with some minor changes such as adapting the notations to ensure homogeneity between the chapters. Some complementary results are presented in the two appendices at the end of Part 1. Additional remarks, or cross-references between the chapters are made via footnotes, in order to preserve the original content of the articles. The corresponding reference is mentioned in each chapter heading page and the co-authors are gratefully acknowledged here:

Chapter II to Chapter VI:

− Prof.dr.ir. Bert Blocken from the Department of the Built Environment (unit Building Physics & Services) of Eindhoven University of Technology (Eindhoven, The Netherlands).

− Prof.dr.ir. GertJan van Heijst from the Department of Applied Physics (Fluid Dynamics Laboratory) of Eindhoven University of Technology (Eindhoven, The Netherlands).

Chapter V and Chapter VI:

− Prof. Ted Stathopoulos from the Building, Civil and Environmental Engineering Department of Concordia University (Montreal, Canada).

The valuable comments of Dr.-Ing. Jörg Franke from Siegen University (Germany) on the manuscript of Chapter II are also gratefully acknowledged.

The thesis is therefore composed of self-contained chapters which can be read independently. This implies however the possibility of over-lapping information between chapters, especially concerning the method description.

− Chapter II (p. 21) presents the validation and solution verification of the LES computation of wind flow around a high-rise building. The accuracy of this turbulence modeling approach is evaluated and analyzed. In Appendix A (p. 89),

the same case is simulated with two RANS models to provide support for the following chapters.

– Chapter III (p. 47) reports a detailed analysis of the performance of RANS and LES applied to two cases of pollutant dispersion around isolated buildings. The relative effects of the mean and turbulent flow fields on dispersion are weighted. The streamwise counter-gradient mechanism of turbulent mass transport is identified.

– Chapter IV (p. 71) uses LES to further analyze one of the cases simulated in the previous chapter. The concentration and velocity statistics are analyzed in detail and some insight into the dispersion process is provided in this way. The influence of the vortical structures on turbulent dispersion is demonstrated, and illustrated in more detail in Appendix B (p. 97) where some complementary results are presented.

– Chapter V (p. 103) deals with the simulation of dispersion in a real urban environment with multiple buildings (downtown Montreal, Canada) and emphasizes the challenges proper to applied cases. The RANS and LES turbulence modeling approaches are evaluated and compared. With the former, the high influence of the turbulent Schmidt number is underlined.

– Chapter VI (p. 123) constitutes an attempt to link the results obtained on the generic cases of isolated buildings to the applied case of dispersion in downtown Montreal. It supports the study of environmental processes on simplified configurations.

Part 1

Idealized Buildings

Chapter II
Large-Eddy Simulation of wind flow around an isolated building

P. Gousseau, B. Blocken, G.J.F. van Heijst
Quality assessment of Large-Eddy Simulation of wind flow around a high-rise building:
Validation and solution verification

When undertaking wind engineering problems such as urban pollutant dispersion or pedestrian wind comfort with Computational Fluid Dynamics, an accurate simulation of the flow field around buildings is required. In this respect, the good performance of Large-Eddy Simulation has already been established but because the formulation and the use of this turbulence modeling approach are complex, the uncertainty on the results is relatively high. This implies the need for validation and verification (V&V) studies like the one performed in the present chapter for the wind flow around an isolated high-rise building with aspect ratio 1:1:2. In the first part of the study, the numerical results are compared with measurements from a reference wind-tunnel experiment and the agreement is quantified by validation metrics. The vortex method to generate inflow turbulence is shown to provide accurate results. Unexpectedly, the best agreement with the experiments is obtained on the coarsest computational grid, with 20 cells per building side, while a finer grid with 30 cells per building side over-estimates the turbulent kinetic energy measurements. A similar result was also found by earlier studies for different flow configurations. In the second part of the study, solution verification is performed. The Systematic Grid and Model Variation technique is used to provide estimates of the modeling and numerical error contributions. The LES_IQ indicator shows that a grid with 20 (resp. 30) cells per building side allows resolving 80% (resp. 91%) of the total turbulent kinetic energy in the region around the building.

II.1 Introduction

Computational Fluid Dynamics (CFD) is increasingly used to solve wind engineering problems such as pollutant dispersion in the built environment, pedestrian wind comfort, wind loads on buildings or natural ventilation of buildings [Hanna et al., 2006; Yoshie et al., 2007; Nozu et al., 2008; Blocken et al., 2012; Ramponi and Blocken, 2012]. In all these cases, an accurate simulation of the wind flow around buildings by the CFD model is needed. This is the reason why – supported by the increase of computational power – the use of the Large-Eddy Simulation (LES) turbulence modeling approach is nowadays becoming more widespread in Computational Wind Engineering (CWE). Several earlier studies [Murakami, 1993; Rodi, 1997; Shah and Ferziger, 1997; Tominaga et al., 2008a], have indeed demonstrated that LES can provide an accurate description of the mean and instantaneous flow field around bluff bodies like buildings. In general, it performs better than the Reynolds-Averaged Navier-Stokes (RANS) turbulence modeling approach[1], at the expense of much larger requirements in terms of computational resources.

Most of the aforementioned studies have established the good performance of LES based on comparison of the numerical results with measurements, often provided by wind-tunnel experiments. However, despite the increasing attention given to the quantification of error and uncertainty in CFD, the techniques that have been developed for general fluid engineering problems to assess the quality of CFD simulations are still marginally used in CWE [Franke, 2010]. This is particularly true for LES.

The aim of the present study is to provide a Validation and Verification (V&V) study of the LES computation of wind flow around an isolated building. To the best of the authors' knowledge, this V&V strategy that has been developed for general fluid engineering problems has not yet been applied to such a flow.

Validation is defined as "the process of determining the degree to which a model is an accurate representation of the real world from the perspectives of the intended uses of the model" [AIAA, 1998]. It will be performed here by comparing the numerical results with the measurements from a reference wind-tunnel experiment and by quantifying the agreement with validation metrics (Section II.4). The influence of the subgrid-scale (SGS) model and grid resolution will be assessed. In particular, the standard and dynamic Smagorinsky SGS models will be compared and, for the former, an appropriate value for the Smagorinsky coefficient will be determined in what is usually referred to as "calibration" in the V&V process [AIAA, 1998].

Verification is defined as "the process of determining that a model implementation accurately represents the developer's conceptual description of the model and the solution to the model" [AIAA, 1998]. Note that other definitions for the terms "validation" and "verification" can be found for example in [Casey and Wintergerste,

---

[1] See Appendix A.

2000] or [Srebric and Chen, 2002]. The process of verification is twofold: on the one hand the code verification and on the other hand the solution verification [AIAA, 1998; Roache, 1998; Oberkampf and Trucano, 2002] The former will not be treated here: the CFD code used is a commercial code (Ansys/Fluent 12.1) and is assumed to be verified in the development process. The solution verification will be performed in four steps:

1. Evaluating the turbulent inflow generation technique. Here, the Vortex Method (VM) [Sergent, 2002; Mathey et al., 2006] is used. Besides testing the influence of inflow turbulence on the flow field around the building (validation), a posteriori verification will be performed indicating that the mean inflow is a good representation of the experimental one (Section II.4.1).

2. Assessing the statistical convergence of the numerical solution. The LES results are compared to the measurements in terms of mean values. It will be verified that the first moments of velocity are sufficiently converged (Section II.5.1).

3. Evaluating the modeling and numerical error contributions in the LES solution. For basic flows at low Reynolds numbers, this can be achieved using Direct Numerical Simulation (DNS) results [Vreman et al., 1996; Geurts and Fröhlich, 2002; Meyers et al., 2003]. However, in the present study the high Reynolds number of the flow prohibits the application of DNS so a multi-grid technique is used: the Systematic Grid and Model Variation (SGMV) [Klein, 2005; Freitag and Klein, 2006; Klein et al., 2008; Celik et al., 2009] (Section II.5.2).

4. Evaluating the proportion of the total turbulent kinetic energy which is resolved by the LES model with the LES Index of Quality (*LES_IQ*) [Celik et al., 2005; Celik et al., 2006; Celik et al., 2009] (Section II.5.3).

The reference experiment that will be reproduced with CFD is described in the next section. Next, the computational model is outlined, before presenting and analyzing the results.

II.2   Description of the experiment

The wind-tunnel experiment by Meng and Hibi [1998] is used as a validation experiment. A building with dimensions $B \times B \times H$ ($B=H/2=0.08$ m) in the streamwise (x), lateral (y) and vertical (z) direction, respectively, is placed in the test section of a wind tunnel where an atmospheric boundary layer (ABL) flow is simulated. The Reynolds number based on B and the mean velocity of the incident flow at building height (U_H) is equal to 2.4×10^4. The origin of the coordinate system is the center of the building's ground face. The streamwise turbulence intensity at $z/B=0.125$, 2 and 7.5 is equal to 22.8%, 18% and 4.5%, respectively. The undisturbed ABL profiles of mean streamwise velocity ($U=\langle u \rangle$), standard deviation of velocity in the three directions (σ_u, σ_v, σ_w) and shear stress ($-\langle u'w' \rangle$,

where $u_i'=u_i-U_i$ denotes the fluctuation of the velocity in the direction x_i) are provided in the experimental report.

The mean (U, V, W) and standard deviation of the three velocity components have been measured with a constant-temperature anemometer with split-fiber probe at 186 points around the building. 66 of these points are in the vertical mid-plane $y/B=0$, hereafter denoted by V0. Two horizontal planes at $z=1$ cm (H1; $z/B=0.125$) and $z=10$ cm (H10; $z/B=1.25$) contain 60 additional measurement points each. In each plane, the points are distributed along 9 lines at $x/B=-0.75$; -0.5; -0.25; 0; 0.5; 0.75; 1.25; 2; 3.25. Because of space limitations, the graphical comparison (profiles) of experimental and numerical data will be performed only in the planes V0 and H10 for a limited number of points (5 out of 9 measurement lines per plane) and variables (U and the turbulent kinetic energy $k=0.5\times(\sigma_u^2+\sigma_v^2+\sigma_w^2)$). The validation metrics, however, take into account all the data points. Note that this experiment has been reproduced with CFD before by Tominaga et al. [2008a]; their LES results will also be used in our study for comparison purposes.

II.3   Computational model

II.3.1   LES modeling

The commercial CFD code Ansys/Fluent 12.1 is used here, with LES as a turbulence modeling approach. The filtered incompressible Navier-Stokes equations are given by:

$$\frac{\partial \bar{u}_i}{\partial x_i}=0 \tag{II.1}$$

$$\frac{\partial \bar{u}_i}{\partial t}+\bar{u}_j\frac{\partial \bar{u}_i}{\partial x_j}=\frac{\partial}{\partial x_j}\left(\nu\frac{\partial \bar{u}_i}{\partial x_j}\right)-\frac{1}{\varrho}\frac{\partial \bar{p}}{\partial x_i}-\frac{\partial \tau_{ij}}{\partial x_j} \tag{II.2}$$

where the overbar denotes the filtering operator (with filter width equal to grid size), ϱ and ν are the air density and kinematic viscosity, respectively, p the pressure and τ_{ij} the components of the SGS stress tensor:

$$\tau_{ij}=\overline{u_i u_j}-\bar{u}_i\bar{u}_j \tag{II.3}$$

The Smagorinsky SGS model [Smagorinsky, 1963] is applied to close the system of equations and determine the SGS stresses via the SGS turbulent viscosity ν_{sgs} and the filtered rate of strain $\bar{S}_{ij}=(\partial\bar{u}_i/\partial x_j+\partial\bar{u}_j/\partial x_i)/2$:

$$\tau_{ij}-\frac{1}{3}\tau_{kk}\delta_{ij}=-2\nu_{sgs}\bar{S}_{ij} \tag{II.4}$$

with:

$$\nu_{sgs}=L_{sgs}^2\bar{S} \tag{II.5}$$

where $\bar{S}=(2\bar{S}_{ij}\bar{S}_{ij})^{1/2}$ is the characteristic filtered rate of strain and $L_{sgs}=\min(\varkappa d, C_s V_c^{1/3})$ is the SGS mixing length, with $\varkappa$ the von Karman constant, d the distance to the closest wall, V_c the volume of the computational cell and C_s the Smagorinsky coefficient. Note that Equation (II.2) corresponds to the momentum equation filtered with a uniform filter width and the commutation error that arises when filtering the equation on a non-uniform grid is neglected [Manickam et al., 2012].

The distinction is made here between the so-called standard Smagorinsky model, where C_s is a user-prescribed constant, and the dynamic version [Germano et al., 1991; Lilly, 1992], where C_s is computed at each time step with a test-filter (whose width is twice the grid size) and clipped to the range [0; 0.23] to avoid numerical instabilities [Ansys Inc., 2009]. These two versions of the model will be used and compared in the present study. For the standard version, two different values of C_s will be tested: 0.1 and 0.15. They belong to the range of values that can be found in the literature for the simulation of flow around a bluff body, e.g. 0.1 in [Rodi et al., 1997; Rodi, 1997; Thomas and Williams, 1997; Lim et al., 2009; Xie and Castro, 2009], 0.12 in [Murakami, 1993; Tominaga et al., 2008a; Tominaga and Stathopoulos, 2010; Tominaga and Stathopoulos, 2011], or 0.16 in [Tseng et al., 2006]. Note that the simulations with these two model coefficients will be used in the solution verification procedure to evaluate the modeling error (Section II.5.2).

II.3.2   Computational domain and grid

The computational domain has been created and meshed with the Gambit software following the surface-extrusion technique [van Hooff and Blocken, 2010]. The domain dimensions are $2.64 \times 0.9 \times 0.9$ m³ (Fig. II.1-a), with a distance of $4H$ between the inflow boundary and the windward facade of the building. This value is set slightly below the recommendations by COST Action 732 [Franke et al., 2007] and AIJ [Tominaga et al., 2008b] guidelines in order to limit the deterioration of the prescribed inflow profiles along the empty fetch upstream of the building [Blocken et al., 2007a; Blocken et al., 2007b]. In the vertical direction, the height of the wind-tunnel test section is used (0.9
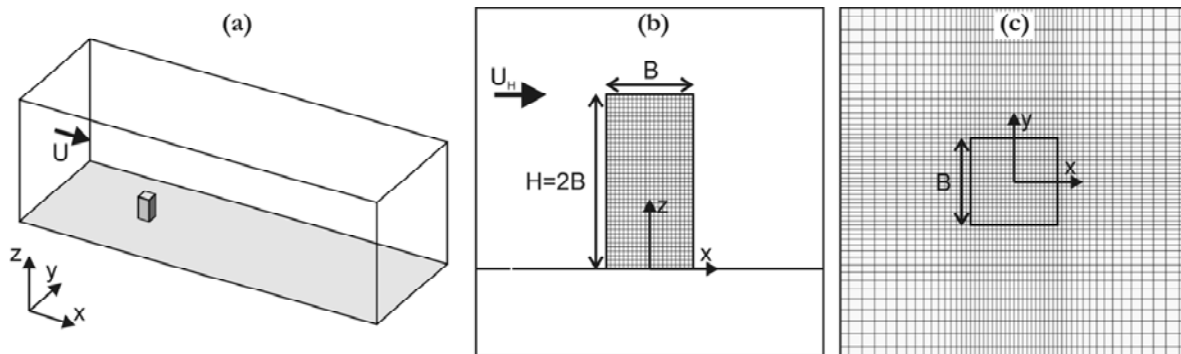

Figure II.1. (a) Computational domain. (b) Side and (c) top view of the grid on the building and ground surfaces for Grid20 (total number of cells: 737,920).

Table II.1. Characteristics of the two computational grids.

Name	Nb of cells: Total	Nb of cells: Building	Cell size: Building [m]	Cell size: Maximum [m]
Grid20	737,920	20×20×40	0.004	0.036
Grid30	2,504,160	30×30×60	0.0027	0.024

m=5.625H) and the top wall boundary is modeled. To avoid modeling the side walls of the wind tunnel (which would require grid refinement and increase the total number of cells significantly), the width of the domain has been chosen slightly smaller than the test-section width (0.9 m=11.25B vs. 1.1 m). Nevertheless, this dimension implies an empty distance of 5.125B on each side of the building, which ensures a small influence of the side boundary conditions on the flow around the building. The resulting blockage ratio is equal to 1.6%, which is below the maximum values recommended by the aforementioned guidelines [Franke et al., 2007; Tominaga et al., 2008b].

Two computational grids are used in this study, namely Grid20 and Grid30. The suffix corresponds to the number of cells used to discretize the building in the x- and y-directions. The same uniform grid spacing ($B/20$ or $B/30$) is applied on the building in the vertical direction. Away from the building, the cell size is increased by a factor kept around 1.08 to limit the commutation error. Note that the resulting high aspect ratio of the computational cells in some regions of the domain is not optimal for LES (using cubic cells is generally advised) but appears to be inevitable for applied cases with complex geometries (see Chapter V). The characteristics of the two grids are summarized in Table II.1 and the grid on the building and ground surfaces for Grid20 is shown in Figures II.1-b,c. As will be explained later (Section II.5), the solution verification methods used here are based on the numerical solutions of the LES equations on these two grids. An important parameter in this procedure is the grid coarsening factor $a=\Delta_{20}/\Delta_{30}$, equal to the ratio of the coarse filter width/cell size (Δ_{20}) and the fine one (Δ_{30}). Ideally, a should be kept constant everywhere in the domain. This is straightforward in the case of a uniform grid but in the case of more complex grid
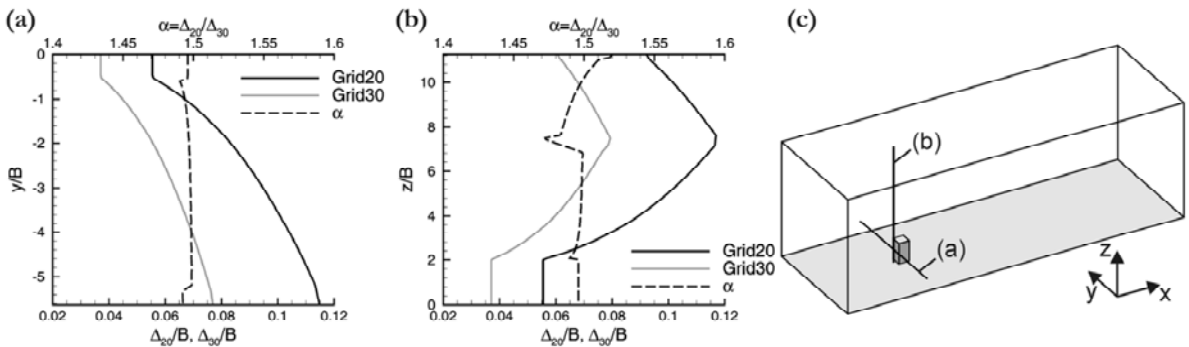
Figure II.2. Profiles of non-dimensional filter width Δ_{20}/B and Δ_{30}/B along the lines (a) (x/B=-0.75; z/B=1.25) and (b) (x/B=-0.75; y/B=0) for the two computational grids used in this study. The grid coarsening factor a is also shown (dashed line and secondary axis). (c) shows the position of the plotting lines.

systems like the one used here, special care must be taken to achieve this. As an example, the evolution of $\lrcorner_{20}$, $\lrcorner_{30}$ and a along two lines crossing the domain is shown in Figure II.2. For geometrical reasons, deviations from the intended value (a=1.5 imposed at the building) are inevitable but they have been kept very limited.

II.3.3 Boundary conditions

Symmetry boundary conditions are imposed at the sides of the domain ($y=\pm0.45$ m), implying zero normal velocity and zero gradients of all variables at these boundaries. At the outlet of the domain, zero static pressure is imposed.

The building and ground surfaces as well as the top boundary of the domain are defined as walls. The centroids of the wall-adjacent cells are assumed to lie either in the linear sub-layer, in the buffer layer or in the logarithmic zone of the boundary layer, depending on the distance to the wall [Ansys Inc., 2009]. For Grid20, z^+ values ($z^+=zu^*/\nu$, where $u^*=(\tau_w/\varrho)^{1/2}$ is the friction velocity with τ_w the wall shear stress) at the centroids of the wall-adjacent cells reach values up to 50 at the ground, 75 at the building surface and 225 at the ceiling. Note that no special treatment has been applied to the ground surface to take into account its roughness but the inflow boundary is located close enough to the building to limit the appearance of longitudinal gradients in the ABL profiles [Blocken et al., 2007a; Blocken et al., 2007b]. This has been verified by looking at the flow at a point P located at the same streamwise position as the windward facade of the building but relatively far from it in the lateral direction, in such a way that the ABL flow is not disturbed by the presence of the building. P is the point of non-dimensional coordinates (x/B=-0.5; y/B=3.75; z/B=2), i.e. the point located at building height, at the level of the windward facade, 3.25B away from the side wall. At P, the deviations from the prescribed inlet values of U and k at building height are equal to 1% and 5%, respectively, showing the good homogeneity of the prescribed profiles along the empty fetch upstream of the building.

Since LES is an unsteady model, the velocity profile imposed at the inlet of the domain must be time-dependent. Several techniques exist to achieve this, see for example [Tamura, 2008; Yoshie et al., 2011] for a review. Here it has been chosen to use the Vortex Method (VM) [Sergent, 2002; Mathey et al., 2006]. It consists in generating and transporting randomly in the inlet plane a given number (here: 200) of 2D-vortices whose intensity and size depends on the local value of k and the turbulence dissipation rate, for which profiles are prescribed based on the experiment. The turbulence dissipation rate is calculated assuming equilibrium between production and dissipation of turbulent kinetic energy in the ABL flow. The vortices generate unsteady perturbations v_{in}' and w_{in}' on the prescribed profiles of V and W, respectively. The perturbations u_{in}' on the imposed profile of U are deduced from v_{in}' and w_{in}' following $u_{in}'=-\vec{v'}.\vec{e}$ where $\vec{v'}$ is the vector of components (0; v_{in}'; w_{in}') and $\vec{e}$ is the unit vector aligned with the gradient of mean velocity in the inlet plane. The perturbations on the imposed profile of U are deduced from the

vortex-generated perturbations on the profiles of V and W. The advantage of this method is that it requires neither additional simulation nor extra domain length. This technique has been used in earlier studies by the authors (e.g. Chapter III, Chapter V) and showed good performance in LES of pollutant dispersion around buildings. Here, the accuracy and relevance of the VM will be analyzed in more detail (Section II.4.1).

II.3.4   Numerical procedure

The bounded central-differencing scheme is used to discretize the convection term in the filtered momentum equation. In comparison with pure central-differencing, this scheme switches to first-order upwind scheme when the convection boundedness criterion [Gaskell and Lau, 1988] is violated, which avoids the appearance of unphysical oscillations in the numerical solution. It has an order of accuracy between one and two. From the pressure values at the cell centers, the face values are computed with a second-order scheme. Pressure-velocity coupling is performed with the fractional step method [Kim and Moin, 1985; Bell et al., 1989].

Time discretization is second-order implicit. The non-iterative scheme is used for time advancement: each set of equations is solved iteratively (inner iterations) but not in combination. Performing only one outer iteration per time step decreases the computational time significantly without affecting the overall accuracy of the simulation [Ansys Inc., 2009]. For the pressure equation, the sub-iterations end within a time step when the ratio of the residual at the current sub-iteration and the first sub-iteration is less than 0.25, with a maximum of 10 sub-iterations per time step. For the momentum equation, this ratio and this maximum are 0.05 and 5, respectively. Note that the influence of these parameters has not been tested: the convergence of each simulation has been verified here in the sense that a sufficient number of time steps is performed to get converged average values (see Section II.5.1) but the convergence within each time step has not been monitored. The time-step value (Δt) has been adapted for each computational grid: it is equal to 8×10^{-4} s for Grid20 and 5.33×10^{-4} s for Grid30, corresponding to 0.045 and 0.03 time units ($t_u=B/U_H$), respectively. Similar values for the Courant number ($=u\times\Delta t/h_c$, with u the local velocity value and h_c the local cell size) are therefore found on both grids, the maximum on the whole domain being approximately 2.3. Each simulation is initialized with the solution of a preceding RANS simulation on which random noise is super-imposed. After an initialization period $T_{init}=3.2$ s corresponding to 5.4 flow-through times ($T_{ft}=L_x/U_H$, where L_x is the length of the computational domain), the statistics are sampled for $T_{avg}=12.8$ s$=21.8T_{ft}=718t_u$. It will be demonstrated in Section II.5.1 that this averaging period is sufficiently long to provide converged mean values of velocity.

II.3.5 List of cases

The name and description of the seven cases that will be presented in this chapter are summarized in Table II.2.

   The simulations have been run in parallel on eight processors (2.33 GHz; 64 GB memory). In total the LES20-1 simulation lasted approximately 30 hours, including the initialization phase. The use of the dynamic Smagorinsky model (LES20-3) did not strongly increase the computational time (ratio 1.15:1). Because of the increase in number of time steps and in computational time per time step, the simulations on Grid30 demanded significantly more time to run on the same computer system (ratio 6:1 for LES30-1 compared to LES20-1).

   To quantify the agreement between numerical and experimental results, validation metrics are used in the next section and reported in Table II.3 for U, V, W and k: hit-rate (q) and fraction of predictions within a factor of 2 of observations ($FAC2$). In addition for k, the Fractional Bias (FB) and Normalized Mean Square Error ($NMSE$) are used. Except for the hit rate, the metrics have been calculated with the BOOT software [www.harmo.org, 2012] and take into account all the 186 measurement points. The definitions of these metrics can be found in Appendix A [Schatzmann et al., 2010]. The ideal value of each metric, corresponding to perfect agreement between CFD and experiment, is indicated in Table II.3. The values of the relative and absolute error thresholds for q have been taken equal to D_q=0.25 and W_q=0.03 for velocity and to D_q=0.25 and W_q=0.003 for k. The threshold for absolute error is based on the uncertainty of the experiment. Here, the uncertainty on velocity measurements was not explicitly mentioned in the experimental report but it was estimated based on the anemometer manufacturer information [Jørgensen, 2002] and experiments performed with the same equipment [Ubertini and Desideri, 2000].

Table II.2. List and description of the cases. VM indicates Vortex Method for inlet boundary condition.

| Case	Grid	SGS model	Constant C_s	Inlet method
LES20-1	Grid20	Standard Smagorinsky	0.1	VM
LES20-2	Grid20	Standard Smagorinsky	0.15	VM
LES20-3	Grid20	Dynamic Smagorinsky	-	VM
LES20-4	Grid20	Standard Smagorinsky	0.1	No perturbation
LES30-1	Grid30	Standard Smagorinsky	0.1	VM
LES30-2	Grid30	Standard Smagorinsky	0.15	VM
LES30-3	Grid30	Dynamic Smagorinsky	-	VM

Table II.3. Validation metrics (hit rate *q*, factor of two of observations *FAC2*, fractional bias *FB* and normalized mean square error *NMSE*) for the seven simulations. The metrics for *U* and *k* take into account the 186 measurement points while *V* is evaluated in the planes H1 and H10 and *W* in the plane V0. Thresholds for *q*: D_q=0.25; W_q=0.03 for *U*, *V* and *W*. D_q=0.25; W_q=0.003 for *k*.

	U/U_H		V/U_H (H1 & H10)		W/U_H (V0)		k/U_H^2			
	q	FAC2	q	FAC2	q	FAC2	q	FAC2	FB	NMSE
Ideal value	1	1	1	1	1	1	1	1	0	0
LES20-1	0.90	0.96	0.78	0.73	0.71	0.76	0.65	0.98	-0.16	0.10
LES20-2	0.87	0.94	0.77	0.76	0.70	0.79	0.34	0.98	-0.28	0.16
LES20-3	0.89	0.95	0.84	0.75	0.73	0.76	0.66	0.99	-0.17	0.10
LES20-4	0.84	0.95	0.88	0.74	0.50	0.70	0.17	0.43	0.69	0.67
LES30-1	0.90	0.96	0.67	0.77	0.62	0.74	0.32	0.98	-0.30	0.19
LES30-2	0.86	0.93	0.71	0.79	0.64	0.76	0.32	0.98	-0.29	0.17
LES30-3	0.90	0.95	0.80	0.76	0.71	0.82	0.16	0.96	-0.33	0.20

II.4   Validation: comparison with the measurements

II.4.1   *Influence of the inlet method*

The profiles of mean streamwise velocity along 5 lines (x/B=-0.75; -0.25; 0.5; 1.25; 3.25) in the planes V0 and H10 obtained for LES20-1 and LES20-4 are compared to the measurements in Figure II.3. The agreement with the experiment is very good for LES20-1, in both planes. The recirculation zones over the roof and in the wake of the building, where U<0, are well described: the computed roof (X_r) and wake (X_w) recirculation lengths compare well with the measurements (Table II.4). Note that the
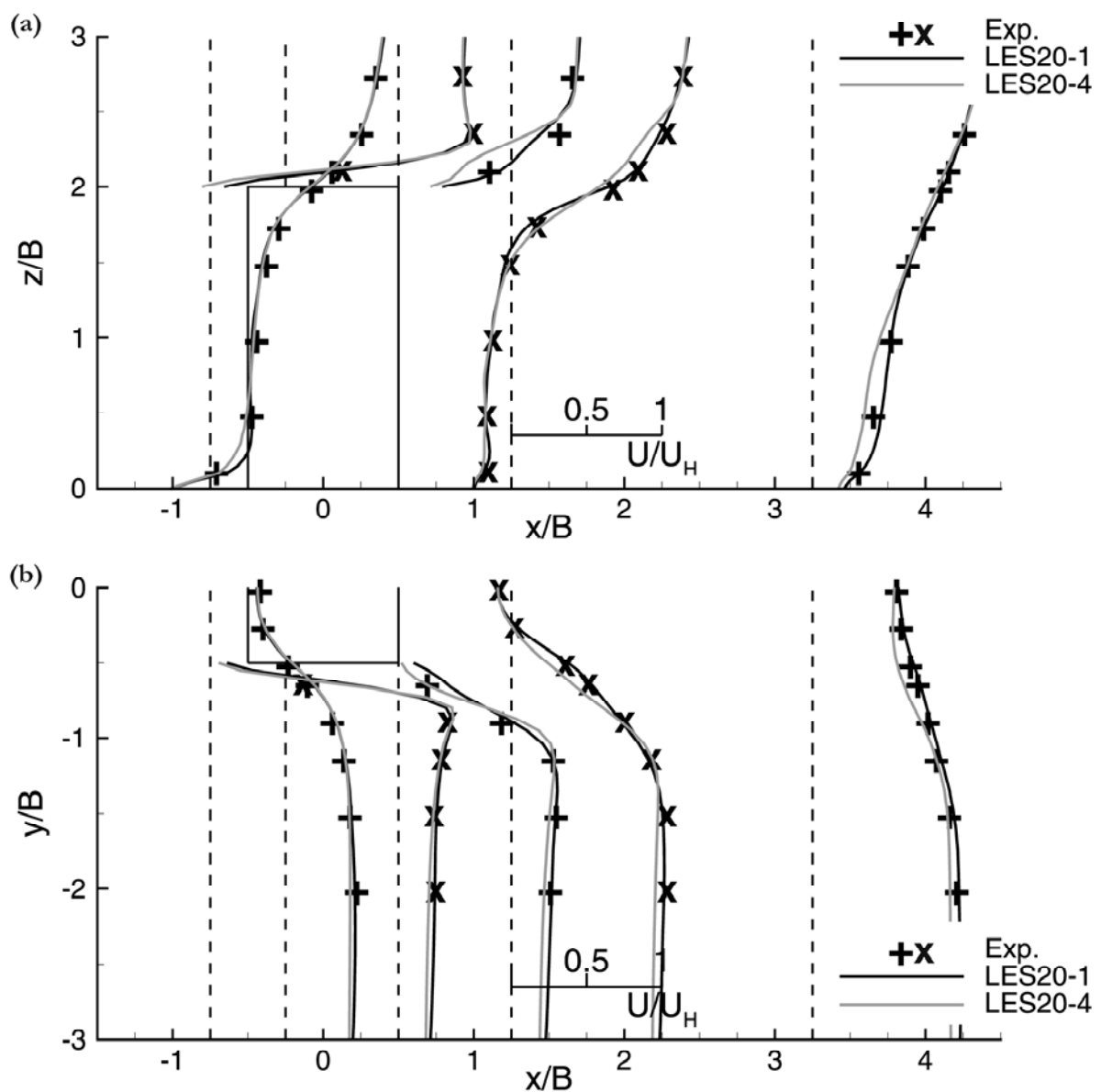

Figure II.3. Validation of the Vortex Method (VM): comparison between LES20-1 (VM) and LES20-4 (no perturbation at inlet). Experimental (symbols) and numerical (lines) profiles of non-dimensional mean streamwise velocity in the planes (a) V0 and (b) H10.

LES simulation by Tominaga et al. [2008a] – for which the results are also shown in Table II.4 – uses a precursor simulation to generate the turbulent inflow. With a steady inlet (LES20-4), discrepancies in the velocity profiles appear around roof level and in the far wake, which is confirmed by the metric values shown in Table II.3. LES20-4 shows a stronger over-estimation of X_r and X_w (Table II.4), in agreement with Yoshie et al. [2011] who performed LES of flow around a building with the same geometry as the one considered here, with and without inflow turbulence.

The main difference between the two simulations is found for the turbulent kinetic energy field (Fig. II.4). The k-values computed by LES20-4 upstream of the building are close to zero, because of the absence of velocity fluctuations at the inlet. The building
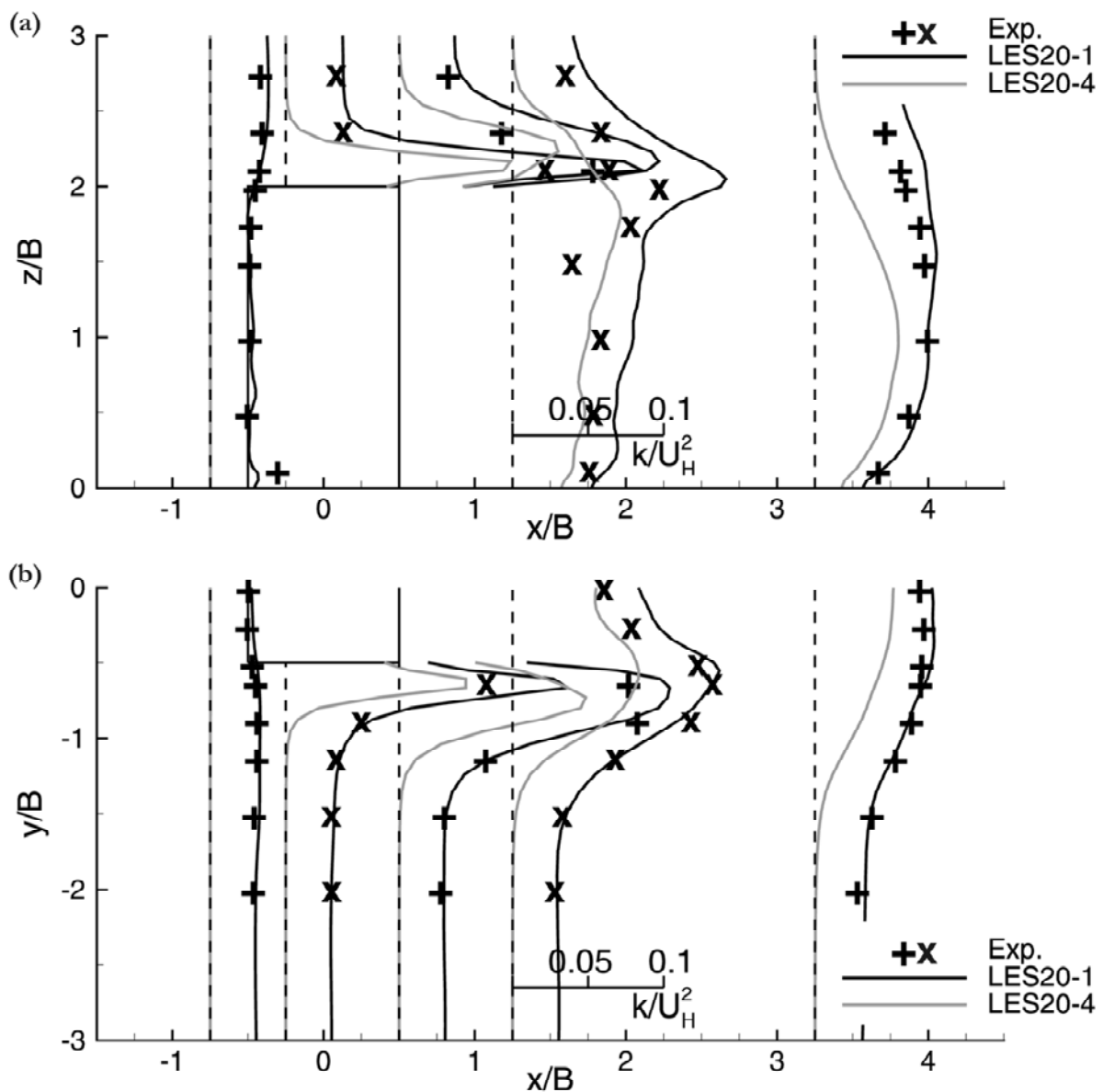
Figure II.4. Validation of the vortex method (VM): comparison between LES20-1 (VM) and LES20-4 (no perturbation at inlet). Experimental (symbols) and numerical (lines) profiles of non-dimensional turbulent kinetic energy in the planes (a) V0 and (b) H10.

Table II.4. Non-dimensional length of the rooftop (X_r/B) and wake (X_w/B) recirculation zones. Results from [Tominaga et al., 2008a] correspond to "Case 2", with inflow turbulence obtained from a precursor simulation.

Case	X_r/B	X_w/B
Exp. [Meng and Hibi, 1998]	0.52	1.42
[Tominaga et al., 2008a]	0.50	2.10
LES20-1	0.59	1.65
LES20-2	0.59	1.66
LES20-3	0.60	1.65
LES20-4	0.75	1.89
LES30-1	0.59	1.78
LES30-2	0.62	1.90
LES30-3	0.57	1.74

generates turbulence in its vicinity but k remains largely under-estimated by LES20-4 on all the measurement lines (hit-rate value: q=0.17). This result is in contradiction with Tominaga et al. [2008a] who found higher k behind the building in the absence of inflow turbulence because of the more intense vortex shedding. Here, when the VM is used to generate inflow turbulence (LES20-1), a rather good agreement is found between CFD and experiment (q=0.65).

It is verified a posteriori that the time-averaged inlet profiles generated by the VM correspond eventually to the experimental/prescribed profiles. The inlet profiles of U/U_H and k/U_H^2 averaged along the y-direction for LES20-1 and LES30-1 are shown in Figure II.5. In both cases, the resulting profile of U is identical to what has been prescribed (Fig. II.5-a). The resulting inlet profile of k (computed based on the velocity fluctuations at every time step of the averaging period of the simulation) is slightly different for LES20-1 and LES30-1, showing that the VM is a grid-dependent technique
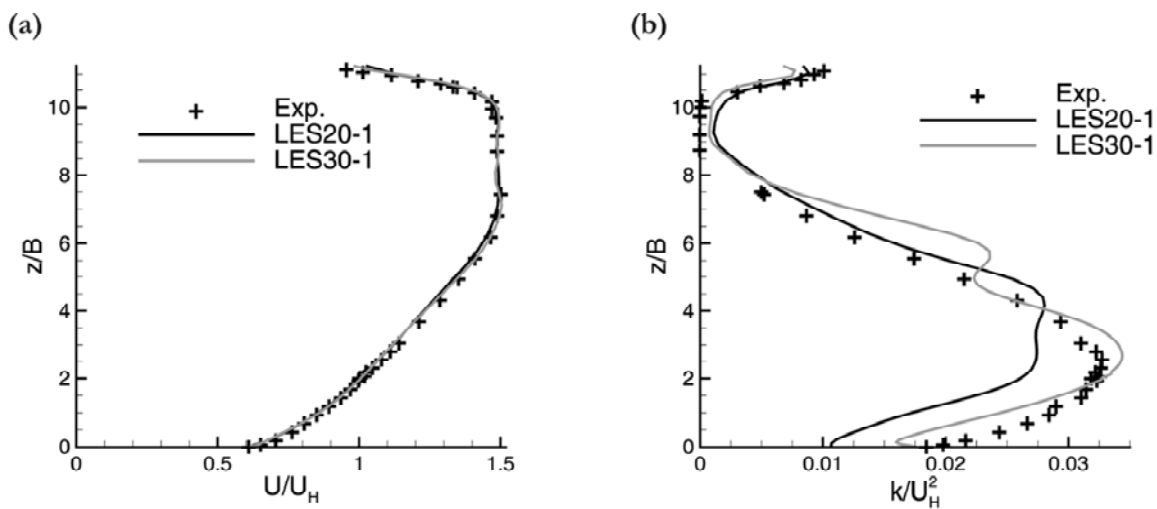
Figure II.5. Experimental/prescribed profiles (symbols) and resulting time-average profiles at the inlet for LES20-1 and LES30-1 (lines) of (a) non-dimensional streamwise velocity and (b) non-dimensional turbulent kinetic. The numerical results are averaged in the lateral direction.

(Fig. II.5-b). This should be kept in mind when comparing the results of these two simulations. The symmetry boundary conditions used on the sides of the domain limit the fluctuations of the lateral velocity at these locations, resulting in a decrease of k. This explains the slight under-estimation of the y-averaged k-profiles compared to the prescribed values. If the vertical centerline of the inlet plane is considered, a good agreement is found between the prescribed and resulting k-profiles (not shown here). A closer look at the individual normal stresses reveals however that the VM under-estimates σ_u on this line (by about 30% and 10% at building height for LES 20-1 and LES30-1, respectively), which is compensated by the over-estimation of σ_w. The standard deviation of the lateral velocity component (σ_v) computed by the VM is in good agreement with the measurements.
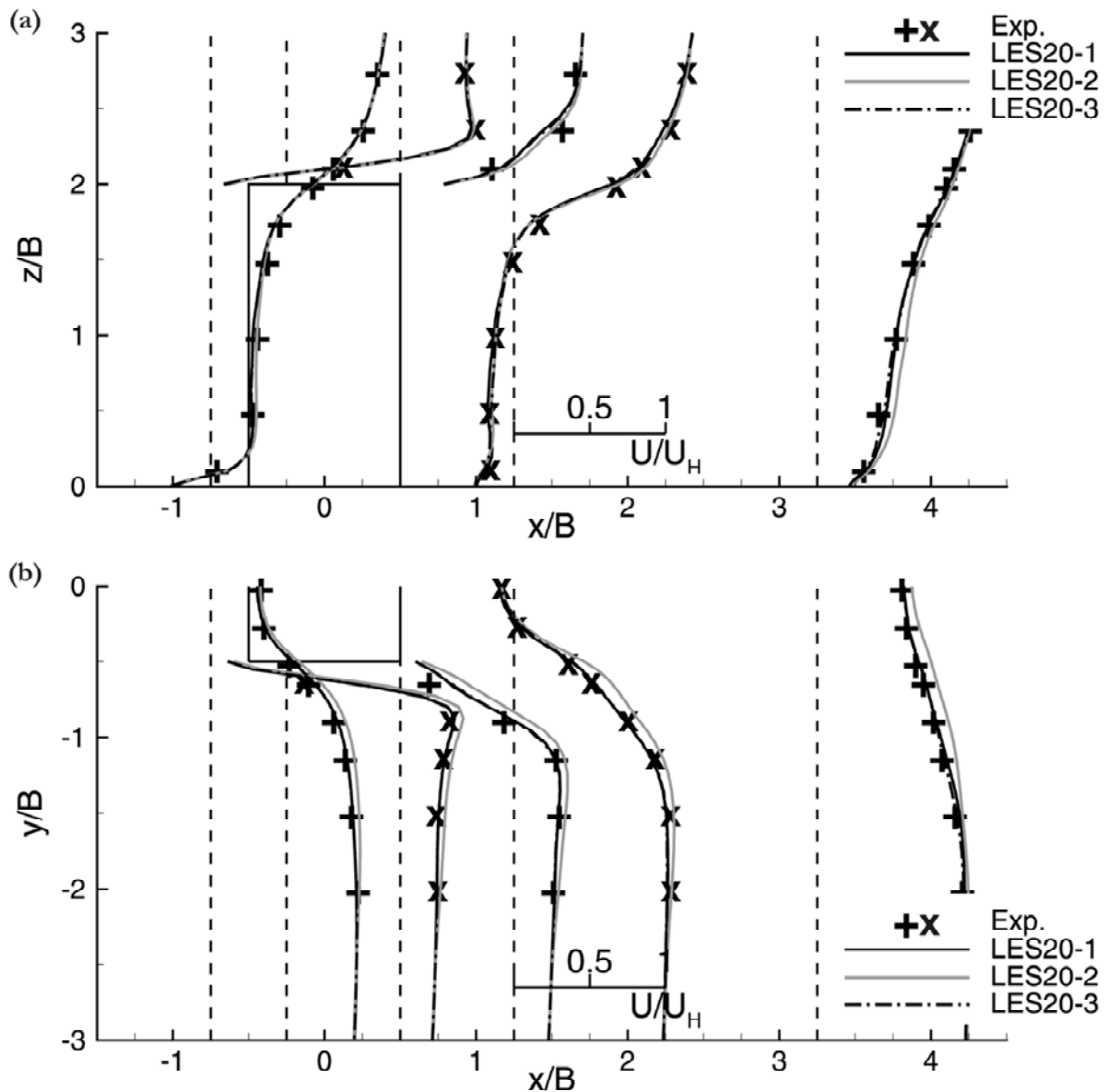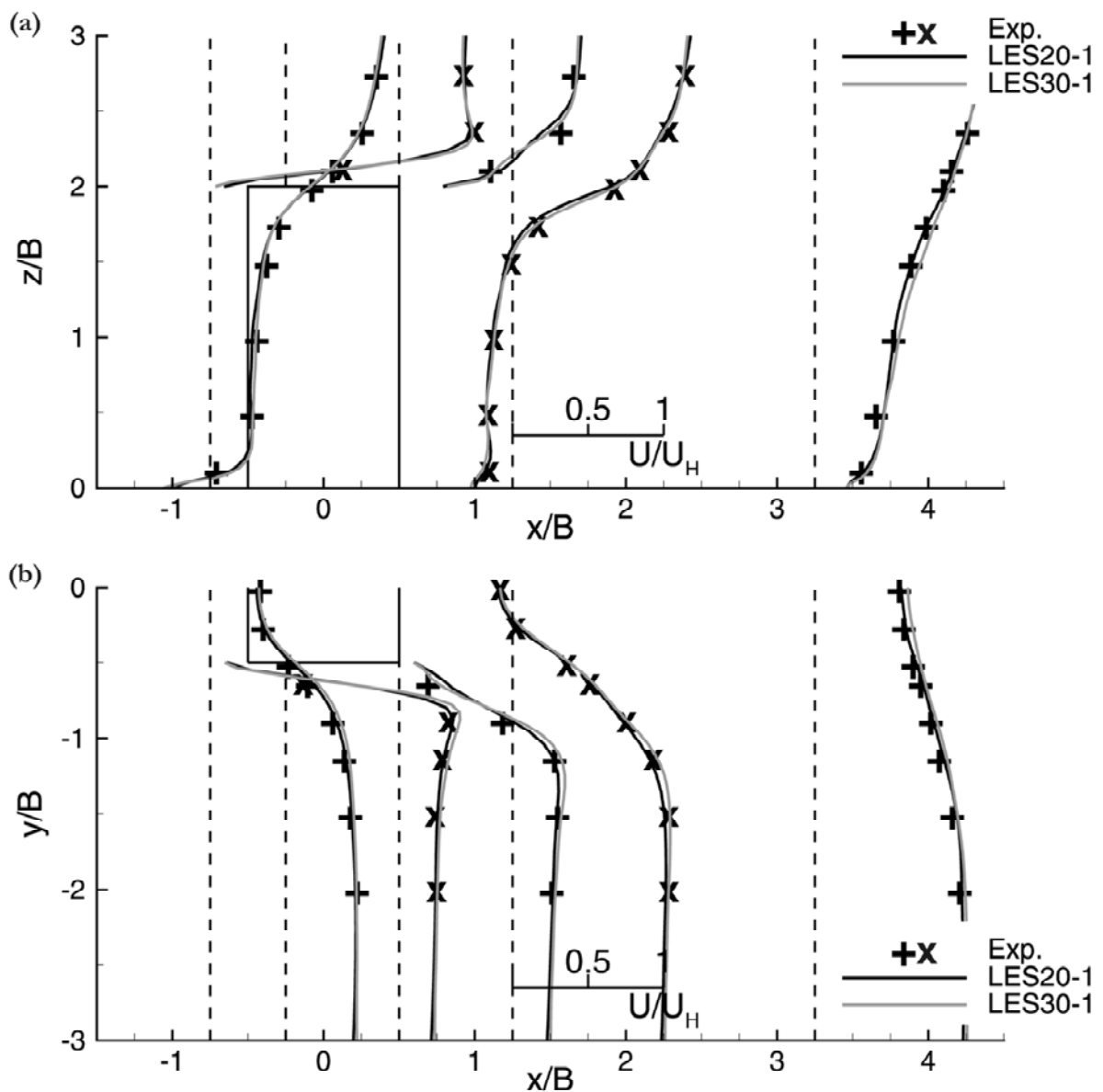

Figure II.6. Influence of the SGS model: comparison between LES20-1 (C_s=0.1), LES20-2 (C_s=0.15) and LES20-3 (dynamic). Experimental (symbols) and numerical (lines) profiles of non-dimensional mean streamwise velocity in the planes (a) V0 and (b) H10.

II.4.2 Influence of the SGS model

The influence of the SGS model is presented here for Grid20. The standard Smagorinsky model with C_s=0.1 (LES20-1), C_s=0.15 (LES20-2), and the dynamic Smagorinsky model (LES20-3) are compared. The results obtained with the latter model in terms of mean streamwise velocity are very close to those from LES20-1 (Fig. II.6) and in very good agreement with the measurements (q=0.89). With C_s=0.15 (LES20-2), U is slightly over-estimated in the plane H10 but the agreement remains good, with an overall hit-rate value of 0.87. The recirculation lengths predicted by the three simulations are very close to each other and slightly over-estimate the measured ones (Table II.4).

Like for U/U_H, the k-values computed with LES20-1 and LES20-3 are very similar
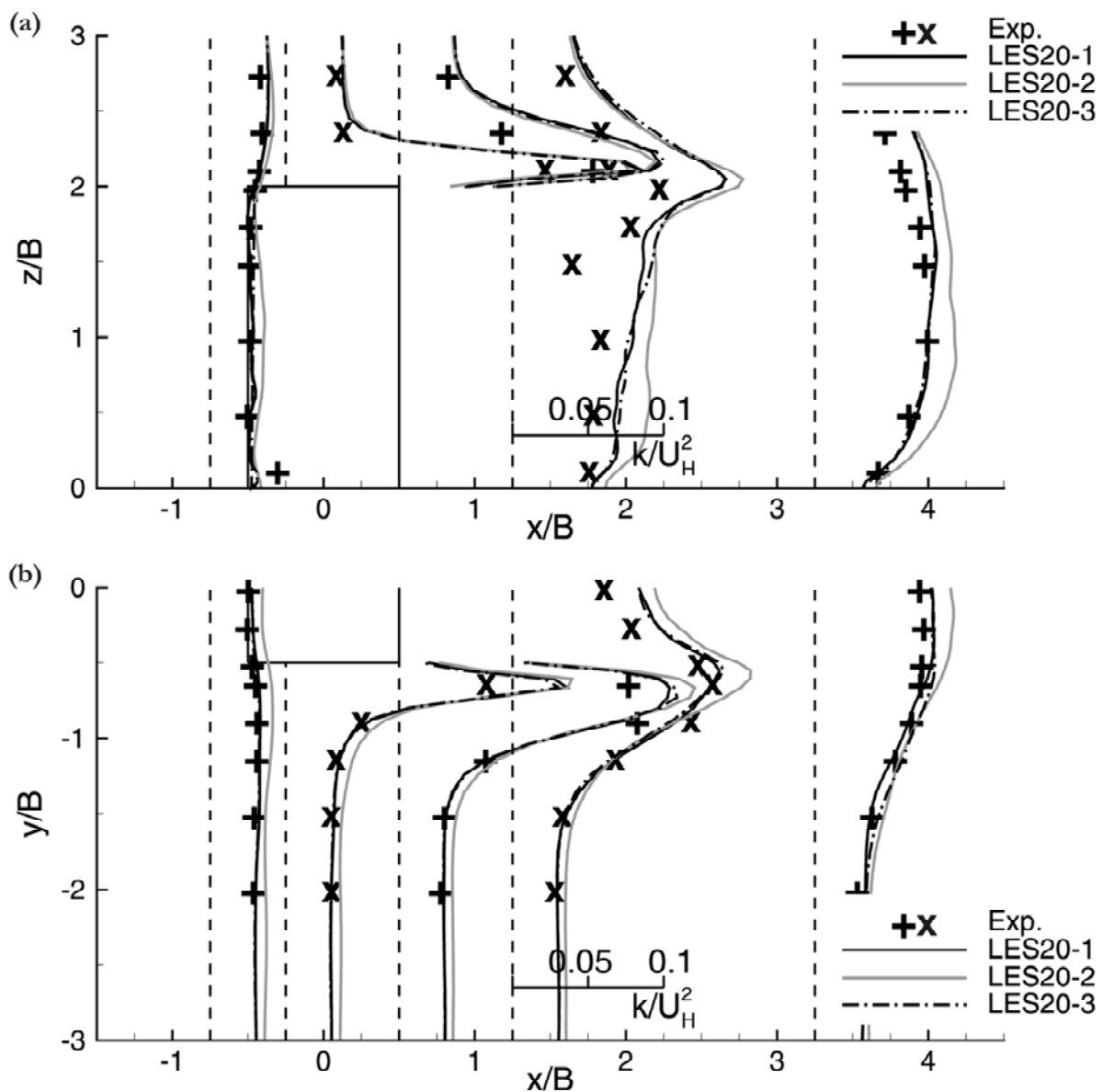
Figure II.7. Influence of the SGS model: comparison between LES20-1 (C_s=0.1), LES20-2 (C_s=0.15) and LES20-3 (dynamic). Experimental (symbols) and numerical (lines) profiles of non-dimensional turbulent kinetic energy in the planes (a) V0 and (b) H10.

(Fig. II.7). LES20-2 over-estimates k in comparison with experimental results – especially in the wake of the building – and provides higher values than LES20-1. This lower performance of the Smagorinsky model with C_s=0.15 is also seen in the validation metrics in Table II.3 and supports the appropriateness of C_s=0.1 to simulate the flow around this isolated bluff body. Note that the difference between the different SGS models is smaller on Grid30 (not shown here).

II.4.3 Influence of the grid resolution

With LES and implicit filtering, the model depends inherently on the grid size. When refining the grid, the model contribution is also changing and consequently a grid-


Figure II.8. Influence of the grid resolution: comparison between LES20-1 and LES30-1. Experimental (symbols) and numerical (lines) profiles of non-dimensional mean streamwise velocity in the planes (a) V0 and (b) H10.

independent solution cannot be found [Freitag and Klein, 2006]. Nevertheless, LES20-1 and LES30-1 are compared here to investigate the influence of the grid resolution on the results. Both computations use the standard Smagorinsky SGS model with C_s=0.1. No major changes in the computed values of U/U_H are implied by the use of the fine grid, as can be seen in Figure II.8 and from the validation metrics values (Table II.3). The low dependence of the mean velocity results on the grid resolution was also observed with C_s=0.15 and with the dynamic Smagorinsky SGS model (not shown here).

The smaller the grid size, the larger is the range of eddy scales which are resolved by the LES model. As a consequence, the contribution of a larger range of scales to the velocity fluctuations is taken into account by the simulations on Grid30, and the resolved
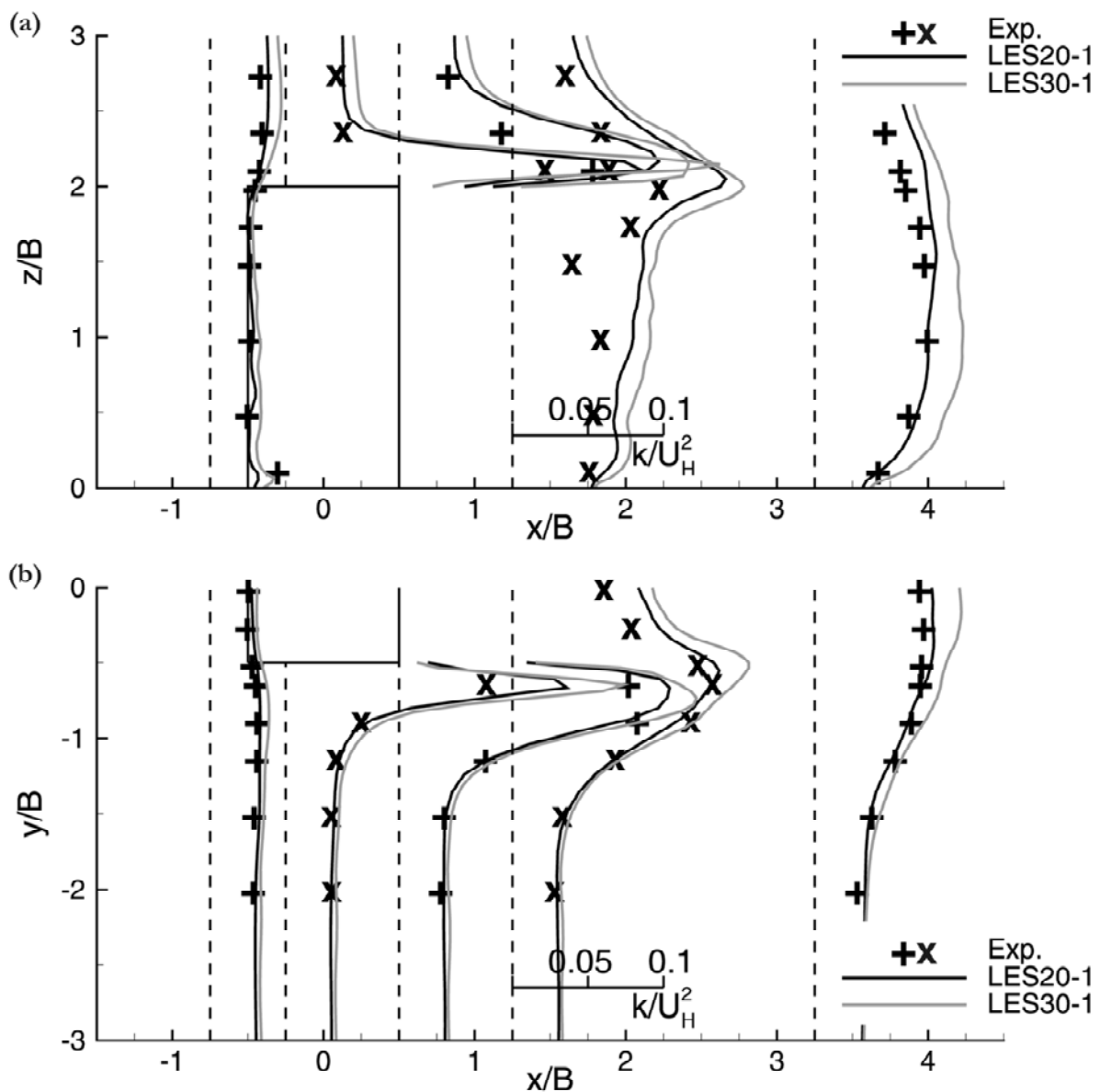
Figure II.9. Influence of the grid resolution: comparison between LES20-1 and LES30-1. Experimental (symbols) and numerical (lines) profiles of non-dimensional turbulent kinetic energy in the planes (a) V0 and (b) H10.

turbulent kinetic energy with this grid is higher than with Grid20. These considerations are eventually observed in our results but in this particular case the agreement with the measurements deteriorates (Fig. II.9). The conclusion is therefore rather counter-intuitive: the coarsest mesh is the one which provides the best agreement with the measurements. A discussion on this issue can be found in [Celik et al., 2005], giving the under-estimation of the turbulence dissipation rate as a possible explanation for the over-estimation of k by LES on the fine grid. Similar results can also be found in [Meyers et al., 2003] and [Klein, 2005]. In the former reference, the authors show that the modeling and numerical error on the computation of k counteract. Hence, although the two error components are higher in magnitude on a coarse grid than on a finer one, the sum (total error) is higher on the fine grid. Bias error in the measurements of the velocity fluctuations is another possible explanation for the discrepancy between CFD and experiment in terms of k, as well as the difference between the sampling frequency used in the measurements and the one used in the CFD simulations.

II.5 Solution verification

II.5.1 Monitoring of statistical convergence

Figure II.10-a shows the evolution of the non-dimensional moving-average of the streamwise velocity $<u>_t/U_H$ as a function of time in the averaging period $(0 \leq t \leq T_{avg})$ at four monitoring points located in different zones of the flow field (see Fig. II.10-b). These results correspond to the simulation on the coarse grid with the dynamic Smagorinsky SGS model (LES20-3). It appears that the variations of $<u>_t$ are relatively
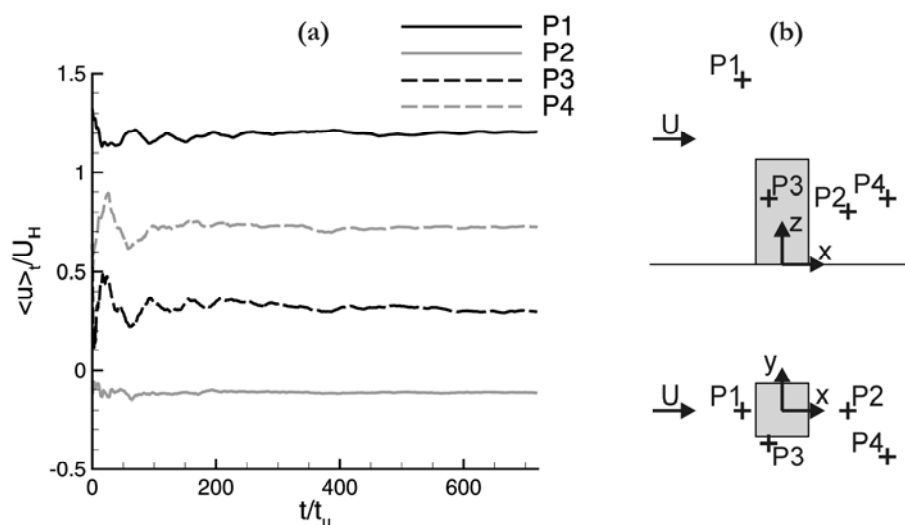
Figure II.10. Convergence monitoring: (a) moving-average of the non-dimensional streamwise velocity at four monitoring points as a function of time in the averaging period for LES20-3. (b) Position of the monitoring points. Non-dimensional coordinates: P1 (-0.75; 0; 3.5); P2 (1.25; 0; 1); P3 (-0.25; -0.625; 1.25); P4 (2; -0.875; 1.25).

Table II.5. Convergence monitoring on LES20-3: e_{conv} (%) at P1, P2, P3 and P4 for eight successive equal ranges of time steps in the averaging period. Total number of time steps in the averaging period: 16,000.

Range of time steps	P1	P2	P3	P4
1-2000	15.8	74.7	182.5	49.8
2001-4000	4.3	11.5	27.4	6.7
4001-6000	2.5	10.6	15.9	3.3
6001-8000	1.3	7.0	13.8	3.5
8001-10000	1.5	4.5	10.0	3.3
10001-12000	1.0	3.8	5.1	1.5
12001-14000	1.0	5.1	7.9	1.6
14001-16000	0.5	3.8	4.1	1.1

low at the end of the averaging period (16,000 time steps in this case). The convergence of the mean value is quantified by e_{conv} (%), defined for a given range of time steps I by:

$$e_{conv}(I)=100\times\left|\frac{\max_{k\in I}(<u>_{k\Delta t}) - \min_{k\in I}(<u>_{k\Delta t})}{<u>_{T_{avg}}}\right| \tag{II.6}$$

This indicator corresponds to the range of values that the moving-average takes within an interval I of time step numbers in the averaging period (for example I=1,…,2000), normalized by the final average value at t=T_{avg}. The 16,000 time steps of the averaging period of LES20-3 have been divided into eight equal intervals for which the values of e_{conv} are reported in Table II.5 for P1, P2, P3 and P4. At the beginning of the averaging period (time steps 1 to 2000) each instantaneous flow pattern has a high influence on $<u>_t$ and the values of e_{conv} are therefore high at every point, especially at P2 and P3. e_{conv} shows a decreasing trend and reaches low values ($\leq$4.1%) at the end of the averaging period, which indicates sufficient statistical convergence of the simulation. Note that the points P2 and P3 are located in regions of the flow field where quasi-periodic flow patterns occur [Wang and Zhou, 2009] and limit the convergence of the statistics. Observing the evolution of e_{conv} at these points is therefore a conservative way to assess the statistical convergence of the simulation.

II.5.2 Systematic Grid and Model Variation (SGMV)

When the filter width and the grid spacing are independent (explicit filtering), the modeling (e_m) and numerical (e_n) errors can be estimated separately: the "grid-independent" LES solution – which does exist for a given filter width in the context of explicit filtering – is compared on the one hand to the filtered DNS solution to provide an estimation of e_m, and on the other hand to the LES solution on a coarse grid (at constant filter width) to provide an estimation of e_n [Vreman et al., 1996; Geurts and Fröhlich, 2002; Meyers et al., 2003]. By contrast, in the context of implicit filtering, as already mentioned, the modeling and numerical errors interact and cannot be evaluated separately. The SGMV [Klein, 2005] is therefore used here to provide an estimation of
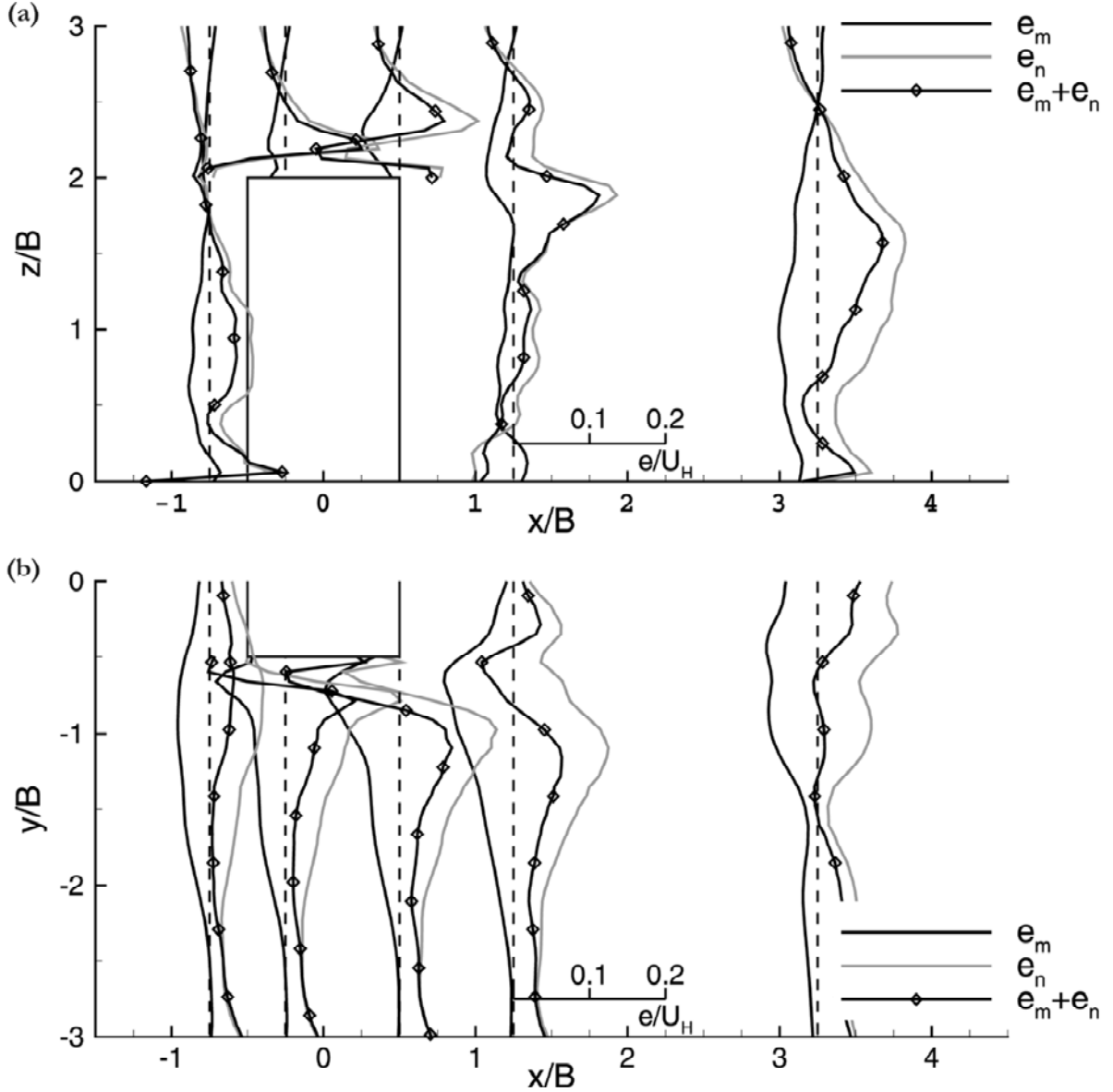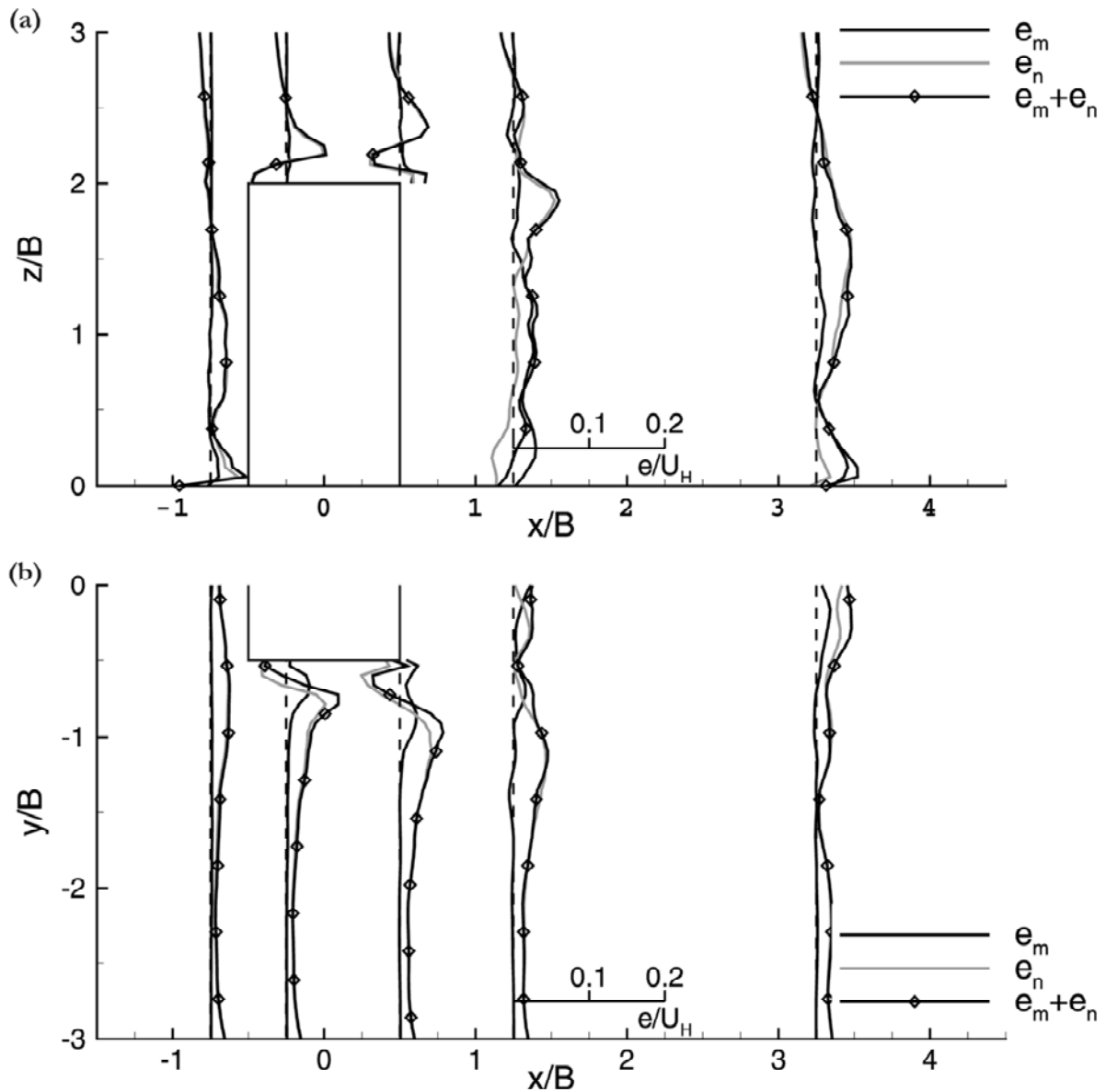
Figure II.11. Results of SGMV technique for LES20-1: Estimation of the non-dimensional modeling, numerical and total error on mean streamwise velocity prediction in the planes (a) V0 and (b) H10.

these two types of error, based on Richardson extrapolation. The difference between the exact solution of the flow equations (u_e) and the numerical solution on a given grid (say $u_{20\text{-}1}$ for LES20-1) is equal to the sum of these two error contributions which are assumed to scale with the filter width:

$$u_e - u_{20\text{-}1} = e_m^{20\text{-}1} + e_n^{20\text{-}1} = c_m \Delta_{20}^m + c_n \Delta_{20}^n \tag{II.7}$$

where n is the order of accuracy of the numerical scheme (taken here equal to 2 [Manickam et al., 2012]), m is set to its theoretical value 2/3 as suggested in [Freitag and Klein, 2006], c_m and c_n are coefficients to be determined. Following the same approach for LES20-2 and LES30-1 yields:

$$u_e - u_{20\text{-}2} = e_m^{20\text{-}2} + e_n^{20\text{-}2} = \beta c_m \Delta_{20}^m + c_n \Delta_{20}^n \tag{II.8}$$

Figure II.12. Results of SGMV technique for LES30-1: Estimation of the non-dimensional modeling, numerical and total error on mean streamwise velocity prediction in the planes (a) V0 and (b) H10.

$$u_e - u_{30-1} = e_m^{30-1} + e_n^{30-1} = c_m(\Delta_{20}/a)^m + c_n(\Delta_{20}/a)^n \tag{II.9}$$

where $\beta = C_s^2|_{20-2}/\ C_s^2|_{20-1} = 2.25$ is the model variation factor and a is the grid coarsening factor defined earlier. Hence, the combination of the numerical solutions of these three simulations allows determining the unknowns of the problem (u_e, c_m and c_n) and estimating the numerical and SGS modeling errors. The SGMV technique has been applied here for the mean velocity. The procedure has been repeated on LES30-1, LES30-2 and LES20-1 to evaluate the numerical and modeling errors for LES30-1.

Figures II.11 and II.12 show the resulting estimation of e_m and e_n normalized by U_H for LES20-1 and LES30-1, respectively. The sum of these two error contributions is also shown. Note that it is advised to use the sum of the magnitudes $|e_m| + |e_n|$ as a

conservative estimate of the total error [Freitag and Klein, 2006]. The numerical error is relatively high for LES20-1, especially above roof level and in the wake of the building (Fig. II.11-a) as well as in the side shear layer (Fig. II.11-b) where it can reach up to 15% of the reference velocity. Noticeably, the SGS modeling error is generally of opposite sign than the one of e_n, with similar order of magnitude, which significantly decreases the total error on mean velocity (see [Vreman et al., 1996] and [Meyers et al., 2003] for similar results in the case of mixing layer and homogeneous isotropic turbulence, respectively). Concerning LES30-1, a similar trend is observed for the numerical error but its magnitude is lower than on the coarse grid (Fig. II.12). As mentioned earlier, the SGS model had low influence on the mean velocity with Grid30; it is confirmed here by the very low estimated values of e_m. Despite the higher magnitude of errors on LES20-1, the compensation that operates between e_m and e_n leads to a similar level of total error in this case in comparison with LES30-1, which explains why similar results were obtained for the mean velocity field on the two grids. The conservative estimate of the total error $|e_m|+|e_n|$, however, is clearly higher on the coarse mesh.

II.5.3   LES Index of Quality

Since a grid-independent solution cannot be achieved with LES and implicit filtering, a way to determine whether a given grid is suitable is to evaluate the amount of turbulent kinetic energy that it allows resolving. This is the purpose of the LES index of quality (*LES_IQ*) [Celik et al., 2005]. The total kinetic energy (k_{tot}) can be decomposed into the resolved part (k), the contribution of the SGS model (k_{sgs}), and the contribution of the numerical dissipation (k_{num}):

$$LES\_IQ = \frac{k}{k_{tot}} = \frac{k}{k + k_{sgs} + k_{num}} = 1 - \frac{k_{tot} - k}{k_{tot}} \tag{II.10}$$

As suggested by Pope [2000], an LES computation can be judged to be well-resolved when 80% of the turbulent kinetic energy is resolved. In some cases, k is found to be higher on a coarser grid than on a finer one [Celik et al., 2005]. This was observed in the present computations (above roof level and in regions of very low k) so the generalized formula has been used to keep *LES_IQ* below the ideal value of 1:

$$LES\_IQ = 1 - \frac{|k_{tot} - k|}{k_{tot}} \tag{II.11}$$

Based on Richardson extrapolation, the combined contribution of SGS model and numerical dissipation is assumed to scale with the grid size/filter length [Celik et al., 2005]:

$$k_{tot} - k = a_k \Delta^n \tag{II.12}$$

where n is the order of accuracy of the numerical scheme ($n=2$) and a_k is a coefficient that can be determined by running the simulation on two grids with different resolution (cases LES20-1 and LES30-1 here).
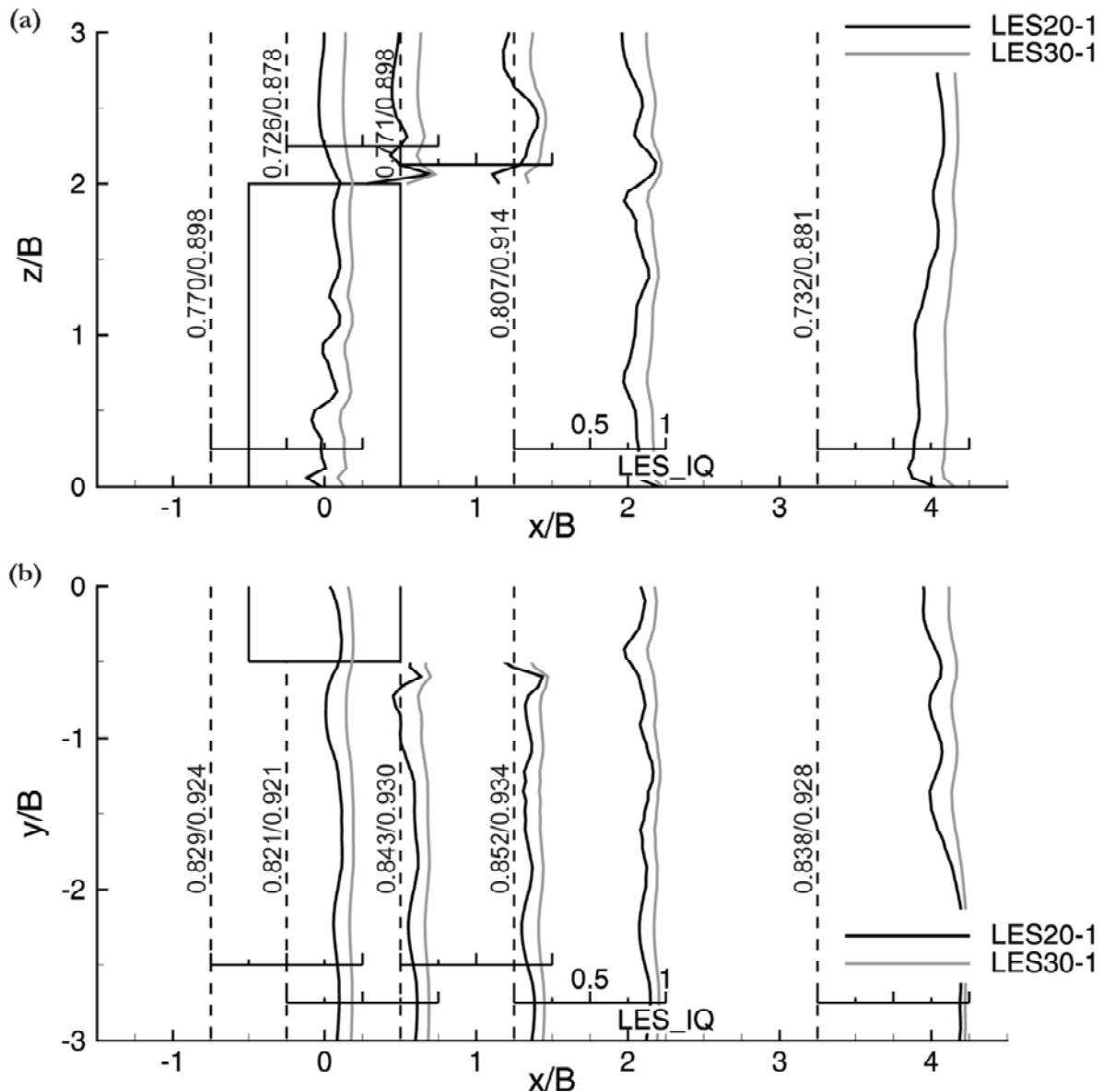
Figure II.13. Profiles of *LES_IQ* for cases LES20-1 and LES30-1 in the planes (a) V0 and (b) H10. The values averaged on (a) 0<z/B<3 and (b) -3< y/B<0 are indicated on each line (the first/lowest value corresponds to LES20-1 and the second/highest value to LES30-1).

Figure II.13 shows the profiles of *LES_IQ* along the same lines that were used in the validation part, as well as the averaged values of *LES_IQ* on each line for z/B<3 (plane V0) and -3<y/B<0 (plane H10). As expected, the simulation on Grid30 resolves a larger part of the total turbulent kinetic energy. On the nine measurement lines in the plane V0 for z/B<3, on average 89% of k_{tot} is resolved by LES30-1 compared to 76% by LES20-1 (Fig. II.13-a). The flow regions where the least energy is resolved are the upstream part of the roof (-0.5<x/B<0) and the far-wake (x/B≈3.25). Keeping the grid uniform in these regions instead of imposing a cell growth would help increasing the amount of resolved energy. On the measurement lines in H1 and H10, for -3<y/B<0, LES30-1 resolves on average 91% and 93% of k_{tot}, respectively, while LES20-1 resolves

80% and 84%. The profiles of *LES_IQ* in the plane H10 are shown in Figure II.13-b. On average over all the measurement lines, LES20-1 and LES30-1 resolve 80% and 91% of k_{tot}, respectively. Thus, if the threshold of 80% is used to define a well-resolved LES, both simulations can be classified in this category. Noticeably, while LES30-1 resolves a larger proportion of the turbulent kinetic energy, Section II.4 has also shown that this simulation over-estimates the experimental values.

II.6   Summary and chapter conclusions

Large-Eddy Simulation of wind flow around a high-rise building has been performed with the commercial CFD code Ansys/Fluent 12.1. Several cases have been run and analyzed, on two different grids (Grid20 and Grid30) and with two different SGS models, namely the standard Smagorinsky model and its dynamic version. For the former, C_s=0.1 and 0.15 have been tested. The results have been compared with wind-tunnel measurements in terms of non-dimensional mean velocity U/U_H and turbulent kinetic energy k/U_H^2. The agreement between numerical and experimental results has been quantified by validation metrics (hit rate, FAC2, FB and NMSE). A posteriori solution verification has been performed with Systematic Grid and Model Variation (SGMV) and the *LES_IQ* indicator. These techniques have been developed for general fluid engineering problems and, to the best of the authors' knowledge, have been applied here for the first time to LES of wind flow around a building. From this study, the following conclusions can be drawn:

– The vortex method to generate time-dependent velocity profile at the inlet of the domain has been shown to be suitable for atmospheric boundary layer flows.

– A suitable length for the averaging period has been determined by monitoring the moving average of velocity at several points in the flow field.

– Very good agreement was found for all cases for the mean streamwise velocity field (hit rate values between 0.84 and 0.90). The other components and the velocity fluctuations appeared to be more challenging to predict (e.g. hit rate values below 0.66 for k).

– With the standard Smagorinsky SGS model, the use of C_s=0.1 provided the most accurate results, very close to those of the dynamic Smagorinsky model.

– Unexpectedly, the best agreement between numerical and experimental values of k was found on the coarse grid. Note however that similar results were found by other authors in the past.

– The SGMV technique showed that the SGS modeling and numerical errors were rather high for the simulation on Grid20. However, both error contributions are of opposite sign and eventually compensate each other, leading to a total error

comparable to the one on the fine grid and explaining the similarity of the computed values of U on the two grids.

– The estimation of the modeling error for U by SGMV showed that it was very low for C_s=0.1 on Grid30, which is linked to the small difference in mean velocity results obtained on the fine grid with different C_s values (no plots were shown here).

– According to the *LES_IQ* indicator, the simulations with the standard Smagorinsky model and C_s=0.1 with 20 (LES20-1) and 30 cells (LES30-1) per building side can be both classified as well-resolved LESs in the sense that they resolve at least 80% of the total turbulent kinetic energy in the region around the building (LES20-1: 80% on average; LES30-1: 91%)

– The over-estimation of the measured values of k by LES30-1 was observed. The reason for this is not totally clear and this result needs to be confirmed on another test case.

Future research on this topic will consist of:

– Applying the SGMV procedure to the turbulent kinetic energy, on the same validation case.

– Repeating the complete procedure on another validation experiment of flow around bluff bodies, for confirmation.

– Testing the influence of the time step size and verifying the iterative convergence within each time step. In particular, the spectra of velocity fluctuations should be analyzed to further explain the k-values computed by LES.

– Repeating the study with another CFD code (e.g. OpenFOAM).

– Applying the procedure to other configurations representative of the built environment.

Guidelines on the use of LES in wind engineering could be deduced from the presented results.

In the following chapters, the superior performance of LES compared to RANS in terms of simulation of wind flow around bluff bodies is claimed, supported by research articles on the topic. However, to ensure completeness, the same case has been simulated with three different RANS models (those used in the next chapter to simulate dispersion around isolated buildings) and the results are presented in Appendix A (p. 89).

Chapter III
Pollutant dispersion around buildings: CFD modeling

Computational Fluid Dynamics (CFD) is increasingly used to predict wind flow and pollutant dispersion around buildings. The two most frequently used approaches are solving the Reynolds-averaged Navier-Stokes (RANS) equations and Large-Eddy Simulation (LES). In the present study, we compare the convective and turbulent mass fluxes predicted by these two approaches for two configurations of isolated buildings with distinctive features. We use this analysis to clarify the role of these two components of mass transport on the prediction accuracy of RANS and LES in terms of mean concentration. It is shown that the proper simulation of the convective fluxes is essential to predict an accurate concentration field. In addition, appropriate parameterization of the turbulent fluxes is needed with RANS models, while only the subgrid-scale effects are modeled with LES. Therefore, when the source is located outside of recirculation regions (case 1), both RANS and LES can provide accurate results. When the influence of the building is higher (case 2), RANS models predict erroneous convective fluxes and are largely outperformed by LES in terms of prediction accuracy of mean concentration. These conclusions suggest that the choice of the appropriate turbulence model depends on the configuration of the dispersion problem under study. It is also shown that for both cases LES predicts a counter-gradient mechanism of the streamwise turbulent mass transport, which is not reproduced by the gradient-diffusion hypothesis that is generally used with RANS models.

III.1 Introduction

Computational Fluid Dynamics (CFD) is increasingly explored and used to predict wind flow and pollutant dispersion around buildings. Accurate numerical simulation of this complex coupled process requires careful simulation of each of its constituents: (1) the incoming atmospheric boundary layer (ABL) flow; (2) the turbulent wind flow around the buildings submerged in the ABL; and (3) the transport process of the pollutant by convection and diffusion in the turbulent wind-flow pattern. Because of the turbulent and inherently transient nature of the flow around buildings, the accuracy of pollutant dispersion simulations is strongly influenced by the turbulence modeling approach used, which is generally either steady Reynolds-Averaged Navier-Stokes (RANS) or Large-Eddy Simulation (LES).

In turbulent flows, dispersion can be seen as the combination of the molecular, convective and turbulent mass transport, where the first is often negligibly small compared with the two others. Several earlier research efforts have compared the performance of RANS and LES approaches for pollutant dispersion in idealized urban geometries like street canyons (e.g. [Walton and Cheng, 2002; Salim et al., 2011a; Salim et al., 2011b; Tominaga and Stathopoulos, 2011]) and arrays of buildings (e.g. [Chang, 2006; Dejoan et al., 2010]). Other efforts have compared RANS and LES for isolated buildings (e.g. [Tominaga and Stathopoulos, 2010; Yoshie et al., 2011]), or in real urban environments (e.g. [Hanna et al., 2006; Gousseau et al., 2011a]). Overall, LES appears to be more accurate than RANS in predicting the mean concentration field because it captures the unsteady concentration fluctuations. Moreover, this approach provides the statistics of the concentration field which can be of prime importance for practical applications.

Most of the aforementioned studies have analyzed the prediction accuracy of CFD by comparing the resulting mean concentrations on and around building surfaces. Only few of them have analyzed the performance of RANS and LES by focusing on the mass transport process itself. Tominaga and Stathopoulos [2011] compared the lateral and vertical turbulent fluxes inside a street canyon computed with RANS and LES. Yoshie et al. [2011] employed these two approaches to illustrate the horizontal distribution of the lateral turbulent mass flux around an isolated building with non-isothermal ABL flow. Rossi et al. [2010] compared the performance of different turbulent-flux models for RANS for dispersion around a cube. Direct Numerical Simulation was also performed for a uniform inflow profile and a Reynolds number equal to 5000. To the best of our knowledge, only Tominaga and Stathopoulos [2010] provided some information about convective and diffusive fluxes for the case of dispersion around a building in an ABL flow, but their study focused at only a few locations on the roof.

In this paper, we present a detailed analysis of the transport process of a pollutant in the turbulent wind-flow pattern around isolated buildings. The relative influence of

convective and turbulent fluxes in the transport process is analyzed and the role of these fluxes in the prediction accuracy of RANS and LES simulations is clarified. For this purpose, two cases with distinctive features in terms of the transport process are selected, for which also detailed wind tunnel experiments are available:

1. Dispersion from a stack located immediately downstream of an isolated rectangular building [Huber et al., 1980];

2. Dispersion from a rooftop vent on an isolated cubical building [Li and Meroney, 1983a].

In case 1, the stack is relatively high and discharges the pollutants outside the building wake, which decreases the influence of the building on the dispersion of the plume. In case 2, the source is located directly on the roof of the building and the pollutant gas is released with low velocity ratio into the rooftop separation bubble. Validation of the CFD simulations is performed by comparing the numerical results with the wind-tunnel concentration measurements presented in [Huber et al., 1980] and [Li and Meroney, 1983a]. For case 1, concentration profiles along three lines located five building heights downstream of the building are used whereas for case 2, concentration contours on the roof and in the wake of the building are used.

Some details about the numerical procedure are given in the next section. Then, for each case, the experiment is outlined, the numerical model is described and the results are presented and analyzed.

III.2 Governing equations

III.2.1 RANS and turbulence models

With the RANS approach, the Reynolds-averaging operator is applied to the flow equations. Only the averaged quantities are computed and the effect of turbulence on the average flow field – symbolized by the Reynolds stresses – is modeled with turbulence models. In this study, four turbulence models will be used and compared: the standard k-ε model (SKE) [Jones and Launder, 1972], the realizable k-ε model (RLZ) [Shih et al., 1995], the renormalization-group (RNG) k-ε model [Yakhot et al., 1992], and the Reynolds-Stress model (RSM) with a linear pressure-strain model and wall-reflection effects [Launder et al., 1975; Gibson and Launder, 1978]. The relevant equations can be found in the references. For brevity, only the model constants are given here. They are the default values in Fluent 6.3. For SKE: C_μ=0.09; $C_{1\varepsilon}$=1.44; $C_{2\varepsilon}$=1.9; σ_k=1.0; σ_ε=1.3. For RLZ: $C_{1\varepsilon}$=1.44; $C_{2\varepsilon}$=1.9; σ_k=1.0; σ_ε=1.2. For RNG: C_μ=0.0845; $C_{1\varepsilon}$=1.42; $C_{2\varepsilon}$=1.68. For RSM: C_μ=0.09; $C_{1\varepsilon}$=1.44; $C_{2\varepsilon}$=1.92; C_1=1.8; C_2=0.6; C'_1=0.5; C'_2=0.3; σ_k=1.0; σ_ε=1.3.

III.2.2 LES and subgrid-scale models

With LES, a spatial-filtering operator is applied to the Navier-Stokes equations to separate the smallest scales of motion, which have a more universal behavior and can therefore be modeled, and the large scales, which are explicitly resolved. The effect of the smallest scales on the resolved flow field is modeled with a subgrid-scale (SGS) model. In this study, the dynamic Smagorinsky SGS model [Smagorinsky, 1963; Germano et al., 1991; Lilly, 1992] is used. LES is particularly interesting when dealing with mass transport phenomena since this process is mainly governed by the largest scales of motion.

III.2.3 Numerical procedure

For the RANS simulations presented here, all the transport equations (momentum, energy, turbulence variables and concentration) are discretized using a second-order upwind scheme. Pressure interpolation is second order. The SIMPLE algorithm is used for pressure-velocity coupling. Convergence is assumed to be obtained when the scaled residuals [Fluent Inc., 2006] reach 10^{-5}.

For LES, the filtered momentum equation is discretized with a bounded central-differencing scheme. A second-order upwind scheme is used for the energy and concentration equations. Pressure interpolation is second order. Time integration is second-order implicit. The non-iterative fractional step method [Kim and Moin, 1985] is used for time advancement.

III.2.4 Wall treatment

In order to properly simulate the approaching ABL flow in the computational domain, horizontal homogeneity must be achieved, i.e. the vertical flow profiles that are prescribed at the inlet must be preserved along the domain before reaching the buildings [Blocken et al., 2007a; Blocken et al., 2007b].

For RANS simulations with the Fluent 6.3 CFD code, the standard wall functions [Launder and Spalding, 1974] are applied to the wall boundaries (ground, building and stack surfaces). For the ground, the wall functions are modified for roughness [Cebeci and Bradshaw, 1977], which is specified by an equivalent sand-grain roughness height k_s and a roughness constant C_r. Horizontal inhomogeneity of the ABL can be limited by adapting k_s and C_r to the inlet ABL profiles, following the equation by Blocken et al. [2007b]: $k_s=9.793z_0/C_r$, where z_0 is the aerodynamic roughness length of the terrain.

To the authors' best knowledge, such a relation does not exist for LES with Fluent. In this case, the law-of-the-wall is used and the wall roughness is not taken into account [Fluent Inc., 2006]. The same boundary condition is used for the smooth walls, i.e. the building and stack surfaces.

In both RANS and LES simulations, the upstream domain length is kept as short as possible ($5H$) to limit horizontal inhomogeneity [Blocken et al., 2007b]. A posteriori verification showed that the maximum wall-normal distance of the first centroid at the wall boundaries was approximately 100 wall units ($z^+ = z u^*/v$, where z is the wall-normal distance, u^* is the friction velocity and v is the kinematic viscosity of the fluid) for case 1 and 40 for case 2.

III.2.5 Dispersion modeling

The instantaneous pollutant concentration (c [kg m⁻³]) is treated as a scalar transported by an advection-diffusion equation (Eulerian approach):

$$\frac{\partial c}{\partial t} + \vec{u}.\nabla c = -\nabla.\vec{q_m} + s_c \tag{III.1}$$

where $\vec{u}$ is the velocity vector; s_c is a source term; and $\vec{q_m}$ is the mass flux due to molecular diffusion.

Applying the Reynolds decomposition to the variables ($x = X + x'$ where $X = <x>$ and x' are the mean and fluctuating components of x, respectively) and averaging Equation (III.1) yields:

$$\nabla.(\vec{Q_m} + \vec{Q_c} + \vec{Q_t}) = S_c \tag{III.2}$$

In this equation, $\vec{Q_m}$ is the mean molecular mass flux [kg m⁻² s⁻¹], proportional to the gradient of mean concentration:

$$Q_{m,i} = -D_m \frac{\partial C}{\partial x_i} \tag{III.3}$$

where D_m is the molecular mass diffusivity [m² s⁻¹]. In general, the molecular mass flux is negligible in comparison with the mean convective (the adjective "mean" will be omitted in what follows) and turbulent mass fluxes, symbolized by $\vec{Q_c}$ and $\vec{Q_t}$, respectively. The former corresponds to the advection of the mean concentration by the mean flow; it is defined by:

$$Q_{c,i} = U_i C \tag{III.4}$$

The turbulent mass flux is given by:

$$Q_{t,i} = <u_i'c'> \tag{III.5}$$

Neither the velocity nor the concentration fluctuations are computed by the RANS models so, with this approach, the turbulent flux must be linked to the mean variables. Generally, the gradient-diffusion hypothesis is adopted, by analogy with molecular diffusion:

$$Q_{t,i,RANS} = -D_t \frac{\partial C}{\partial x_i} \tag{III.6}$$

where D_t is the turbulent mass diffusivity whose value is deduced from the computed turbulent viscosity ν_t and the input value of the turbulent Schmidt number $Sc_t=\nu_t/D_t$. This parameter is known to have a large influence on the simulation of dispersion, with an optimum value that strongly depends on the configuration under study [Tominaga and Stathopoulos, 2007; Blocken et al., 2008].

With LES, the effect of the smallest scales of motion on dispersion is modeled by the SGS mass flux $\overrightarrow{q_{sgs}}$ that appears in the filtered dispersion equation:

$$q_{sgs,i}=\overline{u_i c}-\overline{u}_i\overline{c}=-D_{sgs}\frac{\partial\overline{c}}{\partial x_i} \tag{III.7}$$

where the overbar denotes the filtering operation and D_{sgs} is the SGS mass diffusivity computed via the SGS viscosity ν_{sgs} and the SGS Schmidt number $Sc_{sgs}=\nu_{sgs}/D_{sgs}$. Here, Sc_{sgs} is computed dynamically, with a similar procedure as the Smagorinsky coefficient C_s [Moin et al., 1991]. In the LES results presented here, the convective and turbulent fluxes are computed based on the resolved variables:

$$Q_{c,i,LES}=<\overline{u}_i><\overline{c}> \tag{III.8}$$

$$Q_{t,i,LES}=<\overline{u}_i'\overline{c}'>+<q_{sgs,i}>\cong<\overline{u}_i'\overline{c}'> \tag{III.9}$$

The subscript "LES" will be omitted in what follows, as well as the subscript "RANS" in Equation (III.6). The mean SGS mass flux $<q_{sgs,i}>$ is neglected in the computation of the turbulent mass flux (Eq. (III.9)): in the two cases considered here it is generally at least two orders of magnitude lower than $<\overline{u}_i'\overline{c}'>$[1].

All concentrations are expressed in non-dimensional form. The instantaneous concentration coefficient is defined by:

$$K_{inst}=\frac{c}{C_0} \tag{III.10}$$

where C_0 is the reference concentration [kg m^{-3}] given by:

$$C_0=\frac{Q_e}{H^2 U_{ref}} \tag{III.11}$$

with Q_e the pollutant exhaust rate [kg s^{-1}]; H the building height and U_{ref} the mean wind speed at reference height z_{ref} ($z_{ref}=1.5H$ for case 1; $z_{ref}=H$ for case 2). The mean non-dimensional concentration coefficient K is defined as the average value of K_{inst}. A reference flux magnitude $Q_0=C_0 U_{ref}$ is used to make the convective and turbulent mass fluxes non-dimensional.

---

[1] See proof for case 2 in Section IV.3.

III.3 Case 1: dispersion from a stack downstream of an isolated rectangular building

III.3.1 Description of the experiment

Huber et al. [1980] performed detailed experiments of gas dispersion around a rectangular building model in a wind tunnel. The building dimensions are $H \times 2H \times H$ in the longitudinal (x), lateral (y) and vertical (z) direction, respectively, where H=0.25 m. An ABL flow is simulated in the wind tunnel, with a Reynolds number based on U_{ref} and z_{ref} (Re) equal to 6.0×10^4 and with z_0=6.5×10^{-4} m at model scale (1:200). Immediately downstream of the building, a stack of height $1.5H$ and diameter $0.042H$ is emitting a mixture of air and methane[1] with a velocity ratio (M) equal to 1.5. M is defined as the ratio W_e/U_{ref} where W_e is the vertical exhaust velocity. The origin of the coordinate system is shown in Figure III.1-a.

Experimental data used to validate the present simulations are the profiles of K along three lines $5H$ downstream of the source (Fig. III.1-a): H5-0 and H5-1.5 are horizontal lines located at ground (z/H=0.1) and stack (z/H=1.5) level, respectively, and V5 is a vertical line in the mid-plane (y/H=0). It should be stressed that the conclusions drawn here on the performance of each turbulence model hold for this particular location. The results are indeed quite different closer to the building (see case 2) or farther downstream, where the accurate simulation of the ABL is crucial.

III.3.2 Domain, computational grid and boundary conditions

The domain dimensions follow the COST 732 and AIJ guidelines [Franke et al., 2007; Tominaga et al., 2008b]: $26H$ (length)$\times 14H$ (width)$\times 7H$ (height), based on the model scale. An upstream length of $5H$ and a downstream length of $20H$ are provided to place the boundaries out of the zone of influence of the building (Fig. III.1-a).

RANS and LES computations are performed on the same computational grid composed of 1,450,960 prismatic cells and constructed using the surface-grid extrusion procedure [van Hooff and Blocken, 2010]. The growth ratio of adjacent cells does not exceed 1.1. The building height and the stack circumference are divided into 20 and 64

---

[1] Properties of methane (CH_4): ϱ_{CH4}=0.6679 kg m^{-3}; μ_{CH4}=1.087×10^{-5} kg m^{-1} s^{-1}.
Properties of air (also used in the next chapters): ϱ_{air}=1.225 kg m^{-3}; μ_{air}=1.7894×10^{-5} kg m^{-1} s^{-1}.
Molecular diffusivity of methane in air: $D_{m,CH4/air}$=2.88×10^{-5} m^2 s^{-1}.
The density of the mixture ϱ_{mix} is computed based on a volume-weighted mixing law: ϱ_{mix}=$1/\left(\sum_i \chi_i/\varrho_i\right)$, where χ_i and ϱ_i are the mass fraction and density of the species i, respectively. The viscosity of the mixture μ_{mix} is computed based on a mass-weighted mixing law: ϱ_{mix}=$\sum_i \chi_i \mu_i$, where μ_i is the dynamic viscosity of the species i. These laws are also used in the next chapters.
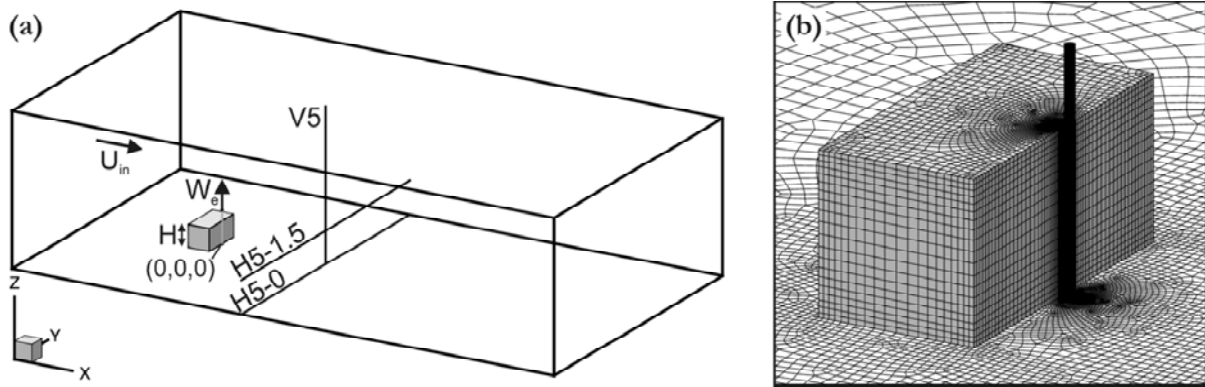
Figure III.1. Case 1: (a) Domain, measurement lines for CFD validation and definition of parameters. Measurement lines: H5-0 corresponds to $x/H=5$ and $z/H=0.1$; H5-1.5 corresponds to $x/H=5$ and $z/H=1.5$; V5 corresponds to $x/H=5$ and $y/H=0$. (b) Grid on building, stack and ground surfaces (total number of cells: 1,450,960).

cells, respectively (Fig. III.1-b). A grid-sensitivity analysis showed that grid refinement did not lead to significant change in the concentration results.

The inlet profiles of U_{in}, k and ε are based on the wind-tunnel measurements reported in [Huber et al., 1980]. At the outlet, zero static pressure is prescribed. At the top and lateral boundaries, a symmetry boundary condition is imposed. The bottom boundary as well as the building and stack surfaces are defined as no-slip walls; wall treatment is set as described in Section III.2.4. A velocity inlet is defined at the top face of the stack, with an assumed turbulence intensity of 10%[1] and a methane volume fraction of 1%, as in the experiment.

For the LES computations, a time-dependent inlet profile is generated by using the vortex method [Sergent, 2002] with a number of vortices N_v=190. As shown by Sergent [2002], this parameter has only little influence on the generated velocity fluctuations. Furthermore, previous CFD simulations of air flow around a cube (not presented here) have shown that this method is suitable to generate turbulent fluctuations at the inlet in the case of ABL flow around a bluff body[2]. The results of the LES computation presented here are averaged over a period of 312 time units ($t_u=z_{ref}/U_{ref}$) with a constant non-dimensional time step $\varDelta t^*=\varDelta t/t_u=0.062$. It was verified that the averaging time is sufficient to obtain statistically-steady results by monitoring the evolution of K with time (moving average).

III.3.3 Results

The first three graphs of Figure III.2 (Figs. III.2-a,b,c) show the influence of Sc_t on the concentration values obtained with RLZ 5H downstream of the building model. For the

---

[1] Note that this value has been used for the RANS simulations only. With LES, no perturbations were super-imposed to the mean velocity at this boundary.

[2] See also Chapter II.

three measurement lines, RLZ can predict K-values in close agreement with the experiments when Sc_t is set to 0.5. A lower (resp. higher) value of Sc_t leads to an under- (resp. over-) estimation of the concentration values along lines H5-1.5 and V5. The sensitivity to Sc_t is lower on line H5-0 (Fig. III.2-a) because, close to the ground, turbulent mass transport – which is governed by this parameter – is limited by the presence of the wall.

The other RANS models have been tested with Sc_t=0.5 (Figs. III.2-d,e,f). For this case, the difference between SKE and RLZ results is negligible. RSM also provides accurate results, with a slight overestimation of K in comparison with the measurements. RNG largely overestimates the concentration and should be used here with a lower Sc_t value. On line H5-0, the computed variables depend more on the wall treatment than on the turbulence model itself, explaining why the difference between the RANS models is low (Fig. III.2-d).
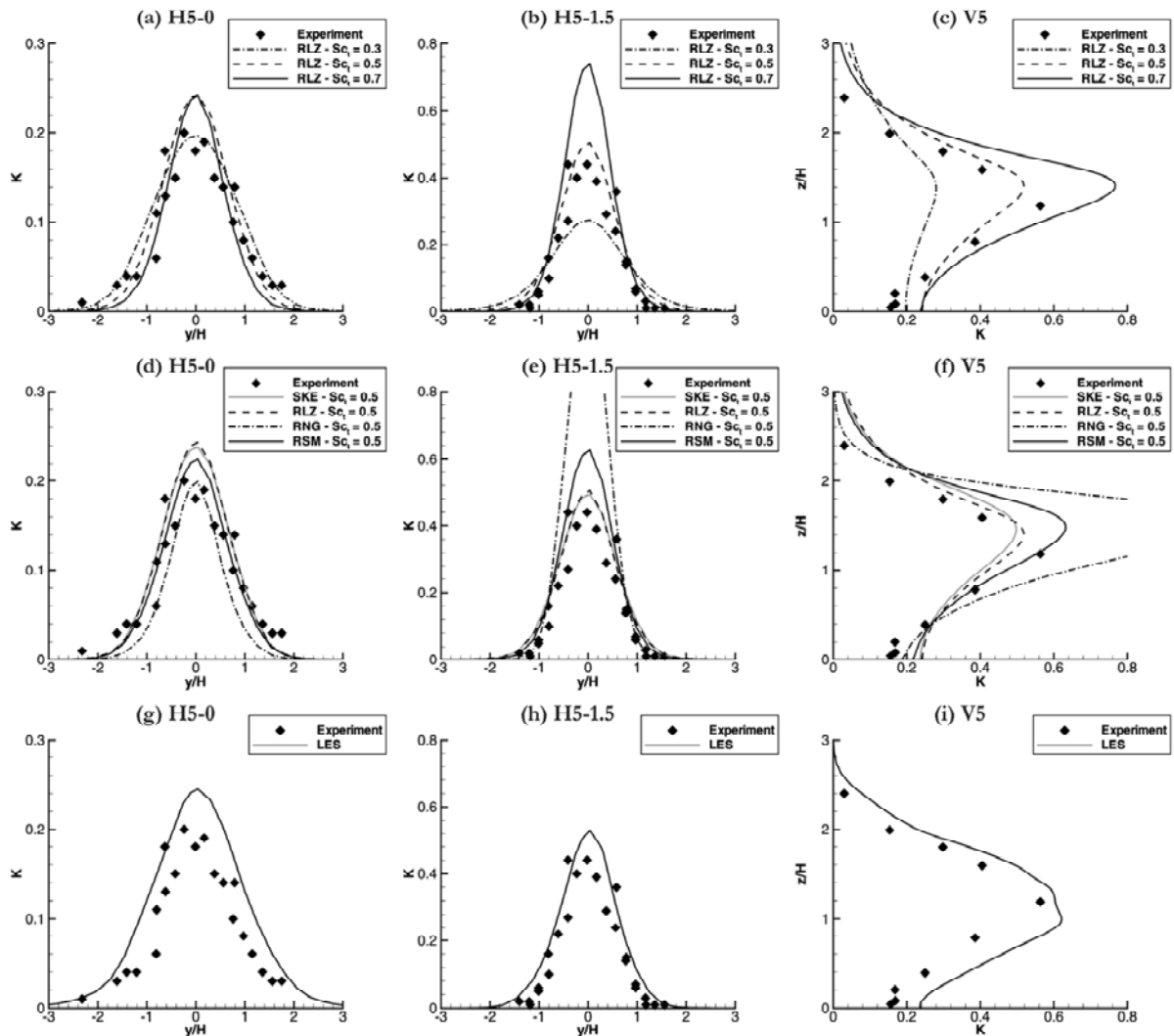
Figure III.2. Profiles of K along H5-0 (left), H5-1.5 (middle) and V5 (right). (a,b,c) Influence of Sc_t value with RLZ. (d,e,f) Comparison between the four RANS models with Sc_t=0.5. (g,h,i) LES results.

The average LES results agree fairly well with the experiment on the three measurement lines. Figure III.2-i shows that, contrary to RANS models which compute the local maximum of concentration at the level of the stack (z/H=1.5), LES predicts that the centerline of the plume is shifted downwards, in agreement with the experiment. This deviation can also be observed when looking at the average shape of the plume symbolized by the isosurface K=1 in Figure III.3. As already suggested by the concentration profiles, the plume shape is rather similar with SKE, RLZ and RSM: it extends horizontally downstream without being much disturbed by the presence of the building, whereas the isosurface computed with RNG extends farther downstream. Figure III.3-f shows the isosurface K_{inst}=1 at t^*=t/t_u=312 computed with LES. At this instant, the plume is largely different from its average shape: the region where K exceeds
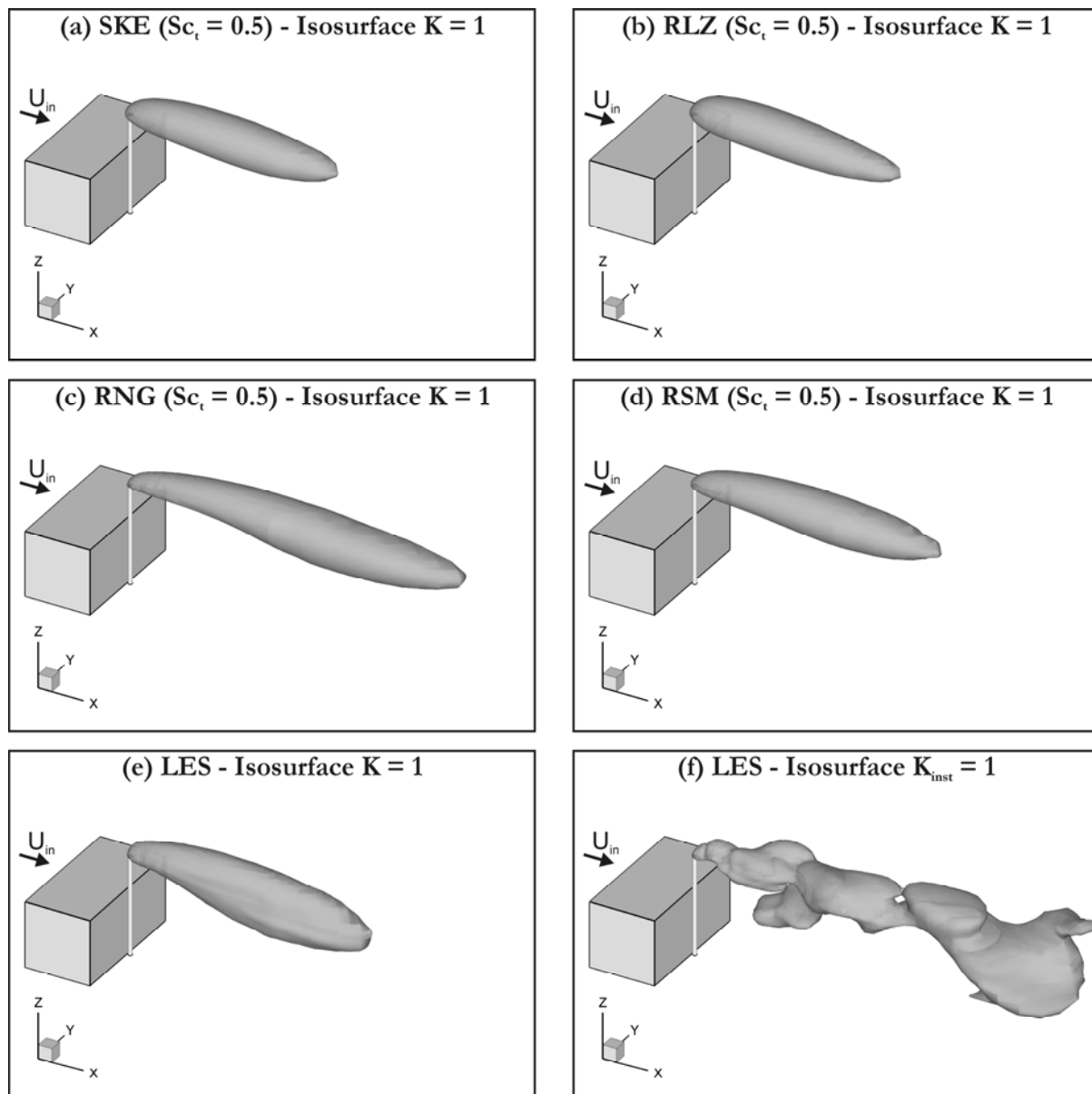
Figure III.3. (a,b,c,d,e) Average plume shape obtained with the five turbulence models. (f) Instantaneous plume shape obtained with LES at t^*=312.

1 can extend farther downstream and reach zones close to the ground.

The non-dimensional convective and turbulent mass fluxes are depicted in Figures III.4 and III.5, respectively. Because of the similarity between SKE and RLZ results, it has been chosen to show only the fluxes computed by the latter model for sake of brevity. The emitted pollutant gas is mainly convected downstream, as shown by the contours of convective flux in the streamwise direction (Figs. III.4-a,c,e,g). In these figures, the blue zone downstream of the building indicates the backflow of the wake recirculation zone, whose length is largely overestimated by the RANS models in comparison with LES. However, since only little pollution reaches this zone, the magnitude of the flux is low and only marginally influences the final concentration field.

The vertical exhaust velocity from the stack creates a positive $Q_{c,z}$ around this position (Figs. III.4-b,d,f,h). Further downstream, the negative vertical velocity due to flow reattachment transports the pollutant towards the ground. Figure III.4-h shows that with LES, this downward convective flux occurs closer to the building – due to the smaller recirculation zone – and is more intense than with the RANS models. As a consequence, the centerline of the plume is deviated downwards, as already observed in the previous figures and in agreement to what was measured in the wind tunnel.

In this case, the main difference between the mass fluxes computed by RANS and LES approaches lies in the streamwise turbulent flux $Q_{t,x}$, shown in Figures III.5-a,c,e,g. Let us consider the concentration level at stack height. Following the gradient-diffusion hypothesis (Eq. (III.6)), the decrease of the concentration in the x-direction ($\partial C / \partial x < 0$) generates a positive flux, represented in red in Figures III.5-a,c,e. Although the evolution of C is similar with LES, it is clear that the turbulent mass transport in this direction does not obey the gradient-diffusion hypothesis: $Q_{t,x}$ is negative and counters convective effects in the region above the stack ($z/H > 1.5$) and it is positive below the stack for $x/H > 1$ (Fig. III.5-g). It can also be noted that the values of $|Q_{t,x}/Q_0|$ computed by LES are higher than with RANS. However, by comparing the left column of Figure III.4 with the one of Figure III.5 (the same contour levels are used for both figures), it is clear that the main mechanism of mass transport in the streamwise direction is convection. Hence, the deficiencies of the RANS models – and more particularly of the gradient-diffusion hypothesis – in terms of streamwise turbulent transport do not significantly affect the final concentration field. This explains why fairly accurate results can be obtained with these models and hypothesis.

The balance between convective and turbulent mass transport is different in the vertical direction: the comparison of the right columns of Figures III.4 and III.5 shows that both mechanisms act with similar intensity. Turbulent vertical fluxes are even stronger, except in the near wake of the building and at the plume centerline. The roles of these mechanisms are different, however: while convection tends to act on the plume as a "block" (i.e. by moving its centerline), turbulence tends to "stretch" the plume in the
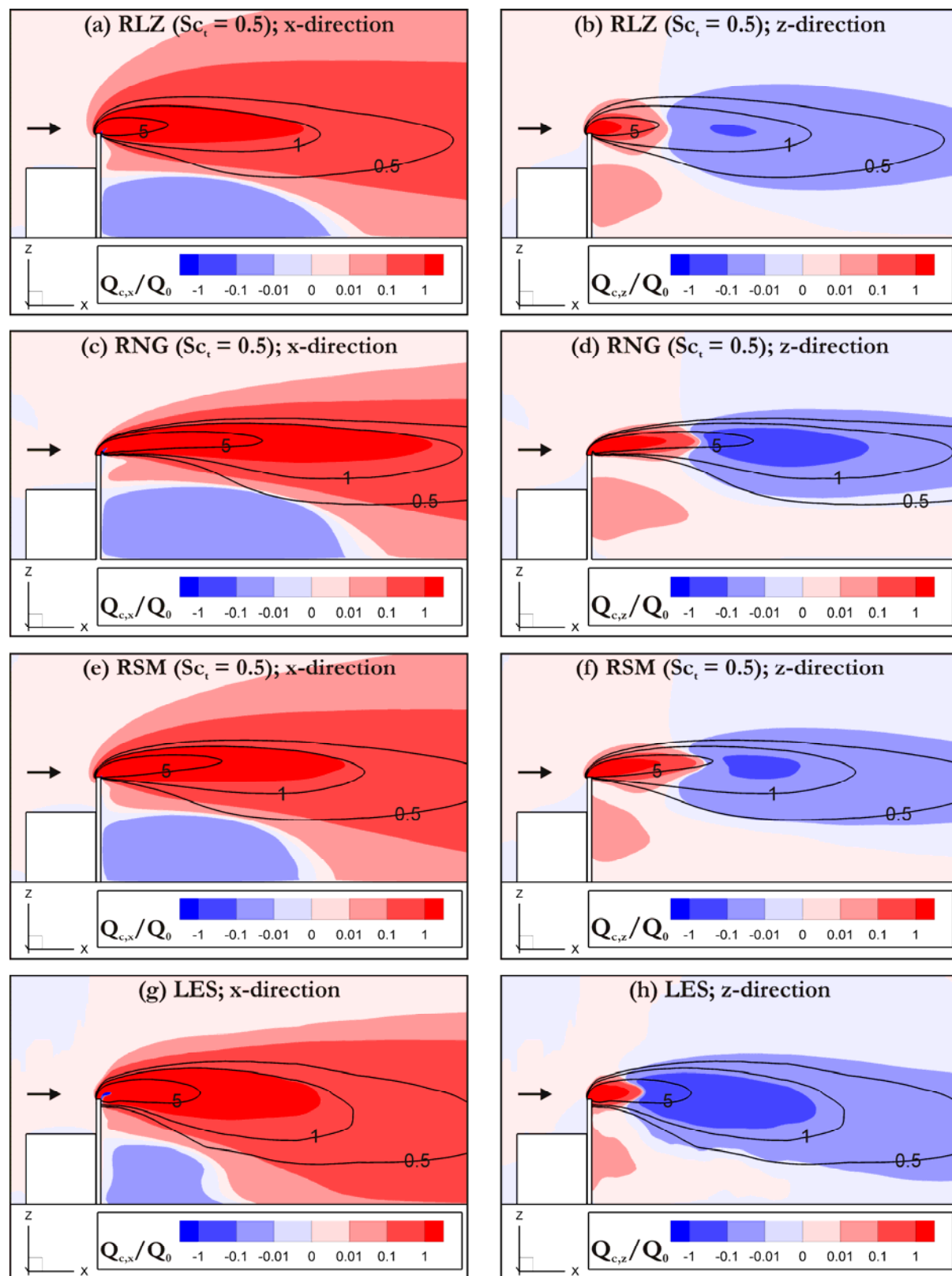
Figure III.4. Streamwise (left; $Q_{c,x}/Q_0$) and vertical (right; $Q_{c,z}/Q_0$) non-dimensional convective fluxes in the vertical mid-plane ($y/H=0$) obtained with (a,b) RLZ; (c,d) RNG; (e,f) RSM; and (g,h) LES. The isolines $K=0.5$; 1; 5 are also shown.
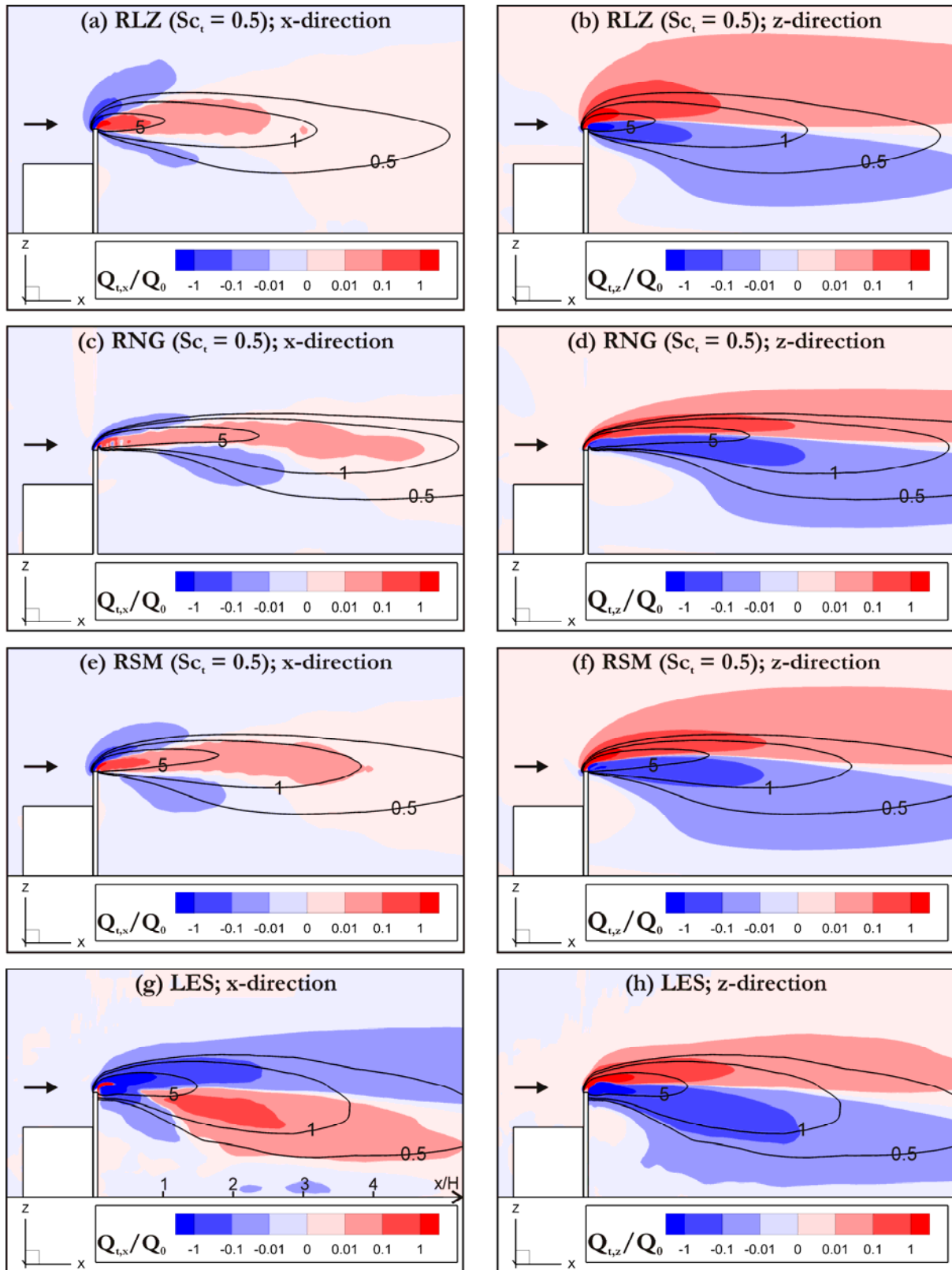
Figure III.5. Streamwise (left; $Q_{t,x}/Q_0$) and vertical (right; $Q_{t,z}/Q_0$) non-dimensional turbulent fluxes in the vertical mid-plane ($y/H=0$) obtained with (a,b) RLZ; (c,d) RNG; (e,f) RSM; and (g,h) LES. The isolines $K=0.5$; 1; 5 are also shown.

vertical (and lateral) direction. Indeed, it was already observed in Figure III.2-b, for instance, that if Sc_t is decreased (i.e. $Q_{t,z}$ is increased), the stretching effect becomes stronger in the vertical and lateral directions. Both RANS (Figs. III.5-b,d,f) and LES (Fig. III.5-h) models predict a similar trend for the contours of $Q_{t,z}/Q_0$, which supports the validity of the gradient-diffusion hypothesis in the vertical direction. This also holds for the lateral direction (not shown here).

III.4 Case 2: dispersion from a rooftop vent on an isolated cubical building

III.4.1 Description of the experiment

The experiment by Li and Meroney [1983a] involves a cubic obstacle with height H=0.05 m placed in the test section of a wind tunnel, with the windward face perpendicular to the ABL flow (Re=1.1×10⁴; z_0=7.5×10⁻⁵ m at model scale 1:2000). At the center of the roof, pure helium[1] is emitted by a circular exhaust with relatively low velocity (M=0.19). Concentration contours on the top face of the cube and in the vertical mid-plane (y/H=0) downstream of the cube are presented here for CFD validation – contrary to case 1 where line profiles were used.

III.4.2 Domain, computational grid and boundary conditions

The domain is 26H long (5H upstream and 20H downstream of the cube), 11H wide and 6H high (Fig. III.6-a) with the origin of the coordinate system at the center of the cube's bottom face. The computational grid consists of 1,480,754 cells with 40 segments around the exhaust circumference (Fig. III.6-b). The cube was discretized using 25 cells in the
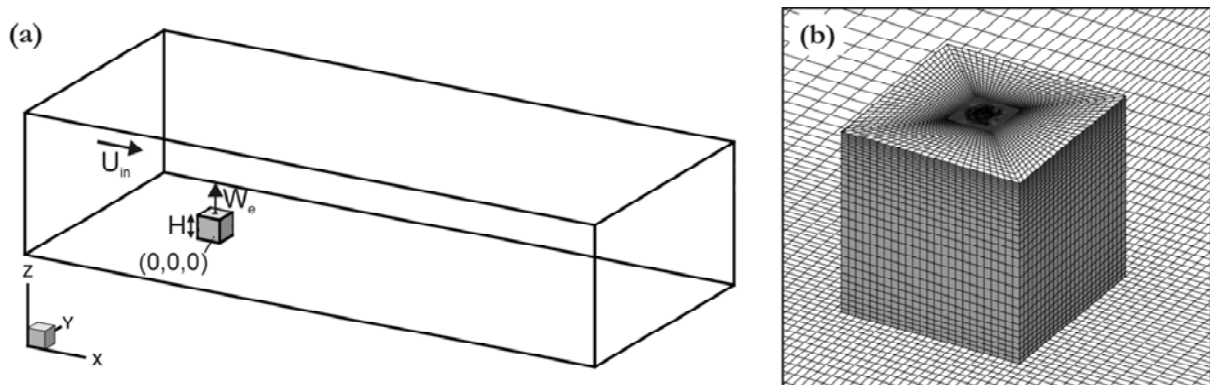
Figure III.6. Case 2: (a) Domain and definition of parameters. (b) Grid on building and ground surfaces (total number of cells: 1,480,754).

---

[1] Properties of helium (He): ϱ_{He}=0.1625 kg m⁻³; μ_{He}=1.99×10⁻⁵ kg m⁻¹ s⁻¹.
Molecular diffusivity of helium in air: $D_{m,He/air}$=6.7635×10⁻⁵ m² s⁻¹.

horizontal directions and 32 cells in the vertical direction in order to increase resolution close to the roof where high concentration gradients occur. The ratio of two neighboring cell dimensions was kept below 1.1. This grid was selected after a grid-sensitivity analysis: the accuracy of the results was improved in comparison with a coarser grid and the use of a finer grid with twice the total number of cells lead to identical results with the RANS models and only a slight change in the LES concentration contours – since this model is by definition grid-dependent. However, we argue that this change did not justify the increase in computational resources required.

The profiles of U_{in}, k and ε were imposed at the inlet, based on the experimental data. For LES, perturbations around the average velocity profile were imposed with the vortex method (N_v=190). The other boundary conditions are identical to those in case 1. The LES results are averaged over t^*=594, with a constant time step Δt^*=0.066. Note that a longer averaging period was required to get statistically-steady results compared to case 1, because the pollutant source is located in a zone of higher turbulence intensity.

III.4.3 Results

The measured and computed contours of K on the roof of the building are shown in
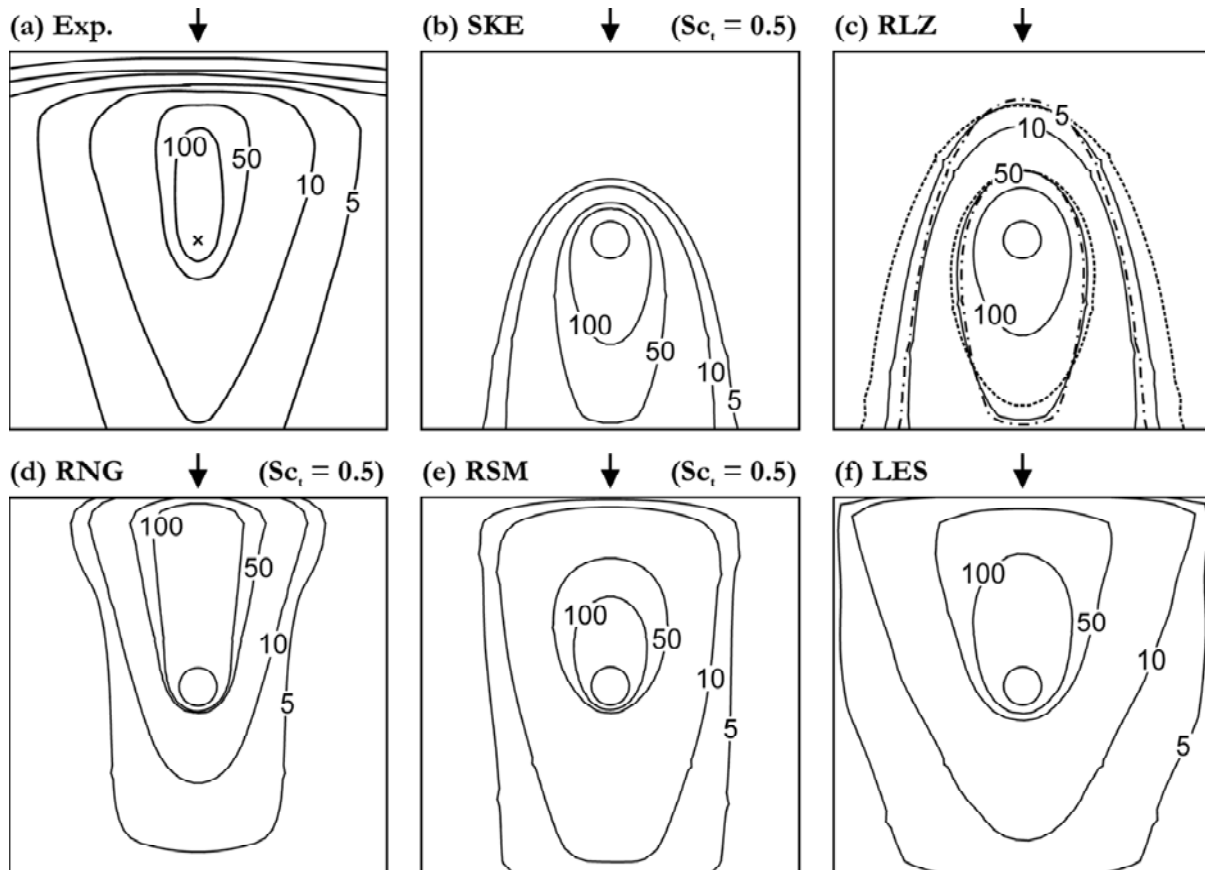
Figure III.7. (a) Experimental and (b,c,d,e,f) numerical contours of K on the roof. The arrows indicate the wind direction. The influence of Sc_t is depicted in (c): - - -: Sc_t=0.3; —: Sc_t=0.5; - —: Sc_t=0.7.

Figure III.7. In the experiment, because of the low velocity ratio of the exhaust, the pollutant gas gets "trapped" in the rooftop recirculation zone and is transported upstream by the backflow, as can be seen in Figure III.7-a. SKE and RLZ fail to reproduce this backward transport: the emitted gas is mainly "blown away" in the wind direction. RNG and RSM are more accurate and clearly reproduce the upstream transport of the pollutant (Figs. III.7-d,e). Nevertheless, these two models are outperformed by LES (Figs. III.7-f) which predicts concentrations in good agreement with the measurements, although the lateral diffusion is slightly over-predicted. Similar conclusions about the prediction accuracy of the different models are made based on the K contours in the wake of the building (Fig. III.8).

The Sc_t value does not strongly influence the RLZ results on the roof, as shown in Figure III.7-c where the isolines $K=5$ and $K=50$ are plotted for $Sc_t=0.3$ and 0.7. As in case 1, the reason is that turbulent mass transport is limited by the presence of the wall. In the wake of the building, the influence of this parameter is stronger and similar to the one in case 1 (Fig. III.8-c): when Sc_t decreases the plume becomes shorter and stretched in the vertical direction. However, changing the Sc_t value cannot compensate for the RANS model deficiencies in terms of flow field and the predicted levels of concentration remain high with RLZ, as well as with SKE. The use of RNG or RSM enhances the accuracy of the results but still LES is clearly better (Figs. III.8-d,e,f).

The structures of the plumes computed by RNG and RSM are similar to the one by LES, yet slightly longer (Figs. III.9-c,d,e). SKE and RLZ show a totally different result: only little pollutant reaches the leading edge of the roof and the zone close to the ground downstream of the building is contaminated in the sense that $K>1$. This is not the case with LES although some puffs of pollutant can reach this zone intermittently (Fig. III.9-f).

Several numerical simulations of air flow around a bluff body (e.g. [Murakami et al., 1990; Rodi, 1997; Tominaga et al., 2008a][1]) have demonstrated the superior performance of LES with respect to RANS in properly simulating several features of such a flow, including the rooftop and wake recirculation zones. This difference is verified in the present study: see Figures III.10-a,c,e,g, where these two backflow regions lead to an upstream mass transport (blue zones in the contour plots of $Q_{c,x}/Q_0$) while pollutant is convected downstream in the rest of the domain. The rooftop recirculation zone is almost nonexistent with RLZ whereas its size is over-predicted by RNG and RSM compared with LES, with consequences on the concentration contours as already observed in Figure III.7. It can also be seen in Figure III.10 that the reattachment length in the wake is overestimated by the RANS models (due to the underestimation of k), which partly explains the higher levels of concentration observed in Figure III.8. Like in

---

[1] See also Chapter II and Appendix A.
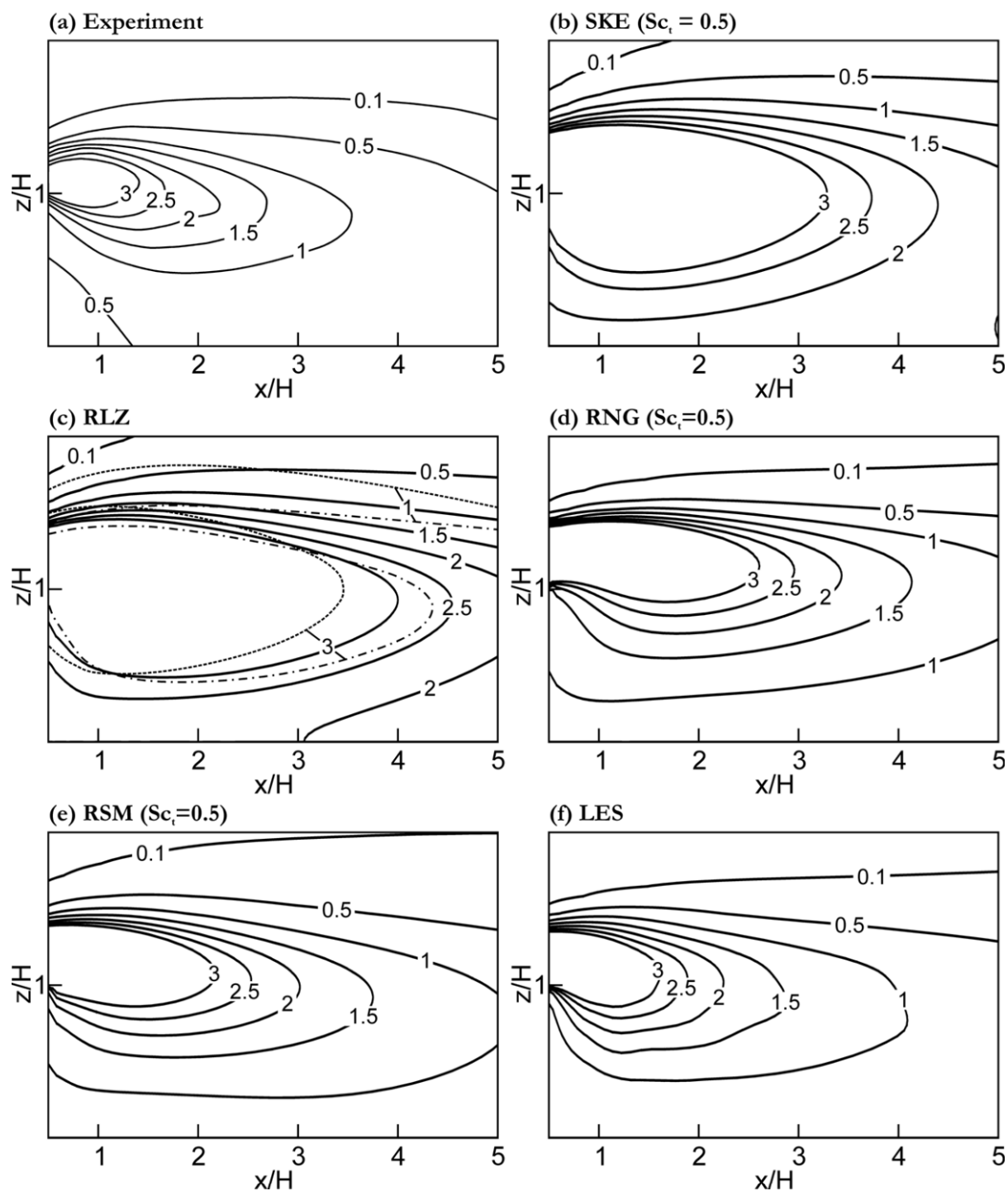
Figure III.8. (a) Experimental and (b,c,d,e,f) numerical contours of K in the wake of the building (y/H=0). x/H=0.5 corresponds to the leeward facade of the building. The influence of Sc_t is depicted in (c): - - -: Sc_t=0.3; —: Sc_t=0.5; - —: Sc_t=0.7.

case 1, this flow reattachment is responsible for a downward convective mass flux (Fig. III.10-b,d,f,h).

It must be emphasized that, contrary to case 1, these recirculation regions are colored in dark blue when plotting the contours of $Q_{c,x}/Q_0$. In other words, these regions are the place of intense convective fluxes because they contain higher pollutant
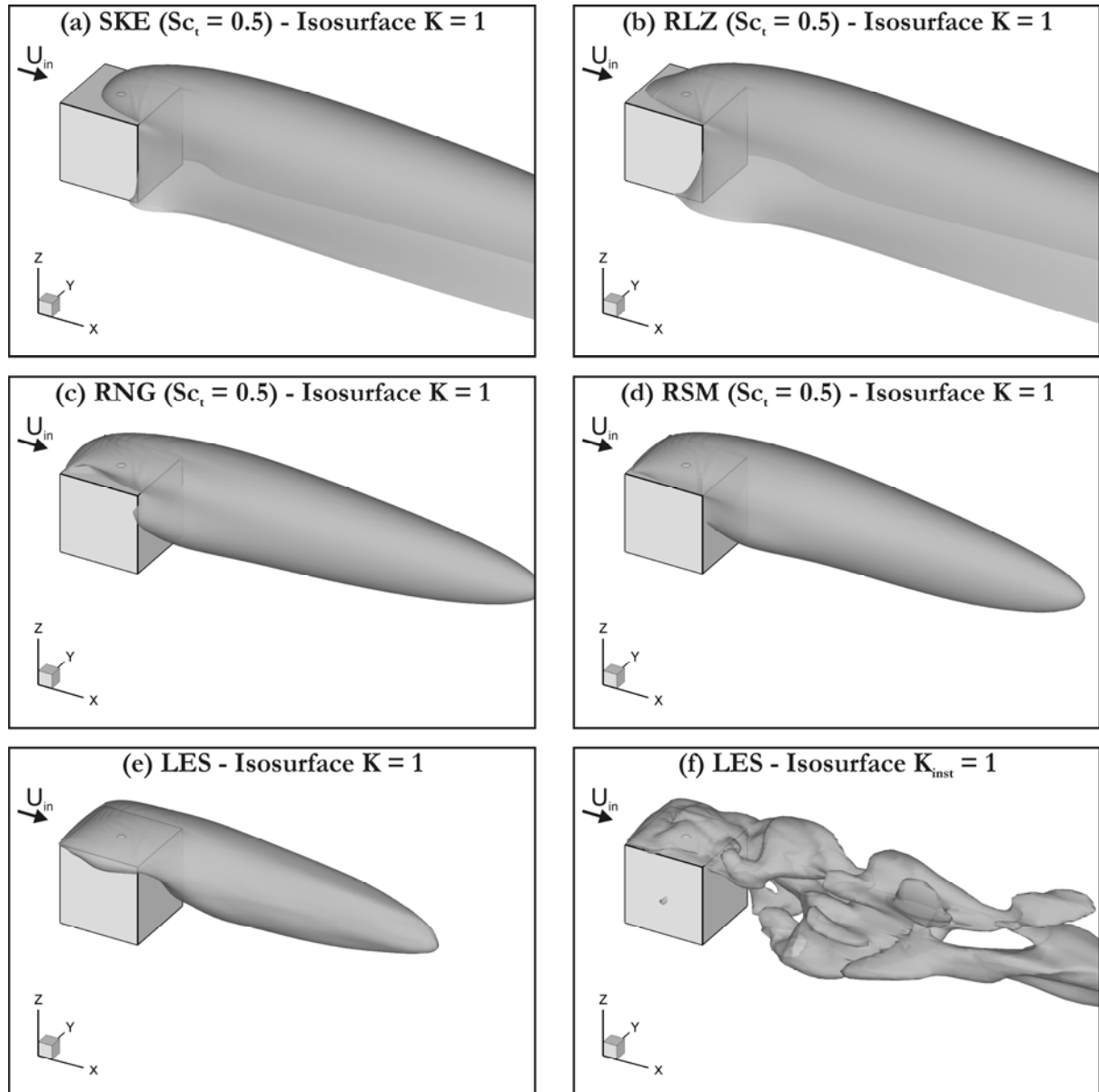
Figure III.9. (a,b,c,d,e) Average plume shape obtained with the five turbulence models. (f) Instantaneous plume shape obtained with LES at t^*=594.

concentrations. This shows the importance of the contribution of the recirculation zones to the overall mass transport and the necessity for the turbulence model to simulate them properly.

Above the source, downstream of the building, the mean concentration decreases along the x-direction. The gradient-diffusion hypothesis adopted with RANS leads to positive values for $Q_{t,x}/Q_0$, as can be seen in Figures III.11-a,c,e. By contrast, LES predicts a negative streamwise turbulent mass flux in this zone (blue zone in Fig III.11-g), in qualitative agreement with the low Reynolds number DNS simulations by Rossi et al. [2010]. It proves the ability of the present LES modeling to reproduce this so-called counter-gradient mechanism that acts in the streamwise direction. This, together with the smaller reattachment length, contributes to a shorter plume predicted by LES (Fig. III.9-

e). In the vertical direction, the turbulent mass flux is predicted by LES with similar trend than RANS models, i.e. with a gradient-diffusion mechanism (Figs. III.11-b,d,f,h).

The observation of the contours of $|Q_{t,i}/Q_{c,i}|$ (not shown here) shows that for the x-direction the magnitude of the convective flux is generally one order of magnitude higher than the turbulent flux (except in the zones of very low streamwise velocity), proving the dominant role of convection as a mechanism of mass transport streamwise. In this direction, the turbulent mass transport plays a secondary role on the prediction accuracy of concentration. By contrast, convective and turbulent fluxes are of the same order of magnitude in the vertical direction. Turbulence even dominates convection, except on the centerline of the plume.
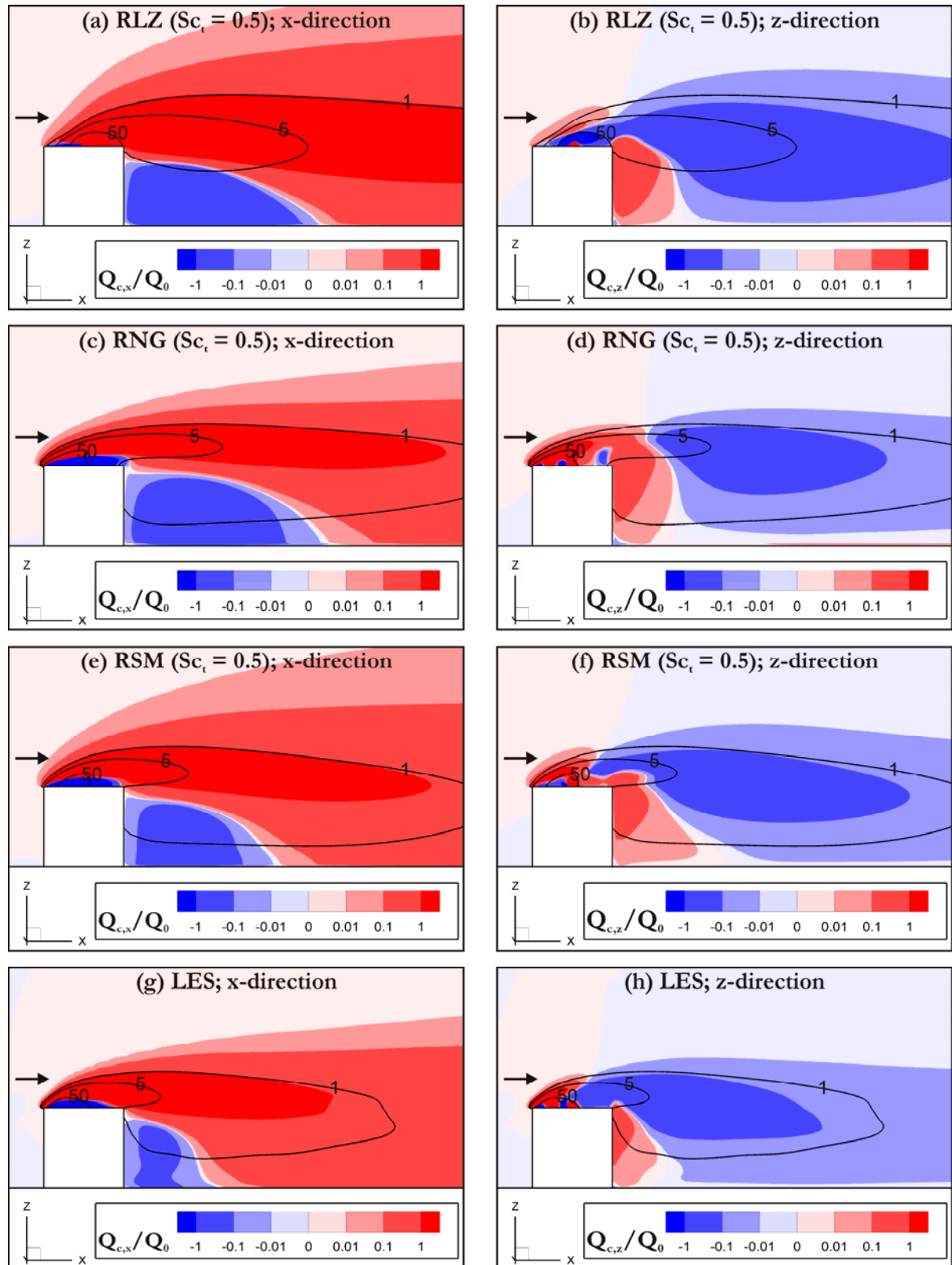
Figure III.10. Streamwise (left; $Q_{c,x}/Q_0$) and vertical (right; $Q_{c,z}/Q_0$) non-dimensional convective fluxes in the vertical mid-plane (y/H=0) obtained with (a,b) RLZ; (c,d) RNG; (e,f) RSM; and (g,h) LES. The isolines K=1; 5; 50 are also shown.
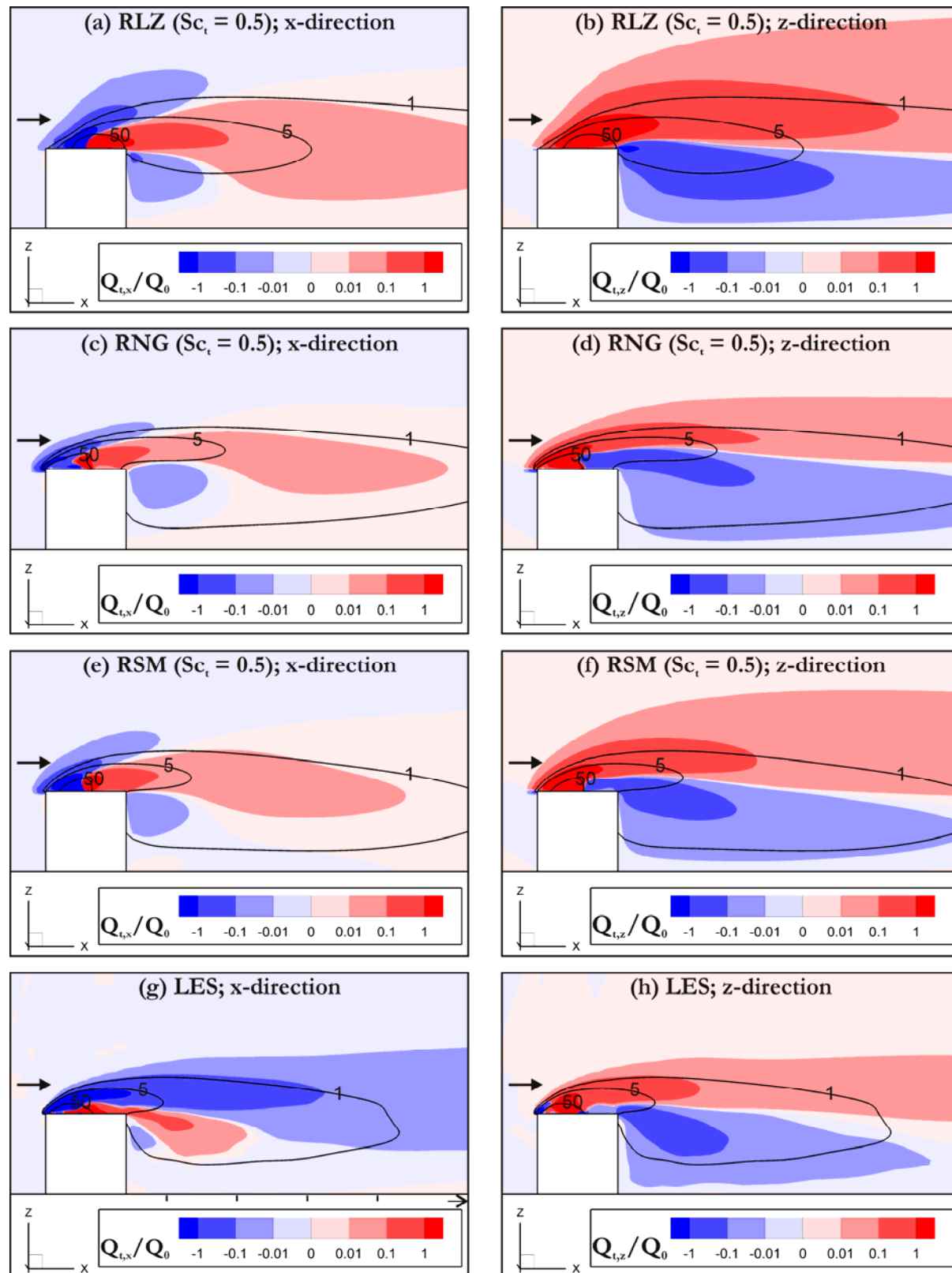
Figure III.11. Streamwise (left; $Q_{t,x}/Q_0$) and vertical (right; $Q_{t,z}/Q_0$) non-dimensional turbulent fluxes in the vertical mid-plane ($y/H=0$) obtained with (a,b) RLZ; (c,d) RNG; (e,f) RSM; and (g,h) LES. The isolines $K=1$; 5; 50 are also shown.

III.5 Summary and chapter conclusions

Most previous studies on the prediction accuracy of RANS and LES have focused on the comparison of the resulting simulated and measured mean concentrations, rather than on the transport process itself. In this chapter, a detailed analysis of the transport process of a pollutant in the turbulent wind flow patterns around isolated buildings has been presented, for two configurations with distinctive features in terms of the transport process. Apart from comparing mean concentrations, the relative influence of convective and turbulent fluxes in the transport process has been analyzed and the role of these fluxes in the prediction accuracy of RANS and LES has been clarified.

It was shown that LES is able to reproduce the counter-gradient mechanism that governs turbulent mass transfer in – and only in – the streamwise direction. This phenomenon was also pointed out by Rossi et al. [2010] who performed DNS of dispersion around a cube with uniform inflow at Re=5000. They attributed this mechanism to the large-scale structures that emanate from the leading edge of the cube[1]. In the present study, it was shown that the counter-gradient mechanism occurs not only for the cubic building with rooftop source immerged in a turbulent ABL flow, but also when the source is 1.5H high and a priori less affected by the building-generated turbulence. The very widespread gradient-diffusion hypothesis is therefore not valid in the x-direction for the two cases considered here[2].

However, this erroneous prediction of the streamwise turbulent mass flux by the RANS models did not influence significantly the results since convection was shown to act as the dominant mechanism of mass transport in this direction – contrary to laterally and vertically. Hence, if the pollutant source is located outside of detachment regions or any notable zone of the flow field that RANS models fail to reproduce (case 1), this class of models can predict fairly accurate convective fluxes around the source and, as a result, a fairly accurate concentration field. This requires correct parameterization of the turbulent fluxes via the turbulent Schmidt number, though.

When the influence of the building on the dispersion process is higher (case 2), the accuracy of LES is clearly better because this model computes more accurate convective fluxes, especially in separation regions on the roof and in the wake of the building. In such cases, modifications of Sc_t will influence the spread of pollutant predicted by RANS models but cannot compensate for their deficiencies in terms of flow field. The use of LES is recommended in this situation despite the increase in required computational time (RANS approximately seven times faster than LES for this case).

---

[1] Further investigation of the physical mechanism of turbulent mass transport is presented in the next chapter.

[2] And more generally for shear-dominated flows; see Section IV.1 for a review of flow configurations characterized by the counter-gradient mechanism of turbulent mass transport.

Further research will focus on configurations where the role of turbulent mass transport is more important in the streamwise direction, in order to assess the need of more elaborate models for turbulent mass fluxes.

Chapter IV
Pollutant dispersion around buildings: Physical mechanism

Pollutant transport due to the turbulent wind flow around buildings is a complex phenomenon which is challenging to reproduce with Computational Fluid Dynamics (CFD). In the present study we use Large-Eddy Simulation (LES) to investigate the turbulent mass transport mechanism in the case of gas dispersion around an isolated cubical building. Close agreement is found between wind-tunnel measurements and the computed average and standard deviation of concentration in the wake of the building. Since the turbulent mass flux is equal to the covariance of velocity and concentration, we perform a detailed statistical analysis of these variables to gain insight into the dispersion process. In particular, the fact that turbulent mass flux in the streamwise direction is directed from the low to high levels of mean concentration (counter-gradient mechanism) is explained. The large vortical structures developing around the building are shown to play an essential role in turbulent mass transport.

IV.1 Introduction

Computational Fluid Dynamics (CFD) is increasingly used to predict pollutant dispersion around buildings and in cities (e.g. [Tominaga et al., 1997; Meroney et al., 1999; Meroney, 2004; Hanna et al., 2006; Tominaga and Stathopoulos, 2007; Blocken et al., 2008; Gromke et al., 2008; Balczó et al., 2009; Tominaga and Stathopoulos, 2010; Gousseau et al., 2011a; Gousseau et al., 2011b; Tominaga and Stathopoulos, 2011]). While most of these studies used the steady Reynolds-Averaged Navier-Stokes (RANS) approach, there is a consensus on the fact that Large-Eddy Simulation (LES) is more accurate for modeling of wind flow and dispersion. LES temporally resolves the flow and dispersion equations and gives access to the concentration statistics. This is important because in many environmental applications, not only the accurate prediction of the mean flow and/or concentration field(s) is needed, but also time-dependent information. This time-resolving feature of LES also explains why this class of models generally performs better than RANS in simulating the inherently unsteady wind flow around buildings [Murakami, 1993; Rodi, 1997; Tominaga et al., 2008a] and the dispersion process itself (e.g. [Tominaga and Stathopoulos, 2010; Gousseau et al., 2011a; Gousseau et al., 2011b; Tominaga and Stathopoulos, 2011]). Consequently, LES can be used as a research tool to evaluate less sophisticated turbulence modeling approaches such as steady RANS.

With RANS, the turbulence-induced transport of concentration – and more generally, of scalars – is almost exclusively computed based on the gradient of the mean value, with the so-called gradient-diffusion hypothesis, or first-order closure [Franke et al., 2007; Franke et al., 2011]. For a transported variable a, this hypothesis is expressed as:

$$\overrightarrow{Q_{a,t}} = -D_{a,t} \vec{\nabla} A \qquad \text{(IV.1)}$$

where $\overrightarrow{Q_{a,t}}$ is the turbulent flux of a, $D_{a,t}$ is the turbulent diffusivity and $A = \langle a \rangle$ is the mean value of a.

Although this assumption is generally valid, some cases exist where turbulent transport behaves in a different way. Dispersion from a rooftop vent on a cube is one of them, as shown in [Rossi et al., 2010] and [Gousseau et al., 2011b]. Rossi et al. [2010] performed Direct Numerical Simulation of scalar dispersion around a cubic obstacle in a uniform air stream at Reynolds number Re=5000. Downstream of the cube, the so-called counter-gradient (CG) mechanism was observed in the streamwise direction: the turbulent mass flux was directed backwards, from the low to high levels of concentration, in contradiction with Equation (IV.1). This phenomenon was also pointed out in Chapter III [Gousseau et al., 2011b], where LES was used to show that this CG mechanism is also present in the case of turbulent inflow at higher Reynolds numbers, also when the location of the pollutant source is higher (half the building height above the roof).

CG turbulent scalar transport has also been reported for other configurations, for example in the case of a ground-level line source downstream of a wall-mounted 2D

square obstacle [Vinçont et al., 2000], a ground-level line source in a street canyon [Simoëns and Wallace, 2008], a line source in a turbulent boundary layer [Raupach and Legg, 1983; Lavertu and Mydlarski, 2005], or a stratified shear flow [Meroney, 1976][1].

These examples from literature show that the concentration and velocity statistics can provide physical insight into the turbulent mass transport. However, to the best of the authors' knowledge, detailed analysis of concentration and velocity unsteady statistics for the case of an isolated building have not yet been published. The present study provides such an analysis, based on LES. As opposed to our previous paper [Gousseau et al., 2011b], a closer look at the concentration and velocity statistics is provided here, in order to better understand the CG mechanism of mass transport in the streamwise direction and in particular which instantaneous events lead on average to this phenomenon. The configuration under study is briefly described in the next section; it is based on wind-tunnel experiments [Li and Meroney, 1983a; 1983b] whose concentration measurements are used to validate our numerical results (Section IV.3). In section IV.4, the concentration and velocity statistics at three monitoring points are presented and analyzed. Then, an attempt to relate these results to the turbulent flow patterns around the building is made (Section IV.5), after which conclusions are provided.

IV.2   Computational model[2]

IV.2.1 Domain, grid and boundary conditions

The Ansys/Fluent 12 CFD code has been used to simulate dispersion around a cubical building model of side H=0.05 m immersed in a turbulent atmospheric boundary layer (ABL). The mean velocity profile is a power law with exponent 0.19. The aerodynamic roughness length z_0=7.5×10^{-5} m. The longitudinal turbulence intensity of the approaching flow is equal to 11.8% at building height and to 15.2% at 0.015 m from the ground. Wind direction is perpendicular to the windward facade. At the center of the roof, helium is emitted by a 5 mm diameter circular exhaust with a low velocity ratio M=0.19 (M=W_e/U_H where W_e is the vertical exhaust velocity and U_H is the mean velocity in the approaching ABL at building height). The Reynolds number based on H and U_H is equal to 1.1×10^4.

The computational domain and grid used in this study are the same as those in [Gousseau et al., 2011b]. The domain has been conceived following the COST Action 732 [Franke et al., 2007; Franke et al., 2011] and AIJ [Tominaga et al., 2008b] guidelines. Its dimensions are equal to 26H×11H×6H in the streamwise (*x*), lateral (*y*) and vertical

---

[1] All these cases are characterized by regions of high shear caused by the presence of obstacles or by the boundary layer flow.

[2] The computational model is the same as the one used for Case 2 in Chapter III.
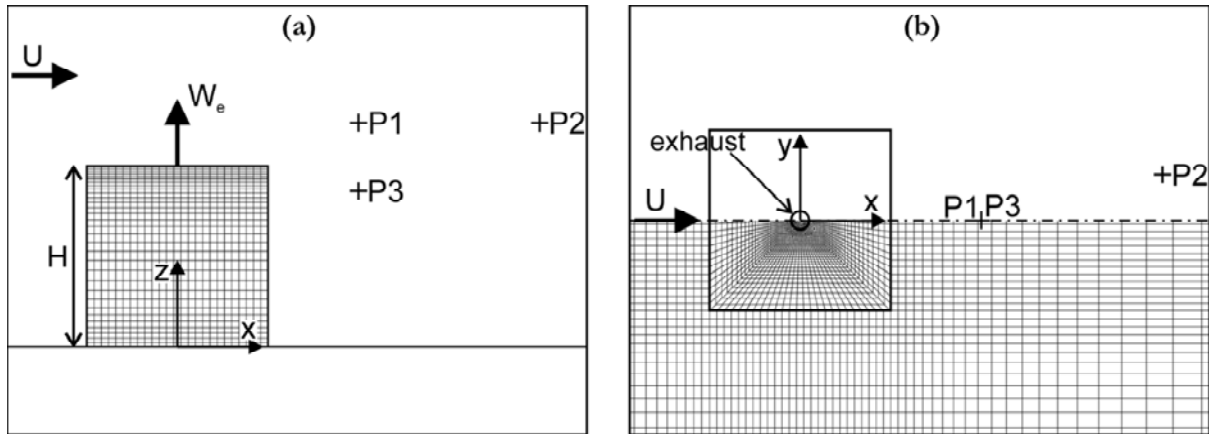
Figure IV.1. Side view (a) and top view (b) of the computational grid on the building and ground surfaces (total number of cells: 1,480,754). For readability, only part of the grid is shown in (b).

(z) directions, respectively. The grid was generated using the surface-extrusion procedure by van Hooff and Blocken [2010], yielding a grid with 1,480,754 hexahedral cells. Part of the grid on the building and ground surfaces is shown in Figure IV.1; 32 cells are used for the building in the vertical direction and 25 in the longitudinal and lateral directions. The circular edge corresponding to the exhaust is discretized into 40 cells. Away from the building, the growth rate of the cell size has been kept below 1.1 to limit truncation and commutation errors [Franke et al., 2007]. The simulation was performed on two other computational grids with 20 and 30 cells per building side. Neither the average nor the standard deviation of concentration was significantly affected by grid refinement.

Figure IV.1 also shows the location of the points P1, P2 and P3; they will be used as monitoring points to analyze the statistics of concentration and velocity in the near-wake of the building. Their coordinates are summarized in Table IV.1.

The profiles of mean velocity, turbulent kinetic energy and turbulent dissipation rate are prescribed at the inlet of the domain, $5H$ upstream of the windward facade of the building. The vortex method [Sergent, 2002] is used to generate a turbulent inflow: a given number of vortices (here: 190) whose size and intensity depend on the local values of the prescribed variables are randomly generated and transported at the inlet plane to generate fluctuations on the mean velocity profiles. At the outlet of the domain, zero static pressure is imposed. Symmetry boundary conditions are used at the top and sides of the domain. The building and ground surfaces are defined as no-slip walls. No particular treatment has been applied to the ground surface to take into account its roughness but the length of the domain upstream of the cube is short enough to limit

Table IV.1. Non-dimensional coordinates of the monitoring points used in the present study.

Point	x/H	y/H	z/H
P1	1	0	1.24
P2	2	0.25	1.24
P3	1	0	0.86

horizontal inhomogeneity affecting the inlet profiles [Blocken et al., 2007a; Blocken et al., 2007b]. The exhaust face is a velocity inlet injecting pure helium in the domain, with a constant exhaust rate Q_e [kg s^{-1}].

IV.2.2 LES modeling

In the remainder of the paper, the Reynolds decomposition is used for all variables; for example a is decomposed into its time-average component $A=<a>$ and its fluctuation a' such that $a=A+a'$. Furthermore, in what follows, the overbar is used to symbolize the spatial-filtering operator. Note that it will be used only in this section and will be omitted in the remaining of the paper.

LES is used with the dynamic Smagorinsky subgrid-scale (SGS) model [Smagorinsky, 1963; Germano et al., 1991; Lilly, 1992]. The SGS Reynolds stresses τ_{ij} are computed based on the SGS viscosity v_{sgs} and the filtered rate of strain $\overline{S}_{ij}=(\partial \overline{u}_i/\partial x_j+\partial \overline{u}_j/\partial x_i)/2$, where u_i is the component of the velocity vector in the direction i:

$$\tau_{ij}-\frac{1}{3}\tau_{kk}\delta_{ij}=-2v_{sgs}\overline{S}_{ij} \tag{IV.2}$$

The SGS viscosity is computed following:

$$v_{sgs}=L_{sgs}^2\overline{S} \tag{IV.3}$$

where $\overline{S}=(2\overline{S}_{ij}\overline{S}_{ij})^{1/2}$, $L_{sgs}=\min(\varkappa d,C_s V_c^{1/3})$ is the SGS mixing length, with $\varkappa$ the von Karman constant, d the distance to the closest wall, V_c the volume of the computational cell and C_s the Smagorinsky coefficient evaluated at each time step, based on the smallest resolved scales of motion. To avoid numerical instabilities, its value is clipped to the range [0; 0.23].

In the filtered dispersion equation, the instantaneous SGS mass flux $\overrightarrow{q_{sgs}}$ is assumed to be proportional to the gradient of resolved concentration. The i-th component of this vector ($i=1, 2, 3$) is given by:

$$q_{sgs,i}=\overline{u_i c}-\overline{u}_i\overline{c}=-D_{sgs}\frac{\partial \overline{c}}{\partial x_i} \tag{IV.4}$$

where c is the instantaneous concentration [kg m^{-3}] and D_{sgs} is the SGS mass diffusivity, linked to v_{sgs} by:

$$Sc_{sgs}=\frac{v_{sgs}}{D_{sgs}} \tag{IV.5}$$

where Sc_{sgs} is the SGS Schmidt number, which is computed dynamically here [Moin et al., 1991]. The total turbulent mass flux $\overrightarrow{Q_t}$ is defined in the LES framework as the sum of the flux due to the resolved turbulent fluctuations and the mean SGS mass flux [Porté-Agel, 2004]:

$$Q_{t,i} = <\bar{u}_i \overline{c}'> + <q_{sgs,i}>$$ (IV.6)

Reference concentration (C_0) and flux (Q_0) are used to make the variables non-dimensional. These quantities are defined by:

$$C_0 = \frac{Q_e}{H^2 U_H}$$ (IV.7)

$$Q_0 = C_0 \times U_H$$ (IV.8)

Discretization of the filtered momentum equation is performed with a bounded central-differencing scheme. A second-order scheme is used for the spatial derivatives of the other equations (energy, concentration). Pressure interpolation is second order. The non-iterative time advancement scheme is used for the unsteady solver, with the fractional step method for pressure-velocity coupling [Kim and Moin, 1985]. One single outer iteration is performed per time step, allowing reduction of the computational time needed for the simulation. A fixed non-dimensional time step $\Delta t^* = 0.066$ ($\Delta t^* = \Delta t / t_u$, where Δt is the physical time step and $t_u = H / U_H$) has been set. After an initialization period, which allows losing the dependence on the non-physical initial state (which is here the solution of a preceding RANS simulation), averaging is performed during $t^* = t / t_u = 1584$. The data at the monitoring points are stored at each of these 24,000 time steps. In Chapter III, these settings were shown to accurately reproduce the mean concentration fields on the roof and in the wake of the cube.

IV.3 Mean concentration and turbulent mass flux

The profiles of the non-dimensional concentration coefficient ($K = C / C_0$) and the non-dimensional standard deviation of concentration ($c_{rms} / C_{1G} = (<c'^2>)^{1/2} / C_{1G}$) obtained with LES along three vertical lines ($x/H = 1$; 3; 5) are compared to the wind-tunnel measurements in Figure IV.2. The standard deviation of concentration is normalized by the mean ground concentration value at $x/H = 1$ and $y/H = 0$ (C_{1G}). Along these three lines, a good agreement is obtained for K (Fig. IV.2-a). Close to the building, at $x/H = 1$, the LES results over-estimate the concentration fluctuations (Fig. IV.2-b). Along the two other lines, there is a very close agreement[1].

With LES, the contribution of the non-resolved scales to the turbulent flux is often neglected (e.g. [Tominaga and Stathopoulos, 2010; Gousseau et al., 2011b]). Figure IV.3 shows that with the grid resolution and SGS modeling used here, the SGS contribution to the total turbulent mass flux ($<q_{sgs,i}> = Q_{sgs,i}$ in Eq. (IV.6)) is indeed negligible: the magnitude of $\overrightarrow{Q_{sgs}}$ is several orders of magnitude smaller than the one of $\overrightarrow{Q_t}$.

---

[1] The discrepancies in this case can possibly be attributed to the sampling periods which are different for CFD (0.001 s) and experiment (0.005 s), and/or to the sampling area which is zero in the CFD results, contrary to the measurements.
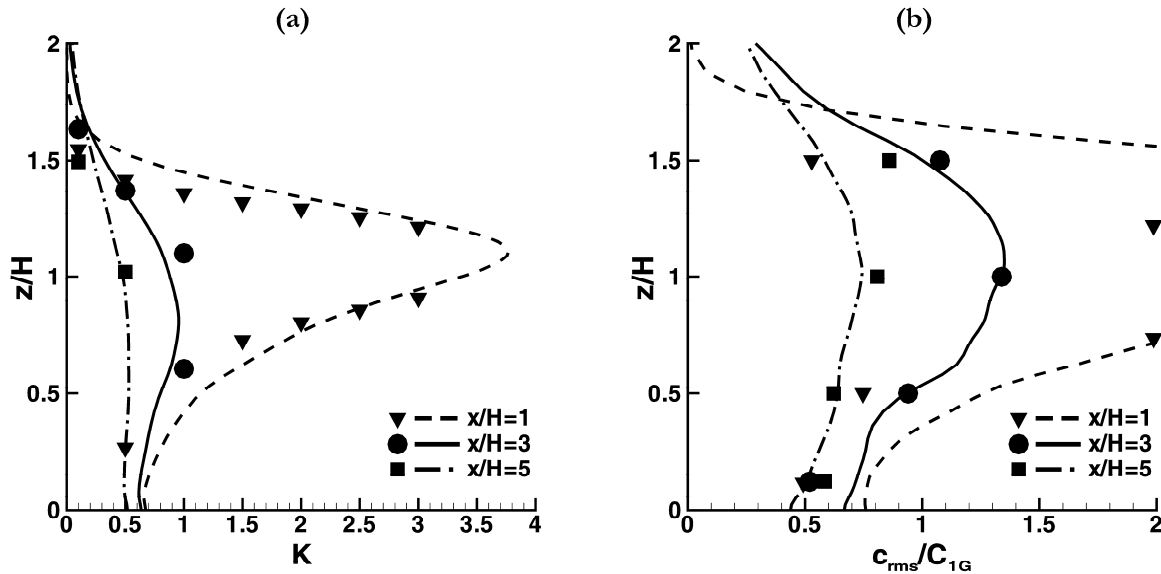
Figure IV.2. CFD validation: profiles of (a) non-dimensional concentration coefficient $K=C/C_0$ and (b) standard deviation of concentration normalized by C_{1G} along three vertical lines in the plane $y/H=0$. Symbols: wind-tunnel measurements [Li and Meroney, 1983a; Li and Meroney, 1983b]; lines: LES in this study.

Contours of the different turbulent mass flux components are depicted in Figure IV.4. In this figure, the isolines $\partial C/\partial x_i=0$ in the corresponding directions are also shown (dashed lines) and, in circles, the sign of $\partial C/\partial x_i$ for each zone delimited by the dashed line. As far as the vertical and lateral components of the turbulent flux ($Q_{t,z}$ and $Q_{t,y}$) are concerned, the color contours in Figures IV.4-c and IV.4-d show that turbulent mass transport operates as a diffusion mechanism directed from the high towards the low concentration values, i.e. from the centerline of the plume to its outer edges. In the streamwise direction, however, the mechanism is different. In the horizontal plane $z/H=1.25$ for example, and more generally in the large region above the roof level colored in blue in Figure IV.4-a, the streamwise turbulent mass flux is negative, i.e. directed towards the high levels of K. In this region where the turbulent mass flux and
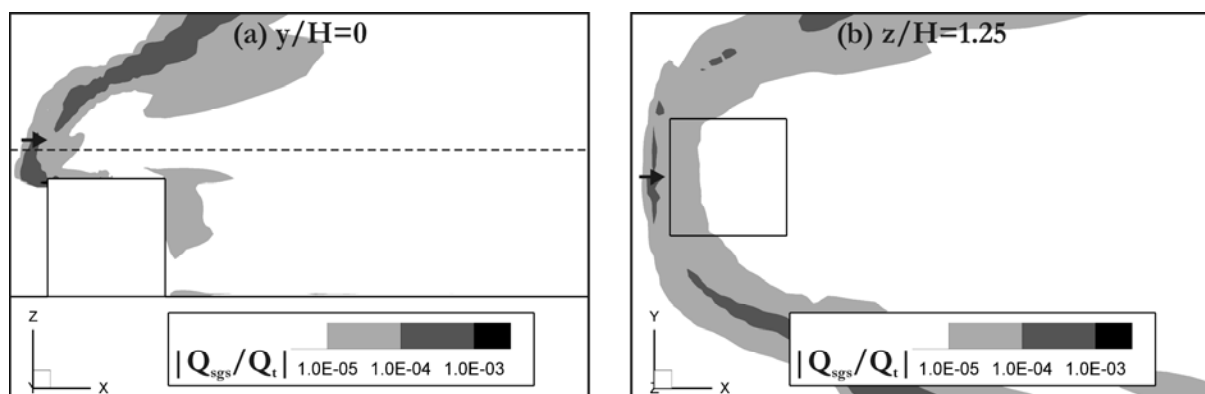
Figure IV.3. Relative contribution of the SGS mass flux to the total turbulent mass flux: contours of $|Q_{sgs}/Q_t|$ in the planes (a) $y/H=0$ and (b) $z/H=1.25$. In (a), the dashed line represents the position of the horizontal plane shown in (b).
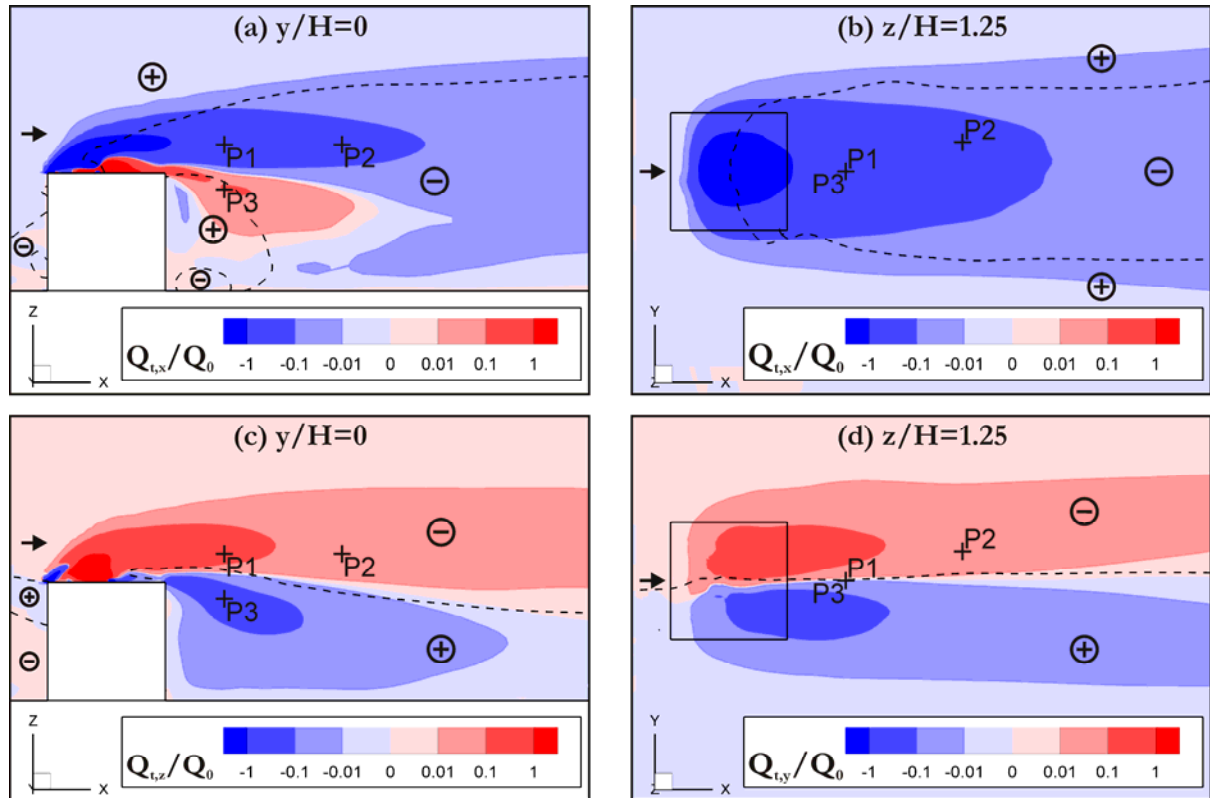
Figure IV.4. Contours of the (a,b) streamwise, (c) vertical, and (d) lateral components of the turbulent mass flux vector. The dashed lines represent the isolines $\partial C/\partial x_i = 0$ in the corresponding direction: (a,b) $x_i = x$, (c) $x_i = z$, (d) $x_i = y$. On each side of the isoline, the sign of $\partial C/\partial x_i$ is indicated in circles (+: positive; -: negative). The CG mechanism of turbulent mass transport is characterized by $Q_{t,i}$ and $\partial C/\partial x_i$ of the same sign for a given direction.

the mean concentration gradient are of the same sign, the CG mechanism of turbulent mass transport is present. Another CG zone is present in the near-wake of the building (where P3 is located) where both $Q_{t,x}$ and $\partial C/\partial x$ are positive. Note that the monitoring points P1, P2 and P3 have been selected in such a way that they are located in different characteristic zones of the $\overrightarrow{Q_t}$ field.

IV.4 Concentration and velocity statistics at the monitoring points

The resolved concentration (c) and velocity components (u, v, w) have been recorded at the three monitoring points at each of the 24,000 time steps of the simulation. Various descriptive statistics of these variables are reported in Tables IV.2 to IV.5 for these three points. The subscript 'rms' indicates the standard deviation; S_a and K_a correspond to the skewness and kurtosis of the variable a, respectively; a'_{min} and a'_{max} stand for the minimum and maximum fluctuations of a. The sign of the local spatial derivative value of mean concentration is also included in Table IV.2 to verify that it corresponds to the sign of

Table IV.2. Non-dimensional statistics of concentration at the three monitoring points. The signs of the local spatial derivative of mean concentration are also given.

Point	$K=C/C_0$	c_{rms}/C_0	c_{rms}/C	S_c	K_c	c'_{min}/c_{rms}	c'_{max}/c_{rms}	$\partial C/\partial x$	$\partial C/\partial y$	$\partial C/\partial z$
P1	3.00	3.62	1.21	2.39	11.10	-0.83	13.08	<0	≈ 0	<0
P2	0.50	0.97	1.94	2.98	11.42	-0.52	8.60	<0	<0	<0
P3	2.46	1.74	0.71	2.20	8.38	-1.39	8.97	>0	≈ 0	>0

Table IV.3. Non-dimensional statistics of streamwise velocity at the three monitoring points.

Point	U/U_H	u_{rms}/U_H	$|u_{rms}/U|$	S_u	K_u	u'_{min}/u_{rms}	u'_{max}/u_{rms}	$<u'c'>/Q_0$
P1	0.84	0.26	0.31	-0.57	-0.20	-3.51	2.33	-0.403
P2	0.94	0.18	0.19	-0.67	0.71	-4.87	2.85	-0.094
P3	0.15	0.20	1.33	0.06	-0.30	-3.15	3.54	0.089

Table IV.4. Non-dimensional statistics of lateral velocity at the three monitoring points.

Point	V/U_H	v_{rms}/U_H	$|v_{rms}/V|$	S_v	K_v	v'_{min}/v_{rms}	v'_{max}/v_{rms}	$<v'c'>/Q_0$
P1	0.01	0.17	17	0.02	0.34	-4.33	4.21	-0.008
P2	-0.04	0.11	2.75	0.52	0.87	-4.27	4.83	0.040
P3	0.00	0.20	-	0.04	-0.06	-3.58	3.46	-0.006

Table IV.5. Non-dimensional statistics of vertical velocity at the three monitoring points.

Point	W/U_H	w_{rms}/U_H	$|w_{rms}/W|$	S_w	K_w	w'_{min}/w_{rms}	w'_{max}/w_{rms}	$<w'c'>/Q_0$
P1	-0.11	0.15	1.36	0.80	0.63	-3.97	5.29	0.160
P2	-0.08	0.11	1.37	0.88	1.61	-2.89	6.08	0.023
P3	-0.08	0.21	2.62	0.04	-0.16	-3.26	3.46	-0.127

$<u'c'>$ (CG mechanism) in the x-direction (Table IV.3) and to the opposite sign of $<v'c'>$ and $<w'c'>$ in the y- and z-direction, respectively (Tables IV.4 and IV.5).

For the four variables of interest, the range of the non-dimensional fluctuations (a'_k/a_{rms}, where k is the sample number) has been divided into 50 equal intervals I_i ($i=1,\ldots,50$) and the frequency f_i of occurrence of a'_k/a_{rms} belongs to I_i has been calculated following Equation (IV.9) to build the histogram of frequency distribution:

$$f_i = \frac{n_i}{N} \quad (i=1,\ldots,50) \tag{IV.9}$$

where n_i is the number of samples such as a'_k/a_{rms} belongs to I_i and N is the total number of samples.

The histograms for point P1 are shown in Figure IV.5. The histogram of concentration fluctuations (Fig. IV.5-a) has an exponential-like shape, which indicates that P1 is most of the time characterized by a low background concentration level and the occurrence of rare but extremely high peaks of concentration – also indicated by the high value of K_c, see Table IV.2. Approximately 60% of the samples are of negative fluctuation and the average is raised by peaks of c' reaching up to 13 times the standard deviation. This asymmetry around the mean is quantified by the high skewness value. This shape of frequency distribution corresponds to measurements by Fackrell and

Robins [1982] far from the ground in the case of an elevated point source and was attributed to the meandering motion of the plume caused by large turbulent eddies. Here, the largest turbulence scales are of the order of the cube size, larger than the size of the plume at P1, and tend to move the plume as a block, resulting in the high intermittency observed at this monitoring point.

The frequency distribution of u'/u_{rms} shows negative skewness (Fig. IV.5-b): among the samples, the majority is of positive fluctuation but some of them are characterized by a large negative u'. The opposite holds for the vertical velocity fluctuations, whose frequency distribution is right-tailed (Fig. IV.5-d). Considering that P1 lies in the vertical symmetry plane of the computational domain, it is logical that the frequency distribution of v'/v_{rms} is symmetric with respect to its zero mean (Fig. IV.5-c).

A similar approach can be used to analyze the statistics of the variables two by two. The bivariate histograms have been built for the three couples of variables (c'/c_{rms}; $u_i'/u_{i,rms}$). For example, for two variables a and b, the range of the non-dimensional fluctuations has been divided into an arbitrary number of intervals (here: 20), say I_i for a'_k/a_{rms} and J_j for b'_k/b_{rms}. For given i and j, the frequency $f_{i,j}=f(I_i,J_j)$ is the ratio of the number of samples $n_{i,j}$ for which a'_k/a_{rms} belongs to I_i and simultaneously b'_k/b_{rms} belongs to J_j to the total number of samples N:

$$f_{i,j} = \frac{n_{i,j}}{N} \quad (i,j=1,\ldots,20) \tag{IV.10}$$

Each of the four combinations of signs of (c'/c_{rms}; $u_i'/u_{i,rms}$) is associated with a specific event of pollutant transport. Observing the bivariate histograms gives therefore an indication of which events are the most frequent among the samples and/or contribute the most to the turbulent flux. This so-called quadrant analysis was first introduced for momentum transfer [Shaw et al., 1983] but is also widely used in the case of scalar dispersion (e.g. [Chen, 1990; Katul et al., 1997; Cheng and Liu, 2011]). The definitions of the quadrants are shown in Table IV.6, together with the name given to the corresponding event in the vertical direction, for which quadrant analysis is often used. Note that this nomenclature can also be used here for the lateral direction, considering the symmetry of our problem. The frequency of occurrence of a given quadrant Q_m is equal to the sum of the frequencies of the intervals which compose Q_m. This frequency multiplied by the average of $u_i'c'$ on Q_m ($<u_i'c'>_{|Q_m}$) gives the contribution of the quadrant Q_m to the turbulent flux in the direction i.

Table IV.6. Numbering and definitions of the quadrants. The names of the corresponding events hold for the vertical direction, following [Chen, 1990].

Quadrant	u_i'	c'	Name (z-direction)
Q1	>0	>0	Ejection
Q2	<0	>0	Inward interaction
Q3	<0	<0	Sweep
Q4	>0	<0	Outward interaction
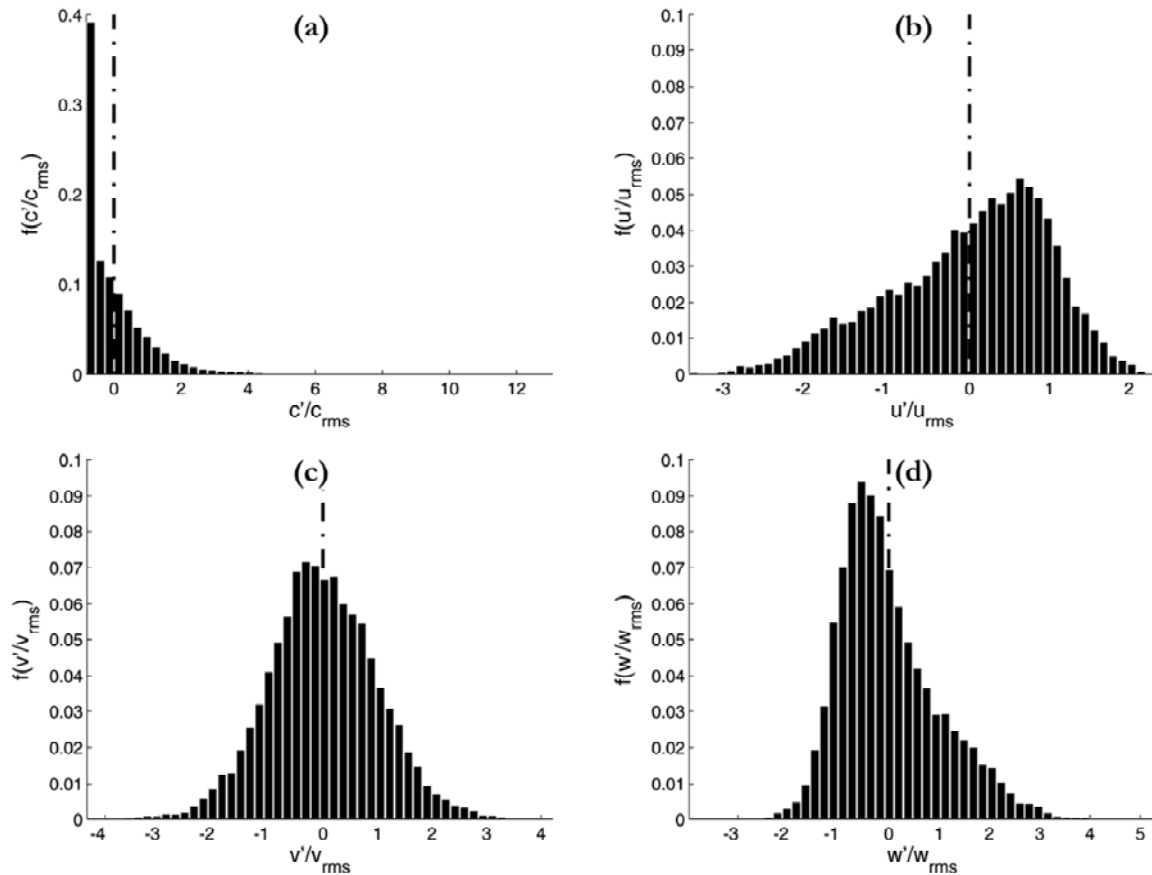
Figure IV.5. Point P1: frequency distribution histograms of (a) c'/c_{rms}, (b) u'/u_{rms}, (c) v'/v_{rms}, and (d) w'/w_{rms}. For each variable, the x-axis limits correspond to the minimum and maximum sample values. The dashed line indicates the mean (zero) values of the fluctuations. Mean values: K=3.00; U/U_H=0.84; V/U_H=0.01; W/U_H=-0.11.

The contours of $f_{i,j}$ in the planes (c'/c_{rms}; $u_i'/u_{i,rms}$) for P1 are shown in Figure IV.6. In the streamwise direction (Fig. IV.6-a), the most frequent situation among the samples is simultaneously u'>0 and c'<0 (Q4): 46% of the samples are in this zone. Nevertheless, the most important contribution to the total turbulent flux is due to Q2, for which the
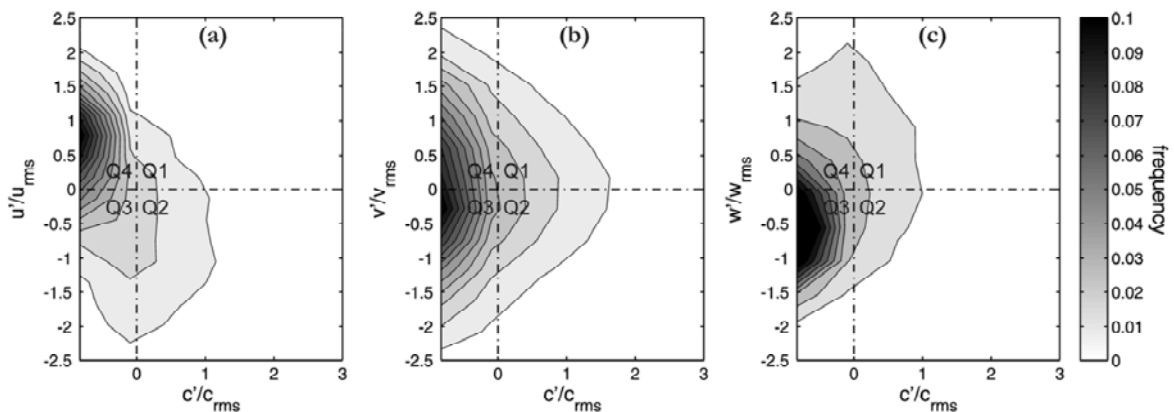
Figure IV.6. Point P1: bivariate histogram of frequency distribution for (a) (c'/c_{rms}; u'/u_{rms}), (b) (c'/c_{rms}; v'/v_{rms}), and (c) (c'/c_{rms}; w'/w_{rms}).
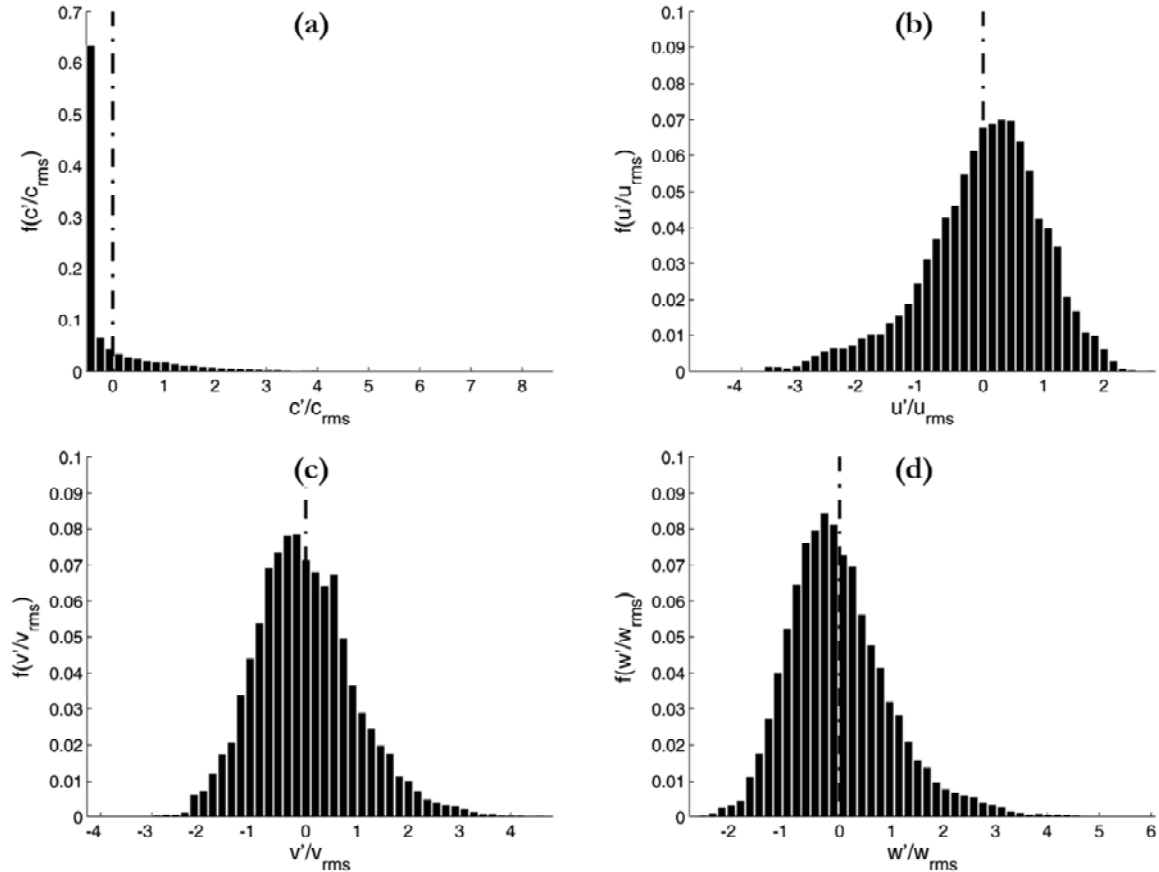
Figure IV.7. Point P2: frequency distribution histograms of (a) c'/c_{rms}, (b) u'/u_{rms}, (c) v'/v_{rms}, and (d) w'/w_{rms}. For each variable, the x-axis limits correspond to the minimum and maximum sample values. The dashed line indicates the mean (zero) values of the fluctuations. Mean values: K=0.50; U/U_H=0.94; V/U_H=-0.04; W/U_H=-0.08.

frequency (27%) is lower than for Q4 but for which the individual contributions $u'c'$ are on average higher in magnitude. The contributions of Q1 and Q3 are minor in this case, both in terms of frequency and magnitude. The dominant contributions of Q2 and Q4,
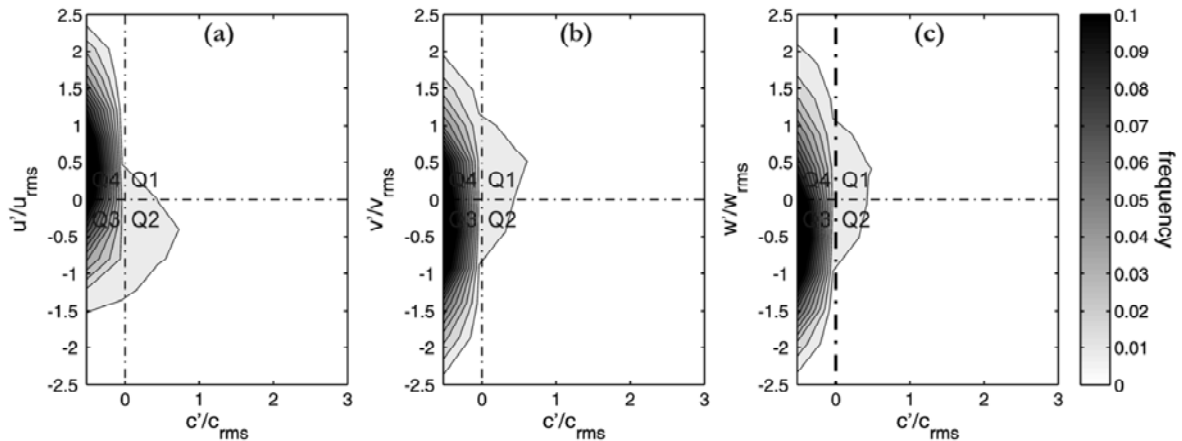
Figure IV.8. Point P2: bivariate histogram of frequency distribution for (a) (c'/c_{rms}; u'/u_{rms}), (b) (c'/c_{rms}; v'/v_{rms}), and (c) (c'/c_{rms}; w'/w_{rms}).
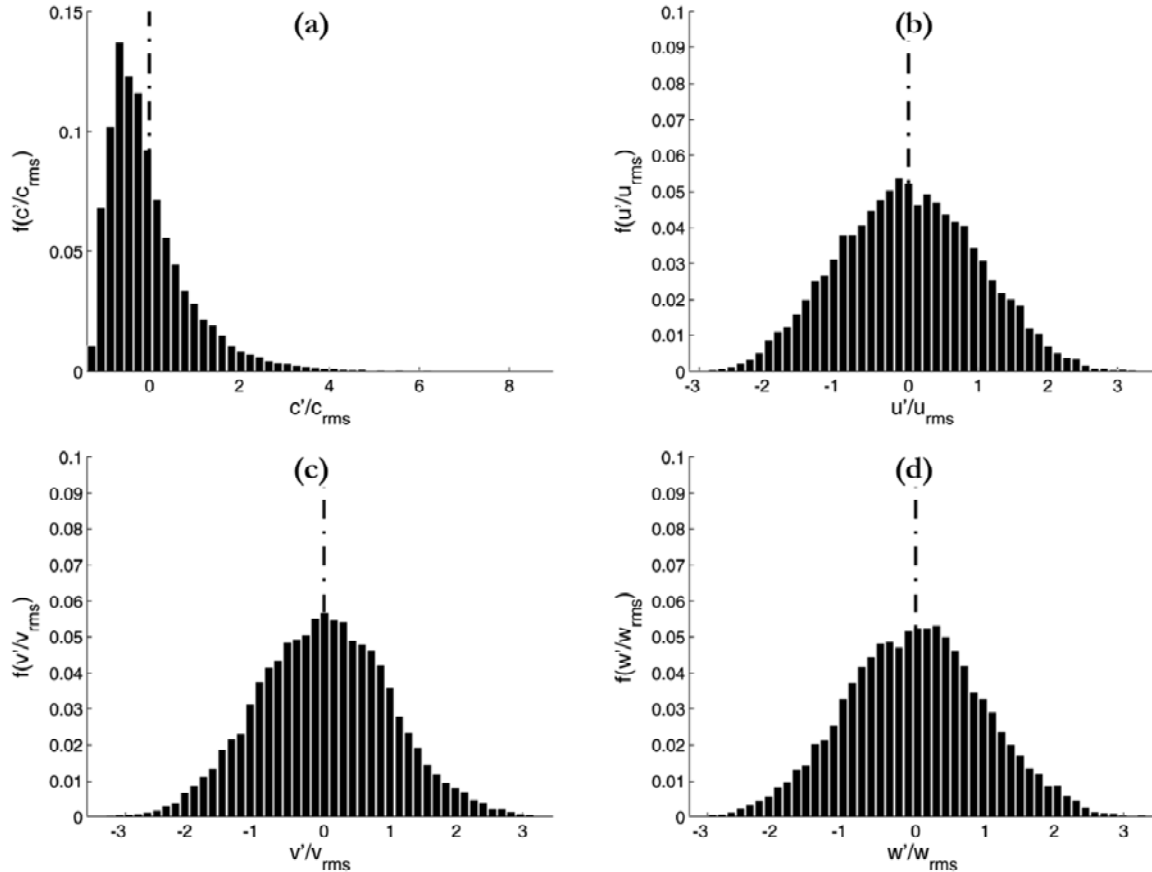
Figure IV.9. Point P3: frequency distribution histograms of (a) c'/c_{rms}, (b) u'/u_{rms}, (c) v'/v_{rms}, and (d) w'/w_{rms}. For each variable, the x-axis limits correspond to the minimum and maximum sample values. The dashed line indicates the mean (zero) values of the fluctuations. Mean values: K=2.46; U/U_H=0.15; V/U_H=0; W/U_H=-0.08.

where u' and c' are of opposite signs, result on average in a negative turbulent flux $<u'c'>$. Concerning the lateral direction, the frequency distribution of (c'/c_{rms}; v'/v_{rms}) is approximately symmetrical with respect to the axis v'=0, leading to a zero turbulent mass
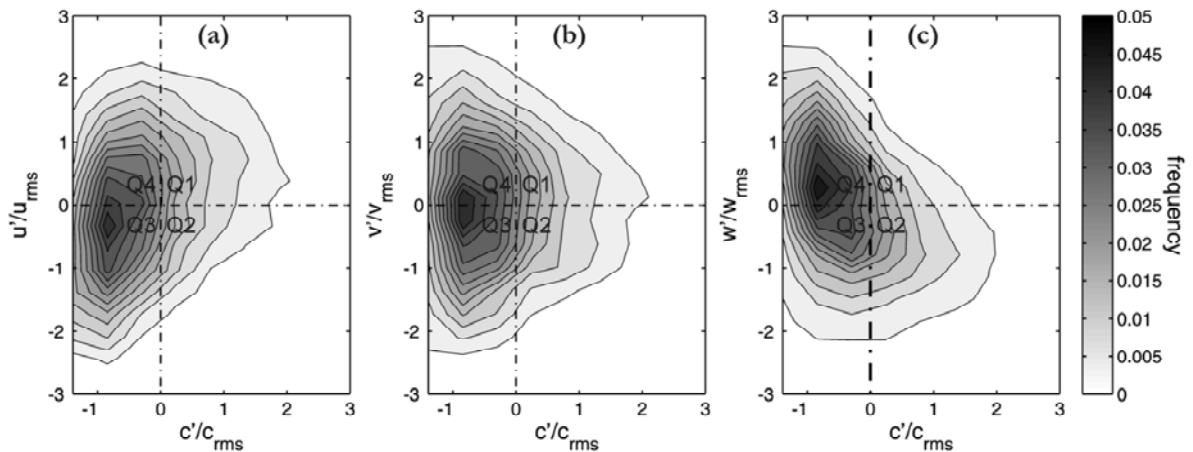
Figure IV.10. Point P3: bivariate histogram of frequency distribution for (a) (c'/c_{rms}; u'/u_{rms}), (b) (c'/c_{rms}; v'/v_{rms}), and (c) (c'/c_{rms}; w'/w_{rms}).

flux in the lateral direction (Fig. IV.6-b). Concerning the vertical direction, sweeps (Q3) are the most frequent events of vertical mass transfer at P1 (Fig. IV.6-c); they correspond to downward motions of fresh air. However, the calculation of the contribution of each quadrant to $Q_{t,z}$ shows that the dominant contribution is made by ejections (Q1), which occur less often but are more intense.

One step further in the statistical analysis is to analyze the variables three by three, following the octant analysis by Vinçont et al. [2000]. The repartition of the samples among the eight octants of the three-dimensional space (c'/c_{rms}; u'/u_{rms}; w'/w_{rms}) shows that the Q2 events in the x-direction coincide with the Q1 events in the z-direction (not shown here). Hence, the largest contribution to both $Q_{t,x}$ and $Q_{t,z}$ is due to samples for which ($c'>0$; $u'<0$; $w'>0$) i.e. upwards movement of polluted air coming from the plume centerline with lower streamwise velocity. The most frequent octant and second largest contribution to $Q_{t,x}$ and $Q_{t,z}$ corresponds to ($c'<0$; $u'>0$; $w'<0$): fresh air entrained from the top of the plume with relatively high streamwise velocity and downward motion.

Figure IV.7-a shows the frequency distribution of c'/c_{rms} for P2. The trend is similar as for P1, with even higher values of skewness and kurtosis (see Table IV.2), because of the off-center position of the sampling point at which the plume intermittency is higher [Fackrell and Robins, 1982]. Approximately 65% of the samples have concentration values between zero and one third of the mean concentration value at this point. The velocity fluctuations in the x- and z-directions also have similar frequency distributions as those at P1, with a negative and positive skewness, respectively. The main difference with point P1 is the asymmetry of the histogram of v'/v_{rms}, quantified by the non-zero skewness S_v=0.52. This feature is due to the position of P2 out of the symmetry plane of the geometry.

The bivariate histogram of (c'/c_{rms}; v'/v_{rms}) is similar in shape to the one of (c'/c_{rms}; w'/w_{rms}) (Figs. IV.8-b,c): a large majority of the samples belongs to Q3 and the main contribution to the mass flux is due to intense ejections corresponding to quadrant Q1. Hence, both $Q_{t,y}$ and $Q_{t,z}$ are positive at P2. Concerning the streamwise direction, the bivariate histogram (Fig. IV.8-a) is similar in shape to the one at P1 and the octant analysis (not shown here) indicates that intense Q2 events in the x-direction coincide with Q1 events in the y- and z-directions.

For P3, the frequency distribution of concentration fluctuations is different (Fig. IV.9-a). Its shape resembles a log-normal distribution, similar to what can be observed close to the ground in the case of an elevated point source in a turbulent boundary layer [Fackrell and Robins, 1982]. Note that at this location, in the near wake of the building, the intensity of the concentration fluctuations c_{rms}/C is weaker in comparison with P1 and P2 (Table IV.2). Noticeably, the three velocity components have a similar, symmetric distribution with a skewness value close to zero (Figs. IV.9-b,c,d).

Despite the symmetry of the velocity frequency distributions, the bivariate analysis shows that simultaneity of concentration and velocity fluctuations of particular signs lead

on average to non-zero mass fluxes. The main contribution to streamwise mass transfer at P3 is due to Q1 and Q3 quadrants, the former being the most intense events and the latter the most frequent (Fig. IV.10-a). It explains the positive $Q_{t,x}$ at this location. The bivariate frequency distribution of (c'/c_{rms}; v'/v_{rms}) is symmetric around the abscissa axis, resulting in a negligible $Q_{t,y}$ in comparison with Q_0 (Fig. IV.10-b). Vertically, mass transfer is governed by frequent inward (Q4) and intense outward (Q2) interactions (Fig. IV.10-c).

The octant analysis shows the simultaneity of Q1 events in the x- and Q2 events in the z-direction. The event ($c'<0$; $u'<0$; $w'>0$) is the most frequent at P3, corresponding to motions of fresh air originating from zones closer to the ground. The other dominant contribution to the mass flux is due to the events ($c'>0$; $u'>0$; $w'<0$) which are less frequent but more intense. They correspond to movements of high streamwise velocity polluted air directed downwards.

IV.5 Further analysis and discussion

The contours of streamwise (R_{uu}) and vertical (R_{ww}) two-point correlation coefficients in the plane $y/H=0$ are shown in Figure IV.11. $R_{u_i u_j}$ is defined by:

$$R_{u_i u_j}(\vec{x}, \vec{x}_{ref}) = \frac{<u_i'(\vec{x})u_j'(\vec{x}_{ref})>}{u_{i,rms}(\vec{x})u_{j,rms}(\vec{x}_{ref})} \qquad (IV.11)$$

The reference point P_{ref} is taken at $x_{ref}/H=1.020$, $y_{ref}/H=0$ and $z_{ref}/H=1.245$. The computation of these coefficients is made by user programming (User-Defined Function) which allows accessing the data at cell centers; this is the reason why P_{ref} is not located exactly at P1, but very close to it. By definition, the correlation coefficients take the value 1 at P_{ref}, as can be seen in Figure IV.11.

The negative values of R_{uu} in the wake of the cube indicate the backflow characteristic of the recirculation zone (Fig. IV.11-a). In Figure IV.11-b, one can notice the alternation of zones with negative (blue) and positive (red) correlation coefficient R_{ww} in the shear layer, starting from the top of the windward facade. This feature can be interpreted as an indication of the presence of large vortical structures in this zone [Savory et al., 2011], generated at the front corner and transported downstream with an increasing length scale. One can infer the occurrence of a similar flow phenomenon on the sides of the cube (not shown in figure), from which shear layers develop as well.

Experimental investigation of the flow around a circular cylinder [Ong and Wallace, 1996] shows that the vortex shedding which takes place in the wake of the cylinder acts on the skewness of the velocity. For the streamwise component, the skewness is low and positive at the center of the wake and turns to large negative values at its outer edges. Concerning the transverse velocity, if $y=0$ is the plane aligned with the flow direction and corresponding to the symmetry plane of the z-axis cylinder, the skewness tends to be
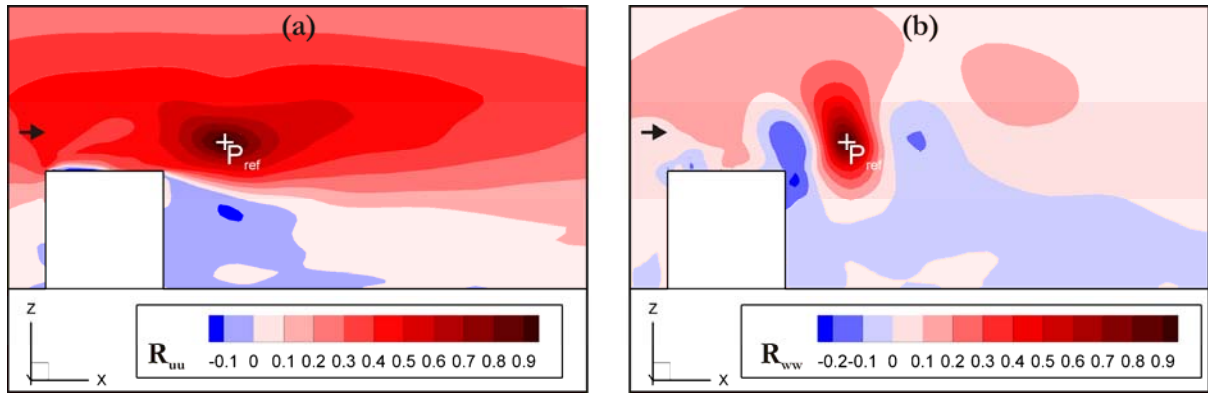
Figure IV.11. Contours of two-point velocity correlation coefficient in the vertical mid-plane $y/H=0$. (a) $R_{uu}(x,y,z,x_{ref},y_{ref},z_{ref})$ and (b) $R_{ww}(x,y,z,x_{ref},y_{ref},z_{ref})$, with $x_{ref}/H=1.020$, $y_{ref}/H=0$ and $z_{ref}/H=1.245$.

positive for $y>0$ and negative for $y<0$. Although the flow around a wall-mounted cube is fully three-dimensional and more complex (see e.g. [Wang and Zhou, 2009]) for a description of the flow around wall-mounted finite-length square cylinders), the link between vortical structures and velocity skewness appears to be similar. Figure IV.12-b shows the contours of S_u in the horizontal plane $z/H=0.75$. In the wake of the building, the trend is the same as described above: S_u is low and positive at the center of the wake and negative and high in magnitude at the outer edges, because of the presence of vortical structures in the side shear layers. The analogy with the circular cylinder holds
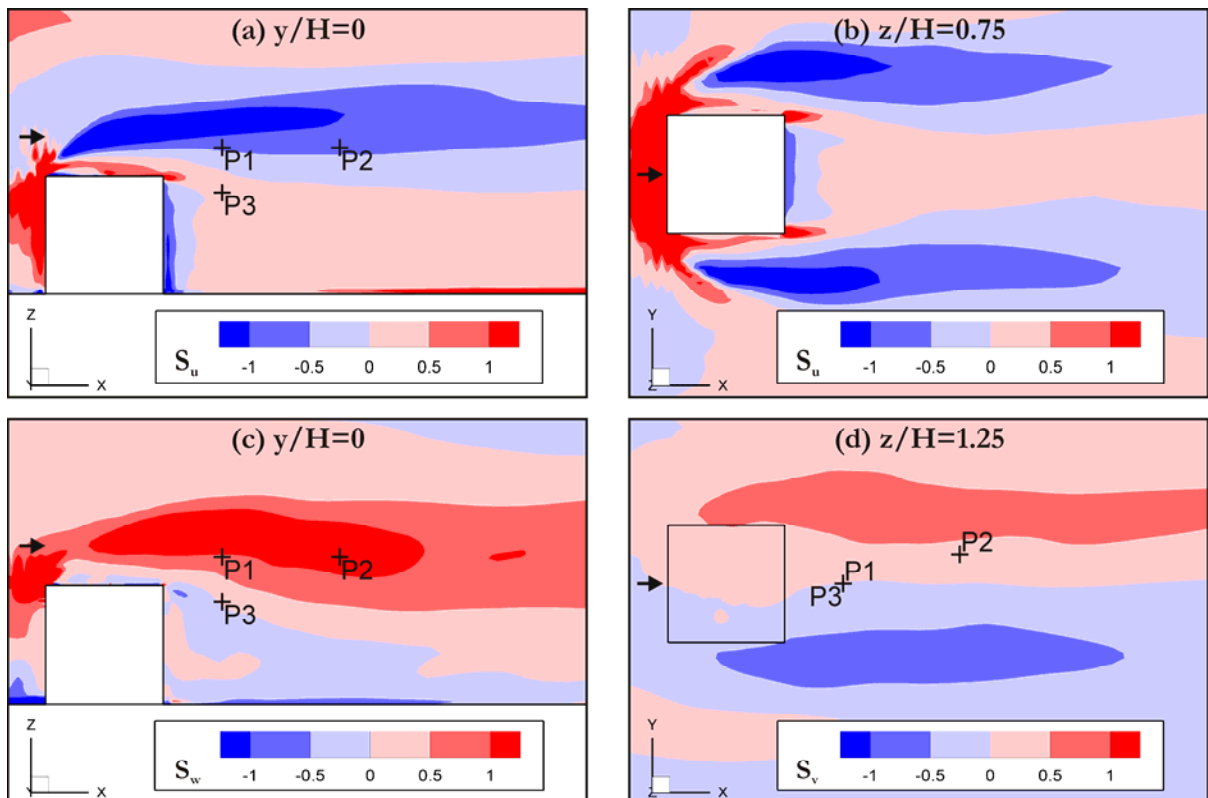
Figure IV.12. Contours of the skewness of the (a,b) streamwise, (c) vertical, and (d) lateral velocity in (a,c) the vertical mid-plane, (b) the horizontal plane $z/H=0.75$ and (d) the horizontal plane $z/H=1.25$.

also for S_v which is positive for $y>0$ and negative for $y<0$ (Fig. IV.12-d). The plane $z/H=1.25$ is shown and the trend is the same for $z/H\leq1$. What occurs above the building is similar to what has been described above for the horizontal planes, as can be seen in Figures IV.12-a,c. However, the presence of the ground wall breaks the symmetry: large negative (resp. positive) values of S_u (resp. S_w) are found in the shear layer above the building containing P1 and P2 but in the wake – where the large recirculation operates but only small-scale vortices are present [Li and Meroney, 1983b] – the trend is less marked and the skewness values are low in magnitude.

In the shear layers, the peaks of velocity fluctuations – positive or negative, depending on the location and the velocity component – created by the instantaneous flow patterns often coincide with a preferred sign of concentration fluctuation. This was shown to be true at P1 and P2 and can reasonably be generalized to the roof and side shear layers. At these two points, for example, low-speed motions of polluted air originating from the center of the plume could be identified. They are rare but very intense and constitute the main contribution to the turbulent mass flux in the streamwise and vertical directions (and also laterally if an off-center point is considered).

Behind the building and below $z/H=1$, in the near-wake recirculation zone, no large vortical structures are present, which seems to be the reason why no particular trend was observed for the skewness of the three velocity components. However, the bivariate analysis at P3 showed that, at this location too, the peaks of concentration fluctuations are likely to be associated with a preferred sign of velocity fluctuations, and generate a non-zero turbulent mass flux. At P3, intense motions of polluted air coming from the center of the plume with high streamwise velocity and frequent movements of fresh air coming from zones close to the ground were observed. Note that these results have been confirmed by the observation of the statistics at seven additional monitoring points located in various regions of the flow, which have not been reported due to space limitations.

IV.6   Summary and chapter conclusions

Wind-induced pollutant dispersion from a rooftop vent on top of a cubical building model has been simulated with Large-Eddy Simulation and the dynamic Smagorinsky SGS model. The unsteady statistics of concentration and velocity at three monitoring points located in the near-wake of the building have been collected for a sufficiently long period for a detailed analysis of turbulent mass transport. Mono- and bivariate histograms of concentration and velocity fluctuations at these three points have been built to detect the events contributing to turbulent mass transport. Octant analysis has also been performed and provided valuable insights (although no plots were shown here). A generalization of these results to the near-wake of the building has been proposed.

First, by comparing our numerical results with the wind-tunnel measurements of mean value and standard deviation of concentration, the good accuracy of the present LES modeling in predicting concentration statistics has been demonstrated for the case of dispersion around an isolated building. Moreover, the mean SGS mass flux has been shown to be negligible compared to the total turbulent mass flux with the grid resolution and SGS modeling used here.

Due to the presence of large-scale vortices around the cube, the plume exhibits a meandering motion, as can be seen in the frequency distribution of the concentration fluctuations: it has approximately an exponential shape in the wake of the building above roof level (points P1 and P2) and a log-normal shape below roof level (P3). In both cases, the skewness and kurtosis values are high, indicating the existence of a relatively low background concentration punctuated by rare but extremely high peaks.

The frequency distributions of the velocity fluctuations are also affected by the turbulent flow patterns. In the absence of large vortical structures (P3), the frequency distributions of u', v' and w' are symmetric, with skewness values close to zero, whereas in the shear layers developing from the roof and side walls of the buildings (P1 and P2) the large vortical structures are responsible for peaks of velocity fluctuations quantified by the non-zero skewness values of the frequency distributions.

In summary, the frequency distributions of both concentration and velocity fluctuations are affected by the same flow phenomenon. As a consequence, it seems logical to observe a direct link between u_i' and c' events. The bivariate analysis showed indeed that for a given sign of c' there is a preferred sign of u_i' which is more likely to occur. In the streamwise direction, it was shown at P1 and P2 that c' and u' most of the time have opposite signs, leading on average to a negative turbulent mass flux $Q_{t,x}$ and explaining the CG mechanism in this zone.

It has been shown that specific unsteady events govern turbulent mass transport, which explains the failure of the first-order closure model (Eq. (IV.1)). If used, this model should be adapted to reproduce the CG mechanism of turbulent mass transport – for example by taking out the minus sign from the right-hand side of Equation (IV.1) – and to take into account the flow anisotropy, by use of a diffusivity vector.

Some additional results of this simulation are presented in Appendix B: a few snapshots of the flow and concentration fields illustrate in which way the vortical structures act on the pollutant plume.

Appendix A

RANS simulations of the wind flow around the 1:1:2 building

In this appendix, the same case as the one simulated with LES in Chapter II is simulated with three RANS models: the realizable k-ε model (RLZ), the renormalization group k-ε model (RNG), and the Reynolds-stress model (RSM). These models are those used in Chapter III to simulate dispersion around isolated buildings.

A.1 Computational model

A.1.1 Turbulence models

Three RANS models are used here and compared, with the values of the model constants corresponding to the default settings in Fluent 12.1 [Ansys Inc., 2009]:

- The realizable k-ε model (RLZ) [Shih et al., 1995] with $C_{1\varepsilon}$=1.44; $C_{2\varepsilon}$=1.9; σ_k=1.0; σ_ε=1.2.

- The renormalization group k-ε model (RNG) [Yakhot et al., 1992] with C_μ=0.0845; $C_{1\varepsilon}$=1.42; $C_{2\varepsilon}$=1.68.

- The Reynolds-stress model (RSM) with a linear pressure-strain model and wall-reflection effects [Launder et al., 1975; Gibson and Launder, 1978] and with C_μ=0.09; $C_{1\varepsilon}$=1.44; $C_{2\varepsilon}$=1.92; C_1=1.8; C_2=0.6; C'_1=0.5; C'_2=0.3; σ_k=1.0; σ_ε=1.3.

Note that the results of the standard k-ε model are in this case rather close to those of RLZ and therefore this model is not used here.

A.1.2 Domain, grid and boundary conditions

The same computational domains and grids as those used with LES in Chapter II are used here: Grid20 and Grid30 with 20 and 30 cells per building side, respectively. The sensitivity of the results to the resolution will be tested in the next section with the RLZ model. The numerical results will be observed in the measurement planes introduced in Chapter II: V0 at y/B=0 and H10 at z/B=1.25.

At the inlet of the domain, the profiles of mean velocity (U), turbulent kinetic energy (k) and turbulence dissipation rate (ε) are prescribed for the three models, based on flow measurements in the test section of the wind tunnel [Meng and Hibi, 1998]. The building, ground and ceiling surfaces are defined as no-slip walls, with standard wall functions [Launder and Spalding, 1974] as a wall treatment. Symmetry boundary conditions are set at the sides of the domain and zero static pressure is imposed at the outlet.

All the transport equations (momentum, k, ε) are discretized using a second-order upwind scheme. Pressure interpolation is second order. The SIMPLE algorithm is used for pressure-velocity coupling. Convergence is assumed to be obtained when the scaled residuals reach 10^{-5}.

A.2   Results

A.2.1   Grid-sensitivity analysis

Figure A.1 shows the profiles of non-dimensional velocity (Fig. A.1-a) and turbulent kinetic energy (Fig. A.1-b) in the vertical mid-plane V0 for the RLZ turbulence model on Grid20 (RLZ20) and Grid30 (RLZ30). The agreement of the numerical results with the measurements will be analyzed in the next section; the focus is here on the comparison of the CFD results on Grid20 and Grid30. The velocity profiles obtained on the fine grid are nearly identical to those obtained on the coarse grid (Fig. A.1-a). Some minor differences exist in the k-profiles computed by RLZ20 and RLZ30 but they are clearly negligible (Fig. A.1-b). Note that the grid-sensitivity analysis is presented here with the RLZ turbulence model but it has been checked that similar results are obtained with RNG and RSM. As a conclusion, the grid with 20 cells per building side is sufficiently fine to provide grid-independent results with the RANS models used here.

A.2.2   Validation: comparison with the measurements

The quantification of the agreement between CFD and experiment is performed by using the same validation metrics as in Chapter II. The definitions are given hereafter and the metrics values for the three simulations are reported in Table A.1.

Hit rate (q):

$$q = \frac{1}{N}\sum_{i=1}^{N} n_i \quad \text{with} \quad n_i = \begin{cases} 1 & \text{for} \quad \left|\dfrac{P_i\text{-}O_i}{P_i}\right| \leq D_q \quad \text{or} \quad |P_i\text{-}O_i| \leq W_q \\ 0 & \text{else} \end{cases} \tag{A.1}$$
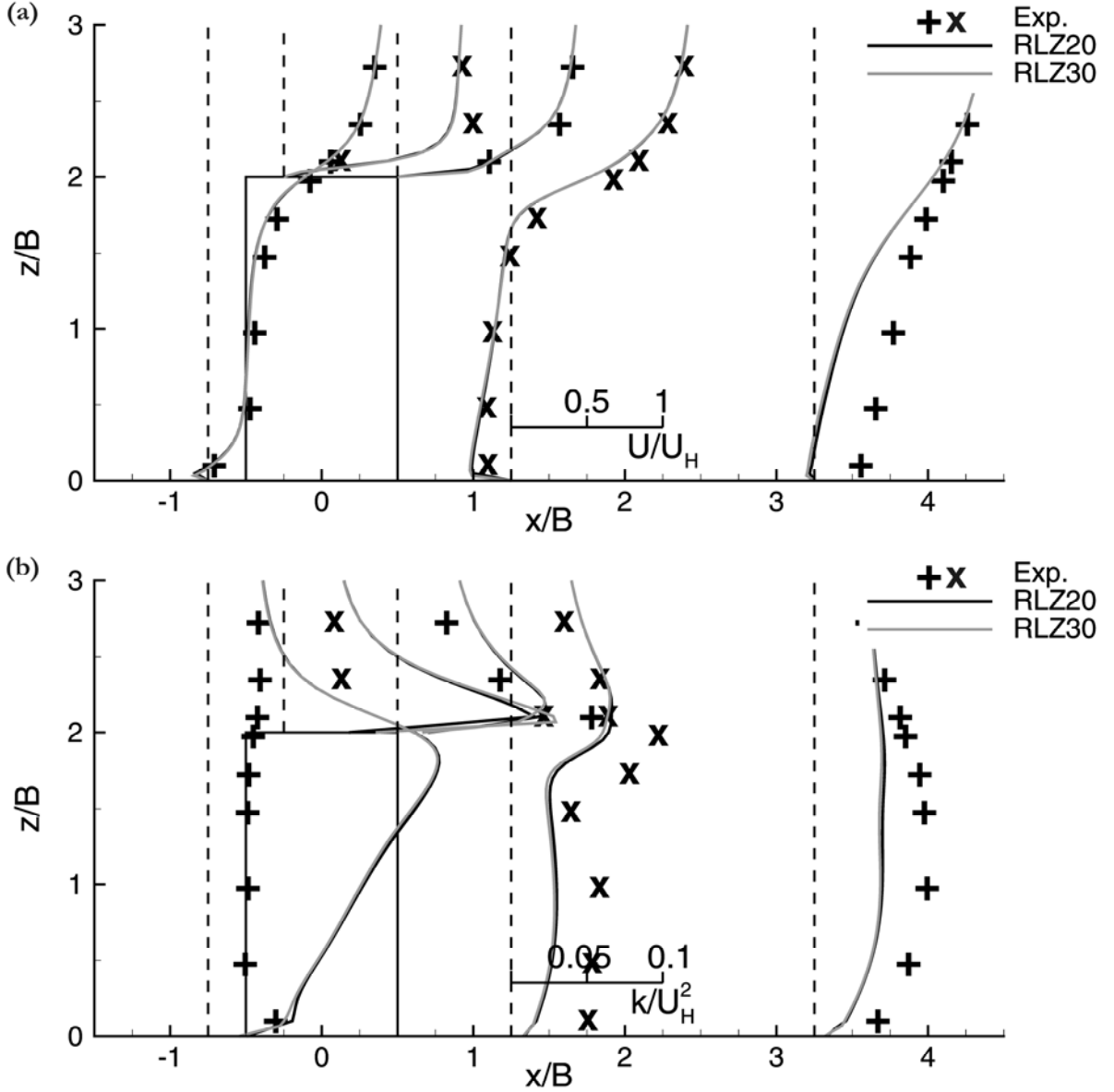
Figure A.1. Grid-sensitivity analysis: comparison between RLZ20 and RLZ30. Experimental (symbols) and numerical (lines) profiles of non-dimensional (a) mean streamwise velocity and (b) turbulent kinetic energy in the plane V0.

Fraction of predictions within a factor of 2 of observations (*FAC2*):

$$FAC2 = \frac{1}{N}\sum_{i=1}^{N} n_i \quad \text{with} \quad n_i = \begin{cases} 1 & \text{for } 0.5 \le \dfrac{P_i}{O_i} \le 2 \\ 0 & \text{else} \end{cases} \tag{A.2}$$

Fractional bias (*FB*):

$$FB = FB_{fn} - FB_{fp} \quad \text{with} \quad FB_{fn} = \frac{[O]_{fn} - [P]_{fn}}{0.5\big([O]_{fn} + [P]_{fn}\big)} ; FB_{fp} = \frac{[O]_{fp} - [P]_{fp}}{0.5\big([O]_{fp} + [P]_{fp}\big)} \tag{A.3}$$

Normalized mean square error (*NMSE*):

$$NMSE = \frac{[(O\text{-}P)^2]}{[O][P]} \qquad (A.4)$$

In these definitions, O_i and P_i correspond to the observed (measured) and predicted (computed) values of a given variable for the sample i, respectively; N is the number of data points; D_q and W_q are the allowed relative and absolute deviations, respectively. The square brackets denote averaging on the whole dataset or on all the under- (resp. over-) predictions when they are followed by the subscript fn (resp. fp). Note that FB and $NMSE$ cannot be used for variables that can take both positive and negative values and have therefore been used only for k.

The streamwise velocity computed by RLZ, RNG and RSM on Grid20 is plotted along 5 lines in the planes V0 and H10 in Figure A.2. Overall, the agreement between CFD and experiment is fairly good, although some discrepancies are present in the far-wake and at roof level. When taking into account the 186 measurement points, the hit rate for U/U_H is equal to 0.74 for RLZ20 and 0.7 for both RNG20 and RSM20, which is below the values found with LES (between 0.85 and 0.9, see Table II.3, p. 29). One common feature of the three turbulence models is the large under-estimation of the velocity values at $x/B=3.25$. This can also be seen in the computed values of the recirculation length in the wake of the building (X_w) reported in Table A.2: they are about twice the one measured in the wind tunnel. The recirculation length above the roof (X_r) is also over-estimated by RNG and RSM, while RLZ does not predict any flow detachment at this location. This is of prime importance when the source is located on

Table A.1. Validation metrics (hit rate q, factor of two of observations $FAC2$, fractional bias FB and normalized mean square error $NMSE$) for the three simulations. The metrics for U and k take into account the 186 measurement points while V is evaluated in the planes H1 and H10 and W in the plane V0. Thresholds for q: $D_q=0.25$; $W_q=0.03$ for U, V and W. $D_q=0.25$; $W_q=0.003$ for k.

	U/U_H		V/U_H (planes H1 & H10)		W/U_H (plane V0)		k/U_H^2			
	q	FAC2	q	FAC2	q	FAC2	q	FAC2	FB	NMSE
Ideal value	1	1	1	1	1	1	1	1	0	0
RLZ20	0.74	0.817	0.68	0.608	0.53	0.576	0.31	0.769	0.138	0.50
RNG20	0.70	0.780	0.55	0.558	0.56	0.591	0.33	0.785	0.295	0.41
RSM20	0.70	0.817	0.72	0.625	0.53	0.667	0.18	0.715	0.375	0.40

Table A.2. Non-dimensional length of the rooftop (X_r/B) and wake (X_w/B) recirculation zones.

Case	X_r/B	X_w/B
Exp. [Meng and Hibi, 1998]	0.52	1.42
RLZ20	0	2.97
RNG20	0.70	3.21
RSM20	0.76	2.57
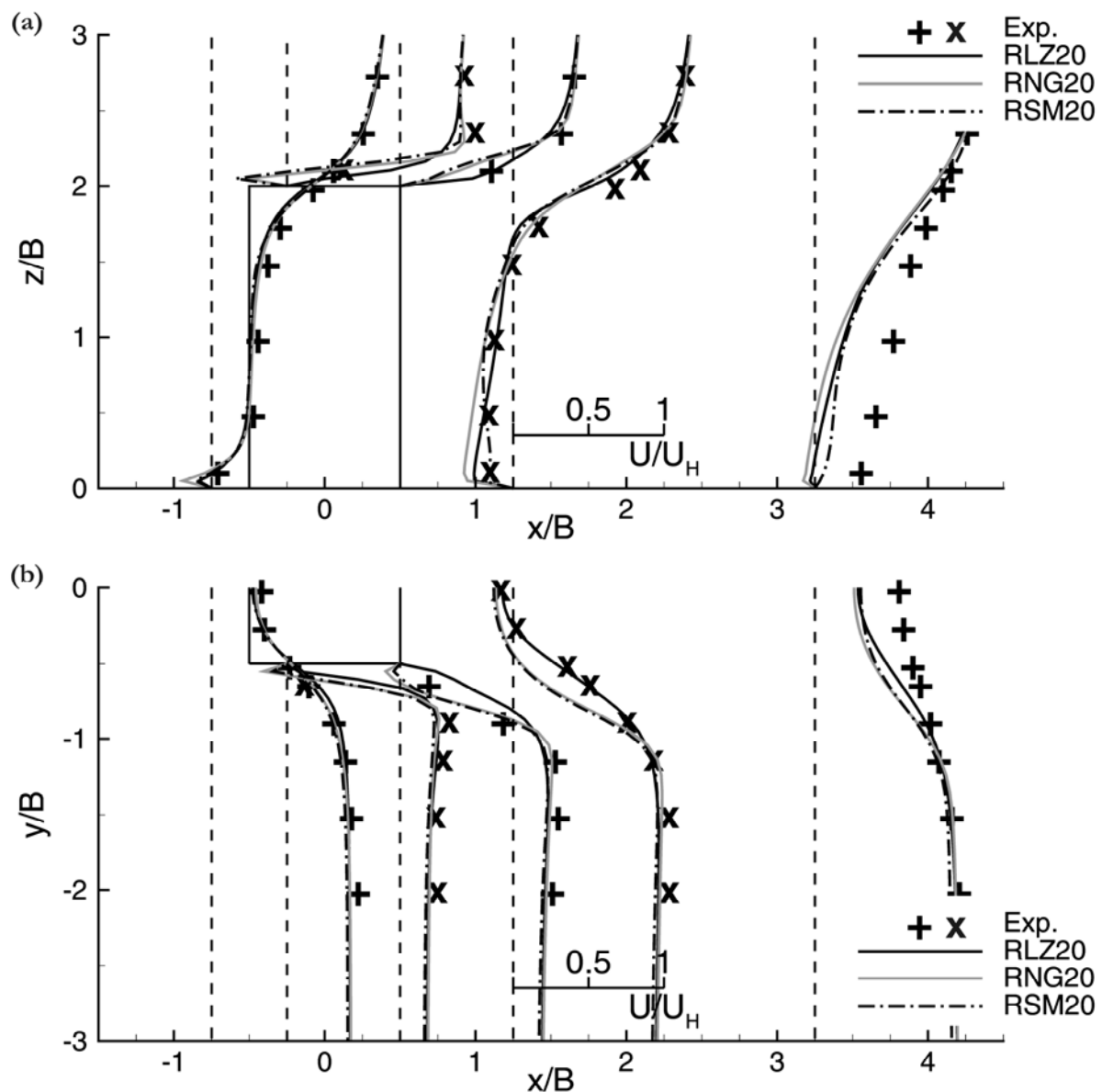
Figure A.2. Experimental (symbols) and numerical (lines) profiles of non-dimensional mean streamwise velocity in the planes (a) V0 and (b) H10.

the roof of the building, as shown in Chapter III.

Figure A.3 shows the k-profiles for RLZ, RNG and RSM in the planes V0 and H10. In comparison with the measurements, the three models largely over-estimate the turbulent kinetic energy upstream of the building at x/B=-0.75. The inverse trend is observed downstream of the building: k is under-estimated, which explains partly the over-estimation of the wake recirculation length pointed out earlier. The maximum hit-rate value for this variable is for RNG: q=0.33, to be compared to q=0.66 obtained with LES and the dynamic Smagorinsky SGS model on the same grid (Chapter II).
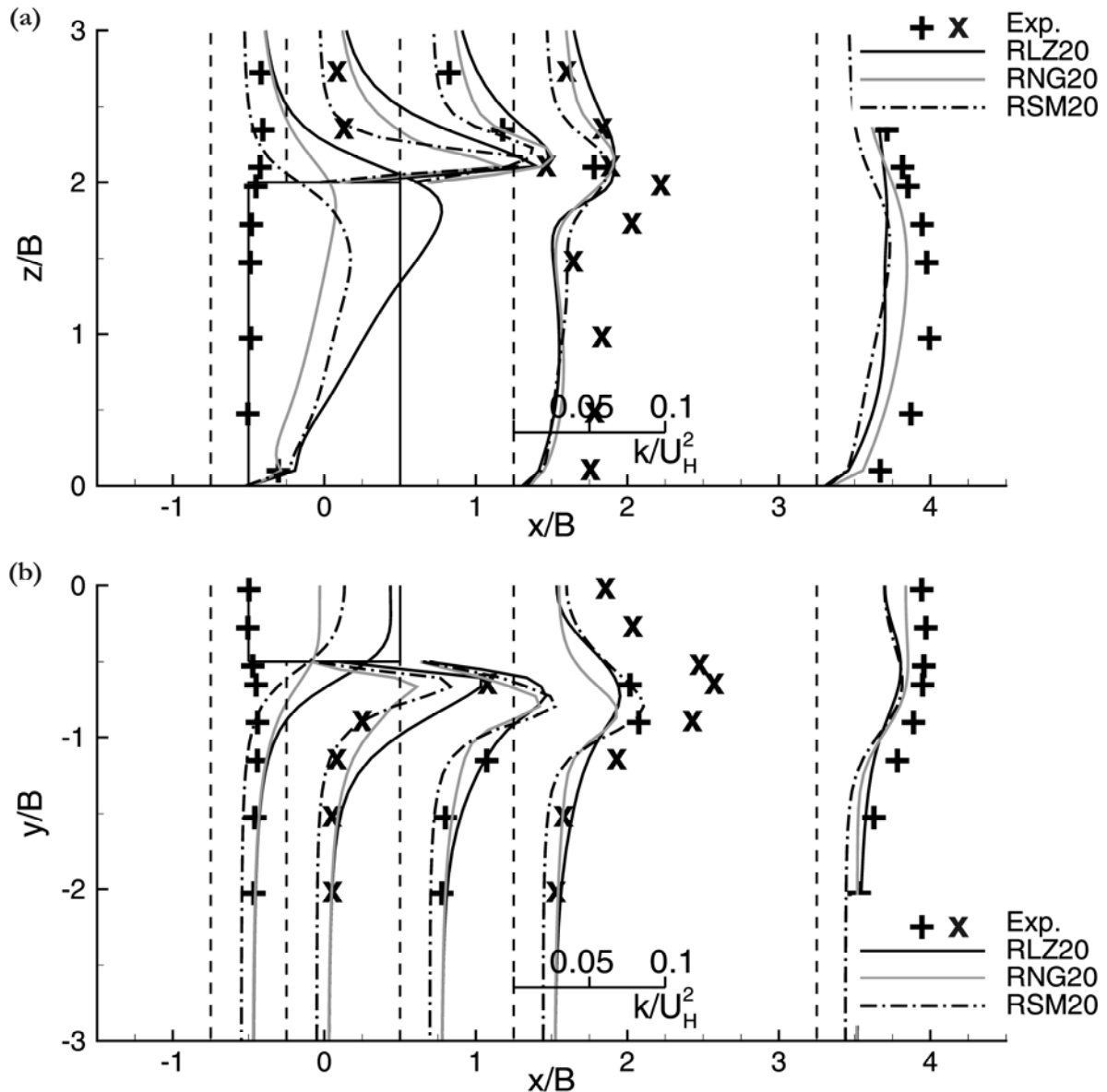
Figure A.3. Experimental (symbols) and numerical (lines) profiles of non-dimensional turbulent kinetic energy in the planes (a) V0 and (b) H10.

A.3   Conclusion

The performance of three RANS models (RLZ, RNG and RSM) applied to the simulation of wind flow around a high-rise building has been tested. A computational grid with 20 cells per building side was shown to be sufficiently fine to provide grid-independent results: no significant changes in the U- and k-profiles were observed with further grid refinement. Fairly good agreement with the wind-tunnel measurements was found in terms of mean streamwise velocity, with hit-rate values from 0.70 to 0.74. However, the recirculation regions in the wake of the building and above the roof region were not well described. According to the metrics (no plots were shown here), the

agreement was poorer for the other components of velocity V and W. In dispersion studies, the accurate prediction of the turbulent kinetic energy k is needed because the turbulent diffusivity governing the dispersion process is directly linked to this variable. For k, the accuracy of RLZ, RNG and RSM is limited: the k-values are over-estimated around the front corner of the building and under-estimated in the wake. The hit-rate evaluated on all the measurement lines is below 0.33 for the three models tested here. Overall, when confronting the results presented here to those of Chapter II, it appears that LES is more accurate than the RANS models tested here to simulate the wind flow around an isolated building.

Appendix B
Dispersion around a cubical building: Snapshots of the flow and concentration fields

In this appendix, we present some additional results from the LES computation of dispersion around a cubical building of Chapter IV. The description of the numerical model is not repeated. The purpose is to help visualizing the instantaneous events that have been identified to contribute to turbulent mass transport.

In Chapter IV, pollutant dispersion from the rooftop vent on a cubical building has been studied from a statistical point of view with LES. This statistical analysis takes into account 24,000 time steps, which is long enough to obtain converged values for C, U, V and W, i.e. the mean values of the variables c, u, v and w. To obtain the results presented here, the simulation has been run for an extra period and the contours of the fluctuations $c'=c\text{-}C$, $u'=u\text{-}U$ and $w'=w\text{-}W$ as well as the y-vorticity $\omega_y=\partial u/\partial z\text{-}\partial w/\partial x$ in the vertical mid-plane $y=0$ have been monitored. Figure B.1 shows these contours at four instants t_1, t_2, t_3 and t_4 with 12 time steps (0.792 time units) between two successive instants. In the figure, each line of four images corresponds to a given time step. Note that the contours depicted here correspond to the dimensional variables with blue (resp. red) contours for negative (resp. positive) values; the non-dimensional values at P1 are indicated in each figure. These four particular instants have been selected because they correspond to a typical event of turbulent mass transport and allow clarifying the influence of the vortical structures on dispersion.

In Chapter IV, the presence of vortical structures in the shear layer developing above the roof had been detected thanks to the contours of the two-point correlation coefficient of vertical velocity, which is an average quantity. In the vertical mid-plane, the axis of these vortices is approximately aligned with the y-axis. One of these vortical structures is circled with a dashed line in Figure B.1; it is located above the roof at t_1 and is travelling downstream with an increasing size until t_4. It can be identified in several ways. First, as can be seen in the first column of the figure, the vortex is characterized by $u'<0$ on its bottom side and $u'>0$ on its top side. Indeed, since the vortex is rotating clockwise, it accelerates (resp. decelerates) the mean flow on its upper (resp. lower) half.
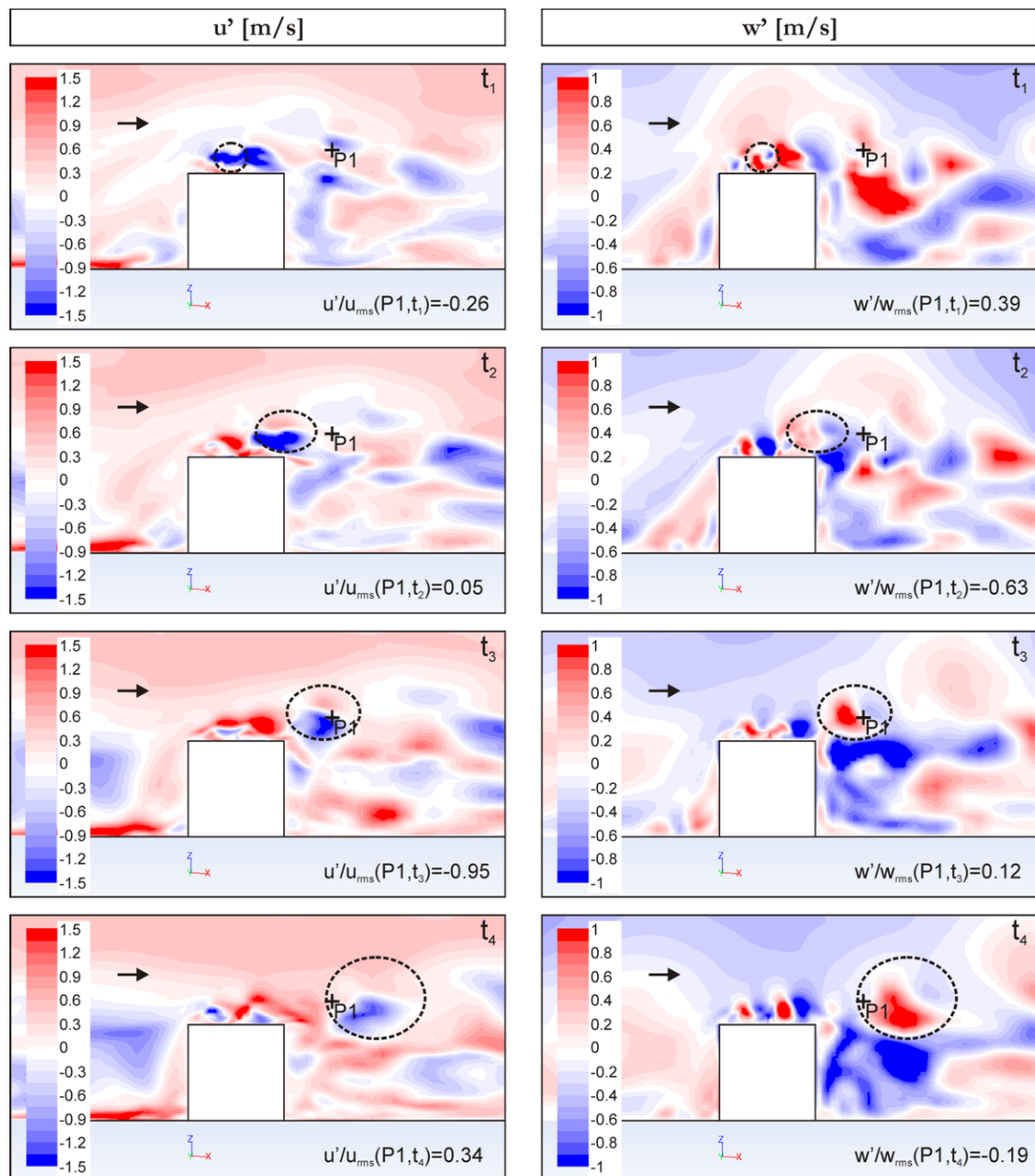
Figure B.1. Contours of (first column) u', (second column) w', (third column) ω_y and (fourth column) c' in the vertical mid-plane at four successive instants.

Similarly, in the vertical direction, the vortical structure we are looking at is characterized by a positive vertical velocity fluctuation w' on the upstream side and a negative one on the downstream side (see second column of Fig. B.1). It also corresponds to a red spot in the contours of y-vorticity. However, high values of ω_y can also be associated to a high-shear region without any vortex. It should be noted here that the reason why the velocity fluctuations created by the vortex in both streamwise and vertical directions are generally more intense in the direction opposite to the mean flow is not clear and should be investigated further.
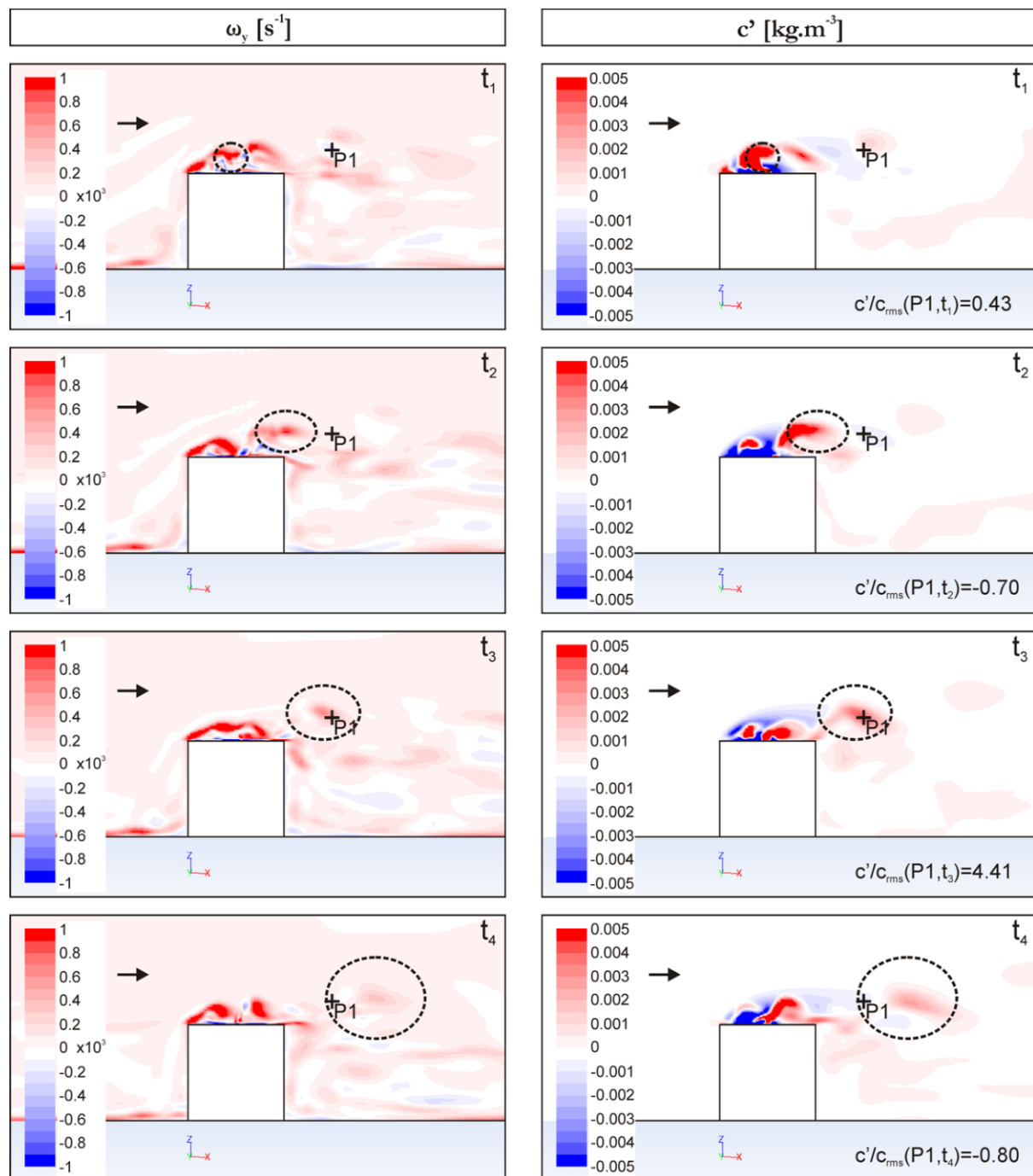
Figure B.1 (cont'd). See page 98.

At t_1, the vortex we are following is located above the building roof, in the vicinity of the pollutant source. It originates from the shear layer that develops from the front corner of the cube. It is small in size and rather difficult to identify (first line of Fig. B.1). The backflow that it creates transports the pollutant emitted by the roof-centered source in the upstream direction, as can be seen in the last column of Figure B.1, on page 99. This puff of pollutant is then carried downstream by the vortex; it reaches the leeward facade of the building at t_2, the point P1 at t_3 and farther downstream at t_4. The transport of the
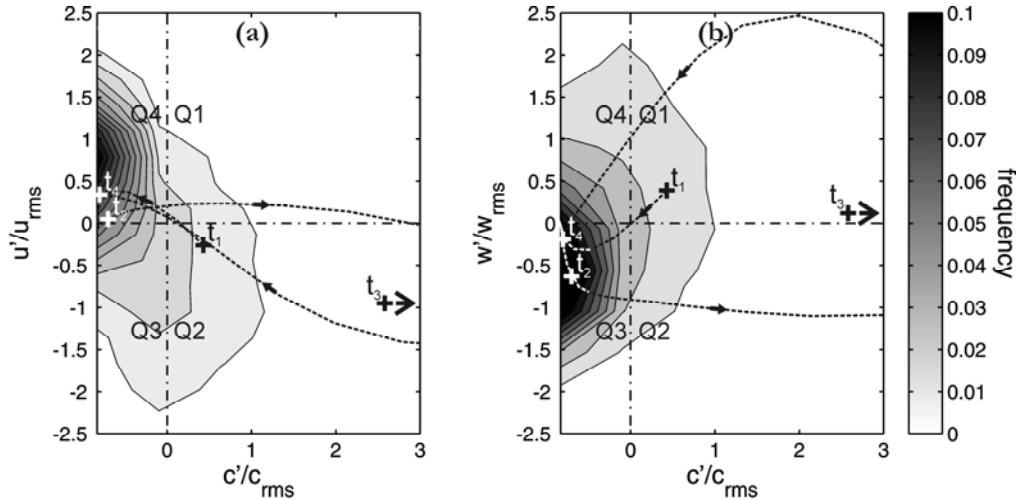
Figure B.2. Bivariate histogram of frequency distribution at P1 for (a) (c'/c_{rms}; u'/u_{rms}) and (b) (c'/c_{rms}; w'/w_{rms}). The fluctuation values at t_1, t_2, t_3 and t_4 are indicated by crosses. The values at the intermediate time steps are indicated by the dashed lines.

highly polluted air by the vortex is clear in these snapshots: the pollutant is "trapped" in the vortex core that is transported downstream by the bulk flow.

Let us now focus on what is occurring at P1 instead of following the vortex. It can be observed that at t_1 this monitoring point is characterized by a high concentration value (red spot in the last column of Fig. B.1) coinciding with the presence of a vortical structure just above (see for example the contours of ω_y in the third column). At this instant, the streamwise velocity fluctuation is negative and the vertical one is positive. Following the terminology used in Chapter IV, the couple (c'/c_{rms}; u'/u_{rms}) at t_1 belongs to the quadrant Q2 of the bivariate histogram of P1 and (c'/c_{rms}; w'/w_{rms}) belongs to Q1, corresponding to an ejection event. This is illustrated in Figure B.2 where the events at the four instants have been marked in the bivariate histogram presented in the above-mentioned chapter. The intermediate values between the four instants considered here are also indicated by dashed lines. At t_2 (second row of plots of Fig. B.1), P1 is in fact located between two pollutant-carrying vortices and consequently the concentration value is low, lower than the average value ($c'<0$). At the same time, $u'>0$ and $w'<0$. This is the most frequent situation at P1, as shown in the bivariate histograms. At t_3, the vortex marked in Figure B.1 has reached P1 and a peak of concentration is observed. P1 is located in the lower part of the vortex and consequently a negative streamwise velocity fluctuation is observed. As far as the vertical component of velocity is concerned, the sign of w' becomes positive at P1 after being negative (Fig. B.2-b). After the vortical structure has passed P1, the situation at the monitoring point becomes "normal" again until the passage of the next vortex: the values of the concentration and velocity fluctuations at t_4 belong to the range of values which have been shown to be the most frequent.

Part 2
Actual Urban Areas

Chapter V
CFD simulation of pollutant dispersion in an actual urban area

Turbulence modeling and validation by experiments are key issues in the simulation of micro-scale atmospheric dispersion. This study evaluates the performance of two different modeling approaches (RANS standard k-ε and LES) applied to pollutant dispersion in an actual urban environment: downtown Montreal. The focus of the study is on near-field dispersion, i.e. both on the prediction of pollutant concentrations in the surrounding streets (for pedestrian outdoor air quality) and on building surfaces (for ventilation system inlets and indoor air quality). The high-resolution CFD simulations are performed for neutral atmospheric conditions and are validated by detailed wind-tunnel experiments. A suitable resolution of the computational grid is determined by grid-sensitivity analysis. It is shown that the performance of the standard k-ε model strongly depends on the turbulent Schmidt number, whose optimum value is case-dependent and a priori unknown. In contrast, LES with the dynamic subgrid-scale model shows a better performance without requiring any parameter input to solve the dispersion equation.

V.1   Introduction

Outdoor air pollution is associated with a broad spectrum of acute and chronic health effects [Brunekreef and Holgate, 2002]. The pollutants that are brought into the atmosphere by various sources are dispersed (advected and diffused) over a wide range of horizontal length scales. Micro-scale dispersion refers to processes acting within horizontal length scales below about 5 km. It can be studied in detail by wind-tunnel modeling and by numerical simulation with Computational Fluid Dynamics (CFD). Wind-tunnel modeling is widely recognized as a valuable tool in wind flow and gas dispersion analysis but it generally only provides data at a limited number of discrete positions and it can suffer from incompatible similarity requirements. CFD does not have these two disadvantages; it provides "whole flow-field" data and it can be performed at full scale. Furthermore, it is very suitable for parametric studies for various physical flow and dispersion processes. On the other hand, the accuracy of CFD is a main concern, and grid-sensitivity analysis and experimental validation studies are imperative.

In the past decades, CFD has been used extensively in micro-scale pollutant dispersion studies. A distinction can be made between generic studies and applied studies. Generic studies include configurations such as idealized isolated buildings (e.g. [Leitl et al., 1997; Li and Stathopoulos, 1997; Meroney et al., 1999; Blocken et al., 2008; Santos et al., 2009; Tominaga and Stathopoulos, 2009]), idealized isolated street canyons (e.g. [Leitl and Meroney, 1997; Chan et al., 2002; Gromke et al., 2008]) or regular building groups (e.g. [Kim and Baik, 2004; Shi et al., 2008; Wang et al., 2009; Buccolieri et al., 2010; Dejoan et al., 2010]). Applied studies refer to actual (isolated) buildings or actual building groups (urban areas) (e.g. [Hanna et al., 2006; Patnaik et al., 2007; Baik et al., 2009; Pontiggia et al., 2010]).

Many previous studies have indicated that CFD simulations based on the steady Reynolds-Averaged Navier-Stokes (RANS) equations are deficient in reproducing the wind-flow patterns (e.g.[Murakami et al., 1992]) and near-field pollutant dispersion concentrations around buildings (e.g. [Leitl et al., 1997; Meroney et al., 1999; Blocken et al., 2008; Tominaga and Stathopoulos, 2010]), which motivates the use of Large-Eddy Simulation (LES) for micro-scale pollutant dispersion. A number of authors have applied LES to dispersion around isolated buildings (e.g. [Tominaga et al., 1997; Sada and Sato, 2002]) and in street canyons (e.g. [Li et al., 2008; Hu et al., 2009]). One of the main concerns in micro-scale atmospheric dispersion modeling, however, is determining the spread of pollutants from sources in actual urban environments. During the past decade, the continuous progress in computational power has allowed us to also apply LES to this kind of street-scale dispersion problems. An overview of previous LES studies in actual urban areas is provided in Table V.1. For every study, the city name and location, the spatial extent of the urban study (near-field or far-field) and the subgrid-closure scheme are listed. It is also indicated whether RANS simulations were performed and whether validation by comparison with experiments was conducted. Finally, also the cell type and

Table V.1. Overview of previous and present LES computations of atmospheric dispersion in actual urban areas.

Reference	City	Spatial extent	Closure	RANS	Validation by exp.	Cell type	Resolution
[Camelli et al., 2005]	Tysons Corner, VA, USA	Far-field	Smagorinsky	No	No	Tetrahedral	0.22-6.1 m
	New York, NY, USA	Far-field	Smagorinsky	No[a]	No[a]	Tetrahedral	≥ 2 m
[Tseng et al., 2006]	Baltimore, MD, USA	Far-field	Scale-dependent Lagrangian dynamic	No	No	Hexahedral	6-8 cells/ building
[Patnaik et al., 2007]	Los Angeles, CA, USA	Far-field	Monotone Integrated	No	Yes (field exp.)	Hexahedral	6 m
[Tamura, 2008][b]	Tokyo, Japan	Far-field	N/A	No	No	N/A	N/A
[Xie and Castro, 2009]	London, UK	Far-field	Smagorinsky	No	Yes (wind tunnel)	Polyhedral	≥ 1.5 m
Present simulation	Montreal, PQ, Canada	Near-field	Dynamic Smagorinsky	Yes	Yes (wind tunnel)	Hexahedral (Body-fitted)	0.04-8 m (full-scale)

[a] Comparisons with RANS simulations and field measurements of velocity vectors at several points in Hanna et al. (2006)
[b] Details in [Tamura et al., 2006], in Japanese

the grid resolution are reported. The present study aims at expanding the current state of the art in LES dispersion modeling, as discussed below.

The previous studies all involved a large group of buildings (13 or more) with the primary intention to determine the far-field spread of contaminants released from a source through the network of city streets and over buildings. This type of studies is called "far-field" dispersion studies in the framework of this paper. Given the extent of the computational domains involved, the grid resolutions in these far-field studies are generally relatively low, with a minimum cell size of the order of 1 m. An exception to this is the study by Camelli et al. [2005], who used cell sizes down to 0.22 m. Although the results provided by LES are generally promising, comparison with experimental data was only performed in two studies. For dispersion in actual urban areas, the relative performance of LES compared to RANS is not well known, as this was not addressed in previous studies.

Up to now, to the knowledge of the authors, no high-resolution CFD studies of near-field gas dispersion for relatively large building groups which are accompanied by grid-sensitivity analysis and validation by comparison with experiments have been performed. The aim of this paper is to present this kind of study for pollutant dispersion around a building group in downtown Montreal. The focus is both on the prediction of pollutant concentrations in the surrounding streets (for pedestrian outdoor air quality) and on the prediction of concentrations on building surfaces (for ventilation system inlets placement and indoor air quality), i.e. two zones close to the source where the computation of the concentration distribution is known to be particularly challenging.
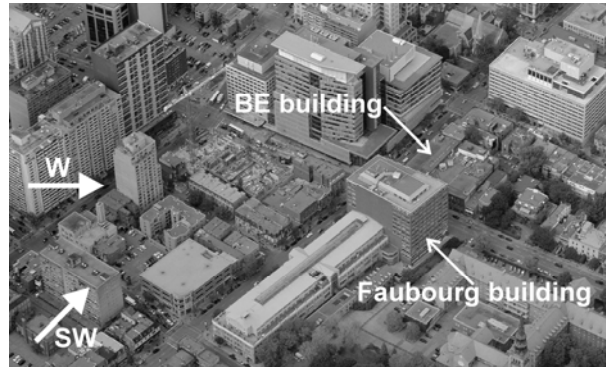
Figure V.1. View from south of the BE building and its surroundings in downtown Montreal and wind directions considered in the present study.

The CFD simulations are validated by detailed wind-tunnel experiments performed earlier by Stathopoulos et al. [2004], in which sulfur-hexafluoride (SF$_6$) tracer gas was released from a stack on the roof of a three-story building and concentrations were measured at several locations on this roof and on the facade of a neighboring high-rise building. Note that earlier CFD studies for the same case included none or only one of the neighboring buildings [Blocken et al., 2008; Lateb et al., 2010], while in the present study, surrounding buildings are included up to a distance of 300 m. For this purpose, a high-resolution grid with minimum cell sizes down to a few centimeters (full-scale) is used. The grids are obtained based on detailed grid-sensitivity analysis. Both LES and RANS simulations are performed.

V.2   Description of the experiments

Experiments of pollutant dispersion in downtown Montreal were conducted in 2004 by Concordia University and the IRSST (*Institut de recherche Robert-Sauvé en Santé et en Sécurité du Travail*) [Stathopoulos et al., 2004]. Two types of experiments were conducted: on-site and in the Concordia University boundary-layer wind tunnel [Stathopoulos, 1984], with a scale factor of 1/200. SF$_6$ was used as tracer gas and released from a stack located on the roof of the BE building, which is a three-story building in the city center (Fig. V.1). In the present study, the laboratory experiments are reproduced. The reason for this choice is the higher controllability of the boundary conditions offered by wind-tunnel modeling, which allows a more reliable evaluation of the CFD simulations. The dimensions are expressed at model scale unless specified otherwise.

The test section of the wind tunnel is 12.2 m long, 1.8 m high and 1.8 m wide. A combination of vortex generators and roughness elements along the test section floor allows the simulation of the atmospheric boundary layer (ABL). The mean velocity profile of the neutral ABL is given by:

$$\frac{U(z)}{U_{ref}} = \left(\frac{z}{z_{ref}}\right)^n \qquad\qquad (\text{V.1})$$

Table V.2. Parameters for the two case studies.

Case	Wind direction	θ [°]	Stack location	hs [m]	M [-]
SW	South-West	220	3	1	5
W	West	270	1	3	3

where the power-law exponent n is equal to 0.3, corresponding to urban exposure; U_{ref}=12.5 m s^{-1} is the mean wind velocity at reference height z_{ref}=0.6 m (full-scale: 120 m); and z is the height above the ground. The streamwise turbulence intensity at the position of the model is 35% at ground level and 5% at reference height. The aerodynamic roughness length z_0 is 0.0033 m and the longitudinal integral length scale $L_{int,x}$ is 0.4 m.

Measurements were performed for different wind directions, stack locations, stack heights and velocity ratios. The two cases used for the validation study are summarized in Table V.2 and illustrated in Figures V.2-a and V.3-a. In the table, θ is the angle between the north direction and the wind direction, as indicated in Figure V.4, h_s is the stack height and M is the velocity ratio defined as $M=W_e/U_H$, where W_e is the stack exhaust velocity and U_H=6.5 m s^{-1} is the upstream undisturbed mean wind velocity at building height (H=6.8 cm). The stack location numbering corresponds to that by Stathopoulos et al. [2004] where in total four stack locations were considered.

For the south-west wind direction (Fig. V.2-a), the BE building is located immediately downstream of the high-rise Faubourg building. It can be expected that plume dispersion will be strongly linked to the simulation of the recirculation zone in the wake of the Faubourg building. Concerning the westerly wind direction, the flow around
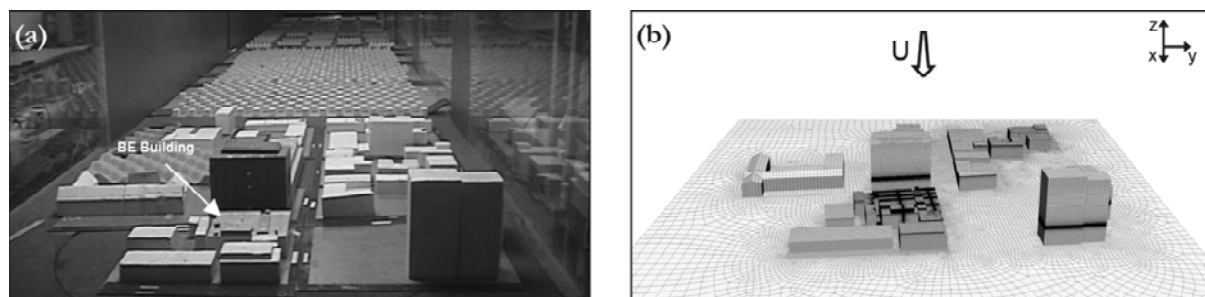
Figure V.2. Case SW: (a) wind-tunnel model and (b) corresponding computational grid on the building and ground surfaces.
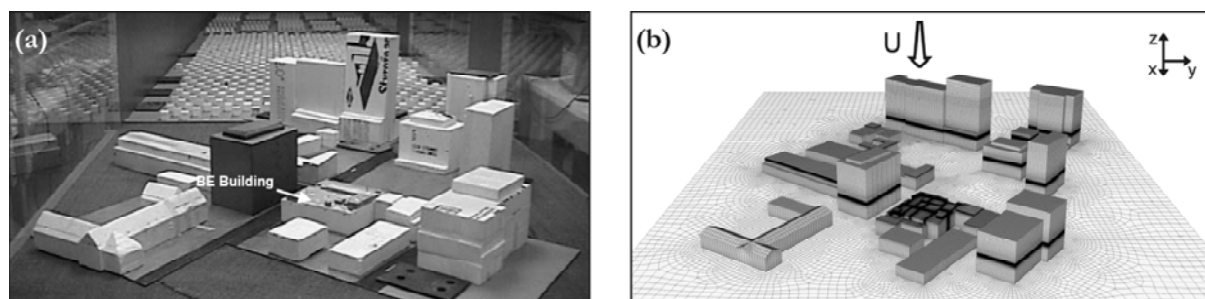
Figure V.3. Case W: (a) wind-tunnel model and (b) corresponding computational grid on the building and ground surfaces.

the BE building will supposedly be influenced by the far wake of the two high-rise buildings upstream and the corner vortex of the Faubourg building. These two configurations have been selected because the above-mentioned features make them highly challenging test cases for CFD simulation.

SF$_6$ was released from the 2 mm-diameter stack with a concentration of 10 ppm. In the wind tunnel, one-minute air samples were taken at several locations on the BE building roof, plus two locations at the top of the leeward facade of the Faubourg building in the case SW; the concentration was measured with a gas chromatograph with a precision of ±5%. The locations and labels of the measurement points for the two case studies are shown in Figure V.4 together with the measured values of 100×K, where K is the non-dimensional concentration coefficient given by:

$$K=\frac{\chi U_H H^2}{Q_e} \tag{V.2}$$

In this equation, χ is the mean mass fraction of SF$_6$ and Q_e is the SF$_6$ emission rate [m^3 s^{-1}].

V.3   Governing equations

RANS turbulence models can provide accurate solutions for a wide range of industrial flow problems while requiring relatively low computational resources. The basic principle of this turbulence modeling approach is the application of the Reynolds-averaging operator to the Navier-Stokes equations, resulting in the appearance of new unknowns: the Reynolds stresses. These stresses can be linked to the flow variables in different ways, which defines the type of turbulence model.
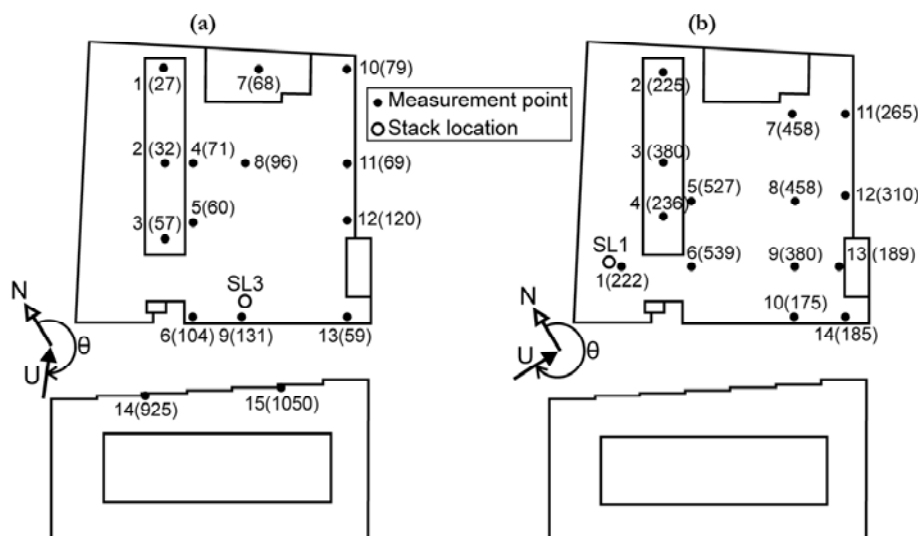
Figure V.4. Measurement points on the roof of the BE building and facade of the Faubourg building and measured concentration values (100×K, between brackets) for (a) case SW and (b) case W. The stack location is indicated by SL3 and SL1, respectively.

With LES, a spatial filtering operator is used to separate two categories of motion scales. On the one hand, the large eddies are highly problem-dependent and are directly resolved. On the other hand, the smallest scales of motion are known to have a more universal behavior and their effect on the flow field can therefore be modeled by a so-called subgrid-scale (SGS) model. Contrary to steady RANS, the LES approach computes a time-dependent solution; it is usually more demanding in terms of computational resources.

In this paper, the Eulerian approach is used to model the dispersion process for both RANS and LES methodologies. The concentration in SF$_6$ is considered as a scalar transported by an advection-diffusion equation:

$$\frac{\partial c}{\partial t} + \vec{u}.\nabla c = D_m \nabla^2 c + s_c \qquad (V.3)$$

where c is the mass concentration in SF$_6$ [kg m^{-3}]; $\vec{u}$ is the velocity vector [m s^{-1}]; D_m is the molecular diffusion coefficient [m^2 s^{-1}]; and s_c is a source term [kg m^{-3} s^{-1}].

V.3.1   The RANS standard k-ε model

All the steady RANS simulations presented in this paper use the standard k-ε turbulence model (SKE) [Jones and Launder, 1972]. The intention is to test the ability of this widely used model to predict concentration distributions in complex geometries. In addition to the averaged momentum, continuity and energy equations, two other equations are solved for the transport of k, the turbulent kinetic energy, and ε, the turbulence dissipation rate. SKE is used in combination with the Boussinesq hypothesis, which relates the Reynolds stresses to the mean-velocity gradients. This relation involves the turbulent viscosity ν_t, which can be calculated from k and ε.

When using SKE in the present study, all the transport equations are discretized using a second-order upwind scheme. Pressure interpolation is second order. The SIMPLE algorithm is used for pressure-velocity coupling. The gradients are computed in a discrete way, based on the Green-Gauss theorem [Fluent Inc., 2006]. Convergence is assumed to be obtained when all the scaled residuals [Fluent Inc., 2006] reach 10^{-6}. The values of the model constants are: $C_{1\varepsilon}$=1.44; $C_{2\varepsilon}$=1.92; C_μ=0.09; σ_k=1.0; σ_ε=1.3.

The application of the Reynolds-averaging operator to Equation (V.3) leads to the appearance of the turbulent mass flux $\vec{Q_t}$ representing the effects of turbulence on mass transfer. Since in turbulent flows this flux largely dominates molecular diffusion, the accuracy of the concentration field prediction is strongly linked to the model used to determine $\vec{Q_t}$. By analogy with molecular diffusion, it is assumed to be proportional to the gradient of mean concentration: $\vec{Q_t}$=-$D_t\nabla C$, where D_t is the turbulent mass diffusivity [m^2 s^{-1}] and C is the mean concentration [kg m^{-3}]. D_t is often assumed to be proportional to the turbulent viscosity. The relation involves a dimensionless parameter known as the turbulent Schmidt number (Sc_t=ν_t/D_t). Variations in the value of Sc_t are known to have a

large influence on the concentration field [Tominaga and Stathopoulos, 2007; Blocken et al., 2008]. In this study, three values of Sc_t are used: 0.3, 0.5 and 0.7, which are in the range of those used in previous studies (e.g. [Tominaga and Stathopoulos, 2007; Blocken et al., 2008]).

V.3.2   Large-Eddy Simulation

In the filtered Navier-Stokes equations, the SGS stresses τ_{ij} represent the effect of the small eddies on the resolved field of motion. In order to close the equations for the filtered velocity, the dynamic Smagorinsky SGS model [Smagorinsky, 1963; Germano et al., 1991; Lilly, 1992] is used in this study: the components of the deviatoric SGS stress tensor (τ_{ij}^d) are linked to the filtered rate of strain by a linear relation:

$$\tau_{ij}^d = -2\nu_{sgs}\overline{S}_{ij} \tag{V.4}$$

where ν_{sgs} is the SGS turbulent viscosity [m² s⁻¹] and $\overline{S}_{ij}=(\partial\overline{u}_i/\partial x_j+\partial\overline{u}_j/\partial x_i)/2$ is the filtered rate of strain tensor.

The mixing-length hypothesis is used to evaluate the SGS turbulent viscosity:

$$\nu_{sgs} = L_{sgs}^2\overline{S} \tag{V.5}$$

where $\overline{S}=(2\overline{S}_{ij}\overline{S}_{ij})^{1/2}$ is the characteristic filtered rate of strain and $L_{sgs}=\min(\varkappa d, C_s V_c^{1/3})$ is the SGS mixing length, with $\varkappa$ the von Karman constant, d the distance to the closest wall, V_c the volume of the computational cell and C_s the so-called Smagorinsky coefficient. In the present study, a dynamic procedure is used to evaluate this parameter, based on the resolved field. To avoid instabilities, the C_s value is kept in the range [0; 0.23] [Fluent Inc., 2006].

In the LES computations in this chapter, the momentum equation is discretized with a bounded central-differencing scheme and a second-order upwind scheme is used for the energy and SF₆ concentration equations. Pressure interpolation is second order. Time integration is second order implicit. The non-iterative fractional step method [Bell et al., 1989] is used for time advancement. This method allows reducing computational time by performing only a single outer iteration per time step. For the pressure equation, the sub-iterations end within a time step when the ratio of the residual at the current sub-iteration and the first sub-iteration is less than 0.25, with a maximum of 10 sub-iterations per time step. For all the other equations, this ratio and this maximum are 0.05 and 5, respectively.

The application of the filtering operator to Equation (V.3) leads to the appearance of an SGS mass flux term $\overrightarrow{q_{sgs}}$, which represents the effects of the scales that are smaller than the filter size on the resolved concentration field. It is assumed to be proportional to the gradient of filtered concentration: $\overrightarrow{q_{sgs}}=-D_{sgs}\nabla\overline{c}$, where D_{sgs} is the SGS mass diffusivity [m² s⁻¹]. In the present study, it is evaluated dynamically at each time step based on the resolved concentration field, in the same way as C_s.

V.4   Domain, grid and boundary conditions

V.4.1   Domain

Two computational domains have been created, one for each wind direction (see Figs. V.2-b and V.3-b). The inlet and outlet planes are perpendicular to the flow direction, as required by the vortex method [Mathey et al., 2006] used to generate a time-dependent velocity profile at the inlet (more details in Section V.4.4). The streamwise, spanwise and vertical coordinates are denoted by x, y and z, respectively. The BE building is modeled in detail, including the rooftop structures. The other buildings are modeled based on the available full-scale data; they can therefore show some slight differences with the wind-tunnel model. Some simplifications are made to limit the number of cells and to make the simulations computationally "affordable": the vegetation is omitted (see Fig. V.2-a, on the left side), the side walls of the test section are not included as "walls" and, in the case SW, the most upstream buildings are not explicitly modeled because they are assumed to have limited influence on the plume dispersion. Note that in both case SW and W, at least one street block in each direction is explicitly modeled, in agreement with [Tominaga et al., 2008b]. The domain dimensions are based on the COST Action 732 guidelines [Franke et al., 2007]. For case SW, the domain dimensions are 5×2.125×1.65 m³ (full-scale: 1000×425×330 m³) in x, y, z direction. For case W, the domain dimensions are 5.75×2.3×1.65 m³ (full-scale: 1150×460×330 m³).

V.4.2   Computational grids

The high-resolution computational grids are composed of hexahedral cells arranged in a horizontally-unstructured and vertically-structured way. They have been created by using the surface-grid extrusion technique by van Hooff and Blocken [2010]. In the present study, the grid is first created in a horizontal plane and then swept in the vertical direction. This technique allows a large degree of control over cell shapes and sizes and avoids the use of tetrahedral and pyramid cells. For each case, RANS and LES are applied on the same computational grid. Previous numerical simulations of pollutant dispersion from a stack in a simple configuration (not presented here; see also [Tominaga et al., 1997]) have shown the importance of meshing the outlet face of the stack with a high resolution. Hence, the range of cell dimensions is broad: from a few centimeters around the stack exhaust to several meters close to the boundaries of the domain, in full-scale dimensions. The ratio of two neighboring cell dimensions is kept around a value of 1.1.

For case SW, three different grid resolutions are used to analyze the grid sensitivity of the results. The medium grid, named SW-m, is composed of 4,791,744 cells. The stack circumference is divided into 32 segments. To ensure a reasonable aspect ratio of the cells around the stack exhaust, their vertical dimension is kept small. Because the grid

Table V.3. Main characteristics of the computational grids.

Grid	Nb of cells: Total	Nb of cells: Stack circumf.	Nb of cells: BE building	Cell size at other buildings [m][a]	Cell size at exterior domain boundaries [m][a]
SW-m	4,791,744	32	130×96×49	1.5 to 3	8
SW-c	2,860,531	24	104×77×42	1.9 to 3.8	10
SW-f	6,651,874	40	164×118×60	1.5 to 3	8
W-m	5,257,343	32	136×104×51	1.5 to 3	8

[a] Full-scale dimensions

includes the four stack locations, the resolution on the surface of the BE building is very high: 130×96×49 cells including the rooftop structures. The resolution of the grid on the neighboring buildings ranges from 0.005 to 0.015 m (full-scale: 1 to 3 m), depending on the dimensions and the location of the building. In any case, a minimum of 10 cells per building height and between buildings in the horizontal plane has been used [Franke et al., 2007]. Away from the area of interest, the grid size tends progressively to 0.04 m (full-scale: 8 m). To analyze the effect of grid resolution on RANS and LES simulations, two additional computational grids are created: one finer (SW-f) and one coarser (SW-c). Refinement and coarsening are performed by multiplying the cell dimensions on the edges of the buildings by a constant factor (1.26 for SW-c and 0.8 for SW-f). For case SW-f, refinement is not performed farther than one street block away from the BE building to limit the total number of cells. The main grid characteristics are summarized in Table V.3.

Following the conclusions of the grid-sensitivity analysis for case SW (see Section V.5.1), the computations for case SW are performed with grid SW-m, and those for case W with a grid with a similar resolution (named W-m) which contains 5,257,343 cells.

V.4.3   Boundary conditions

With SKE, the profiles of U, k and ε are prescribed at the inlet of the domain, based on the measurements in the test section of the wind tunnel (see Section V.2). To generate a time-dependent velocity profile with LES, the vortex method is used [Sergent, 2002; Mathey et al., 2006]. In the inlet plane, a given number N_v of vortices are generated and convected randomly at each time step. Their intensity and size depends on the local value of k and ε whose profiles are prescribed at the inlet like for SKE. The fluctuations around the prescribed mean streamwise velocity are deduced from the perturbation caused by the vortices in the inlet plane. More details about this technique and validation studies can be found in [Mathey et al., 2006]. Previous studies on air flow around a wall-mounted cube (not presented here[1]) have shown that the flow field can be simulated in

---

[1] See also Chapter II.

an accurate way with N_p=190; this value has therefore been retained for the present LES computations.

The exit face of the stack is defined as a velocity inlet with a uniform velocity profile[1]. Turbulence quantities are computed based on the hydraulic diameter (D_b=0.002 m) and an assumed value of turbulence intensity of 10%[2].

At the top and lateral boundaries, symmetry boundary conditions are prescribed. At the outlet plane, zero static pressure is imposed. All building surfaces are defined as smooth no-slip walls. For simulations with the SKE turbulence model, the standard wall functions [Launder and Spalding, 1974] are applied to compute the variables – including c – in the wall-adjacent cells. For case SW-m, the maximum value of z^* on the building walls is equal to 830 ($z^*=C_\mu^{1/4}k_P^{1/2}z_P/\nu$, where k_P is the value of k at the centroid P of the wall-adjacent cells, z_P is the height of P and ν is the kinematic viscosity of the fluid). However, in a large majority of the cells, z^* is below 300, which justifies the use of the wall functions. With LES, the centroids of the wall-adjacent cells are assumed to fall either in the logarithmic-law region or in the linear sub-layer of the boundary layer, depending on their distance to the wall [Fluent Inc., 2006].

The ground is defined as a rough wall boundary to take into account the effects of the surrounding terrain (i.e. all the buildings that are not explicitly modeled in the computational domain) on the ABL flow. With SKE and the standard wall functions, the roughness of the wall is characterized by the sand-grain roughness height k_s [m] and the roughness constant C_r. In order to limit the longitudinal gradients which occur because of the incompatibility of the wall functions with the ABL profiles, these parameters are chosen according to the relation $k_s=9.793z_0/C_r$ [Blocken et al., 2007b], where k_s is taken smaller than z_P (e.g. z_P=0.00125 m for SW-m and W-m). In Fluent 6.3, a too high input value of C_r can create numerical instabilities so in this case where z_0 is high and k_s is low (e.g. k_s=0.0012 m for SW-m and W-m), the C_r value is bounded to 7. Therefore, some longitudinal gradients will occur. The wall treatment used with LES in Fluent does not take into account the roughness of the wall. To limit the longitudinal gradients of the inflow profiles in both the RANS and LES simulations, the upstream length of the domain has been kept intentionally short (around 0.3 m). In addition, it is reasonable to assume that the flow patterns around the BE building are to a large extent determined by the neighboring buildings and that the influence of the short-fetch upstream degradation of the ABL flow is low.

---

[1] Properties of sulfur hexafluoride (SF_6): ϱ_{SF6}=6.27 kg m^{-3}; μ_{SF6}=1.41×10^{-5} kg m^{-1} s^{-1}. Molecular diffusivity of SF_6 in air: $D_{m,SF6/air}$=6.1×10^{-6} m^2 s^{-1}.

[2] Contrary to the previous cases (Chapter III and Chapter IV), the Reynolds number at the exhaust is relatively high (Re≈4.5×10^3) and therefore turbulent velocity fluctuations have been generated with the vortex method (N_p=50) at this boundary.

V.4.4   Unsteady parameters for LES

As pointed out in Section V.4.2, the large dimensions of the domain combined with the necessity to refine the grid around the source location lead to heterogeneous cells dimensions in the computational grid. On the one hand, the time step size is usually limited by the dimensions of the smallest cells. On the other hand, the large dimensions of the domain require a long averaging time to get a statistically-steady solution: several "flow-through" time units ($T_{ft}=L_x/U_{ref}$ where L_x is the domain dimension in the streamwise direction) are generally used. In practice, satisfying these two conditions is not affordable in terms of computational time and a compromise must be made.

For the medium grid, the time step is set to $\Delta t = 5 \times 10^{-4}$ s, which leads to a Courant number (= $u\Delta t/h_c$, where u is the local velocity magnitude and h_c is the local grid size) below one in the majority of the cells. This value corresponds to the scaled-down model; the equivalent time step at full scale with the same reference velocity is 0.1 s. The grid-sensitivity analysis was performed at constant Courant number: the time step has been increased to 6.3×10^{-4} s for grid SW-c and decreased to 4×10^{-4} s for grid SW-f.

The LES computations are initialized with the solution from the SKE simulations. Before averaging, the computation is run during 2 s to remove the influence of the initial condition. Then, data are averaged over a period of 4 s (full-scale: 800 s), corresponding to $10 T_{ft}$. The monitored evolution of K with time (moving average) at the measurement points indicates that this period is long enough to get statistically-steady values, although it is smaller than the averaging time in the wind tunnel.

V.5   Results and discussion

V.5.1   Grid-sensitivity analysis for case SW

The results of the simulations performed on the grids SW-c, SW-m and SW-f with SKE and Sc_t=0.5 are shown in Figure V.5-a, where the concentration values obtained with the coarse and fine grids (vertical axis) are compared to those on the medium grid (horizontal axis). A slight change in the results can be observed from SW-c to SW-m, whereas the results obtained with SW-m and SW-f are similar.

In the case of LES with implicit filtering, the local filter width is equal to the computational cell size. As a consequence, the LES model is in essence grid dependent and the conclusions of the grid-sensitivity analysis are less straightforward than in the RANS case. In particular, it is known that a grid-independent solution cannot be found [Klein, 2005]. As can be seen in Figure V.5-b, it appears that the values predicted with SW-c are lower than those predicted with SW-m. In contrast, the use of the grid SW-f leads to a slight increase of the concentration values, especially at the points of lower concentration. It is argued that this slight difference does not justify the large increase in
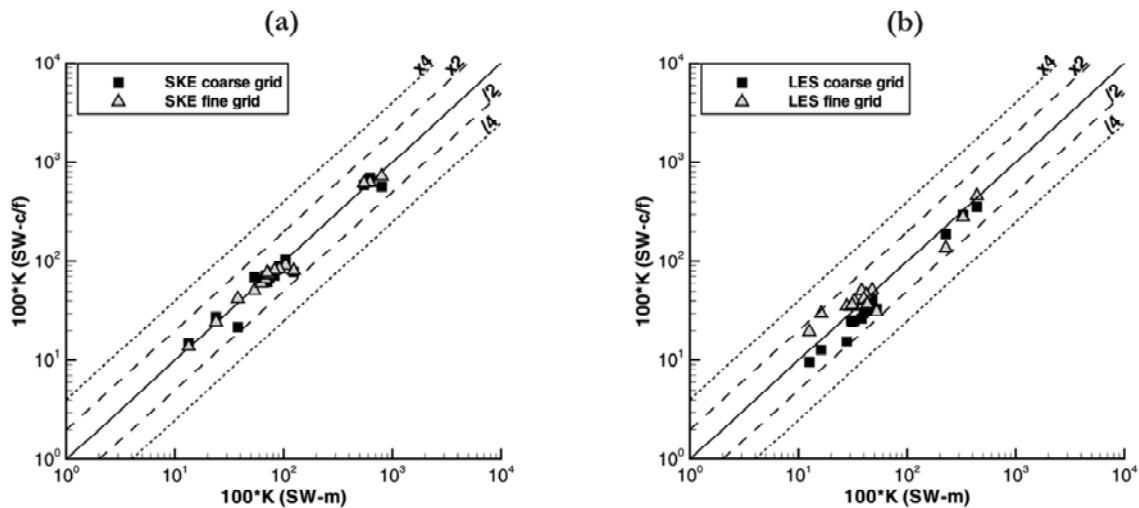
Figure V.5. Grid-sensitivity analysis: scatter plots of $100 \times K$ values for case SW obtained with three different grids with (a) SKE - Sc_t=0.5 and (b) LES.

computational time required with SW-f. Thus, in the next section, the results of SW-m will be presented and a resolution similar to SW-m was adopted for the study of case W.

V.5.2 Comparison between standard k-ε and LES on medium grid for case SW

The values of non-dimensional concentration ($100 \times K$) obtained with the numerical simulations are compared to the wind-tunnel results in the scatter plots of Figure V.6. With SKE, it is clear that – as expected – variations of Sc_t can have a large influence on the concentration values (Fig. V.6-a). No large discrepancies are observed with LES: except for point 15 (on the Faubourg building), the computed K values are within a factor of three from the wind-tunnel measurements (Fig. V.6-b). It should also be noted
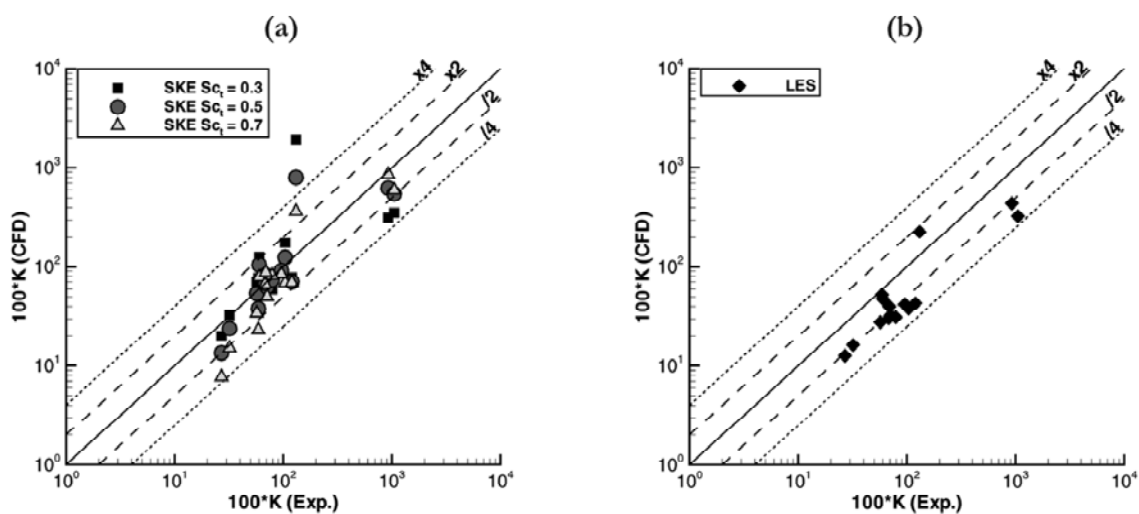
Figure V.6. CFD validation: scatter plots of $100 \times K$ values for case SW with (a) SKE and (b) LES in comparison with experiments.

that, except for point 9 (close to the stack), the values of K provided by the LES computation are all under-estimated compared to the experiment.

The average (e_{avg}), maximum (e_{max}) and median (e_{med}) values of the relative error over all the data points are given in Table V.4. The relative error e (%) is defined for each data point by:

$$e = 100 \times \frac{|K_{Exp} - K_{CFD}|}{K_{Exp}} \qquad (V.6)$$

where K_{Exp} and K_{CFD} are the measured and computed values of the concentration coefficient, respectively. The lowest values of e_{avg} and e_{max} with SKE are obtained with $Sc_t=0.7$; e_{max} remains high, however. With LES, both e_{avg} and e_{max} are low, and e_{med} is very close to the average value, which shows the symmetric distribution of the error values around e_{avg}. By contrast, $e_{med} < e_{avg}$ for SKE denotes a skewed distribution of the error values and the presence of outliers. Indeed, Table V.5 shows that the value of e at point 9 (close to the stack) is very high.

Figure V.7 shows the contours of non-dimensional mean streamwise velocity (U/U_{ref}) in the vertical plane $y=y_{stack}$ which is aligned with the flow direction and contains the center of the stack. In accordance with previous numerical simulations for simplified

Table V.4. Average, maximum and median values of the relative error for case SW-m.

	SKE - $Sc_t=0.3$	SKE - $Sc_t=0.5$	SKE - $Sc_t=0.7$	LES
e_{avg} (%)	125.2	58.9	42.3	51.7
e_{max} (%)	1406.0	508.9	178.8	73.5
e_{med} (%)	25.2	25.2	33.8	54.0

Table V.5. Dimensionless concentration coefficient ($100 \times K$) and relative error values at each measurement point for case SW-m.

Point label	$100K_{Exp}$	SKE - $Sc_t=0.3$		SKE - $Sc_t=0.5$		SKE - $Sc_t=0.7$		LES	
		$100K_{CFD}$	e (%)	$100K_{CFD}$	e (%)	$100K_{CFD}$	e (%)	$100K_{CFD}$	e (%)
1	27	20.2	25.2	13.4	50.4	7.7	71.4	12.6	53.3
2	32	32.7	2.3	23.9	25.2	15.1	52.9	16.2	49.4
3	57	70.1	23.0	53.9	5.4	34.3	39.8	27.8	51.2
4	71	69.7	1.9	62.3	12.2	50.0	29.5	32.7	54.0
5	60	125.5	109.1	104.2	73.7	78.6	31.1	47.8	20.4
6	104	174.2	67.6	124.0	19.3	68.8	33.8	38.1	63.3
7	68	62.4	8.2	68.5	0.8	66.9	1.7	30.5	55.1
8	96	90.5	5.7	91.6	4.6	84.3	12.1	42.1	56.1
9	131	1972.8	1406.0	797.7	508.9	365.2	178.8	227.3	73.5
10	79	59.5	24.7	74.0	6.4	81.7	3.4	31.3	60.4
11	69	73.5	6.6	82.5	19.6	87.8	27.2	40.0	42.0
12	120	77.7	35.2	70.6	41.1	69.2	42.3	43.1	64.1
13	59	77.1	30.7	37.9	35.7	23.2	60.7	52.4	11.2
14	925	314.3	66.0	624.2	32.5	858.3	7.2	439.7	52.5
15	1050	354.0	66.3	548.2	47.8	596.0	43.2	327.2	68.8
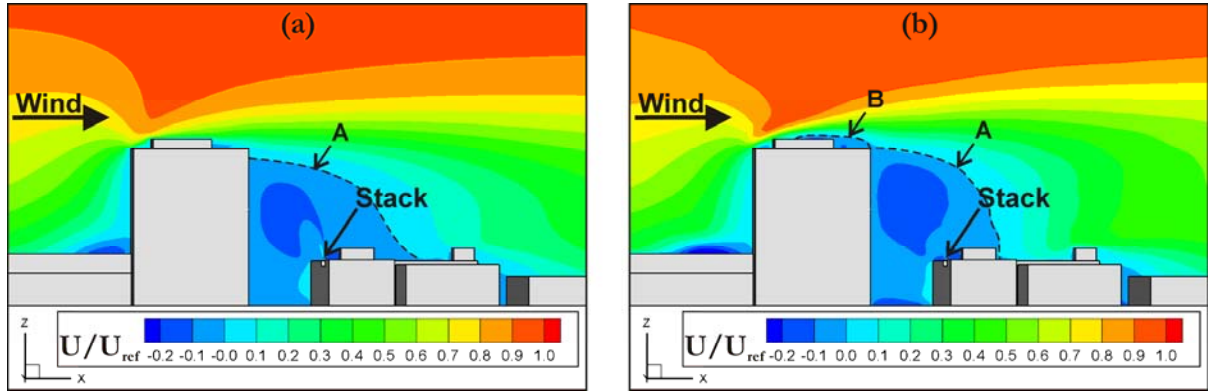
Figure V.7. Contours of mean streamwise velocity (non-dimensionalized by U_{ref}) in the vertical plane $y=y_{stack}$ for case SW obtained with (a) SKE and (b) LES. The dotted lines indicate the limits of the recirculation zones (A: wake; B: rooftop).
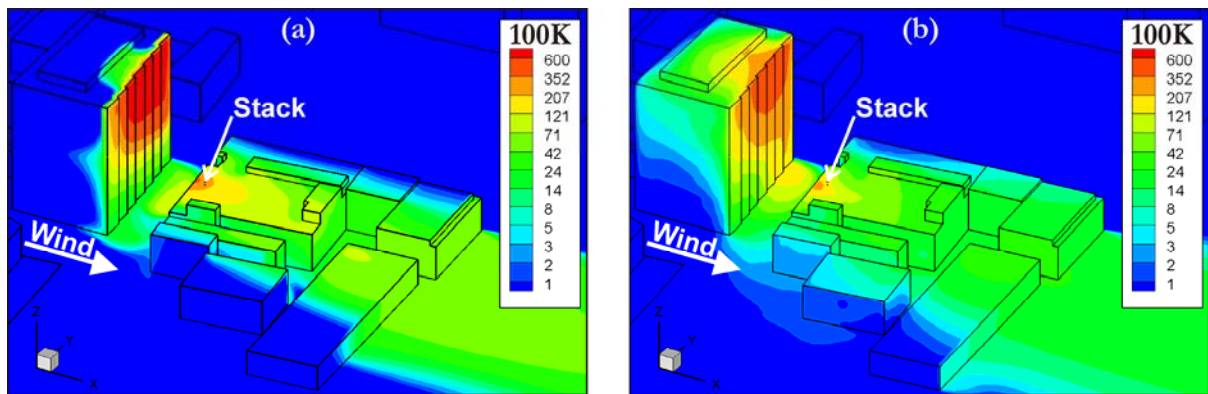
Figure V.8. Contours of $100 \times K$ on building surfaces and surrounding streets for case SW obtained with (a) SKE - Sc_t=0.7 and (b) LES.

building models[1] (e.g. [Murakami et al., 1992; Tominaga et al., 2008a]), the recirculation zone in the wake of the Faubourg building (denoted by A) extends farther downstream with SKE than with LES because of the under-estimation by SKE of the turbulent kinetic energy at this location. In this region, the backflow tends to transport the pollutant towards the Faubourg building. Indeed, with both models, the maximum concentrations occur on the leeward facade of the Faubourg building (Fig. V.8) and the concentration values on the building surfaces and the surrounding streets predicted with LES (Fig. V.8-b) are overall lower than those predicted with SKE with Sc_t=0.7 (Fig. V.8-a). However, on the roof of the Faubourg building, LES predicts high concentration values. This is not the case with SKE, and is attributed to the fact that this model does not reproduce the rooftop separation and recirculation zone B (Fig. V.7).

---

[1] See also Appendix A.

V.5.3 Comparison between standard k-ε and LES on medium grid for case W

Figure V.9-a shows that the simulations of case W with SKE show a poor agreement with the measurements. The discrepancy between CFD and experiments is minimal for $Sc_t=0.3$, as confirmed by the relative errors shown in Table V.6. Figure V.9-b shows the
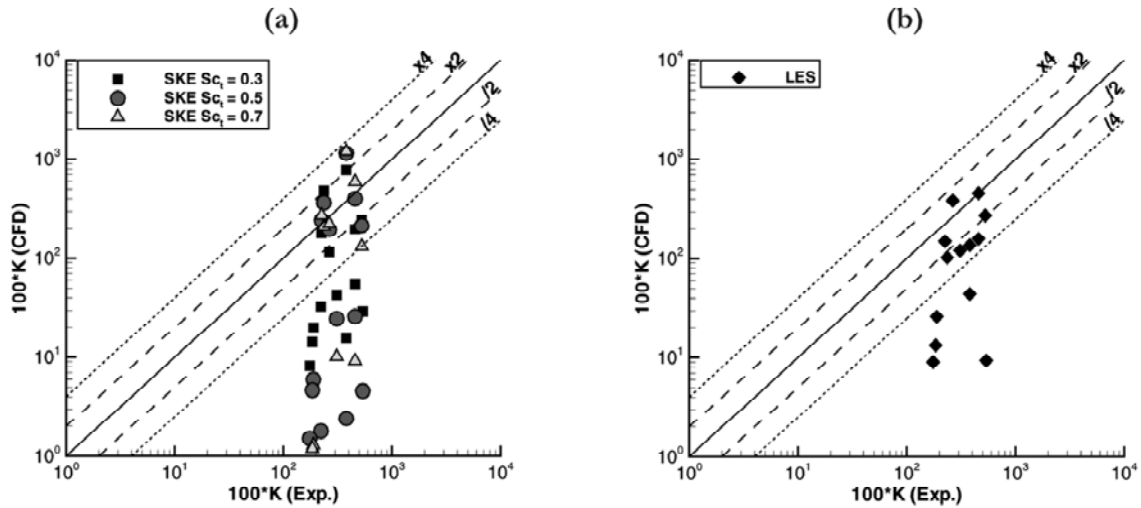
Figure V.9. CFD validation: scatter plots of $100 \times K$ values for case W with (a) SKE and (b) LES in comparison with experiments.

Table V.6. Average, maximum and median values of the relative error for case W-m.

	SKE - $Sc_t=0.3$	SKE - $Sc_t=0.5$	SKE - $Sc_t=0.7$	LES
e_{avg} (%)	80.2	81.5	82.9	66.8
e_{max} (%)	104.5	201.9	215.3	99.9
e_{med} (%)	88.6	95.6	98.7	64.9

Table V.7. Dimensionless concentration coefficient ($100 \times K$) and relative error values at each measurement point for case W-m.

Point label	$100K_{Exp}$	SKE - $Sc_t=0.3$		SKE - $Sc_t=0.5$		SKE - $Sc_t=0.7$		LES	
		$100K_{CFD}$	e (%)	$100K_{CFD}$	e (%)	$100K_{CFD}$	e (%)	$100K_{CFD}$	e (%)
1	222	32.9	85.2	1.8	99.2	0.1	100.0	0.1	99.9
2	225	178.3	20.8	244.7	8.7	273.8	21.7	148.4	34.1
3	380	776.6	104.4	1147.2	201.9	1198.3	215.3	135.7	64.3
4	236	482.6	104.5	364.9	54.6	209.9	11.1	102.2	56.7
5	527	244.5	53.6	214.3	59.3	130.9	75.2	274.8	47.9
6	539	29.2	94.6	4.6	99.1	0.6	99.9	9.3	98.3
7	458	198.1	56.7	401.4	12.4	593.4	29.6	458.1	0.0
8	458	55.4	87.9	26.1	94.3	9.2	98.0	157.7	65.6
9	380	15.7	95.9	2.4	99.4	0.3	99.9	44.2	88.4
10	175	8.2	95.3	1.5	99.1	0.3	99.9	9.0	94.9
11	265	115.7	56.4	194.8	26.5	224.4	15.3	385.2	45.4
12	310	43.0	86.1	24.7	92.0	10.1	96.7	120.1	61.3
13	189	20.1	89.4	6.0	96.8	1.3	99.3	26.2	86.1
14	185	14.2	92.3	4.7	97.5	1.2	99.4	13.3	92.8

scatter plots for the LES computation. Although maximum errors remain large, on average the accuracy is improved: the average relative error drops to 66.8% (Table V.6).

The contours of $100 \times K$ on the building roofs and on the surrounding streets are shown in Figure V.10. With SKE, the horizontal spread of the plume increases as the value of Sc_t decreases (not shown in the figure). Among the three values tested here, this spread is maximal for Sc_t=0.3 (Fig. V.10-a). Figure V.10-b shows that it is even higher with LES, resulting in higher concentration levels at the downstream neighboring streets. Note that with both models the centerline of the plume is not aligned with the wind-flow direction: the complex interaction of the oncoming wind-flow with the buildings and the elevated rooftop structures of the BE building results in a velocity component in the y-direction at the location of the stack, which tends to deviate the plume. It seems that this deviation was not observed in the wind tunnel since the concentration values at the points located in the zone $y \le y_{stack}$ (namely: points 6, 9, 10, 13, and 14; see Table V.7) are largely underestimated by the numerical simulations. This can likely be attributed to the complex combination of vortex shedding from the Faubourg building and the long rooftop structure on the BE building. Small deviations in reference wind direction are expected to have a large influence here. Another high discrepancy occurs at point 1, very close to the stack, which appears to be one of the most difficult locations to predict.

V.5.4   Discussion

Numerical simulation of atmospheric dispersion in urban environments is difficult and the selected turbulence modeling approach largely determines the quality of the results. In the present study, the case where the BE building is located in the wake of a high-rise building (case SW) shows the best agreement between CFD and experiments, especially with LES. In this case, the pollutant is transported towards the leeward facade of the Faubourg building. From a practical point of view, if this wind direction is likely to occur often (which is the case in reality; see [Stathopoulos et al., 2004]), ventilation intakes of the Faubourg building should preferably not be located on this facade and, according to the LES results, also not on the roof or the sides of the building. Pollutants can also
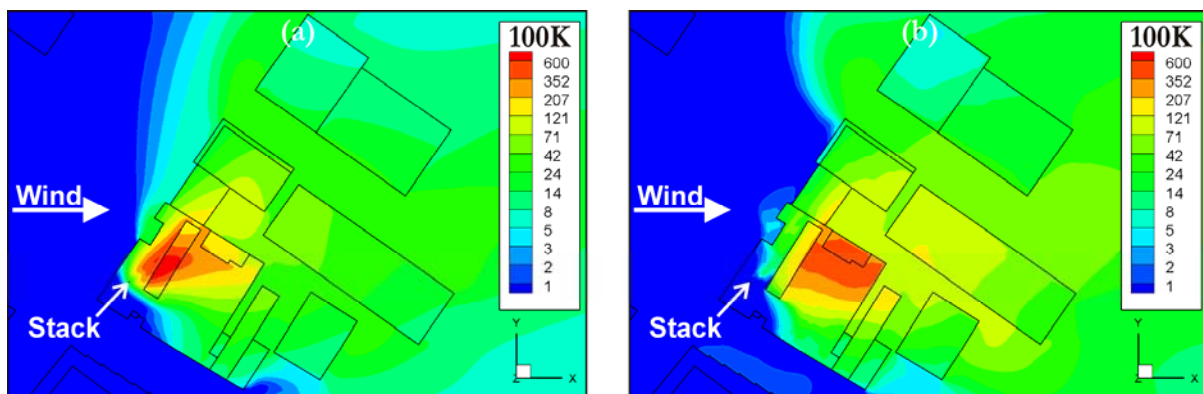
Figure V.10. Contours of $100 \times K$ on building roofs and surrounding streets for case W obtained with (a) SKE - Sc_t=0.3 and (b) LES.

contaminate the indoor air of the Faubourg building if the windows of the leeward facade are open. Air quality can deteriorate in the street between the BE and Faubourg buildings (Fig. V.8) and this can affect pedestrians. Why the concentration values predicted with LES are generally under-estimated compared to the experiment is not totally clear. A possible reason is the way in which the concentration is computed in the cells adjacent to the building surfaces, where all data points are located. Further investigation of near-wall modeling effects on surface concentration predictions is required.

Also for case W, LES provides more accurate concentration values on the roof of the BE building than SKE. For this wind direction, the plume trajectory is less disturbed than for case SW. The buildings located downstream will be affected by pollution. The horizontal spread of pollutant is high and the streets located in a wide region downstream of the BE building will be polluted as well. The numerical simulations also indicate a deviation of the plume which is considered to be responsible for the significant under-estimation of K at the points located in the zone $y \leq y_{stack}$.

For both wind directions under study, it was verified that the results of the SKE simulations are highly dependent on the value of Sc_t. Moreover, its optimum is a priori unknown and strongly case-dependent. For example, among the three values tested, the best value is 0.7 for case SW and 0.3 for case W[1]. By contrast, LES with the dynamic Smagorinsky SGS model and the dynamic computation of D_{sgs} can provide more accurate results without any parameter input to solve the dispersion equation. This is considered a main advantage of the LES approach.

Because it is an unsteady model, LES can also provide the extreme values of the concentration everywhere in the domain. From a practical point of view, this information will be required when dealing with hazardous materials whose concentration must not exceed a certain threshold. However, LES is approximately seven times more demanding in terms of computational cost than SKE in this study where the same grid has been used for both RANS and LES. LES is also very sensitive to the type and resolution of the computational grid used; in the present study, the refinement of the grid has led to an increase in the computed concentration values. Finally, it should be emphasized that wind-tunnel experiments providing both velocity and concentration measurements in an actual urban environment would be of great interest for further evaluation and comparison of turbulence models applied to atmospheric dispersion problems.

V.6   Summary and chapter conclusions

High-resolution CFD simulation of near-field pollutant dispersion in a building group in downtown Montreal was performed with two different turbulence modeling approaches:

---

[1] For case W, the low Sc_t value was an artificial way to increase the lateral spread of the plume and in this way to correct for the unexpected plume deviation mentioned above.

RANS standard k-ε and LES with the dynamic Smagorinsky SGS model. Contrary to most of the previous CFD studies of urban dispersion which focused on the far-field spread of contaminants, the present simulations focused on the concentration values close to the source (on the building surfaces and in the surrounding streets) and were performed on high-resolution grids. They were validated by comparison with wind-tunnel measurements for two different wind directions: south-west, for which a high-rise building is located immediately upstream of the emitting building, and west, for which the obstacles are located farther upstream. Both RANS and LES computations were performed on the same grids. The grid-sensitivity analysis indicated that the medium grid SW-m was suitable for the problem. For this grid, the stack circumference was divided into 32 segments, the BE building was discretized into 130×96×49 cells and a full-scale resolution of 1.5 to 3 m was used for the neighboring buildings. The agreement between numerical simulations and wind-tunnel measurements was good in the case SW but larger discrepancies were observed in the case W. Nevertheless, LES was better in both cases and has the advantage of solving the dispersion equation without any parameter input when the SGS mass diffusivity D_{sgs} is computed with a dynamic procedure. The simulation by the numerical model of the flow separation at the sharp edges of the buildings appears to be crucial for the proper simulation of the concentration field. Future work will consist of testing the ability of various turbulence modeling approaches and turbulence models to accurately reproduce flow separation on computationally affordable grids for generic cases including isolated buildings[1] and street canyons. It will also include investigation of the influence of small deviations in wind direction on the concentration field.

---

[1] Such a study has been presented in Chapter II.

Chapter VI
From generic to applied cases: Evaluation of the mass fluxes in downtown Montreal

P. Gousseau, B. Blocken, T. Stathopoulos, G.J.F. van Heijst
Micro-scale pollutant dispersion in an urban area: Investigation of the mass transport mechanism by Large-Eddy Simulation

Large-Eddy Simulation of micro-scale pollutant dispersion from a stack on the roof of a low-rise building in downtown Montreal is performed. Two wind directions are considered, with different wind flow patterns and plume behavior. The computed mean concentration field is observed and analyzed by means of the convective and turbulent (including subgrid-scale) mass fluxes. This decomposition allows gaining some insight into the dispersion process and evaluating common turbulent transport models used with the Reynolds-Averaged Navier-Stokes approach, such as the gradient-diffusion hypothesis. Despite the specific character of the flow and dispersion patterns due to the complex geometry of the urban area under study, some similarities are found with the generic case of dispersion around an isolated simple building. Moreover, the analysis of dispersion in downtown Montreal is facilitated by the physical insight gained by the study of the generic case. In this sense, the present study supports the use of generic, simplified cases to investigate environmental processes in real and more complex situations. Reciprocally, the results of this applied study show the influence on the dispersion process of the rooftop structures and of the orientation of the emitting building with respect to the incoming wind flow, providing directions for further research on generic cases.

VI.1 Introduction

The turbulent nature of the wind flow around buildings is the reason why the accuracy of Computational Fluid Dynamics (CFD) applied to wind engineering problems strongly depends on the choice of the turbulence modeling approach. Two approaches are generally used in computational wind engineering: steady Reynolds-Averaged Navier-Stokes (RANS) and Large-Eddy Simulation (LES).

In turbulent flows, molecular diffusion of a pollutant gas is generally negligible and pollutant dispersion can be seen as the combination of convective and turbulent mass transport, corresponding to the transport by the mean flow and by the turbulent fluctuations, respectively [Gousseau et al., 2011b]. This decomposition is actually the basic principle of the RANS turbulence modeling approach. With RANS models, the convective mass flux ($Q_{c,i} \equiv U_i \times C$, where $U_i = <u_i>$ is the mean velocity in the direction i and $C = <c>$ is the mean concentration) is computed based on the mean variables while the turbulent mass flux ($Q_{t,i} \equiv <u_i'c'>$, where the angle brackets denote averaging and u_i' and c' are the velocity and concentration fluctuations) needs to be modeled because the turbulent fluctuations of velocity and concentration are not explicitly resolved. The turbulent mass flux is generally assumed to be proportional and opposite to the gradient of mean concentration, with the so-called gradient-diffusion (GD) hypothesis or first-order closure: $Q_{t,i} = -D_t \times \partial C / \partial x_i$, with D_t the turbulent mass diffusivity. A large majority of the CFD studies of pollutant dispersion with the RANS turbulence modeling approach use the GD hypothesis to compute the turbulent mass flux, mainly because of the simplicity of this model (e.g. [Riddle et al., 2004; Blocken et al., 2008; Lateb et al., 2010; Chavez et al., 2011; Hang and Li, 2011]). RANS simulations of pollutant dispersion with other mass-flux models are rather rare in the literature (e.g. [Rossi and Iaccarino, 2009; Wang et al., 2009]). The GD hypothesis has the disadvantage of being strongly dependent on the turbulent Schmidt number ($Sc_t = \nu_t / D_t$) input value that allows computation of D_t based on the turbulent viscosity ν_t [Tominaga and Stathopoulos, 2007]. Furthermore, in some cases like for example dispersion from a rooftop vent on a cubical building and, more generally, for shear-dominated flows, it appears that this hypothesis is not always valid: in the streamwise direction, turbulent mass transport can act from the low to high levels of mean concentration and the GD hypothesis is therefore not valid [Rossi et al., 2010; Gousseau et al., 2011b]. Further investigation of the underlying physical mechanism performed in Chapter III [Gousseau et al., 2012] showed the importance of the large-scale vortical structures present in the shear layers developing from the roof and sides of the cubical building with its windward facade perpendicular to the approach flow. These structures create peaks of both velocity and concentration fluctuations. The fluctuations of streamwise velocity and concentration are most of the time of opposite sign, which explains why the covariance (i.e. $<u'c'>$, the streamwise component of the turbulent mass flux) is negative, hence of the same sign as the mean concentration derivative in this direction.

In the present chapter, micro-scale pollutant dispersion in the real urban environment of downtown Montreal (Canada) is studied with LES. The term "micro-scale" means that horizontal dimensions below 5 km are considered. Pollutant gas is emitted by a stack on the roof of a low-rise building, under two different wind directions. The density of the surrounding buildings is high, which makes the flow and concentration field particularly complex and challenging to predict. The wind-tunnel experiments by Stathopoulos et al. [2004] are reproduced. The comparison of the measured tracer gas concentration values at several locations on the roof of the emitting building with those computed by the CFD model has been performed and reported in [Gousseau et al., 2011a] (Chapter V). By contrast, in the present study, we focus on the plume structure and dispersion process rather than on the near-field mean surface-concentration values.

The evaluation of the convective and turbulent mass fluxes in this urban area is performed by the use of LES. Contrary to steady RANS models which by definition only resolve the mean flow variables, LES provides the time-resolved velocity and concentration fields, which gives access to the time statistics of these variables and hence to the turbulent mass flux. With LES, only the influence of the smallest scales of motion on the dispersion process is modeled. If this influence can be quantified and shown to be minor – which will be the case in this study – LES provides an accurate estimation of the turbulent mass flux and can therefore be used to evaluate various turbulent transport models used with RANS such as the GD hypothesis.

The decomposition of pollutant transport into convective and turbulent components has already been performed by the authors in the past for generic cases of dispersion around isolated buildings (see Chapter III, [Gousseau et al., 2011b]). It was shown to be an effective and efficient way to explain the accuracy of various turbulence models applied to pollutant dispersion problems. Furthermore, it provides some physical insight by representing the transport of pollutant rather than the resulting concentration field. By applying this approach to a real urban area, it is also expected to reveal some similarities and/or differences between a complex applied case and simpler generic cases. Based on this study, conclusions on the relevance of generic studies to investigate environmental processes that in reality occur in more complex applied cases will be drawn.

In summary, the present study aims at: (1) analyzing the wind-induced pollutant transport mechanism in a complex urban area by looking at the convective and turbulent mass fluxes; (2) evaluating the GD hypothesis for this complex case; and (3) observing the link between the present results and those obtained earlier for generic cases of pollutant dispersion.

The numerical model is described in the next section. Then, the results are presented and analyzed separately for each wind direction (namely case SW and case W). In the last section, the results are summarized and discussed before drawing conclusions.

VI.2 Numerical model

VI.2.1 Domains, grids and boundary conditions

Two wind-tunnel experiments of pollutant dispersion in downtown Montreal performed by Stathopoulos et al. [2004] at scale 1:200 are reproduced with ANSYS/Fluent 6.3. SF_6 is used as a tracer gas and is released from a stack on the roof of a three-story building (named 'BE building') in the city center (see Chapter V, Fig. V.1). The first case (case SW) is for South-West wind direction, a stack height h_s=1 m (full-scale dimensions) and a velocity ratio M=5, the latter being defined as the ratio W_e/U_H with W_e the stack exhaust velocity and U_H the mean approach-flow wind velocity at building height (H=13.6 m). For this wind direction, the BE building is located immediately downstream of the Faubourg building (Fig. VI.1). The second case (case W) is for westerly wind direction, h_s=3 m and M=3. In this case, the emitting building is located in the far wake of several high-rise buildings (Fig. VI.2). Note that the stack location is different for these cases.

The computational domains and grids are identical to those used for the simulations in Chapter V [Gousseau et al., 2011a], where they were named "SW-m" and "W-m". The domain dimensions are based on the COST Action 732 and AIJ guidelines [Franke et al., 2007; Tominaga et al., 2008b]: 5×2.125×1.65 m³ (73.5H×31.2H×24.3H) for case SW and 5.75×2.3×1.65 m³ (84.5H×33.8H×24.3H) for case W (at reduced scale 1:200), and the inlet and outlet planes are perpendicular to the flow direction (x) in both cases. The spanwise and vertical coordinates correspond to y and z, respectively.

The high-resolution computational grids are shown in Figures VI.1 and VI.2. They have been created with the surface-grid extrusion technique [van Hooff and Blocken, 2010]. The grids for the cases SW and W are composed of 4,791,744 and 5,257,343 hexahedral cells, respectively, arranged in a horizontally-unstructured and vertically-structured way. The dimension of the cells ranges from a few centimeters around the source (full-scale dimensions) to several meters at the external boundaries of the domain in order to keep a reasonable total number of cells. This inevitably leads to cells with a
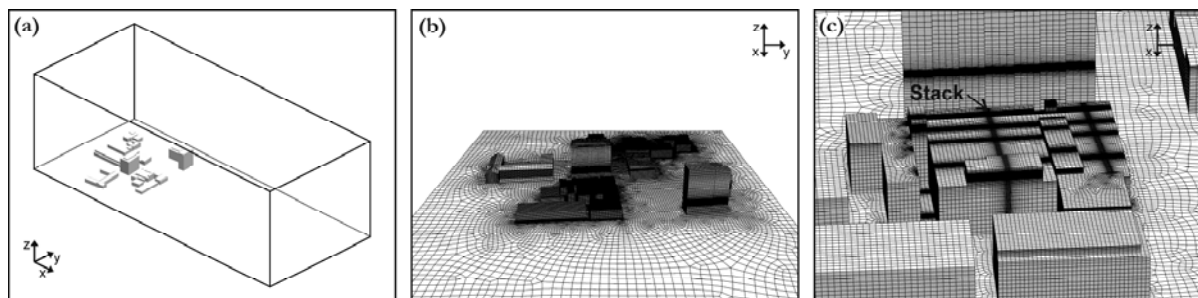
Figure VI.1. Case SW: (a) computational domain, (b) computational grid on the building and ground surfaces (total number of cells: 4,791,744) and (c) a close view of the grid on the BE building. The wind flow is in the x-direction (from back to front of the page in (b) and (c)).
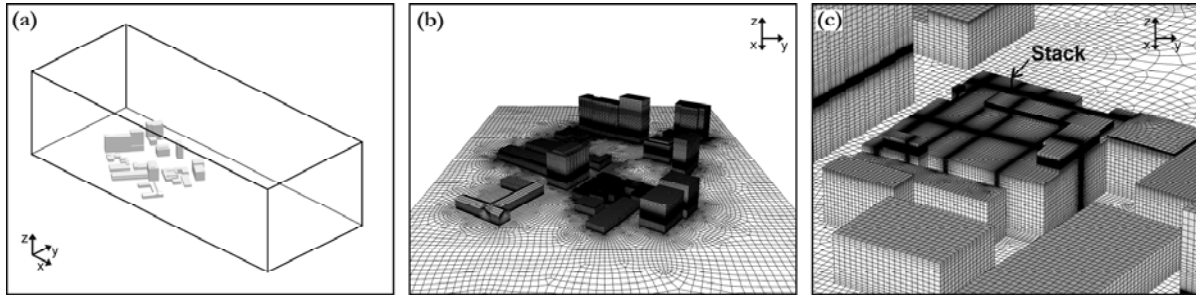
Figure VI.2. Case W: (a) computational domain, (b) computational grid on the building and ground surfaces (total number of cells: 5,257,343) and (c) a close view of the grid on the BE building. The wind flow is in the x-direction (from back to front of the page in (b) and (c)).

high aspect ratio which are not optimal for LES but which can hardly be avoided in practice. Previous LES study of wind flow around an isolated building with aspect ratio 1:1:2[1] have shown that 20 cells per building side are sufficient to ensure a well-resolved LES in the sense that 80% of the total turbulent kinetic energy is resolved. Considering the high-resolution used here to discretize the emitting building (e.g. 130×96×49 for case SW), it can be inferred that the present simulation constitutes a well-resolved LES in the region of interest around the emitting building. The conclusion of the grid-sensitivity analysis that has been conducted for case SW and presented in [Gousseau et al., 2011a] is that for LES the concentration values on the roof of the BE building increase slightly (on average by 11%) when a higher grid resolution is used, but it is argued that this variation does not justify the large increase in computational time required (up to one month for the complete simulation run in parallel on eight processors). Moreover, while a change was observed in the surface concentration values (due to the better resolution of the near-wall gradients), the plume structure and flow field calculated on the two grids were nearly identical away from the wall boundaries.

At the inlet of the domain, the profiles of mean wind speed U, turbulent kinetic energy k and turbulence dissipation rate ε are imposed, based on the wind-tunnel measurements. For both wind directions the mean velocity profile corresponds to a power law with the exponent equal to 0.3; it represents an atmospheric boundary layer flow in an urban environment. The streamwise turbulence intensity I_u ($=\sigma_u/U$ with σ_u the standard deviation of u) is 35% at ground level and 5% at 0.6 m height in the wind tunnel. The k-profile has been deduced following $k=(I_u\times U)^2$, which assumes $\sigma_u^2=\sigma_v^2+\sigma_w^2$ [Tominaga et al., 2008b; Ramponi and Blocken, 2012]. The ε-profile has been computed assuming equilibrium between production and dissipation of turbulent kinetic energy in the incoming flow: $\varepsilon=u^{*3}/\varkappa(z+z_0)$, with $u^*=1.01$ m s^{-1} the friction velocity, $\varkappa=0.41$ the von Karman constant and $z_0=0.0033$ m (model scale) the aerodynamic roughness length. The prescribed profiles allow generating the time-dependent velocity profile at the inlet of the domain using the vortex method [Mathey et al., 2006] with 190 vortices. Two-

---

[1] See Chapter II.
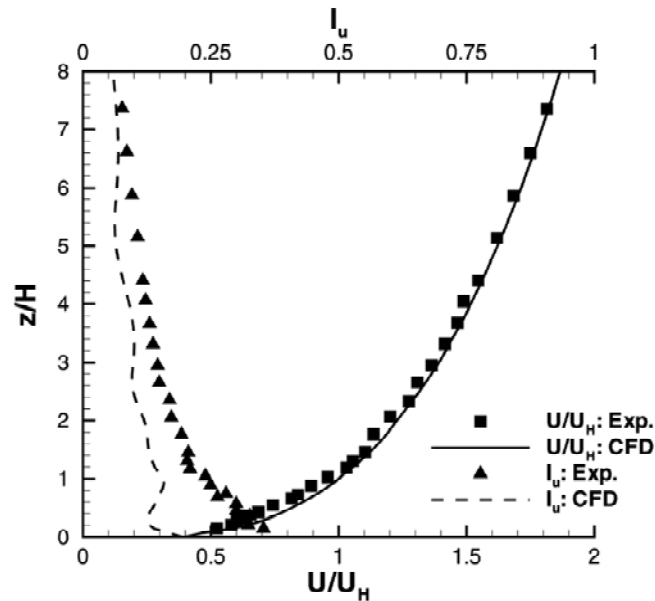
Figure VI.3. Experimental (symbols) and numerical profiles generated at the inlet of the computational domain (lines) of non-dimensional mean streamwise velocity (U/U_H) and streamwise turbulence intensity (I_u).

dimensional vortices whose individual size and intensity depend on the local value of k and ε are created and transported randomly in the inlet plane and generate in this way perturbations on the lateral and vertical velocity components. Perturbations imposed on the mean streamwise velocity are deduced from the perturbations induced in the inlet plane [Mathey et al., 2006]. The resulting vertical profiles of non-dimensional mean streamwise velocity U/U_H and streamwise turbulence intensity I_u obtained with the vortex method are compared to those measured in the wind tunnel in Figure VI.3. Note that the numerical profiles are averaged in the lateral direction. While the agreement is good for U/U_H, one can notice the under-estimation of I_u by the CFD model, by about 36% at the BE building height. This is attributed to the vortex method which generates too low velocity fluctuations in the streamwise direction, and to the assumptions stated earlier for the computation of the turbulent kinetic energy and turbulence dissipation rate at the inlet. However, the under-estimation of I_u at the inlet is argued to have low influence on the plume dispersion since the turbulence at the location of the emitting building is mainly generated by the presence of the surrounding buildings.

The exhaust face of the stack is defined as a velocity inlet. The hydraulic diameter (0.002 m at model scale) and an assumed value of turbulence intensity of 10% are prescribed in order to generate fluctuations on the mean velocity profile (uniform on the exhaust face) with the vortex method [Mathey et al., 2006]. The top and lateral boundaries of the domain are defined as symmetry boundaries. At the outlet plane, zero static pressure is imposed. The ground and building surfaces are defined as walls and each wall-adjacent cell's centroid is assumed to fall either in the linear sub-layer, in the buffer layer or in the logarithmic region of the boundary layer, depending on its distance to the wall [Fluent Inc., 2006]. Note that the roughness of the ground is not taken into

account in the wall treatment imposed at this boundary but the empty length upstream of the buildings is sufficiently short to limit the degradation of the inflow profiles imposed at the inlet of the domain [Blocken et al., 2007a; Blocken et al., 2007b]. In addition, the presence of the upstream buildings and the related building-generated turbulence is expected to significantly reduce the influence of any unintended streamwise gradients [Blocken et al., 2007b] in the empty upstream length of the domain.

VI.2.2 Turbulence and dispersion modeling

With LES, the flow equations are filtered so that the distinction is made between the scales of motion which are smaller than the filter width (equal to the grid size in this case) and those which are larger. Only the largest scales of motion are explicitly resolved. LES is used here with the dynamic Smagorinsky subgrid-scale (SGS) model [Smagorinsky, 1963; Germano et al., 1991; Lilly, 1992] which mimics the influence of the smallest, unresolved scales of motion on the resolved flow field. The Smagorinsky coefficient is computed at each time step based on the smallest resolved scales.

Dispersion of the pollutant gas is treated with the Eulerian approach: the SF_6 concentration (c) is transported by an advection-diffusion equation. The results are expressed in non-dimensional form with the concentration coefficient K:

$$K = \frac{\chi H^2 U_H}{Q_e} \tag{VI.1}$$

where χ is the mean SF_6 mass fraction and Q_e is the exhaust rate [m^3 s^{-1}]. Note that following the definition used in the report of the experiments K is expressed as a function of χ, which is directly linked to the concentration c [kg m^{-3}].

Once filtered, the dispersion equation contains the so-called SGS mass flux $\overrightarrow{q_{sgs}}$, representing the effects of the smallest scales of motion on the resolved concentration field. It is computed based on the gradient of the resolved concentration:

$$q_{sgs,i} \equiv \overline{u_i c} - \overline{u_i}\,\overline{c} = -D_{sgs} \frac{\partial \overline{c}}{\partial x_i} \tag{VI.2}$$

where the overbar represents the filtering operator and D_{sgs} is the SGS mass diffusivity computed via the SGS viscosity ν_{sgs} and the SGS Schmidt number $Sc_{sgs} = \nu_{sgs}/D_{sgs}$ which is here computed at each time step using a test filter, with a similar procedure as the Smagorinsky coefficient C_s [Moin et al., 1991; Porté-Agel, 2004].

To analyze the dispersion process, the mean mass transport is decomposed into the transport by the mean flow field and by the turbulent fluctuations. The former corresponds to the (mean) convective mass flux $\overrightarrow{Q_c}$ and the latter to the turbulent mass flux $\overrightarrow{Q_t}$. In the LES framework, these fluxes are defined as follows:

$$Q_{c,i} = <\overline{u_i}><\overline{c}> \tag{VI.3}$$

$$Q_{t,i} = <\bar{u}_i \bar{c}'> + <q_{sgs,i}>$$ (VI.4)

where the angle brackets denote the averaging operator, the overbar indicates a filtered variable and the apostrophe denotes the fluctuation of a given variable in such a way that $c(t) = <c> + c'(t)$. Note that the mean value of a variable is symbolized by a capital letter: $<c> = C$. By extension, $\overrightarrow{Q_{sgs}}$ corresponds to the vector of components $Q_{sgs,i} = <q_{sgs,i}>$. In the next section the computed fluxes are presented in non-dimensional form with Q_0 the reference flux [kg m^{-2} s^{-1}] defined by:

$$Q_0 = \frac{Q_e \varrho_{SF6}}{H^2}$$ (VI.5)

where ϱ_{SF6} is the density of SF$_6$.

VI.2.3 Numerical procedure

The momentum equation is discretized with a bounded central-differencing scheme and a second-order upwind scheme is used for the energy and SF$_6$ concentration equations. Pressure interpolation is second order. Time integration is second order implicit. The non-iterative fractional step method [Kim and Moin, 1985] is used for time advancement. The time step is set to $\varDelta t = 5 \times 10^{-4}$ s in both cases, leading to a Courant number below 1 in the majority of the cells. The corresponding non-dimensional time step is $\varDelta t^* = \varDelta t \times U_H / H = 0.048$. The results presented hereafter have been averaged over a period of 6 s (12,000 time steps), corresponding to 15 flow-through times ($T_{fl} = L_x / U_{ref}$, where L_x is the length of the domain and U_{ref} is the mean streamwise velocity at 0.6 m height) for case SW.

VI.3 Results: South-West wind direction (case SW)

VI.3.1 Mean concentration field

The comparison between numerical and experimental values of K at 15 measurement points (13 on the roof of the BE building and 2 at the top of the leeward facade of the Faubourg building) has been performed in Chapter V [Gousseau et al., 2011a]. Agreement was fairly good for this case, with computed values within a factor of 3 from the measurements. Here, the focus is on the whole concentration field, contrary to the aforementioned reference where only surface values were considered. The isosurface $K=1$ is a representation of the average plume shape; it is shown in Figure VI.4-a. The contours of K are also shown, in the vertical plane $y = y_{stack}$ aligned with the wind direction and containing the stack (Fig. VI.4-b) and in the horizontal plane $z/H = 1.47$, corresponding to 20 m height in full-scale dimensions (Fig. VI.4-c). The plume is deviated towards the leeward facade of the upstream Faubourg building, against the
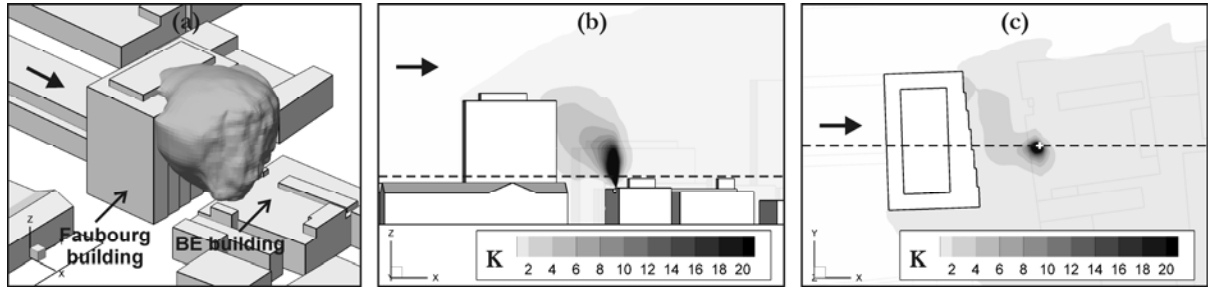
Figure VI.4. Case SW: (a) isosurface *K*=1 and (b,c) contours of non-dimensional concentration coefficient *K* in the planes (b) *y*=*y_stack* and (c) *z*/*H*=1.47. The wind direction is indicated by the arrows. The dashed line in (b) indicates the position of the plane shown in (c), and vice versa.

approach-flow wind direction. This implies that the occupants of the Faubourg building are likely to be exposed to polluted air if the ventilation intakes are located on this facade or if the windows are open. In the horizontal plane, one can notice the asymmetry of the plume shape with respect to the plane *y*=*y_stack* (Fig. VI.4-c). This feature is attributed to the irregular shape of the Faubourg building. Further analysis of the plume features can be performed by the observation of the mass fluxes presented in the next section.

VI.3.2 Mass fluxes

In order to evaluate the relative contribution of mass transport modeling ($\overrightarrow{Q_{sgs}}$) with respect to what is resolved by the LES model ($<\bar{u}_i \overline{c}'>$), the ratio of the SGS mass flux magnitude by the total turbulent mass flux magnitude is depicted in Figure VI.5. Note that the SGS contribution is evaluated here with the model in use (Eq. (VI.2)), whose accuracy is not proven. However, if not perfectly accurate, this model can reasonably be assumed to provide the correct order of magnitude for the SGS mass flux. In the region above the emitting building, the magnitude of $\overrightarrow{Q_{sgs}}$ is at least two orders of magnitude smaller than $\overrightarrow{Q_t}$. This is consistent with the fact that, in turbulent flows, mass transport is mainly governed by the large scales of motion. This is attributed to the high grid resolution that has been used to discretize the BE building and to discretize the stacks on its roof (the four stack locations used in the experiment were included in each computational grid). The contribution of the subgrid scales becomes more important around the Faubourg building and reaches levels above 10%. The reason is twofold: first, larger cells are used in the computational grid around this neighboring building and, second, relatively large gradients of concentration are present at these locations (see Eq. (VI.2)). However, it should be emphasized that since the fluctuations of velocity and concentration are weaker at this location, the magnitude of the total turbulent flux is low and the relatively large contribution of the subgrid scales does not significantly affect the dispersion of the pollutant. Note that the dynamic treatment of *Sc_sgs* dispenses the input of any parameter to compute the SGS mass flux. Otherwise, *Sc_sgs* is a user input. It seems
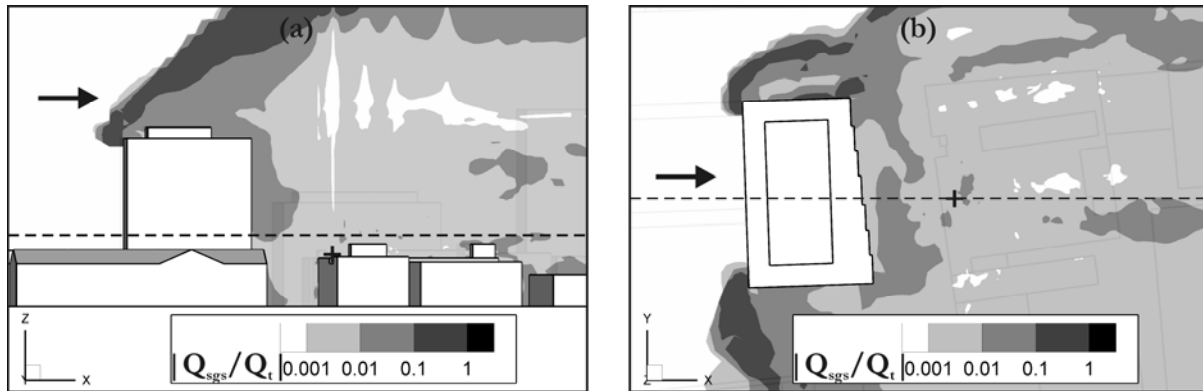
Figure VI.5. Case SW: relative contribution of the SGS mass flux to the total turbulent mass flux. Contours of $|Q_{sgs}/Q_t|$ in the planes (a) $y=y_{stack}$ and (b) $z/H=1.47$.

that no consensus exists in literature on the value to prescribe, considering the various values that can be found, e.g. 0.5 in [Tominaga and Stathopoulos, 2011], 0.6 in [Dejoan et al., 2010], 0.72 in [Cheng and Liu, 2011] or 0.9 in [Boppana et al., 2010].

The contours of non-dimensional convective mass flux in the streamwise direction ($Q_{c,x}/Q_0$) are depicted in Figures VI.6-a,b. In the plane $y=y_{stack}$ (Fig. VI.6-a), the blue zone corresponds to the mean backflow occurring in the wake of the Faubourg building. The negative values of mean velocity observed in this region are partly (together with the turbulence effects, see later) responsible for the backward transport of the pollutant and the resulting K-contours observed earlier. In the upper region (around the Faubourg building's roof level) and farther downstream, the mean streamwise velocity is positive and carries the pollutant gas downstream ($Q_{c,x}>0$). At first, the flow and dispersion patterns in the wake of the Faubourg building seem rather similar to the case of a pollutant source placed in the wake of a generic simple building [Huber et al., 1980; Yoshie et al., 2011]. However, the observation of the contours in the horizontal plane $z/H=1.47$ (Fig. VI.6-b) reveals that small irregularities in the Faubourg building shape are responsible for significantly different flow characteristics. Instead of being negative in the whole region behind the building (i.e. what would happen for a rectangular-shaped building with wind flow perpendicular to the facade), the convective mass flux is positive in the zone colored in red for $y>y_{stack}$, and a totally different plume shape could be expected if the source was located in this region. The asymmetry of the wake can also be observed in the contours of $Q_{c,y}/Q_0$ (Fig. VI.6-d); the stack is located in a region of negative convective flux in the lateral direction, which partly explains the slight deviation towards the negative y-direction at the level of the stack as observed in Figure VI.4-c. The relatively high vertical velocity at the exhaust can be observed in Figure VI.6-c: the vertical convective flux is intense and reaches high values up to the roof of the Faubourg building. Farther downstream, reattachment of the flow occurs, leading on average to negative mean vertical velocity and $Q_{c,z}<0$.

The contours of the turbulent mass flux components normalized by Q_0 are depicted in Figure VI.7. In the streamwise direction (Figs. VI.7-a,b), the sign of the flux is
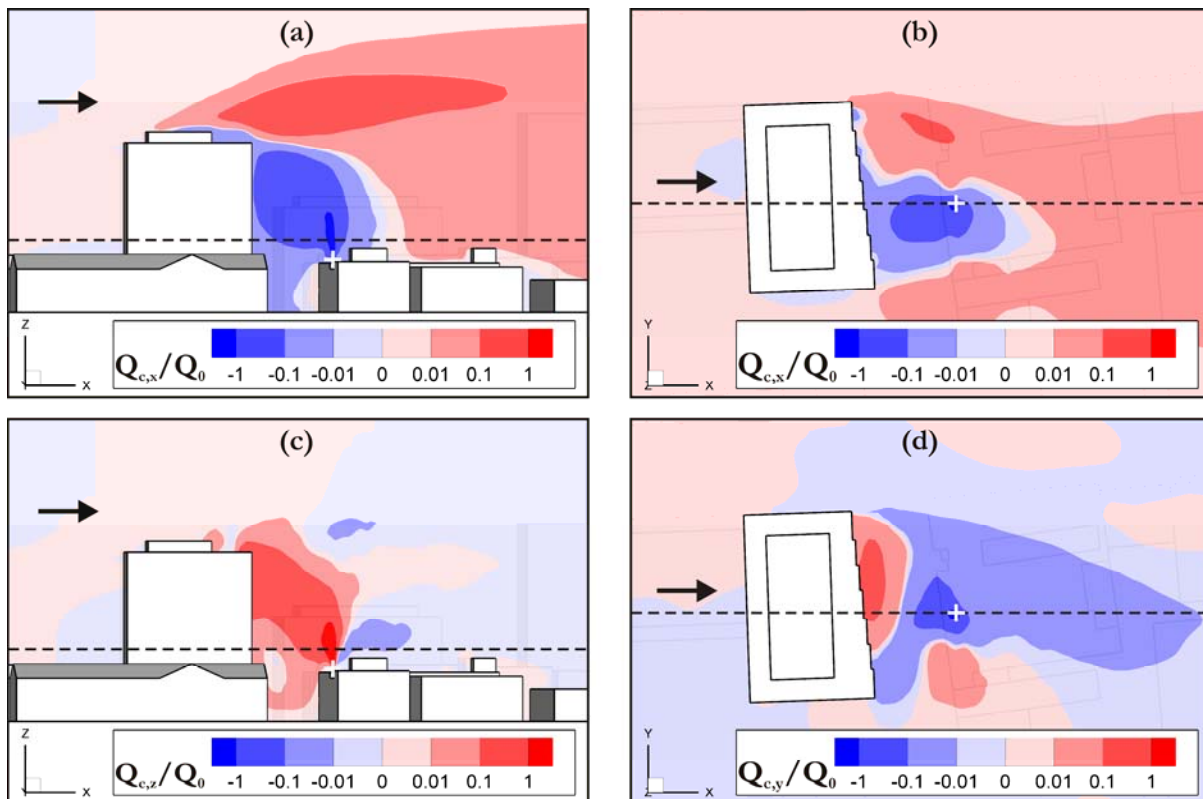
Figure VI.6. Case SW: contours of the (a,b) streamwise, (c) vertical and (d) lateral components of the non-dimensional convective mass flux in the planes (a,c) $y=y_{stack}$ and (b,d) $z/H=1.47$.
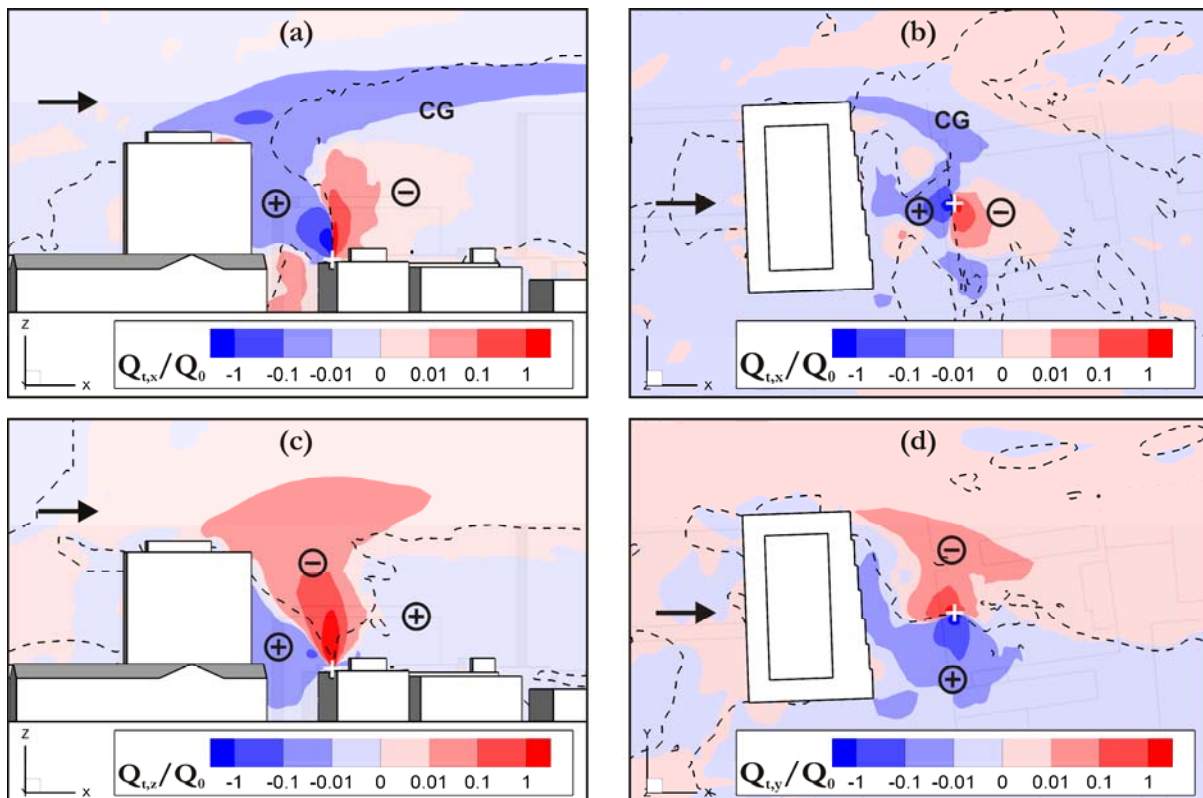
Figure VI.7. Case SW: contours of the (a,b) streamwise, (c) vertical and (d) lateral components of the non-dimensional turbulent mass flux in the planes (a,c) $y=y_{stack}$ and (b,d) $z/H=1.47$. The dashed lines represent the isolines $\partial C/\partial x_i=0$ in the corresponding direction: (a,b) $x_i=x$, (c) $x_i=z$, (d) $x_i=y$. On each side of the isoline, the sign of $\partial C/\partial x_i$ is indicated in circles (+: positive; -: negative).

opposite to that of $\partial C/\partial x$ in the vicinity of the stack, with blue (resp. red) zones corresponding to "+" (resp. "-") sign. Hence, the gradient-diffusion (GD) hypothesis generally used with RANS models is verified in this zone. As stated earlier, it is shown here that the deviation of the plume towards the leeward facade of the Faubourg building is not only due to the mean flow but also to the turbulent fluctuations. At the Faubourg building's roof level, $Q_{t,x}$ is opposite to $Q_{c,x}$ and is relatively less intense (Fig. VI.7-a). This large region colored in blue and light blue is partly characterized by a decrease of mean concentration in the zone marked "CG" in the figure: here the turbulent mass transport obeys a counter-gradient mechanism, presumably due to the vortical structures generated at the front corner of the Faubourg building that are transported downstream in this area [Gousseau et al., 2012]. However, due to the location of the pollutant source in this case, this phenomenon does not play a major role on dispersion, contrary to the case where the emitting building would directly face the ABL flow without upstream obstruction [Gousseau et al., 2011b]. Another CG zone of turbulent mass transport is identified in the horizontal plane z/H=1.47 (Fig. VI.7-b): the blue zone starting from the northern corner of the Faubourg building where $Q_{c,x}$ and $\partial C/\partial x$ are both negative. As described in Chapter IV [Gousseau et al., 2012] for a cubical building, vortical structures are present in the shear layers developing on the sides of the building and are responsible for this mechanism of turbulent mass transport. In the vertical and lateral directions (Figs. VI.7-c,d), the GD hypothesis is generally verified: $Q_{t,z}$ and $Q_{t,y}$ are directed from the high to low levels of mean concentration. In these directions, the convective and turbulent mass transport mechanisms act with similar intensity.

VI.4   Results: West wind direction (case W)

VI.4.1 Mean concentration field

The isosurface K=1 and the contours of K in the planes $y=y_{stack}$ and z/H=1.47 for case W are shown in Figures VI.8. Note that the figures are flipped compared to case SW to allow visualizing the plume: the wind direction is from right to left. The buildings that can be seen upstream of the BE building in Figures VI.8-b,c are relatively far from it, outside of the plane $y=y_{stack}$ (see also Fig. VI.2) and do not significantly disturb the plume trajectory. As a consequence, the pollutant gas is mainly transported downstream by the wind flow. In Figure VI.8-c, it can be seen that the plume centerline is not aligned with the flow direction. The plume is subjected to a deviation towards the positive y-direction which was not observed in the wind-tunnel experiment and was therefore interpreted as the main reason for the relatively large discrepancies observed for this case between numerical and experimental values of concentration on the roof of the emitting building (see Chapter V).
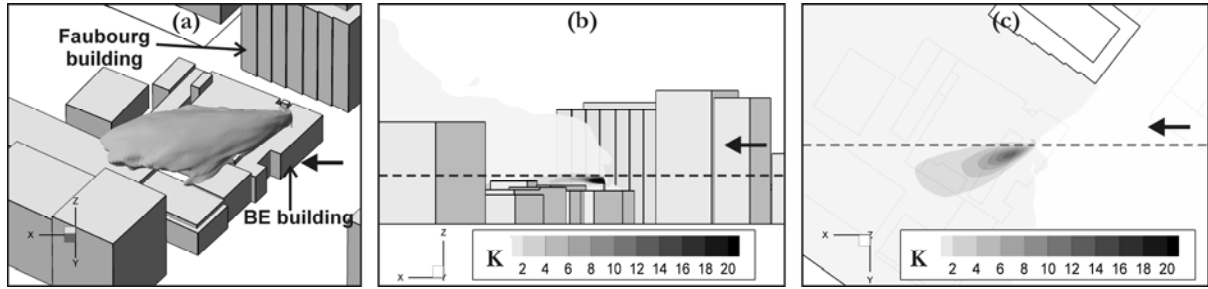
Figure VI.8. Case W: (a) isosurface $K=1$ and (b,c) contours of non-dimensional concentration coefficient K in the planes (b) $y=y_{stack}$ and (c) $z/H=1.47$. The wind direction is indicated by the arrows. The dashed line in (b) indicates the position of the plane shown in (c), and vice versa.

VI.4.2 Mass fluxes

The contribution of the unresolved scales to the total turbulent mass flux in the area of interest is also minor in this case. In the two planes shown in Figure VI.9, the SGS mass flux is about two orders of magnitude smaller in magnitude than the total turbulent mass flux. Higher contributions are observed around the Faubourg building without large impact on the plume dispersion.

Contrary to case SW, the pollutant source in case W is not located in the immediate vicinity of high-rise buildings and the plume is consequently less disturbed, as already shown in the previous section. No backflow is observed at the stack location and the streamwise component of the convective mass flux is therefore positive in this region (Figs. VI.10-a,b). Note that a small region downstream of the Faubourg building is characterized by $Q_{c,x}<0$ (see Fig. VI.10-b) but the magnitude of the associated flux is low because only little pollutant reaches this zone. The vertical velocity is negative in the plane $y=y_{stack}$ (except around the stack exhaust), leading to $Q_{c,z}<0$ (Fig. VI.10-c). This is due to the downflow created by the very high-rise buildings present in the upstream region of the domain (see Fig. VI.2). As far as the lateral component of the convective flux is concerned, Figure VI.10-d shows that it is positive at the stack, which creates the plume deviation observed in the mean concentration contours. The positive V-values at this location are due to the presence of the Faubourg building which causes a change in the direction of the incoming wind flow. It should be noticed that the sign of $Q_{c,y}$ becomes opposite very close to the stack. Therefore, a small change in the stack location towards the zone colored in blue in Figure VI.10-d would cause a very different plume behavior. This constitutes a possible explanation for the poor agreement between the K-values computed by LES and those measured in the wind tunnel, and it underlines the necessity of creating a numerical model with exactly the same geometry as the wind tunnel model. This holds especially for complex configurations in which flow and dispersion are difficult to foresee qualitatively. Here, the CFD model was built based on the geometries of the wind-tunnel model and of the full-scale configuration, and
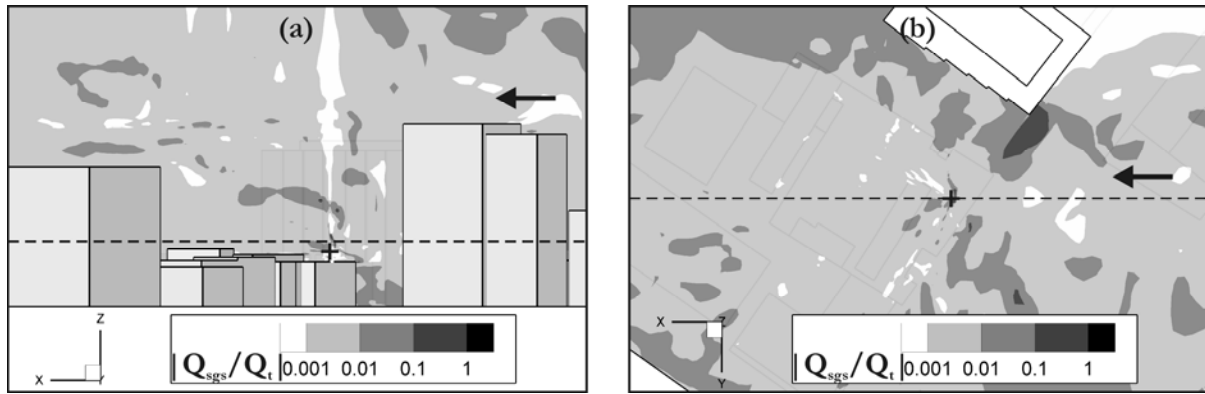
Figure VI.9. Case W: relative contribution of the SGS mass flux to the total turbulent mass flux. Contours of $|Q_{sgs}/Q_t|$ in the planes (a) $y=y_{stack}$ and (b) $z/H=1.47$.

consequently the experimental and numerical models might show some slight geometrical differences.

In Figure VI.11-a, the contours of the streamwise turbulent mass flux in the plane $y=y_{stack}$ are shown. It appears that while the mean concentration is decreasing from the stack exhaust towards the positive x-direction, the streamwise component of the turbulent mass flux is negative. Turbulent mass transport is therefore following a CG mechanism in this direction and at this location, marked "CG" in the figure. However, when observing the field of $Q_{t,x}/Q_0$ in the plane $z/H=1.47$ (Fig. VI.11-b), one can see that the link between the signs of the x-components of the turbulent mass flux and mean concentration gradient is not evident: $Q_{t,x}$ is changing sign along the plume centerline, from negative around the stack to positive farther downstream. Note that this change of sign is occurring at the level of the large structure present on the roof of the BE building. In [Gousseau et al., 2012], the role of the vortical structures on the process of turbulent mass transport was shown. Here, the turbulent eddies generated by the rooftop structure interact with those emanating from the front corner of the emitting building and possibly affect in this way turbulent mass transport in the streamwise direction, resulting in the contours of $Q_{t,x}$ observed. Another important difference with the case of isolated buildings studied in the aforementioned reference is the orientation of the emitting building with respect to the incoming flow direction. It is known indeed that the structure of the flow around bluff bodies is strongly dependent on this parameter [Castro and Robins, 1977]. Further research on the influence of wind direction and of rooftop structures on the turbulent dispersion mechanism is needed to clarify this point. In the vertical direction (Fig. VI.11-c), $Q_{t,z}>0$ in the region where $\partial C/\partial z<0$, and vice versa: the GD hypothesis of turbulent mass transport is verified. The same conclusion holds for the lateral direction, as shown in Figure VI.11-d.
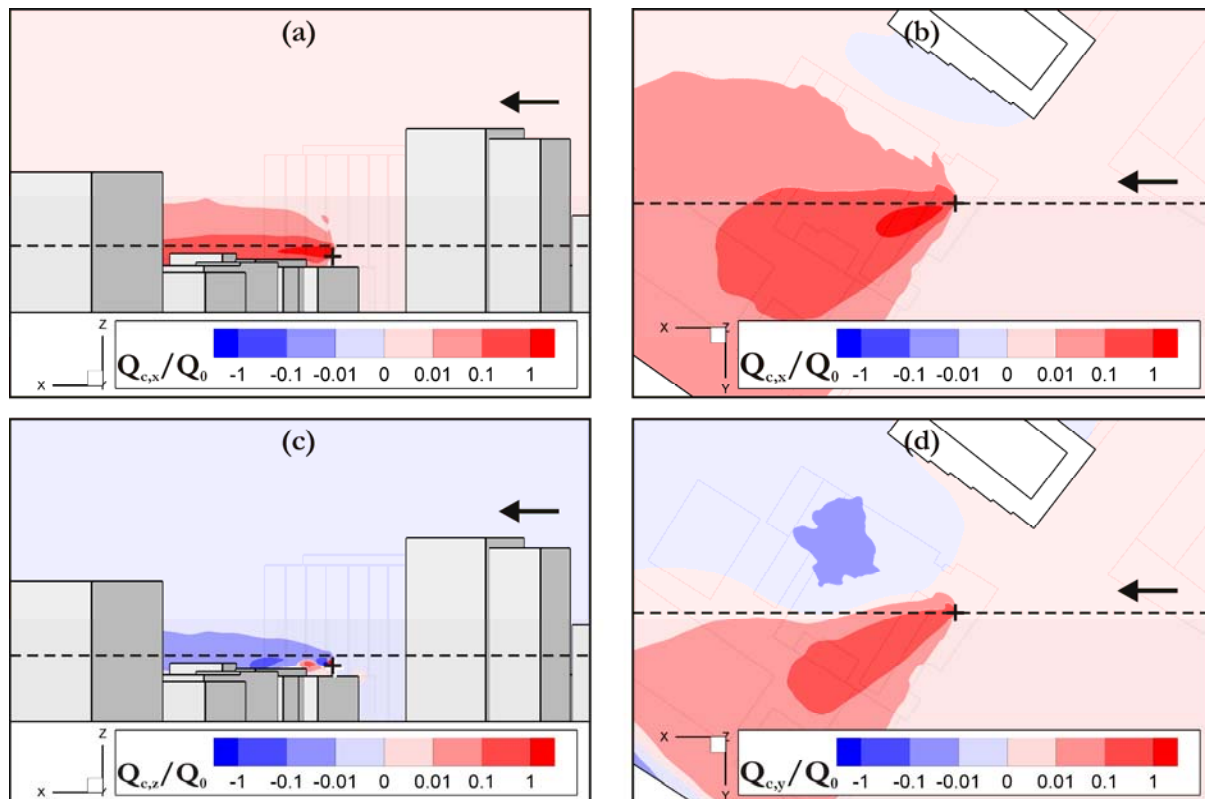
Figure VI.10. Case W: contours of the (a,b) streamwise, (c) vertical and (d) lateral components of the non-dimensional convective mass flux in the planes (a,c) $y=y_{stack}$ and (b,d) $z/H=1.47$.
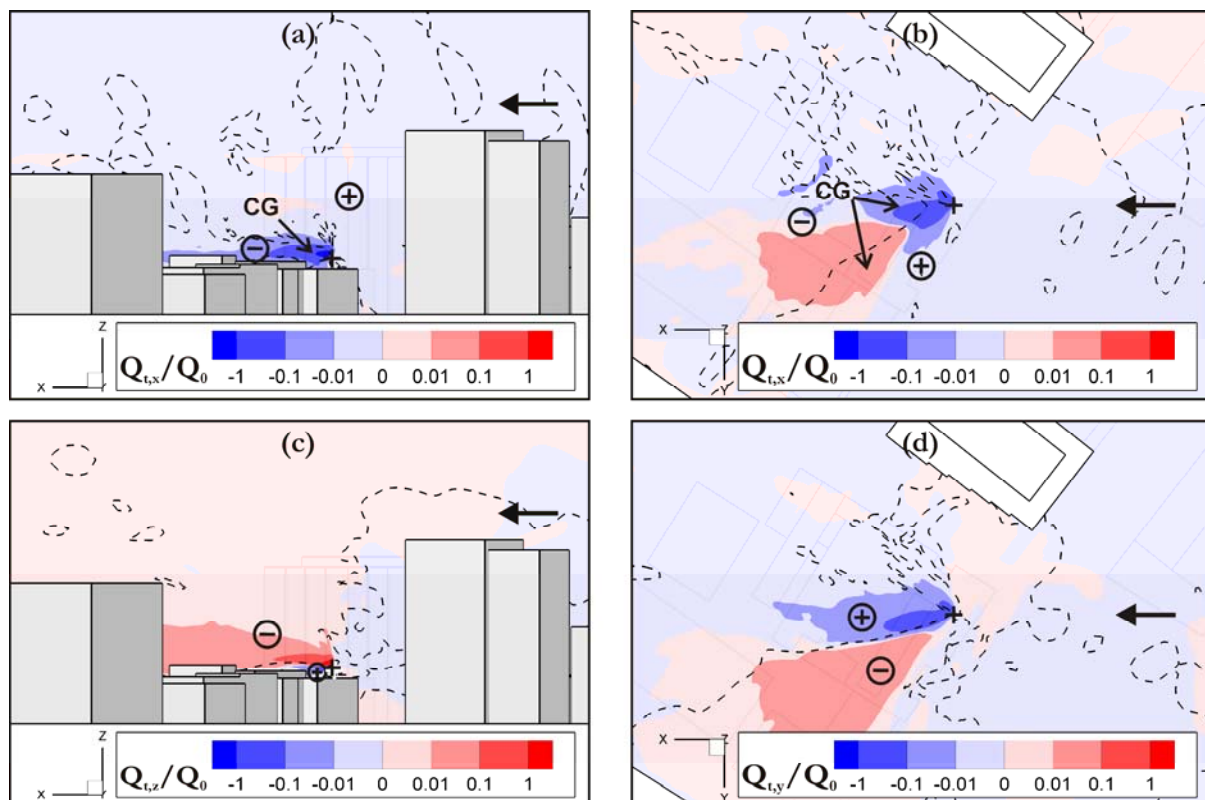
Figure VI.11. Case W: contours of the (a,b) streamwise, (c) vertical and (d) lateral components of the non-dimensional turbulent mass flux in the planes (a,c) $y=y_{stack}$ and (b,d) $z/H=1.47$. The dashed lines represent the isolines $\partial C/\partial x_i=0$ in the corresponding direction: (a,b) $x_i=x$, (c) $x_i=z$, (d) $x_i=y$. On each side of the isoline, the sign of $\partial C/\partial x_i$ is indicated in circles (+: positive; -: negative).

VI.5 Discussion

For case SW, the pollutant source is located in the wake recirculation zone of the high-rise Faubourg building. This wake has a particular asymmetric shape, different from the one downstream of a simple rectangular building because of the irregular shape of the Faubourg building. The plume is deviated towards the leeward facade of the Faubourg building, not only due to the mean backflow, but also because of the turbulent fluctuations. Nevertheless, convection appears to be the dominant mechanism of mass transport in the streamwise direction, emphasizing the need for accurate prediction of the mean flowfield by the CFD model. The use of LES is therefore recommended for this kind of study, taking into account its superior accuracy in comparison with RANS for the simulation of wind flow around bluff bodies.

The analysis of flow and dispersion around an isolated cubical building performed in Chapter IV has shown the crucial role played by the vortical structures in the turbulent dispersion process. These structures are responsible for the counter-gradient mechanism of turbulent dispersion occurring in the streamwise direction. This CG mechanism is not observed around the source for case SW, because of the absence of large-scale vortical structures at this location, in the wake of the Faubourg building. However, in the shear layers developing from the roof and sides of the Faubourg building, regions with a CG mechanism, i.e. where the turbulent mass flux is directed from the low to high levels of mean concentration, are present. Like in the case of dispersion around an isolated building, this is attributed to the vortices generated at the windward edges of the Faubourg building. In the lateral and vertical directions, convective and turbulent mass fluxes are of similar intensity and the turbulent mass flux is directed from the high to low levels of mean concentration, acting like a diffusion process.

For case W, the influence of the surrounding buildings on the dispersion process is less pronounced, as can be seen in the plume shape and mean concentration contours. However, the vertical convective flux is negative, suggesting a significant influence of the high-rise upstream buildings on the local flow pattern around the BE building, even though they are located relatively far away from the BE building. The stack lies in a critical zone of the flowfield where the lateral component of velocity – and of convective mass flux – is changing sign within a short distance. Thus, a small change in the stack location would result in a very different plume behavior, which constitutes a possible explanation for the discrepancy observed in a previous study [Gousseau et al., 2011a] between computed and measured concentration values on the roof of the BE building. The CG mechanism of turbulent mass transport in the streamwise direction can be observed but only in a limited region around the source, which contrasts with the case of dispersion around an isolated building. The location where $Q_{t,x}$ is changing sign coincides with the position of a rooftop structure on the emitting building, which suggests that these structures affect turbulent dispersion and should not be neglected in the CFD model. Similarly, the orientation of the building with respect to the incoming wind flow

direction affects the turbulent flow patterns and constitutes a possible explanation to the complexity of the turbulent mass flux field in this case. In the vertical and lateral directions, turbulent mass transport acts as a diffusion mechanism – like for case SW, with the turbulent mass flux directed from the high to low levels of mean concentration.

These conclusions show the strong anisotropy of turbulent mass transport and the variability of its properties within the flow domain. If LES is applied to derive the turbulent diffusivity D_t to be used with the gradient diffusion hypothesis, a diffusivity vector with space-dependent components will be obtained. Note that a least-square approach can subsequently be applied to derive the turbulent Schmidt number [Tominaga and Stathopoulos, 2012], which will also be a function of the spatial coordinates.

For the two wind directions under study, the magnitude of the SGS mass flux appears to be at least two orders of magnitude smaller than the one of the total turbulent mass flux in the region of interest, i.e. the region with high pollutant concentrations above the emitting building. This is an indication of appropriate grid resolution in this region. Larger contributions (>10%) of the scales smaller than the grid size are observed around the surrounding buildings due to an increase of the cell size and a decrease of the velocity and concentration fluctuations at these locations. However, this is sufficiently far from the source to have a small effect on the plume dispersion. It should be noted that by analogy with RANS modeling of the turbulent mass flux, the SGS mass flux with LES is assumed proportional and opposite to the gradient of resolved concentration. Considering the low contribution of the SGS mass flux, the SGS Schmidt number can be expected to have low influence on dispersion. However, this assumption needs confirmation and further research on and the appropriate value for this parameter is needed. In the present study, it was computed with a dynamic procedure [Moin et al., 1991; Porté-Agel, 2004]. Other SGS models – for both momentum and mass fluxes – should also be tested in future studies.

VI.6 Conclusion

Large-Eddy Simulation of micro-scale pollutant dispersion in the actual urban environment of part of downtown Montreal has been performed. The case under study involves a stack on the roof of a low-rise building in downtown Montreal, for two different wind directions (South-West and West). The focus has been on the convective and turbulent (including subgrid-scale) mass fluxes computed by LES. The latter allows evaluating the gradient-diffusion (GD) hypothesis generally used with the steady RANS turbulence modeling approach for turbulent mass transport. Also, an attempt has been made to link the results obtained here to those of earlier studies of dispersion around isolated buildings, in order to assess the relevance of generic studies for more complex practical applications.

Because of the particular geometry of the building group, the wind flow and dispersion patterns in the modeled part of downtown Montreal are complex and difficult to predict, even qualitatively. In this sense, the present results have shown differences when compared to the simpler case of dispersion around an isolated building. For example the structure of the wake of the irregular-shaped Faubourg building for case SW was significantly different from the one of a rectangular building.

However, also some important similarities with the case of the isolated building were found, such as the occurrence of the CG mechanism of streamwise turbulent mass transport for both wind directions. When using RANS, the turbulent mass flux model should therefore be able to reproduce this mechanism – contrary to the GD hypothesis. Another example is the relative importance of the turbulent and convective mass transport: in the same way as dispersion around an isolated building, convection is dominant in the streamwise direction whereas the two flux types act with similar intensity in the two other directions for both cases SW and W. The physical insight gained in the study of generic cases is also precious when analyzing the results of more complex and applied cases. It has for example been possible to explain the absence of the CG mechanism of the streamwise turbulent mass transport around the source for the case SW, based on the conclusions of an earlier study of dispersion around an isolated building. Furthermore, simple generic cases can generally be simulated on computational grids containing a reasonable number of cells. Hence, the simulations are more economical to run and can be used to test the accuracy of the numerical model which can subsequently be applied to more complex applied cases. In this way, the present study supports the relevance of the investigation of environmental processes on generic, simplified cases.

Reciprocally, it appeared in this study that applied cases are useful to give indications on which parameters are relevant to be tested on simplified cases. For example, the influence of the rooftop structures and of the orientation of the emitting building was indicated by the analysis of dispersion under westerly wind direction. Further research should therefore focus on – among others – the influence of these parameters on micro-scale pollutant dispersion around buildings.

Chapter VII
Conclusion

VII.1 Summary of the results

The results presented in this report are summarized by chapter:

Chapter II

The validation and verification (V&V) procedure was applied to the LES computation of wind flow around an isolated building. Among the SGS models tested, the Smagorinsky model with C_s=0.1 and the dynamic version – the one used in the following chapters – provided the most accurate results. The vortex method was shown to be suitable to generate inflow turbulence in the case of ABL flow. Good agreement was found between the numerical and experimental results for the mean velocity, on the two grid resolutions tested (20 and 30 cells/building side). The SGMV technique showed that numerical and modeling errors were higher in magnitude on the coarse grid but compensated each other, leading to a similar level of total error as on the fine grid. More turbulent kinetic energy was resolved on the fine grid compared to the coarse one (91% vs. 80% around the building) but, unexpectedly, resolving more turbulent kinetic energy led to the overestimation of the experimental results. In addition, the same case was simulated with three different RANS models in Appendix A, demonstrating the superior accuracy of LES with respect to RANS for the simulation of the wind flow around buildings.

Chapter III

The RANS (with four different turbulence models) and LES turbulence modeling approaches were applied to two cases of pollutant dispersion around isolated buildings. CFD validation was performed by comparing the numerical results with mean concentration measurements from reference wind-tunnel experiments. The dispersion process was decomposed into the (mean) convective effects on the one hand and the turbulence effects on the other hand, to facilitate the model evaluation. With RANS, the convective mass fluxes were predicted incorrectly when the source of pollutant was located close to flow detachment regions around the building. Moreover, the turbulent mass fluxes needed correct parameterization (via the turbulent Schmidt number) to ensure the accurate prediction of the mean concentration field. With LES, the convective fluxes showed that the recirculation zones around the building were reproduced. The

turbulent mass flux field was characterized in both cases by a counter-gradient mechanism of turbulent mass transport in the streamwise direction, with the mass flux directed from the low to high levels of mean concentration.

Chapter IV

One of the cases studied in the previous chapter (dispersion from a rooftop vent on a cubical building) was further investigated in an attempt to explain the counter-gradient mechanism of streamwise turbulent mass transport. A detailed multi-variate statistical analysis was performed for this purpose: the time-history of velocity and concentration was observed at three monitoring points in the near wake of the building. Large-scale vortical structures were identified in the shear layer developing from the front corner of the building, acting on the frequency distribution of both velocity and concentration fluctuations. It resulted in the simultaneity of the fluctuation events for these variables; for example the fluctuations of streamwise velocity and concentration were most of the time of opposite sign, leading to a negative covariance, i.e. a negative streamwise component of mass flux corresponding to the CG mechanism. A visualization of these events was proposed in Appendix B, illustrating the crucial role played by the vortical structures in the transport of pollutant.

Chapter V

Contrary to the first three chapters focusing on simplified configurations, pollutant dispersion in an actual urban environment with multiple buildings (part of downtown Montreal) was simulated in this chapter, with the RANS standard k-ε model and LES with the dynamic Smagorinsky SGS model. Two wind directions with different features were studied. A grid-sensitivity analysis was performed, showing the high dependence of the numerical results on the grid resolution – especially with LES. CFD validation was made by comparing the mean concentration values on the roof of the emitting building with wind-tunnel measurements. Better results were obtained with LES, although for the west wind direction the discrepancies remained high (average relative error CFD/experiment equal to 67% with LES compared to 80% with k-ε). With RANS, it was confirmed that the results are sensitive to the Sc_t parameter. The best value for each case is the one that compensates for the deficiencies of the model in terms of turbulent viscosity prediction. Here, it was different for the two wind directions under study: 0.7 for the south-west and 0.3 for the west wind direction. No parameter input was needed with LES and the dynamic computation of the SGS mass flux, which is considered – together with the time resolution of the variables – as one of the main advantages of this approach.

Chapter VI

Following the same approach as in Chapter III, the convective and turbulent mass fluxes were computed with LES for the case of dispersion in downtown Montreal under the two wind directions considered earlier. First, with the present dispersion modeling the SGS contribution to turbulent mass transport was shown to be minor in the region of interest around the emitting building: the SGS mass flux was two to four orders of magnitude smaller than the total turbulent flux. The observation of the convective and turbulent mass fluxes allowed explaining the pollutant plume shape. Similarities were found with the generic case of dispersion around an isolated building, for example the occurrence of the CG mechanism of mass transport in the streamwise direction at certain locations of the flow field. However, due to the particular geometry, the dispersion process was clearly more complex for this applied case. It was influenced by the orientation of the emitting building with respect to the incoming ABL flow and by the presence of rooftop structures on its roof, suggesting future research tracks for dispersion studies on generic configurations.

VII.2 Conclusions

Pollutants emitted in the built environment are transported by the wind flowing around the buildings. The resulting turbulent flow patterns are complex and highly unsteady, which renders the CFD simulation of urban pollutant dispersion very challenging. This is particularly true when multiple buildings with irregular shapes and locations are considered. The study of flow and dispersion around simplified configurations representative of the built environment (e.g. isolated simple-shaped buildings) facilitates the understanding of the physical mechanisms involved. The validation of numerical models is also advised on these generic configurations because of the lower computational requirements and the easier reproducibility in comparison with actual urban areas.

Wind-induced pollutant dispersion around buildings can be decomposed into the effects of the mean flow and those of the turbulent fluctuations. Mathematically, this is done by applying the Reynolds-average operator to the dispersion equation. Both components play an important role in the transport of mass and have to be treated with equal care. This decomposition has been shown to be efficient in evaluating the physical models used in the CFD simulation – in particular the models for turbulence and dispersion – and to investigate the physical mechanism of dispersion. For a cubical building with the windward facade perpendicular to the approach flow and with a pollutant source located on its roof, the vortical structures in the shear layers developing from the front corners of the building carry pollutant gas in their core and cause the meandering motion of the plume. They contribute in this way to the high variance of concentration that occurs in the vicinity of the building. Since it is governed by unsteady

events, turbulent mass transport can hardly be linked to mean variables and modeling is challenging for steady turbulence models.

In comparison with the experimental approach, CFD presents many advantages to undertake wind-induced pollutant dispersion problems. However, since high-accuracy numerical solutions (e.g. with DNS) are so far not available for a large majority of wind engineering problems, the accuracy of a given CFD simulation is usually understood as the agreement with experimental data and therefore these two approaches are inseparable. The CFD simulations presented in this thesis have been validated in this way: by comparing their results with wind-tunnel measurements. This allowed identifying several crucial issues that have to be treated with care in order to guarantee the accuracy of a given CFD simulation of wind-induced pollutant dispersion.

One of them is the precise knowledge and correct implementation of the boundary conditions to be applied at the boundaries of the computational domain. Among them, the ABL profiles at the inlet of the domain as well as the accurate geometrical representation of the urban area under study are particularly important as they significantly affect the computed flow and concentration fields.

For each case encountered in this thesis, several computational grids have been tested to ensure sufficient spatial resolution. Although the generation of each grid has not been described in detail, it should be emphasized that this process can be challenging and time-consuming, in particular for applied studies of dispersion in actual urban areas. Up to several weeks of work can indeed be needed to generate computational grids with a complex arrangement of buildings. The reason is the large range of spatial scales that is encountered in typical urban dispersion studies, for example in the case of Montreal from a few centimeters around the source (full-scale dimensions) up to several meters at the external boundaries of the domain. Note that the numerical schemes to discretize the flow equations also affect the results; those presented in the description of each simulation have been chosen based on considerations on accuracy, stability and rapidity.

Last but not least, the accuracy of CFD applied to the simulation of pollutant dispersion depends strongly on the choice of the physical models used to model turbulence and dispersion. The two main approaches used in wind engineering to model turbulence, namely RANS and LES, have been compared for the wind flow and dispersion around isolated buildings (Chapter II & Appendix A; Chapter III) and in an actual urban environment (Chapter V). Regarding the results, the use of LES is advised for the simulation of pollutant dispersion in the built environment. This turbulence modeling approach has indeed the advantage to provide time-dependent information about the concentration field. It also simulates the flow field around buildings in a more accurate way compared to RANS – without needing significantly higher grid resolution, as sometimes stated. Modeling of the turbulent mass flux is also limited to the smallest scales of motion which have been shown to constitute a non-significant contribution to total turbulent mass transport when the grid is fine enough.

By contrast, with RANS the whole spectrum of the turbulent mass flux is modeled. The mechanism is often assumed to be diffusive, with the mass flux directed from the high to low levels of mean concentration. LES – in this case used as a research tool to evaluate less sophisticated models – has showed that it was not always the case: the counter-gradient mechanism of streamwise turbulent mass transport was identified and explained for dispersion around isolated buildings and encountered later in the applied case of dispersion in downtown Montreal. Furthermore, the degree of freedom let by the prescription of the turbulent Schmidt number value with RANS is high. On the one hand the influence of this parameter on the computed concentration field is high. For example in the Montreal study, the mean concentration value at a point on the emitting building's roof could vary by a factor of 3 between Sc_t=0.3 and 0.7. On the other hand, the optimum value of this parameter is not fixed because it is the one that compensates for the inaccuracies of the turbulence model in terms of turbulent viscosity computation for a particular case. As far as the pollutant transport by the mean flow is concerned, the investigation on the isolated building showed that the RANS modeling approach fails in simulating accurately the flow detachment regions. This will have minor consequences if the pollutant source is located outside of the zone of influence of the building but the accuracy on the concentration prediction will deteriorate in the other cases. Significant differences in terms of flow field prediction were also found between RANS and LES for multiple buildings in a real city, although no validation was shown for this case.

The use of RANS to simulate wind-induced pollutant dispersion in cities can sometimes be justified by the limited computational resources available and/or the need for only the average variables as an output of the simulation. In this case, one must be aware of the deficiencies of the particular turbulence model used in terms of flow-field prediction and make sure that they will not affect the dispersion from the pollutant source in a significant way.

VII.3 Suggestions for future work

The problem of numerical modeling of wind-induced pollutant dispersion offers a multitude of tracks for further research efforts. The scope of the present study can be extended by dropping the assumptions as they were stated in the introduction.

In particular, while the study of the wind flow and dispersion for generic configurations has been chosen to focus on the isolated building case, the method and procedure used in Chapter II to Chapter IV to assess the quality of LES, to evaluate various turbulence models applied to pollutant dispersion and to analyze the physical mechanism of dispersion can be applied to other generic configurations such as the street canyon or the array of buildings.

The numerical simulation of flow and dispersion in the presence of trees and moving vehicles is known to be a challenging task and the effect of these elements on

pollutant dispersion is not fully understood. Further research on these topics is needed to be able to include them in the simulation of dispersion in actual urban environments, with a computational model as close as possible to reality. These efforts should focus on the LES technique, considering the conclusions drawn from the present work, and be initiated by the study of generic configurations (e.g. simplified alley of trees, isolated street with moving vehicles, etc.). As far as dispersion is concerned, chemical reactions and deposition should be included in the numerical model to ensure close agreement between the virtual- and real-world situations.

Some assumptions have also been made in this thesis concerning the features of the generic buildings under study: only sharp-edged buildings with the windward facade perpendicular to the approaching flow direction have been considered. A different orientation of the building with respect to the incoming flow will affect the vortical structures generated at the roof and, following, the dispersion process. This constitutes an interesting case to investigate. Furthermore, buildings of original shape with rounded edges are not rare in modern cities and the study of the flow and dispersion around buildings with this feature would constitute an important step towards simulations that can represent any kind of urban areas. Note that such a study would have to deal with the simulation of boundary layer separation along curved surfaces, a phenomenon known to depend strongly on the surface roughness and the Reynolds number, and challenging to reproduce with CFD. Finally, the last chapter of the thesis has suggested the influence of building elements such as rooftop structures on pollutant dispersion. This certainly holds for other types of building structural elements like for example balconies. These elements should be studied in more detail to assess the level of detail needed to represent the buildings in a model urban area. Note that all the aforementioned suggestions concerning the study of the influence of the building characteristics on flow and dispersion would require new campaigns of wind-tunnel experiments to allow for CFD validation.

In the author's opinion, the present work demonstrates that LES is the most suitable turbulence modeling approach to simulate pollutant dispersion around buildings. As a consequence, future research efforts should naturally focus on this technique. This perspective is supported by the general increase of computational power available, which allows undertaking LES computations on large computational grids. To apply LES trustfully to wind-induced pollutant dispersion problems, the validation and verification study initiated in Chapter II could be extended to other urban configurations. Different techniques to evaluate the various types of error biasing the numerical solution could be considered, in particular the use of DNS of low-Reynolds number flows around bluff bodies. The study of the Montreal configuration presented in the last two chapters of this thesis has shown the complexity of flow and dispersion in such a complex urban environment. The validation of the CFD simulations was performed by comparing surface concentration values on the roof of the emitting building to wind-tunnel measurements, with sometimes limited agreement. A more rigorous validation would require experimental data on both the concentration and velocity fields, with

measurement points distributed in the whole flow domain, not only on the building surfaces. To the author's knowledge, such a validation experiment is not available to date, but would certainly constitute a precious dataset for CFD validation. Concerning LES, the validation of the velocity and concentration statistics would also be needed, including spectral information. The quantification of the agreement between CFD and measurements in this case would require metrics adapted to time-dependent data sets.

As explained earlier, the performance of the RANS turbulence modeling approach applied to dispersion problems is not only limited by the accuracy of this class of models in terms of flow-field prediction, but also by the difficulty to model turbulent mass transport based on average values. While the former aspect seems to be inherent to the RANS approach and no significant improvement can be expected on this side, enhanced models for turbulent mass transport could ameliorate the accuracy of the computed turbulent mass flux and should be investigated. Note that these models are more complex than the gradient-diffusion hypothesis and sometimes require higher-order statistics which are not directly provided by two-equation RANS models.

The inclusion of the temperature stratification in the ABL flow is to date an ongoing research work by the author. Note that experimental data for the case of dispersion under stratified conditions are rare, which limits the options for validation of the numerical models. Another ongoing project is the evaluation of the different turbulent inflow generation techniques for the LES of the ABL, as exposed in the thesis introduction. They are currently being implemented in OpenFOAM, an open-source CFD code, in combination with rough-wall models, to be evaluated and compared.

Finally, the coupling of micro- and meso-scale models should be mentioned here as a future research trend. With the latter class of models (usually used for weather forecasting applications), spatial scales up to several hundred kilometers are simulated and the output is used after down-scaling as a boundary condition for the CFD micro-scale model, allowing to better take into account the variability of the boundary conditions.

Bibliography

http://www.harmo.org/, 2012. Initiative on "Harmonisation within Atmospheric Dispersion Modelling for Regulatory Purposes".

http://glossary.eea.europa.eu/, 2012. Environmental terminology and discovery service (ETDS).

http://www.cerc.co.uk/environmental-software/ADMS-model.html, 2012. Cambridge Environmental Research Consultants - ADMS 4.

http://www.lanl.gov/projects/quic/, 2012. Los Alamos National Laboratory - QUIC dispersion modeling system.

Abe, K., Suga, K., 2001. Towards the development of a Reynolds-averaged algebraic turbulent scalar-flux model. International Journal of Heat and Fluid Flow 22, 19-29.

Abe, K., 2006. Performance of Reynolds-averaged turbulence and scalar-flux models in complex turbulence with flow impingement. Progress in Computational Fluid Dynamics 6, 79-88.

AIAA, 1998. Guide for the verification and validation of Computational Fluid Dynamics simulations. American Institute of Aeronautics and Astronautics, report AIAA-G-077-1998, Reston, VA, USA.

Alinot, C., Masson, C., 2005. k-ε model for the atmospheric boundary layer under various thermal stratifications. Journal of Solar Energy Engineering 127, 438-443.

Ansys Inc., 2009. Ansys Fluent 12.0 - Theory Guide. Ansys Inc., Lebanon, USA.

ASHRAE, 2007. Building air intake and exhaust design, in: ASHRAE applications handbook, Chapter 44, Atlanta, USA.

Baik, J.J., Park, S.B., Kim, J.J., 2009. Urban flow and dispersion simulation using a CFD model coupled to a mesoscale model. Journal of Applied Meteorology and Climatology 48, 1667-1681.

Balczó, M., Gromke, C., Ruck, B., 2009. Numerical modeling of flow and pollutant dispersion in street canyons with tree planting. Meteorologische Zeitschrift 18, 197-206.

Bäumer, D., Vogel, B., Fiedler, F., 2005. A new parameterisation of motorway-induced turbulence and its application in a numerical model. Atmospheric Environment 39, 5750-5759.

Bell, J.B., Colella, P., Glaz, H.M., 1989. A second-order projection method for the incompressible Navier-Stokes equations. Journal of Computational Physics 85, 257-283.

Blocken, B., Carmeliet, J., Stathopoulos, T., 2007a. CFD evaluation of wind speed conditions in passages between parallel buildings–effect of wall-function roughness modifications for the atmospheric boundary layer flow. Journal of Wind Engineering and Industrial Aerodynamics 95, 941-962.

Blocken, B., Stathopoulos, T., Carmeliet, J., 2007b. CFD simulation of the atmospheric boundary layer: wall function problems. Atmospheric Environment 41, 238-252.

Blocken, B., Sathopoulos, T., Saathoff, P., Wang, X., 2008. Numerical evaluation of pollutant dispersion in the built environment: Comparisons between models and experiments. Journal of Wind Engineering and Industrial Aerodynamics 96, 1817-1831.

Blocken, B., Janssen, W.D., van Hooff, T., 2012. CFD simulation for pedestrian wind comfort and wind safety in urban areas: General decision framework and case study for the Eindhoven University campus. Environmental Modelling & Software 30, 15-34.

Boppana, V., Xie, Z.T., Castro, I., 2010. Large-Eddy Simulation of dispersion from surface sources in arrays of obstacles. Boundary-Layer Meteorology 135, 433-454.

Brunekreef, B., Holgate, S.T., 2002. Air pollution and health. Lancet 360, 1233-1242.

Buccolieri, R., Sandberg, M., Sabatino, S.D., 2010. City breathability and its link to pollutant concentration distribution within urban-like geometries. Atmospheric Environment 44 (15), 1894-1903.

Camelli, F.E., Löhner, R., Hanna, S.R., 2005. Dispersion patterns in a heterogeneous urban area, in: Larreteguy A., Mecánica Computacional Vol. XXIV, 1339-1354, Buenos Aires, Argentina.

Casey, M., Wintergerste, T., 2000. Best Practice Guidelines. ERCOFTAC Special interest group on "Quality and trust in industrial CFD".

Castro, I.P., Robins, A.G., 1977. The flow around a surface-mounted cube in uniform and turbulent streams. Journal of Fluid Mechanics 79, 307-335.

Cebeci, T., Bradshaw, P., 1977. Momentum transfer in boundary layers. Hemisphere Publishing Corporation, New York, USA.

Celik, I., Cehreli, Z.N., Yavuz, I., 2005. Index of resolution quality for Large Eddy Simulation. Journal of Fluids Engineering 127, 949-958.

Celik, I., Klein, M., Freitag, M., Janicka, J., 2006. Assessment measures for URANS/DES/LES: an overview with applications. Journal of Turbulence 7, 1-27.

Celik, I., Klein, M., Janicka, J., 2009. Assessment measures for engineering LES applications. Journal of Fluids Engineering 131, 1-10.

Chan, C.K., Yao, X., 2008. Air pollution in mega cities in China. Atmospheric Environment 42, 1-42.

Chan, T.L., Dong, G., Leung, C.W., Cheung, C.S., Hung, T.W., 2002. Validation of a two-dimensional pollutant dispersion model in an isolated street canyon. Atmospheric Environment 36 (5), 861-872.

Chang, C.H., 2006. Computational fluid dynamics simulation of concentration distributions from a point source in the urban street canyons. Journal of Aerospace Engineering 19, 80-86.

Chavez, M., Hajra, B., Stathopoulos, T., Bahloul, A., 2011. Near-field pollutant dispersion in the built environment by CFD and wind tunnel simulations. Journal of Wind Engineering and Industrial Aerodynamics 99, 330-339.

Chen, F., 1990. Turbulent characteristics over a rough natural surface. Part I: Turbulent structures. Boundary-Layer Meteorology 52, 151-175.

Cheng, W.C., Liu, C.H., 2011. Large-Eddy Simulation of flow and pollutant transports in and above two-dimensional idealized street canyons. Boundary-Layer Meteorology 139, 411-437.

Coceal, O., Dobre, A., Thomas, T.G., Belcher, S.E., 2007a. Structure of turbulent flow over regular arrays of cubical roughness. Journal of Fluid Mechanics 589, 375-409.

Coceal, O., Dobre, A., Thomas, T.G., 2007b. Unsteady dynamics and organized structures from DNS over an idealized building canopy. International Journal of Climatology 27, 1943-1953.

Daly, B., Harlow, F., 1970. Transport equations in turbulence. Physics of Fluids 13, 2634-2649.

Dejoan, A., Santiago, J.L., Martilli, A., Martin, F., Pinelli, A., 2010. Comparison between large-eddy simulation and Reynolds-averaged Navier-Stokes computations for the MUST field experiment. Part II: Effects of incident wind angle deviation on the mean flow and plume dispersion. Boundary-Layer Meteorology 135, 133-150.

Endalew, A.M., Hertog, M., Delele, M.A., Baetens, K., et al., 2009. CFD modelling and wind tunnel validation of airflow through plant canopies using 3D canopy architecture. International Journal of Heat and Fluid Flow 30, 356-368.

European Environment Agency, 2011. Revealing the costs of air pollution from industrial facilities in Europe. European Environment Agency, report 15/2011, Copenhagen, Denmark.

Fackrell, J.E., Robins, A.G., 1982. Concentration fluctuations and fluxes in plumes from point sources in a turbulent boundary layer. Journal of Fluid Mechanics 117, 1-26.

Ferziger, J.H., Peric, M., 2002. Computational methods for fluid dynamics. Springer.

Fluent Inc., 2006. Fluent 6.3 User's Guide. Fluent Inc., Lebanon, USA.

Franke, J., Hellsten, A., Schlünzen, H., Carissimo, B., 2007. Best practice guideline for the CFD simulation of flows in the urban environment. COST Action 732.

Franke, J., 2010. A review of verification and validation in relation to CWE. The Fifth International Symposium on Computational Wind Engineering, Chapel Hill, NC, USA, May 23-27.

Franke, J., Hellsten, A., Schlünzen, H., Carissimo, B., 2011. The COST 732 best practice guideline for CFD simulation of flows in the urban environment - A summary. International Journal of Environment and Pollution 44, 419-427.

Freitag, M., Klein, M., 2006. An improved method to assess the quality of large eddy simulations in the context of implicit filtering. Journal of Turbulence 7, 1-11.

Gaskell, P.H., Lau, A.K.C., 1988. Curvature-compensated convective transport: SMART, A new boundedness- preserving transport algorithm. International Journal for Numerical Methods in Fluids 8, 617-641.

Germano, M., Piomelli, U., Moin, P., Cabot, W.H., 1991. A dynamic subgrid-scale eddy viscosity model. Physics of Fluids A 3, 1760-1765.

Geurts, B.J., Fröhlich, J., 2002. A framework for predicting accuracy limitations in large-eddy simulation. Physics of Fluids 14, 41-44.

Gibson, M.M., Launder, B.E., 1978. Ground effects on pressure fluctuations in the atmospheric boundary layer. Journal of Fluid Mechanics 86, 491-511.

Gorlé, C., van Beeck, J., Rambaud, P., Van Tendeloo, G., 2009. CFD modelling of small particle dispersion: The influence of the turbulence kinetic energy in the atmospheric boundary layer. Atmospheric Environment 43, 673-681.

Gorlé, C., 2010. Dispersion of fine and ultrafine particles in urban environment - Contributions towards an improved modeling methodology for Computational Fluid Dynamics. PhD thesis, Universiteit Antwerpen - von Karman Institute for Fluid Dynamics.

Gousseau, P., Blocken, B., Stathopoulos, T., van Heijst, G.J.F., 2011a. CFD simulation of near-field pollutant dispersion on a high-resolution grid: a case study by LES and RANS for a building group in downtown Montreal. Atmospheric Environment 45, 428-438.

Gousseau, P., Blocken, B., van Heijst, G.J.F., 2011b. CFD simulation of pollutant dispersion around isolated buildings: On the role of convective and turbulent mass fluxes in the prediction accuracy. Journal of Hazardous Materials 194, 422-434.

Gousseau, P., Blocken, B., van Heijst, G.J.F., 2012. Large-Eddy Simulation of pollutant dispersion around a cubical building: Analysis of the turbulent mass transport mechanism by unsteady concentration and velocity statistics. Environmental Pollution 167, 47-57.

Gromke, C., Buccolieri, R., Sabatino, S.D., Ruck, B., 2008. Dispersion study in a street canyon with tree planting by means of wind tunnel and numerical investigations - Evaluation of CFD data with experimental data. Atmospheric Environment 42 (37), 8640-8650.

Hajra, B., Stathopoulos, T., Bahloul, A., 2010. Assessment of pollutant dispersion from rooftop stacks: ASHRAE, ADMS and wind tunnel simulation. Building and Environment 45, 2768-2777.

Hang, J., Li, Y., 2011. Age of air and air exchange efficiency in high-rise urban areas and its link to pollutant dilution. Atmospheric Environment 45, 5572-5585.

Hanna, S.R., Brown, M.J., Camelli, F.E., Chan, S.T., et al., 2006. Detailed simulations of atmospheric flow and dispersion in downtown Manhattan. An application of five computational fluid dynamics models. Bulletin of the American Meteorological Society 87, 1713-1726.

Hargreaves, D.M., Wright, N.G., 2007. On the use of the k-ε model in commercial CFD software to model the neutral atmospheric boundary layer. Journal of Wind Engineering and Industrial Aerodynamics 95, 355-369.

Hosker Jr., R.P., 1984. Flow and diffusion near obstacles, in: Randerson, D., Atmospheric science and power production, 241-326, Technical Information Center, United States Department of Energy, Oak Ridge, TN, USA.

Hu, L.H., Huo, R., Yang, D., 2009. Large eddy simulation of fire-induced buoyancy driven plume dispersion in an urban street canyon under perpendicular wind flow. Journal of Hazardous Materials 166, 394-406.

Huber, A.H., Snyder, W.H., Lawson Jr., R.E., 1980. The effects of a squat building on short stack effluents – A wind tunnel study. U.S. Environmental Protection Agency, report EPA-600/4-80-055, North Carolina, USA.

Hunt, J.C.R., Abell, C.J., Peterka, J.A., Woo, H., 1978. Kinematical studies of the flows around free or surface-mounted obstacles; applying topology to flow visualization. Journal of Fluid Mechanics 86, 179-200.

Izarra, R., 2009. Second moment modelling for the numerical simulation of passive scalar dispersion of air pollutants in urban environments. PhD thesis, Fachbereich Maschinenbau der Universität Siegen.

Jiang, G., Yoshie, R., Shirasawa, T., Jin, X., 2012. Inflow turbulence generation for large eddy simulation in non-isothermal boundary layers. Journal of Wind Engineering and Industrial Aerodynamics 104–106, 369-378.

Jones, A.P., 1999. Indoor air quality and health. Atmospheric Environment 33, 4535-4564.

Jones, W.P., Launder, B.E., 1972. The prediction of laminarization with a two-equation model of turbulence. International Journal of Heat and Mass Transfer 15, 301-314.

Jørgensen, F.E., 2002. How to measure turbulence with hot-wire anemometers - A practical guide. Dantec Dynamics.

Kampa, M., Castanas, E., 2008. Human health effects of air pollution. Environmental Pollution 151, 362-367.

Kao, S.K., 1984. Theories of atmospheric transport and diffusion, in: Randerson, D., Atmospheric science and power production, 189-239, Technical Information Center, United States Department of Energy, Oak Ridge, TN, USA.

Kataoka, H., Mizuno, M., 2002. Numerical flow computation around aeroelastic 3D square cylinder using inflow turbulence. Wind and Structures 5, 379-392.

Katul, G., Kuhn, G., Schieldge, J., Hsieh, C.I., 1997. The ejection-sweep character of scalar fluxes in the unstable surface layer. Boundary-Layer Meteorology 83, 1-26.

Kim, J., Moin, P., 1985. Application of a fractional step method to incompressible Navier-Stokes equations. Journal of Computational Physics 59, 308-323.

Kim, J.J., Baik, J.J., 2004. A numerical study of the effects of ambient wind direction on flow and dispersion in urban street canyons using the RNG k-ε turbulence model. Atmospheric Environment 38 (19), 3039-3048.

Klein, M., 2005. An attempt to assess the quality of large eddy simulations in the context of implicit filtering. Flow, Turbulence and Combustion 75, 131-147.

Klein, M., Meyers, J., Geurts, B.J., 2008. Assessment of LES quality measures using the error landscape approach, in: Meyers, J., Geurts, B.J., Sagaut, P., Quality and reliability of Large-Eddy Simulations, 131-142, Springer.

Lateb, M., Masson, C., Stathopoulos, T., Bédard, C., 2010. Numerical simulation of pollutant dispersion around a building complex. Building and Environment 45, 1788-1798.

Launder, B.E., Spalding, D.B., 1974. The numerical computation of turbulent flows. Computer Methods in Applied Mechanics and Engineering 3, 269-289.

Launder, B.E., Reece, G.J., Rodi, W., 1975. Progress in the development of a Reynolds-stress turbulent closure. Journal of Fluid Mechanics 68, 537-566.

Launder, B.E., 1988. On the computation of convective heat transfer in complex turbulent flows. Journal of Heat Transfer 110, 1112-1118.

Lavertu, R.A., Mydlarski, L., 2005. Scalar mixing from a concentrated source in turbulent channel flow. Journal of Fluid Mechanics 528, 135-172.

Lee, J.H., Sung, H.J., Krogstad, P., 2011. Direct numerical simulation of the turbulent boundary layer over a cube-roughened wall. Journal of Fluid Mechanics 669, 397-431.

Leitl, B.M., Kastner-Klein, P., Rau, M., Meroney, R.N., 1997. Concentration and flow distributions in the vicinity of U-shaped buildings: wind-tunnel and computational data. Journal of Wind Engineering and Industrial Aerodynamics 67 & 68, 745-755.

Leitl, B.M., Meroney, R., 1997. Car exhaust dispersion in a street canyon. Numerical critique of a wind tunnel experiment. Journal of Wind Engineering and Industrial Aerodynamics 67 & 68, 293-304.

Li, W.W., Meroney, R.N., 1983a. Gas dispersion near a cubical model building – Part I. Mean concentration measurements. Journal of Wind Engineering and Industrial Aerodynamics 12, 15-33.

Li, W.W., Meroney, R.N., 1983b. Gas dispersion near a cubical model building – Part II. Concentration fluctuation measurements. Journal of Wind Engineering and Industrial Aerodynamics 12, 35-47.

Li, X.X., Liu, C.H., Leung, D.Y.C., 2008. Large-eddy simulation of flow and pollutant dispersion in high-aspect-ratio urban street canyons with wall model. Boundary-Layer Meteorology 129, 249-268.

Li, Y., Stathopoulos, T., 1997. Numerical evaluation of wind-induced dispersion of pollutants around a building. Journal of Wind Engineering and Industrial Aerodynamics 67 & 68, 757-766.

Lilly, D.K., 1992. A proposed modification of the Germano subgrid-scale closure method. Physics of Fluids A 4, 633-635.

Lim, H.C., Thomas, T.G., Castro, I.P., 2009. Flow around a cube in a turbulent boundary layer: LES and experiment. Journal of Wind Engineering and Industrial Aerodynamics 97, 96-109.

Lund, T.S., Wu, X., Squires, K.D., 1998. Generation of turbulent inflow data for spatially-developing boundary layer simulations. Journal of Computational Physics 140, 233-258.

Manickam, B., Franke, J., Muppala, S., Dinkelacker, F., 2012. Large-eddy simulation of triangular-stabilized lean premixed turbulent flames: Quality and error assessment. Flow, Turbulence and Combustion 88, 563-596.

Maruyama, T., Rodi, W., Maruyama, Y., Hiraoka, H., 1999. Large eddy simulation of the turbulent boundary layer behind roughness elements using an artificially generated inflow. Journal of Wind Engineering and Industrial Aerodynamics 83, 381-392.

Mathey, F., Cokljat, D., Bertoglio, J.P., Sergent, E., 2006. Assessment of the vortex method for large eddy simulation inlet conditions. Progress in Computational Fluid Dynamics 6, 58-67.

Meng, Y., Hibi, K., 1998. Turbulent measurements of the flow field around a high-rise building. Journal of Wind Engineering 76, 55-64.

Meroney, R.N., 1976. An algebraic stress model for stratified turbulent shear flows. Computers and Fluids 4, 93-107.

Meroney, R.N., Leitl, B.M., Rafailidis, S., Schatzmann, M., 1999. Wind-tunnel and numerical modeling of flow and dispersion about several building shapes. Journal of Wind Engineering and Industrial Aerodynamics 81, 333-345.

Meroney, R.N., 2004. Wind tunnel and numerical simulation of pollution dispersion: a hybrid approach. Working paper, Croucher Advanced Study Insitute on Wind Tunnel Modeling, Hong Kong University of Science and Technology, 6-10 December.

Meyers, J., Geurts, B.J., Baelmans, M., 2003. Database analysis of errors in large-eddy simulation. Physics of Fluids 15, 2740-2755.

Moeng, C.H., 1984. A large-eddy simulation model for the study of the planetary boundary-layer turbulence. Journal of the Atmospheric Sciences 41, 2052-2062.

Moin, P., Squires, K., Cabot, W., Lee, S., 1991. A dynamic subgrid-scale model for compressible turbulence and scalar transport. Physics of Fluids A3-11, 2746-2757.

Mokhtarzadeh-Dehghan, M.R., Akcayoglu, A., Robins, A.G., 2012. Numerical study and comparison with experiment of dispersion of a heavier-than-air gas in a simulated neutral atmospheric boundary layer. Journal of Wind Engineering and Industrial Aerodynamics 110, 10-24.

Monin, A.S., Obukhov, A.M., 1959. Basic laws of turbulent mixing in the surface layer of the atmosphere. Contrib. Geophys. Inst. Acad. Sci. USSR 24, 163-187.

Monks, P.S., Granier, C., Fuzzi, S., Stohl, A., et al., 2009. Atmospheric composition change – global and regional air quality. Atmospheric Environment 43, 5268-5350.

Murakami, S., Mochida, A., Hayashi, Y., 1990. Examining the k-ε model by means of a wind tunnel test and large-eddy simulation of the turbulence structure around a cube. Journal of Wind Engineering and Industrial Aerodynamics 35, 87-100.

Murakami, S., Mochida, A., Hayashi, Y., Sakamoto, S., 1992. Numerical study on velocity-pressure field and wind forces for bluff bodies by k-ε, ASM and LES. Journal of Wind Engineering and Industrial Aerodynamics 41-44, 2841-2852.

Murakami, S., 1993. Comparison of various turbulence models applied to a bluff body. Journal of Wind Engineering and Industrial Aerodynamics 46 & 47, 21-36.

Nozawa, K., Tamura, T., 2002. Large eddy simulation of the flow around a low-rise building immersed in a rough-wall turbulent boundary layer. Journal of Wind Engineering and Industrial Aerodynamics 90, 1151-1162.

Nozu, T., Tamura, T., Okuda, Y., Sanada, S., 2008. LES of the flow and building wall pressures in the center of Tokyo. Journal of Wind Engineering and Industrial Aerodynamics 96, 1762-1773.

Oberkampf, W.L., Trucano, T.G., 2002. Verification and validation in computational fluid dynamics. Progress in Aerospace Sciences 38, 209-272.

Ong, L., Wallace, J., 1996. The velocity field of the turbulent very near wake of a circular cylinder. Experiments in Fluids 20, 441-453.

Patnaik, G., Boris, J.P., Young, T.R., 2007. Large scale urban contaminant transport simulations with Miles. Journal of Fluids Engineering 129, 1524-1532.

Peterka, J.A., Meroney, R.N., Kothari, K.M., 1985. Wind flow patterns about buildings. Journal of Wind Engineering and Industrial Aerodynamics 21, 21-38.

Pontiggia, M., Derudi, M., Busini, V., Rota, R., 2009. Hazardous gas dispersion: A CFD model accounting for atmospheric stability classes. Journal of Hazardous Materials 171, 739-747.

Pontiggia, M., Derudi, M., Alba, M., Scaioni, M., Rota, R., 2010. Hazardous gas releases in urban areas: assessment of consequences through CFD modelling. Journal of Hazardous Materials 176, 589-596.

Pope, S.B., 2000. Turbulent flows. Cambridge University Press.

Porté-Agel, F., 2004. A scale-dependent dynamic model for scalar transport in large-eddy simulations of the atmospheric boundary layer. Boundary-Layer Meteorology 112, 81-105.

Rabl, A., 1999. Air pollution and buildings: An estimation of damage costs in France. Environmental Impact Assessment Review 19, 361-385.

Ramponi, R., Blocken, B., 2012. CFD simulation of cross-ventilation for a generic isolated building: Impact of computational parameters. Building and Environment 53, 34-48.

Raupach, M.R., Legg, B.J., 1983. Turbulent dispersion from an elevated line source: measurements of wind-concentration moments and budgets. Journal of Fluid Mechanics 136, 111-137.

Richards, P.J., Hoxey, R.P., 1993. Appropriate boundary conditions for computational wind engineering models using the k-ε turbulence model. Journal of Wind Engineering and Industrial Aerodynamics 46–47, 145-153.

Riddle, A., Carruthers, D., Sharpe, A., McHugh, C., Stocker, J., 2004. Comparisons between FLUENT and ADMS for atmospheric dispersion modelling. Atmospheric Environment 38, 1029-1038.

Roache, P.J., 1998. Verification and validation in computational science and engineering. Hermosa Publisher, Albuquerque, NM.

Robins, A., Castro, I., Hayden, P., Steggel, N., Contini, D., Heist, D., 2001a. A wind tunnel study of dense gas dispersion in a neutral boundary layer over a rough surface. Atmospheric Environment 35, 2243-2252.

Robins, A., Castro, I., Hayden, P., Steggel, N., Contini, D., Heist, D., John Taylor, T., 2001b. A wind tunnel study of dense gas dispersion in a stable boundary layer over a rough surface. Atmospheric Environment 35, 2253-2263.

Robins, A., 2003. Wind tunnel dispersion modelling some recent and not so recent achievements. Journal of Wind Engineering and Industrial Aerodynamics 91, 1777-1790.

Rodi, W., 1997. Comparison of LES and RANS calculations of the flow around bluff bodies. Journal of Wind Engineering and Industrial Aerodynamics 69-71, 55-75.

Rodi, W., Ferziger, J.H., Breuer, M., Pourquié, M., 1997. Status of Large Eddy Simulation: Results of a workshop. Journal of Fluids Engineering 119, 248-262.

Rossi, R., Philips, D.A., Iaccarino, G., 2010. A numerical study of scalar dispersion downstream of a wall-mounted cube using direct simulations and algebraic flux models. International Journal of Heat and Fluid Flow 31, 805-819.

Rossi, R., Iaccarino, G., 2009. Numerical simulation of scalar dispersion downstream of a square obstacle using gradient-transport type models. Atmospheric Environment 43, 2518-2531.

Sada, K., Sato, A., 2002. Numerical calculation of flow and stack-gas concentration fluctuation around a cubical building. Atmospheric Environment 36, 5527-5534.

Salim, S.M., Buccolieri, R., Chan, A., Sabatino, S.D., 2011a. Numerical simulation of atmospheric pollutant dispersion in an urban street canyon: Comparison between RANS and LES. Journal of Wind Engineering and Industrial Aerodynamics 99, 103-113.

Salim, S.M., Cheah, S.C., Chan, A., 2011b. Numerical simulation of dispersion in urban street canyons with avenue-like tree plantings: Comparison between RANS and LES. Building and Environment 46, 1735-1746.

Santos, J.M., Reis, N.C., Goulart, E.V., Mavroidis, I., 2009. Numerical simulation of flow and dispersion around an isolated cubical building: The effect of the atmospheric stratification. Atmospheric Environment 43 (34), 5484-5492.

Savory, E., Perret, L., Rivet, C., 2011. Modelling the flow regime in a simple urban-type street canyon. International workshop on physical modelling of flow and dispersion phenonema, Hamburg, Germany, August 22-24.

Schatzmann, M., Olesen, H., Franke, J., 2010. COST 732 model evaluation case studies: approach and results. COST Action 732.

Schumann, U., 1975. Subgrid scale model for finite difference simulations of turbulent flows in plane channels and annuli. Journal of Computational Physics 18, 376-404.

Sergent, E., 2002. Vers une méthode de couplage entre la simulation des grandes échelles et les modèles statistiques. PhD thesis, Ecole Centrale de Lyon.

Shah, K.B., Ferziger, J.B., 1997. A fluid mechanicians view of wind engineering: Large eddy simulation of flow past a cubic obstacle. Journal of Wind Engineering and Industrial Aerodynamics 67-68, 211-224.

Shaw, R.H., Tavangar, J., Ward, D.P., 1983. Structure of the Reynolds stress in a canopy layer. Journal of Climate and Applied Meteorology 22, 1922-1931.

Shi, R.F., Cui, G.X., Wang, Z.S., Xu, C.X., Zhang, Z.S., 2008. Large eddy simulation of wind field and plume dispersion in building array. Atmospheric Environment 42, 1083-1097.

Shih, T.H., Liou, W.W., Shabbir, A., Yang, Z., Zhu, J., 1995. A new k-ε eddy-viscosity model for high Reynolds number turbulent flows. Computers and Fluids 24-3, 227-238.

Simoëns, S., Wallace, J.M., 2008. The flow across a street canyon of variable width—Part 2: Scalar dispersion from a street level line source. Atmospheric Environment 42, 2489-2503.

Smagorinsky, J., 1963. General circulation experiments with the primitive equations. I. The basic experiment. Monthly Weather Review 91, 99-164.

Solazzo, E., Cai, X., Vardoulakis, S., 2008. Modelling wind flow and vehicle-induced turbulence in urban streets. Atmospheric Environment 42, 4918-4931.

Srebric, J., Chen, Q., 2002. An example of verification, validation, and reporting of indoor environment CFD analyses. ASHRAE Transactions 108, 185-194.

Stathopoulos, T., 1984. Design and fabrication of a wind tunnel for building aerodynamics. Journal of Wind Engineering and Industrial Aerodynamics 16, 361-376.

Stathopoulos, T., Lazure, L., Saathoff, P., Gupta, A., 2004. The effect of stack height, stack location and roof-top structures on air intake contamination - A laboratory and full-scale study. IRSST, report R-392, Montreal, Canada.

Sutton, O.G., 1947. The theoretical distribution of airborne pollution from factory chimneys. Quarterly Journal of the Royal Meteorological Society 73, 426-436.

Tamura, T., 2008. Towards practical use of LES in wind engineering. Journal of Wind Engineering and Industrial Aerodynamics 96, 1451-1471.

Tennekes, H., 1973. The logarithmic wind profile. Journal of the Atmospheric Sciences 30, 234-238.

Thomas, T.G., Williams, J.J.R., 1997. Development of a parallel code to simulate skewed flow over a bluff body. Journal of Wind Engineering and Industrial Aerodynamics 67 & 68, 155-167.

Thomas, T.G., Williams, J.J.R., 1999. Generating a wind environment for large eddy simulation of bluff body flows. Journal of Wind Engineering and Industrial Aerodynamics 82, 189-208.

Tominaga, Y., Murakami, S., Mochida, A., 1997. CFD prediction of gaseous diffusion around a cubic model using a dynamic mixed SGS model based on composite grid technique. Journal of Wind Engineering and Industrial Aerodynamics 67 & 68, 827-841.

Tominaga, Y., Stathopoulos, T., 2007. Turbulent Schmidt numbers for CFD analysis with various types of flowfield. Atmospheric Environment 41, 8091-8099.

Tominaga, Y., Mochida, A., Murakami, S., Sawaki, S., 2008a. Comparison of various revised k-ε models and LES applied to flow around a high-rise building model with 1:1:2 shape placed within the surface boundary layer. Journal of Wind Engineering and Industrial Aerodynamics 96, 389-411.

Tominaga, Y., Mochida, A., Yoshie, R., Kataoka, H., Nozu, T., Yoshikawa, M., Shirasawa, T., 2008b. AIJ guidelines for practical applications of CFD to pedestrian wind environment around buildings. Journal of Wind Engineering and Industrial Aerodynamics 96, 1749-1761.

Tominaga, Y., Stathopoulos, T., 2009. Numerical simulation of dispersion around an isolated cubic building: Comparison of various types of k-ε models. Atmospheric Environment 43 (20), 3200-3210.

Tominaga, Y., Stathopoulos, T., 2010. Numerical simulation of dispersion around an isolated cubic building: model evaluation of RANS and LES. Building and Environment 45 (10), 2231-2239.

Tominaga, Y., Stathopoulos, T., 2011. CFD modeling of pollution dispersion in a street canyon: Comparison between LES and RANS. Journal of Wind Engineering and Industrial Aerodynamics 99, 340-348.

Tominaga, Y., Stathopoulos, T., 2012. CFD Modeling of pollution dispersion in building array: Evaluation of turbulent scalar flux modeling in RANS model using LES results. Journal of Wind Engineering and Industrial Aerodynamics 104–106, 484-491.

Tseng, Y.H., Meneveau, C., Parlange, M.B., 2006. Modeling flow around bluff bodies and predicting urban dispersion using large eddy simulation. Environmental Science & Technology 40, 2653-2662.

Ubertini, S., Desideri, U., 2000. Flow development and turbulence length scales within an annular gas turbine exhaust diffuser. Experimental Thermal and Fluid Science 22, 55-70.

van Hooff, T., Blocken, B., 2010. Coupled urban wind flow and indoor natural ventilation modelling on a high-resolution grid: A case study for the Amsterdam ArenA stadium. Environmental Modelling & Software 25, 51-65.

Vinçont, J.Y., Simoëns, S., Ayrault, M., Wallace, J.M., 2000. Passive scalar dispersion in a turbulent boundary layer from a line source at the wall and downstream of an obstacle. Journal of Fluid Mechanics 424, 127-167.

Vreman, A.W., Geurts, B.J., Kuerten, J.G.M., 1996. Comparison of numerical schemes in large eddy simulation of the temporal mixing layer. International Journal for Numerical Methods in Fluids 22, 299-311.

Walton, A., Cheng, A.Y.S., 2002. Large-eddy simulation of pollution dispersion in an urban street canyon–Part II: idealised canyon simulation. Atmospheric Environment 36, 3615-3627.

Wang, B.C., Yee, E., Lien, F.S., 2009. Numerical study of dispersing pollutant clouds in a built-up environment. International Journal of Heat and Fluid Flow 30, 3-19.

Wang, H.F., Zhou, Y., 2009. The finite-length square cylinder near wake. Journal of Fluid Mechanics 638, 453-490.

Xie, Z.T., Castro, I., 2008. Efficient generation of inflow conditions for large eddy simulation of street-scale flows. Flow, Turbulence and Combustion 81, 449-470.

Xie, Z.T., Castro, I.P., 2009. Large-eddy simulation for flow and dispersion in urban streets. Atmospheric Environment 43, 2174-2185.

Xie, Z., Hayden, P., Voke, P.R., Robins, A.G., 2004a. Large-eddy simulation of dispersion: comparison between elevated and ground-level sources. Journal of Turbulence 5, 16 pp.

Xie, Z., Voke, P.R., Hayden, P., Robins, A.G., 2004b. Large-Eddy Simulation of Turbulent Flow Over a Rough Surface. Boundary-Layer Meteorology 111, 417-440.

Yakhot, A., Anor, T., Liu, H., Nikitin, N., 2006a. Direct numerical simulation of turbulent flow around a wall-mounted cube: spatio-temporal evolution of large-scale vortices. Journal of Fluid Mechanics 566, 1-9.

Yakhot, A., Liu, H., Nikitin, N., 2006b. Turbulent flow around a wall-mounted cube: A direct numerical simulation. International Journal of Heat and Fluid Flow 27, 994-1009.

Yakhot, V., Orszag, S.A., Thangam, S., Gatski, T.B., Speziale, C.G., 1992. Development of turbulence models for shear flows by a double expansion technique. Physics of Fluids A4, 1510-1520.

Yoshie, R., Mochida, A., Tominaga, Y., Kataoka, H., Harimoto, K., Nozu, T., Shirasawa, T., 2007. Cooperative project for CFD prediction of pedestrian wind environment in the

Architectural Institute of Japan. Journal of Wind Engineering and Industrial Aerodynamics 95, 1551-1578.

Yoshie, R., Jiang, G., Shirasawa, T., Chung, J., 2011. CFD simulations of gas dispersion around high-rise building in non-isothermal boundary layer. Journal of Wind Engineering and Industrial Aerodynamics 99, 279-288.

Younis, B.A., Speziale, C.G., Clark, T.T., 2005. A rational model for the turbulent scalar fluxes. Proceedings of the Royal Society A 461, 575-594.

List of figures

List of tables

Curriculum vitae and list of publications

Curriculum vitae

Pierre Gousseau was born in 1986 in Douai, France. He studied at *Ecole Centrale de Lille* (Lille, France), a multi-disciplinary engineering school from which he obtained the equivalent of a Master degree in 2007. In the framework of a double-diploma agreement, he spent the last year of this Master program at *Université Libre de Bruxelles* (Brussels, Belgium) to specialize in the field of aeronautics. Afterwards, he enrolled the Research Master program (former Diploma Course) of the *von Karman Institute for Fluid Dynamics* (Brussels region, Belgium) and graduated with honors from the Environmental & Applied Fluid Dynamics department in 2008. The same year he started his PhD on numerical modeling of wind-induced pollutant dispersion at *Eindhoven University of Technology*, in the department of the Built Environment.

Pierre has published 3 papers in international journals (ISI) with peer review, and 7 papers in the proceedings of international conferences. He is a reviewer for several ISI journals, including *Atmospheric Environment*, *Journal of Hazardous Materials* and *Journal of Wind Engineering and Industrial Aerodynamics*. He was also involved in the organization of the *13th International Conference on Wind Engineering* (Amsterdam, The Netherlands) as a member of the scientific working group. Pierre was awarded the Best Student Paper Prize (third place award) at the *2012 International Congress on Environmental Modelling and Software* (Leipzig, Germany). Since 2011, he is working in a collaborative project between *Eindhoven University of Technology* and TNO (*Netherlands Organization for Applied Scientific Research*) on the development of a consistent CFD model for the atmospheric boundary layer.

List of publications

Journal papers

− P. Gousseau, B. Blocken, T. Stathopoulos, G.J.F. van Heijst. *CFD simulation of near-field pollutant dispersion on a high-resolution grid: A case study by LES and RANS for a building group in downtown Montreal.* Atmospheric Environment 45 (2011) 428-438.   IF[1]: 3.465

− P. Gousseau, B. Blocken, G.J.F. van Heijst. *CFD simulation of pollutant dispersion around isolated buildings: On the role of convective and turbulent mass fluxes in the prediction accuracy.* Journal of Hazardous Materials 194 (2011) 422-434.   IF: 4.173

− P. Gousseau, B. Blocken, G.J.F. van Heijst. *Large-Eddy Simulation of pollutant dispersion around a cubical building: Analysis of the turbulent mass transport mechanism by unsteady concentration and velocity statistics.* Environmental Pollution 167 (2012) 47-57.   IF: 3.746

Journal papers – Submitted, under review

− P. Gousseau, B. Blocken, G.J.F. van Heijst. *Quality assessment of Large-Eddy Simulation of wind flow around a high-rise building: validation and solution verification.* Submitted to: Computers & Fluids.   IF: 1.810

− P. Gousseau, B. Blocken, T. Stathopoulos, G.J.F. van Heijst. *Micro-scale pollutant dispersion in an urban area: Investigation of the mass transport mechanism by Large-Eddy Simulation.* Submitted to: Building and Environment.   IF: 2.400

Journal papers – Under preparation

− T. van Hooff, B. Blocken, P. Gousseau, G.J.F. van Heijst. *Analysis of the standard gradient-diffusion hypothesis for indoor dispersion modelling in a slot-ventilated enclosure.*

Peer-reviewed conference papers

− P. Gousseau, B. Blocken, T. Stathopoulos, G.J.F. van Heijst. *CFD simulation of pollutant dispersion around buildings: Comparison between RANS k-ε and LES approaches.* 5th International Symposium on Computational Wind Engineering, Chapel Hill, USA, May 23-27, 2010.

− B. Blocken, P. Gousseau, G.J.F. van Heijst. *A numerical study of gas dispersion over a generic frigate: RANS versus LES CFD simulations.* Developments in Marine CFD, London, March 22-23, 2011

---

[1] Impact Factor (October 2012).

– P. Gousseau, B. Blocken, T. Stathopoulos, G.J.F. van Heijst. *Numerical simulation of near-field pollutant dispersion in downtown Montreal: Comparison between LES and RANS*. 13th International Conference on Wind Engineering, Amsterdam, The Netherlands, July 10-15, 2011.

– P. Gousseau, B. Blocken, G.J.F. van Heijst. *Pollutant dispersion around isolated buildings: On the prediction of convective and turbulence mass fluxes by LES and RANS*. 13th International Conference on Wind Engineering, Amsterdam, The Netherlands, July 10-15, 2011.

– P. Gousseau, B. Blocken, G.J.F. van Heijst. *Large-Eddy simulation of pollutant dispersion in downtown Montreal: Evaluation of the convective and turbulent mass fluxes*. 2012 International Congress on Environmental Modelling and Software, Leipzig, Germany, July 1-5, 2012. <u>Best Student Paper Prize (Third Place Award)</u>

– P. Gousseau, B. Blocken, G.J.F. van Heijst. *Large-Eddy Simulation of wind flow around a high-rise building: validation and quality assurance*. Seventh International Colloquium on Bluff Body Aerodynamics & Applications, Shanghai, China, September 2-6, 2012.

– P. Gousseau, B. Blocken, G.J.F. van Heijst. *Large-Eddy Simulation of pollutant dispersion around an isolated building: unsteady concentration and flow statistics*. Seventh International Colloquium on Bluff Body Aerodynamics & Applications, Shanghai, China, September 2-6, 2012.

Conference papers – Under preparation

– P. Gousseau, B. Blocken, G.J.F. van Heijst. *LES of wind flow around a high-rise building: validation and error estimation*. 2013 European and African Conference on Wind Engineering, Cambridge, United Kingdom, July 7-11, 2013.

– P. Gousseau, B. Blocken, G.J.F. van Heijst, S. van Rattingen, I. Kalkman, C. van Bentum. *Large-Eddy Simulation of wind flow above a two-dimensional fence*. 2013 European and African Conference on Wind Engineering, Cambridge, United Kingdom, July 7-11, 2013.

– B. Blocken, P. Gousseau, C. van Dronkelaar. *CFD study on wind energy potential in passages between converging and diverging building configurations*. Building Simulation 2013, Chambéry, France, August 25-28, 2013.

– T. van Hooff, B. Blocken, P. Gousseau, G.J.F. van Heijst. *An analysis on the validity of the gradient-diffusion hypothesis for indoor pollutant dispersion modelling with CFD*. Building Simulation 2013, Chambéry, France, August 25-28, 2013.